

Decoding nutrient sensing and metabolic regulation in the *Drosophila* Hipp tumor model

by

Kenneth Kin Lam Wong

B.Sc., University of Hong Kong, 2013

Thesis Submitted in Partial Fulfillment of the
Requirements for the Degree of
Doctor of Philosophy

in the

Department of Molecular Biology and Biochemistry
Faculty of Science

© Kenneth Kin Lam Wong 2020
SIMON FRASER UNIVERSITY
Summer 2020

Approval

Name: **Kenneth Kin Lam Wong**

Degree: **Doctor of Philosophy**

Title: **Decoding nutrient sensing and metabolic regulation in the *Drosophila* Hipp tumor model**

Examining Committee:

Chair: **Tim Audas**
Assistant Professor

Esther M. Verheyen
Senior Supervisor
Professor

Sharon M. Gorski
Supervisor
Professor

Nicholas Harden
Supervisor
Professor

Nancy Hawkins
Internal Examiner
Associate Professor

Jason Tennessen
External Examiner
Associate Professor
Department of Biology
Indiana University Bloomington

Date Defended/Approved: June 29, 2020

Abstract

Sustaining proliferative signals and deregulating cellular energetics are two hallmarks of cancer. However, how oncogenic signals respond to nutrients and coordinate with metabolic states remains poorly understood. Here, using *Drosophila melanogaster* as a genetic model organism, we establish an *in vivo* tumor model with elevation of oncogenic fly Homeodomain-interacting protein kinase (Hipk). This tumor model features cell hyperproliferation, tumor invasion, and cellular changes reminiscent of epithelial-to-mesenchymal transition, including induction of matrix metalloproteinases and loss of E-cadherin. The tumor phenotypes arise from the redundant and/or synergistic effects of more than one perturbed oncogenic signaling pathway caused by elevated Hipk, underlying the need for targeting multiple signaling molecules to reduce tumor growth. To search for simpler therapeutic strategies, we examine the metabolic requirements of Hipk tumor growth.

We find that high sugar potentiates the tumorigenic potential of Hipk. Mechanistically, nutrient sensors O-GlcNAc transferase (OGT) in the hexosamine signaling pathway and salt-inducible kinase 2 (SIK2) in the insulin signaling pathway physically bind to Hipk and induce covalent post-translational modifications of Hipk, namely O-GlcNAcylation and phosphorylation, respectively. Both nutrient sensors are required for Hipk protein expression and synergize with Hipk to drive tumor progression. Our works demonstrate two modes of nutritional regulation of Hipk, which can accelerate Hipk tumor growth in nutrient-rich conditions like diabetes. We further characterize the metabolic profile of the Hipk tumor model. The tumor cells display the oncogene Myc-induced aerobic glycolysis, which in turn functions to perpetuate Myc accumulation post-transcriptionally, forming a positive feedback loop. Disruption of the loop abrogates Hipk tumor growth. Downstream of the loop, the tumor cells harbor an accumulation of highly fused, functional mitochondria. Targeted inhibition of a Pd subunit of the respiratory complex I blocks the tumor growth. Our works reveal that both aerobic glycolysis and active mitochondrial metabolism are required to promote Hipk tumor growth.

Taken together, using the *Drosophila* Hipk tumor model, we functionally characterize the nutrient sensing and metabolic crosstalk with cell signaling, and reveal potential metabolic vulnerabilities that could be exploited in cancer treatment.

Keywords: *Drosophila* tumor model; Hipk; OGT; SIK2; aerobic glycolysis; mitochondrial metabolism

Dedication

*When I consider thy heavens, the work of thy fingers, the moon and
the stars, which thou hast ordained;*

*What is man, that thou art mindful of him? and the son of man, that
thou visitest him?*

Psalm 8:3-4

Thanks to God for creating this universe and working wonders in my life.

Acknowledgements

The completion of my PhD studies would not have been possible without the support and nurturing offered by my senior supervisor, **Dr. Esther Verheyen**. Deepest thanks to Esther for taking me in the lab, giving me tons of opportunities to grow and excel as a scientist, encouraging me to be curious and raise questions, connecting me with marvellous scientists and providing insightful guidance whenever I need. Esther, you are a superb mentor.

Thanks to my supervisory committee, **Dr. Sharon Gorski** and **Dr. Nicholas Harden**, for offering continuous support and writing me reference letters for scholarships and job applications. Thanks to my thesis examiners, **Dr. Nancy Hawkins** and **Dr. Jason Tennessen**, for evaluating my work. Thanks to **Dr. Tim Audas** for chairing my defence.

Thanks to the members of Esther's lab who joined before me, **Jessica Blaquiere**, **Elizabeth Hoesing**, **Dr. Eric Hall** and **Nathan Wray**, those who joined after me, **Nicole Yoo**, **Jin Wu**, **Dr. Gritta Tettweiler**, **Stephen Kinsey**, **Landiso Madonsela**, **Thalia Wiens**, **Ronnie Tse**, **Jenny Liao**, **Nivi Ramkumar**, **Katja MacCharles**, and undergraduates, **Jessica Parker**, **Devon Chohan**, **Endre Sinkovics**, **Gerry Shipman** and so forth, for all the help on experiments and discussions. Special thanks to **Jessica Blaquiere** and **Rubia Chung** for the prior screening work.

Thanks to our collaborators **Dr. David Vocadlo**, **Dr. Ta-wei Liu**, **Dr. Don Sinclair**, **Dr. Nicholas Harden**, **Claire Shih**, **Dr. Kay-Hooi Khoo**, **Yi-Yun Chen**, **Dr. Dipankar Sen** and **Prince Lat** for working together as terrific teams. Special thanks to **Dr. Ta-wei Liu**, **Dr. Yanping Zhu** and **Dr. Simon Wang** for sharing reagents and practical advice.

Thanks to the Department staff, **Mimi Fourie**, **Christine Beauchamp** and **Nancy Suda** for administrative work, and **Deidre de Jong-Wong**, **Tim Heslip** and **Ziwei Ding** for technical support.

Finally, thanks to my family, relatives, friends and brothers and sisters in Christ for support throughout my PhD studies.

Table of Contents

Approval	ii
Abstract	iii
Dedication	v
Acknowledgements.....	vi
Table of Contents.....	vii
List of Tables.....	xii
List of Figures.....	xiii
List of Acronyms	xvii
Chapter 1. Introduction	1
1.1. Fundamentals of cancer	1
1.1.1. Cancer as genetic disease	2
1.1.2. Cancer progression and metastasis.....	5
1.1.3. Epithelial-to-mesenchymal transition	7
1.2. Nutrient sensing pathways in cancer.....	8
1.2.1. The hexosamine biosynthetic pathway and O-GlcNAcylation.....	9
1.2.2. The InR/AMPK-mTORC1 signaling network.....	12
1.3. Metabolic reprogramming.....	15
1.3.1. Aerobic glycolysis (the Warburg effect)	16
1.3.2. Mitochondrial metabolism.....	18
1.4. <i>Drosophila</i> as a genetic model of human cancers	20
1.4.1. Models of human carcinomas	23
1.4.2. Models of metabolic reprogramming.....	25
1.5. Homeodomain-interacting protein kinases (HIPKs)	28
1.5.1. Developmental roles of HIPKs	31
1.5.2. Regulation of HIPK2 by post-translational modifications.....	32
1.5.3. Roles of HIPK2 in human diseases.....	34
1.6. Aims of the thesis.....	35
Chapter 2. Hipk promotes tumorigenesis and metastatic-like cell behavior	37
2.1. Contributions to the Chapter.....	37
2.2. Abstract.....	38
2.3. Introduction	38
2.4. Results	41
2.4.1. Elevated Hipk causes tumorous growths.....	41
2.4.2. Elevated Hipk induces cell invasive behaviors	43
2.4.3. Elevated Hipk causes MMP1 induction and disruption in the basement membrane	45
2.4.4. Elevated Hipk alters expression levels of additional EMT markers including E-cadherin and Twist.....	47
2.4.5. Hipk-mediated tumorigenic phenotypes cannot be attributed to a single targeted pathway.....	49

2.4.6.	Hipk-mediated tumorigenic phenotypes are attributed to at least Hippo-Yki and JNK signaling pathways.....	54
2.4.7.	Perturbing signaling pathways individually does not phenocopy Hipk-induced phenotypes.....	55
2.4.8.	Hipk synergizes with perturbed signaling pathways to exacerbate tumor progression.....	57
2.5.	Discussion.....	59
2.5.1.	Elevated Hipk as an <i>in vivo</i> tumor model featuring neoplastic growth with invasion	59
2.5.2.	Hipk tumor growth likely arises from a cumulative effect of perturbations in multiple signaling pathways	60
Chapter 3. The nutrient sensor OGT regulates Hipk stability and tumorigenic activity.....		62
3.1.	Contributions to the Chapter.....	62
3.2.	Abstract.....	63
3.3.	Introduction	63
3.4.	Results	66
3.4.1.	High dietary sugar potentiates Hipk-induced tissue growth abnormalities....	66
3.4.2.	The high sugar effect on Hipk activity depends on the HBP and OGT	71
3.4.3.	OGT synergizes with Hipk to drive tumor growth	74
3.4.4.	OGT is necessary for Hipk-induced tissue growth abnormalities.....	77
3.4.5.	Depletion of OGT or GFAT reduces Hipk protein levels.....	79
3.4.6.	OGT stabilizes Hipk by preventing Hipk from proteasome degradation.	82
3.4.7.	OGT binds to and O-GlcNAcylates Hipk.....	85
3.4.8.	Elevated Hipk may activate the HBP-OGT metabolic pathway, forming a positive feedback loop.....	88
3.4.9.	HIPK2 O-GlcNAcylation by OGT promotes HIPK2 protein stability.....	90
3.5.	Discussion.....	96
Chapter 4. Insulin-InR-SIK2 signaling regulates Hipk phosphorylation and tumorigenic activity.....		98
4.1.	Contributions to the Chapter.....	98
4.2.	Abstract.....	99
4.3.	Introduction	99
4.4.	Results	101
4.4.1.	The high sugar effect on Hipk activity depends on InR and SIKs	101
4.4.2.	Insulin-InR signaling induces Hipk hyper-phosphorylation.....	103
4.4.3.	The insulin-InR effect on Hipk phosphorylation is SIK2-dependent.....	106
4.4.4.	SIK2 binds to Hipk and induces Hipk hyper-phosphorylation.....	107
4.4.5.	InR-SIK2 signaling synergizes with Hipk to drive tumor growth	109
4.4.6.	Loss of SIK2 reduces exogenous Hipk protein levels	111
4.4.7.	Hipk-6A is a hyper-phosphorylated and constitutively active form.....	112
4.4.8.	Elevated Hipk drives InR upregulation, forming a positive feedback loop ..	115
4.5.	Discussion.....	117

4.5.1.	Two modes of nutrient sensing PTMs of Hipk – Phosphorylation and O-GlcNAcylation	117
4.5.2.	Regulation of Hipk by a tight balance of SIK2 and SIK3 activities	119
Chapter 5. A positive feedback loop between Myc and aerobic glycolysis sustains tumor growth in the Hipk tumor model.....		120
5.1.	Contributions to the Chapter.....	120
5.2.	Abstract	121
5.3.	Introduction	121
5.4.	Results	124
5.4.1.	Hipk tumor cells exhibit elevated glucose uptake	124
5.4.2.	Hipk tumor cells exhibit low intracellular glucose levels.	128
5.4.3.	Elevated Hipk induces robust expression of a subset of glycolytic genes ..	130
5.4.4.	Elevated Hipk drives dMyc upregulation in a region-specific manner.....	132
5.4.5.	Elevated Hipk upregulates dMyc likely through convergence of multiple perturbed signaling cascades	135
5.4.6.	Hipk-induced dMyc governs aerobic glycolysis and tumor growth.....	138
5.4.7.	Aerobic glycolysis (the Warburg effect) is essential to tumor growth through sustaining ectopic dMyc expression	140
5.5.	Discussion.....	147
5.5.1.	dMyc-driven aerobic glycolysis in the Hipk tumor model.....	147
5.5.2.	A feedback loop between dMyc and aerobic glycolysis as a metabolic vulnerability in tumor cells	148
5.5.3.	Potential pro-tumorigenic roles of the Pfk and Pfk2 in addition to their core biochemical role in glycolysis.....	150
Chapter 6. Pdsw (NDUFB10) of Respiratory Complex I as a metabolic vulnerability in the Hipk tumor model.....		151
6.1.	Contributions to the Chapter.....	151
6.2.	Abstract	152
6.3.	Introduction	152
6.4.	Results	155
6.4.1.	Elevated Hipk promotes mitochondrial fusion and branching	155
6.4.2.	Hipk tumor cells abound with active mitochondria.....	159
6.4.3.	Hipk tumor cells do not display ROS accumulation	165
6.4.4.	Mitochondrial fusion is dispensable for Hipk-mediated tumorigenesis.....	168
6.4.5.	Targeted but not generic inhibition of mitochondrial activity suppresses Hipk tumor growth.....	171
6.4.6.	Complex subunit-dependent effects on ROS production in Hipk tumor cells	
	174	
6.4.7.	The active mitochondrial metabolism depends on the positive feedback loop between Myc and aerobic glycolysis	177
6.5.	Discussion.....	178
6.5.1.	Hipk elevation as an <i>in vivo</i> tumor model with active mitochondria	178
6.5.2.	Regulation of mitochondrial fusion and activity by separate mechanisms..	179
6.5.3.	A Pd subunit of complex I as a metabolic vulnerability in cancers	180

Chapter 7. Conclusive remark.....	182
Chapter 8. Materials and Methods	184
8.1. Materials and methods for Chapter 2	184
8.1.1. Drosophila culture.....	184
8.1.2. Immunofluorescence staining.....	184
8.1.3. Measurements of proliferation and invasiveness.....	185
8.2. Materials and methods for Chapter 3	186
8.2.1. Drosophila culture.....	186
8.2.2. Immunofluorescence staining.....	186
8.2.3. Quantitative real time-PCR (qRT-PCR)	187
8.2.4. Immunoblotting	187
8.2.5. Cycloheximide (CHX) chase assay.....	188
8.2.6. Co-immunoprecipitation	188
8.2.7. WGA pull down	188
8.2.8. GalNAz feeding and biotin-conjugation reaction.....	189
8.2.9. In vitro GalT labeling.....	189
8.2.10. Mammalian cell culture	190
8.2.11. Site-directed mutagenesis	190
8.2.12. Mapping of O-GlcNAc sites of human HIPK2	191
8.2.13. Statistical analysis.....	192
8.3. Materials and methods for Chapter 4	193
8.3.1. Drosophila culture.....	193
8.3.2. Immunofluorescence staining.....	193
8.3.3. Quantitative real time-PCR (qRT-PCR)	194
8.3.4. Immunoblotting	194
8.3.5. Co-immunoprecipitation	195
8.3.6. Insulin stimulation	195
8.3.7. Lambda phosphatase treatment	195
8.3.8. Site-directed mutagenesis.....	195
8.3.9. Generation of transgenic fly	196
8.4. Materials and methods for Chapter 5	197
8.4.1. Drosophila culture.....	197
8.4.2. Immunofluorescence staining.....	197
8.4.3. Quantitative real time-PCR (qRT-PCR)	198
8.4.4. 2-NBDG uptake	199
8.4.5. Intracellular glucose FRET analysis.....	199
8.4.6. Pyruvate measurement	199
8.4.7. Statistics.....	200
8.5. Materials and methods for Chapter 6	201
8.5.1. Drosophila culture.....	201
8.5.2. Immunofluorescence staining.....	201
8.5.3. Quantification of mitochondrial morphology	202
8.5.4. MitoTracker Red staining	202

8.5.5.	TMRM staining.....	202
8.5.6.	ROS assay.....	202
8.5.7.	Statistics.....	203
References.....		204
Appendix A.		237
Amino acid sequence of the myc-tagged human HIPK2 protein	237	
Amino acid sequence of the HA-tagged <i>Drosophila</i> Hipk protein.....	238	
<i>In silico</i> identification of putative O-GlcNAc sites in human HIPK2 and <i>Drosophila</i> Hipk	239	

List of Tables

Table 1-1. Types of genetic mutations.....	2
Table 1-2. Oncogenes and tumor suppressor genes commonly found in cancer.....	3
Table 1-3. The TNM classification system	5
Table 1-4. Cancer stages	5
Table 1-5. Types of abnormal cell growths	6
Table 1-6. The invasion-metastasis cascade.....	7
Table 1-7. Examples of nutrient sensing pathways	8
Table 1-8. Effects of direct O-GlcNAcylation on protein activity	11
Table 1-9. Six hallmarks of cancer metabolism (Pavlova and Thompson, 2016)	15
Table 1-10. Well-known glycolytic inducers and their actions.	17
Table 1-11. Hyperplastic or neoplastic (benign or malignant) tumor models.	24
Table 1-12. <i>Drosophila</i> tumor models with characterization of metabolic profiles	25
Table 1-13. Binding partners or protein substrates of HIPKs	29
Table 2-1. Genotypes of flies used in the panels of Figure 2.9 for the quantification of the proliferative and invasive indexes.....	51
Table 2-2. Signaling pathway reagents used in this study.....	56
Table 5-1. A list of <i>Drosophila</i> genes studied in this work with their human homologs.	123
Table 6-1. A list of <i>Drosophila</i> mitochondrial complex subunits studied in this work with their human homologs.	174
Table 8-1. Primers used for qRT-PCR	187
Table 8-2. Primers used for site-directed mutagenesis to replace the identified O-GlcNAc sites with alanine.....	191
Table 8-3. Primers used for qRT-PCR	194
Table 8-4. Primers used for site-directed mutagenesis to replace the putative SIK target sites with alanine in <i>Drosophila</i> Hipk.....	196
Table 8-5. Primers used for subcloning.....	196
Table 8-6. Primer sequences for profiling the mRNA expression of glycolytic genes...	198

List of Figures

Figure 1.1. Stepwise progression of carcinoma (epithelial cancer)	6
Figure 1.2. Glycolysis and the hexosamine biosynthetic pathway (HBP)	9
Figure 1.3. O-GlcNAcylation by OGT.....	10
Figure 1.4. The InR/AMPK-mTORC1 signaling network.....	12
Figure 1.5. Wing imaginal discs.....	20
Figure 1.6. Genetic tools to manipulate gene expression.....	21
Figure 1.7. The Gal4-UAS system.....	22
Figure 1.8. The FLP-out system.....	22
Figure 1.9. Schematic diagram of human HIPK2 (hHIPK2).....	28
Figure 1.10. Examples of HIPK2 post-translational modifications.....	32
Figure 1.11. Aims of the thesis	35
Figure 2.1. Hipk regulates numerous signaling pathways.	40
Figure 2.2. Hipk induces overgrowths in larval imaginal discs.	41
Figure 2.3. Hipk induces hyperproliferation, Caspase 3 activation and cell death.....	42
Figure 2.4. Elevated Hipk induces cell invasion and metastatic behaviors.....	43
Figure 2.5. Elevated Hipk induces MMP1 upregulation and disruption of basememt membrane.....	45
Figure 2.6. Elevated Hipk leads to downregulation of E-cadherin and upregulation of Twist.....	47
Figure 2.7. Hipk-mediated tumorigenic phenotypes are completely rescued by co-expression of <i>hipk-RNAi</i>	49
Figure 2.8. Loss of individual signaling pathway components cannot suppress the Hipk tumorigenic phenotypes.....	50
Figure 2.9. Quantification of proliferative areas in wing discs and the degree of invasiveness.....	51
Figure 2.10. Validation of signaling pathway disruptions by reagents used in study.....	52
Figure 2.11. Phenotypes of signaling pathway disruptors used in study.....	53
Figure 2.12. Hipk-mediated tumorigenic phenotypes are largely mediated by Hippo and JNK signaling pathways.....	54
Figure 2.13. Overexpression of individual signaling pathway components does not phenocopy the tumorigenic phenotypes induced by elevated Hipk.....	56
Figure 2.14. Hipk synergizes with other tumor models to exacerbate tumor progression	58
Figure 3.1. The hexosamine biosynthetic pathway HBP	63
Figure 3.2. We used a sensitized Hipk genetic background to investigate potential modifiers of Hipk.	67
Figure 3.3. High dietary sugar potentiates Hipk-induced growth abnormalities.	68
Figure 3.4. High sugar promotes cell proliferation in <i>hipk</i> -overexpressing eye discs.	69

Figure 3.5. High sugar does not induce any tissue growth abnormalities in the absence of <i>hipk</i> overexpression.....	70
Figure 3.6. High sugar potentiates Hipk activity through GFATs and OGT.....	71
Figure 3.7. Validation of tools used in this study to modulate GFAT and OGT expression levels.....	72
Figure 3.8. GFATs and OGT potentiate Hipk-mediated growth abnormalities under normal diet conditions.....	73
Figure 3.9. OGT synergizes with Hipk to drive tumor growth.....	74
Figure 3.10. Co-expression of <i>hipk</i> and <i>OGT</i> causes a developmental delay in the timing of pupariation.....	75
Figure 3.11. Tissues co-expressing <i>hipk</i> and <i>OGT</i> display changes in markers associated with cancer growth.....	76
Figure 3.12. Tissues overexpressing <i>hipk</i> or <i>OGT</i> alone do not show any abnormal phenotypes.....	76
Figure 3.13. OGT is necessary for Hipk-induced severe leg malformation phenotype... ..	77
Figure 3.14. OGT is required for Hipk-induced tumor growth.....	78
Figure 3.15. Depletion of OGT reduces Hipk protein levels.....	79
Figure 3.16. Depletion of GFAT reduces Hipk protein levels.....	80
Figure 3.17. OGT stabilizes Hipk by preventing Hipk from proteasomal degradation.	82
Figure 3.18. Elevated OGT increases protein levels of endogenous Hipk.....	83
Figure 3.19. OGT binds to Hipk.....	85
Figure 3.20. OGT O-GlcNAcylates Hipk.....	86
Figure 3.21. GALT selectively labels Hipk with UDP-GalNAz.....	86
Figure 3.22. Hipk tumor cells display mild OGT upregulation and robust O-GlcNAc signals.....	89
Figure 3.23. OGT modulates HIPK2 protein levels in mammalian cells.....	90
Figure 3.24. Effects of OGT on the HIPK2 transcript levels.	91
Figure 3.25. O-GlcNAc sites in human HIPK2.	92
Figure 3.26. HIPK2 is O-GlcNAcylated at multiple serine and threonine residues.	92
Figure 3.27. The O-GlcNAc sites in HIPK2 are highly conserved in mammals.	93
Figure 3.28. Replacements of HIPK2 O-GlcNAc sites by alanine are confirmed by sequencing.....	93
Figure 3.29. HIPK2 O-GlcNAcylation by OGT promotes HIPK2 protein stability.....	94
Figure 4.1. High dietary sugar modulates Hipk-mediated leg malformation phenotype through InR and SIKs.	102
Figure 4.2. Insulin and InR signaling induce Hipk hyper-phosphorylation.....	104
Figure 4.3. Recombinant human insulin causes the recruitment of tGPH to the plasma membrane.	105
Figure 4.4. The insulin-InR effect on Hipk phosphorylation is SIK2-dependent.....	106
Figure 4.5. SIK2 physically interacts with Hipk.	107
Figure 4.6. SIK2 induces Hipk hyper-phosphorylation.....	108

Figure 4.7. InR-SIK2 signaling synergizes with Hipk to drive tumor growth	110
Figure 4.8. Loss of SIK2 reduces the exogenous Hipk protein levels.	111
Figure 4.9. Putative SIK2 target sites in <i>Drosophila</i> Hipk.	112
Figure 4.10. Replacements of the six putative SIK target sites in <i>Drosophila</i> Hipk by alanine are confirmed by sequencing.....	112
Figure 4.11. Hipk-6A is a hyper-phosphorylated and constitutively active form.....	114
Figure 4.12. Elevated Hipk potentiates InR signaling at least through <i>InR</i> upregulation	116
 Figure 5.1. Hipk tumor cells exhibit elevated glucose uptake.....	124
Figure 5.2. Elevated Hipk stimulates 2-NBDG uptake in a Glut1-dependent manner..	126
Figure 5.3. Knockdown efficiencies of the RNAi lines targeting glycolytic genes.	127
Figure 5.4. Hipk tumor cells display low intracellular glucose levels.	128
Figure 5.5. Elevated Hipk induces robust expression of a subset of glycolytic genes..	130
Figure 5.6. Elevated Hipk drives dMyc upregulation in a region-specific manner.....	132
Figure 5.7. Elevated Hipk induces dMyc accumulation in the wing hinge region.....	133
Figure 5.8. Perturbations in cell signaling induce dMyc accumulation in the wing hinge region.	136
Figure 5.9. dMyc protein levels upon perturbations in cell signaling in the wing pouch region.	136
Figure 5.10. dMyc is required for Hipk-induced aerobic glycolysis.....	138
Figure 5.11. dMyc is required for Hipk tumor growth.	139
Figure 5.12. Knockdown of <i>pfk2</i> or <i>pfk</i> causes decreases in the pyruvate levels.....	141
Figure 5.13. Knockdown of <i>hex-A</i> and <i>hex-C</i> fail to suppress Hipk tumor growth.....	142
Figure 5.14. Non-targeted inhibition of glycolysis is not sufficient to prevent tumor growth nor dMyc accumulation.....	142
Figure 5.15. Pfk2 and Pfk sustain dMyc accumulation and Hipk tumor growth.	143
Figure 5.16, Pfk2 and Pfk do not affect dMyc expression in the absence of <i>hipk</i> overexpression.....	144
Figure 5.17. Knockdown of <i>pfk2</i> or <i>pfk</i> does not affect the transcriptional induction of dMyc by Hipk.....	144
Figure 5.18. Knockdown of <i>pfk2</i> or <i>pfk</i> does not affect Hipk activities.	145
Figure 6.1. Elevated Hipk promotes tumorous growth and mitochondrial fusion.	155
Figure 6.2. Elevated Hipk promotes mitochondrial fusion and branching.	156
Figure 6.3. Quantification of mitochondrial morphology in control and <i>hipk</i> -overexpressing salivary gland cells.....	157
Figure 6.4. Elevated Hipk promotes mitochondrial fusion through Marf and Opa1.....	158
Figure 6.5. Use of $\Delta\psi_m$ -dependent dyes to monitor the respiratory activity	159
Figure 6.6. MitoTracker Red staining in a control wing disc.	160
Figure 6.7. MitoTracker Red staining in a <i>hipk</i> -overexpressing wing disc.	160
Figure 6.8. Hipk tumor cells abound with active mitochondria.	161

Figure 6.9. Elevated Hipk increases mitochondrial respiratory activity in larval muscle cells.....	162
Figure 6.10. Cells with elevated Hipk abound with active mitochondria.....	163
Figure 6.11. Hipk tumor cells do not display ROS accumulation.....	166
Figure 6.12. Mitochondrial fusion is dispensable for Hipk-mediated tumorigenesis.	169
Figure 6.13. Effects by various knockdowns on mitochondrial activity and morphology in <i>hipk</i> -overexpressing salivary gland cells.....	170
Figure 6.14. Targeted but not generic inhibition of mitochondrial activity suppresses Hipk tumor growth.....	172
Figure 6.15. A schematic diagram of the respiratory complex I.	174
Figure 6.16. Mitochondrial impairment leads to JNK activation and the downstream MMP1 induction in Hipk tumor cells.	176
Figure 6.17. The active mitochondrial metabolism in Hipk tumor cells depends on both Myc and Pfk2.	177

List of Acronyms

A/P	Anterior/Posterior
Ci	Cubitus interruptus
D/V	Dorsal/Ventral
Dpp	Decapentaplegic
En	Engrailed
EThcD	Electron-Transfer/Higher-Energy Collision Dissociation
GFP	Green fluorescent protein
HBP	Hexosamine biosynthetic pathway
HCD	Higher-energy collision dissociation
HIPK	Homeodomain-interacting protein kinase
InR	Insulin-like receptor
JNK	c-Jun N-terminal kinase
Marf	Mitochondrial assembly regulatory factor
Mfn	Mitofusin
MS	Mass spectrometry
N	Notch
ND-Pdsw	NADH dehydrogenase [ubiquinone] with a N-terminal sequence Pro-Asp-Ser-Trp
NDUFB10	NADH dehydrogenase [ubiquinone] 1 beta subcomplex subunit 10
O-GlcNAc	O-Linked β -N-acetylglucosamine
O ₂ ⁻ .	Superoxide anion
OGA	O-GlcNAcase
OGT	O-GlcNAc transferase
Opa1	Optic atrophy 1
PFK	Phosphofructokinase
PFK2	6-Phosphofructo-2-kinase/fructose-2,6-bisphosphatase
PI3K	Phosphoinositide 3-kinase
PIP ₂	Phosphatidylinositol 4,5-bisphosphate
PIP ₃	Phosphatidylinositol 3,4,5-trisphosphate
PKB	Protein kinase B (also known as Akt)
RFP	Red fluorescent protein
RNAi	RNA interference

ROS	Reactive oxygen species
SIK	Salt-inducible kinase
UAS	Upstream activation sequence
UDP-GlcNAc	Uridine diphosphate <i>N</i> -acetylglucosamine
Wg	Wingless

Chapter 1.

Introduction

1.1. Fundamentals of cancer

We are witnessing an alarming increase in the global cancer burden. In 2014 and 2018, 14.1 million people and 18.1 million were diagnosed with cancer worldwide, respectively ([Ferlay et al., 2019; McGuire, 2016](#)). By 2040, the incidence is projected to rise to 29-37 million ([World Health, 2020](#)). In 2018, 9.6 million died from cancer, and lung, colorectum, stomach, liver and breast cancers were the top five responsible for the mortality in both sexes combined ([Ferlay et al., 2019](#)). In Canada, cancer is the leading cause of death ([Brenner et al., 2020](#)). It is estimated that 1 in 2.3 Canadians will be diagnosed with cancer in their lifetime, and 1 out of 4.1 will die from cancer ([Canadian Cancer Statistics Advisory Committee, 2019](#)).

Cancer is a generic term for a complex collection of around 200 cancer diseases caused by genetic changes in cancer genes that transform normal cells to malignant tumors ([Luo et al., 2009; Song et al., 2015](#)). Cancer can be hereditary or sporadically induced by endogenous (e.g. cellular reactive oxygen species (ROS)) and environmental sources (e.g. carcinogens) ([Loeb and Loeb, 2000](#)). Of all cancers, 5-10% are due to inherited mutations in cancer predisposition genes that confer high susceptibility to cancer ([Garber and Offit, 2005](#)). The remaining 90-95% can be attributed to non-hereditary risk factors including cigarette smoking, nutrition, infection, radiation, physical inactivity and environmental pollutions ([Anand et al., 2008](#)). In particular, obesity, which is a common health issue in most affluent countries, account for around 20% of all cancer cases ([Wolin et al., 2010](#)), which has drawn considerable attention to the investigations into how diet is related to cancer progression ([Mayne et al., 2016](#)).

1.1.1. Cancer as genetic disease

Genetic mutations take place at both nucleotide and chromosomal levels (**Table 1-1**), leading to altered protein expression, structure, activity and affinity for binding partners (Loeb and Loeb, 2000). Examples include the gain-of-function mutation in *RAS* (G12D; from amino acid 12 glycine to aspartate) in pancreatic ductal adenocarcinoma (Hobbs et al., 2016), aberrant splicing in *APC* in Familial adenomatous polyposis (Aretz et al., 2004), gene amplification of *MYCN* in neuroblastoma (Huang and Weiss, 2013), transcriptional activation of *c-MYC* as a result of chromosomal translocation t(8:14) in Burkitt's lymphoma (Boxer and Dang, 2001), and formation of the chimeric BCR-ABL1 tyrosine kinase due to the translocation t(9;22) in chronic myeloid leukemia (Quintás-Cardama and Cortes, 2009). Mutations in epigenetic chromatin modifiers, which occur in nearly half of human cancers, also lead to gene misexpression (Flavahan et al., 2017).

Table 1-1. Types of genetic mutations.

Genetic mutations	Description
Nucleotide changes	
Missense	Change of nucleotide leads to change in amino acid
Nonsense	Change of nucleotide creates a premature stop codon
INDEL	Insertion or deletion of base(s), may cause frameshift in coding region
Frameshift	Addition or deletion of nucleotide results in a change in the reading frame
Splice-site mutation	Addition, deletion or change of nucleotide leads to gain or loss of splice sites
Chromosomal aberrations	
Reciprocal translocation	Exchange of segments of two non-homologous chromosomes
Insertional translocation	Transfer of a segment of a chromosome to a non-homologous chromosome
Deletion	Loss of a segment of a chromosome; copy number variation
Duplication	Repetition of a segment of a chromosome; copy number variation
Inversion	Internal flipping of a segment of a chromosome
Aneuploidy	An abnormal number of chromosomes in human cells (i.e. numbers other than 46)

Cancer genes are categorized into two broad classes – **oncogenes** and **tumor suppressor genes (TSGs)** (**Table 1-2**). Oncogene proteins promote cell growth and division, and block apoptosis, whereas tumor suppressors restrain cell growth, facilitate DNA repair, maintain cell shape and architecture, and promote apoptosis (Shortt and Johnstone, 2012; Sun and Yang, 2010). In cancer, an oncogene is activated by gain-of-function, dominant mutation or amplification; mutation in only one of the two alleles is sufficient to cause cancer (Payne and Kemp, 2005). In contrast, a TSG is inactivated by loss-of-function, recessive mutation or deletion of both alleles via ‘two hits’ as a mutation

in only one allele is insufficient to cause cancer (Wang et al., 2019). In cases of haplo-insufficient and dominant-negative TSG mutations, one-hit is sufficient for the inactivation of TSG (Payne and Kemp, 2005).

Table 1-2. Oncogenes and tumor suppressor genes commonly found in cancer

Human genes	Fly homologs	Functions	Associated Cancer
Oncogenes			
<i>ABL1</i>	<i>abl</i>	Tyrosine kinase	Chronic myeloid leukemia (CML) (Quintás-Cardama and Cortes, 2009)
<i>BCL-2</i>	<i>debcl</i>	Anti-apoptotic activity	Non-Hodgkin's lymphomas (Yip and Reed, 2008)
<i>BRAF</i>	<i>raf</i>	Serine/threonine kinase	Melanoma (Davies et al., 2002)
<i>c-MYC, MYCN, MYCL</i>	<i>myc</i>	Transcription factor	70% of all cancers (Dang, 2012)
<i>c-SRC</i>	<i>src42A, src64B</i>	Tyrosine kinase	Colon cancer (Irby and Yeatman, 2000)
<i>ERBB2 (HER2)</i>	<i>egfr</i>	Receptor tyrosine kinase	Breast cancer (Yu and Hung, 2000)
<i>K-RAS</i>	<i>ras85D</i>	Membrane-bound GTPases	20-25% of all cancers (Prior et al., 2012)
<i>PIK3CA</i>	<i>pi3k92E (or dp110)</i>	Kinase	Colorectal and breast cancer (Samuels and Waldman, 2010)
<i>v-sis (PDGF)</i>	<i>pvf</i>	Growth factors	Simian sarcoma (Heldin, 2013)
TSGs			
<i>APC</i>	<i>apc</i>	Cell adhesion and signaling	Colon cancer (Aoki and Taketo, 2007)
<i>BRCA1/2</i>	<i>brca2</i>	E3 ubiquitin-protein ligase; DNA repair	Breast and ovarian cancer (Roy et al., 2012)
<i>TP53</i>	<i>p53</i>	Pro-apoptotic activity	Lung cancer (Rivlin et al., 2011)
<i>RB1</i>	<i>rbf</i>	Cell cycle regulator	Retinoblastoma (Giacinti and Giordano, 2006)
<i>PTEN</i>	<i>pten</i>	Phosphatase	Prostate cancer (Song et al., 2012)
<i>SDH</i>	<i>sdh</i>	Electron transfer chain – complex II	Paraganglioma, phaeochromocytoma (Bardella et al., 2011)
<i>VHL</i>	<i>vhl</i>	E3 ubiquitin-protein ligase	Renal cell cancer (Gossage et al., 2015)
<i>LKB1/ STK11</i>	<i>lkb1</i>	Serine/threonine kinase	Lung cancer (Zhao and Xu, 2014)

Oncogene proteins and tumor suppressors constitute a large portion of signaling pathways including receptor tyrosine kinase (RTK)-Ras, Wnt-β-catenin, Notch, Hippo, PI3K-AKT, Myc (Sever and Brugge, 2015). Dysregulated signaling pathways can interact with each other to drive tumor progression (Logue and Morrison, 2012). For example, Notch synergizes with Akt, Myc and Ras-Raf-MAPK to increase prostate cancer malignancy (Stoyanova et al., 2016). Also, Wnt-β-catenin in cooperation with K-Ras

activation accelerates lung cancer progression ([Pacheco-Pinedo et al., 2011](#)). Therefore, when cancer progresses with accumulating gene mutations, the consequent cell signaling heterogeneity highlights the need of a combination of drug therapies as well as precision medicine in cancer treatment ([Sanchez-Vega et al., 2018](#)).

1.1.2. Cancer progression and metastasis

The extent of cancer progression is classified using the tumor-node-metastasis (TNM) system that describes the growth of the primary (original) tumor (T), the spread to the regional (local) lymph nodes (N), and the distant metastases (M) ([Table 1-3](#)) ([AJCC Cancer Staging Manual](#), 2017). Once the T, N, and M categories are determined clinically and/or pathologically, they are combined to give an overall stage of 0, I, II, III or IV ([Table 1-4](#)) (Gress et al., 2017).

Table 1-3. The TNM classification system

T (primary tumor)	N (lymph node)		M (distant metastasis)	
TX	Not evaluated	NX	Not evaluated	M0 Not found
T0	Not found	N0	Not found	M1 Found
Tis	Carcinoma <i>in situ</i> (in its place)	N1-3	Number and/or extent of the spread to regional lymph nodes	
T1-	Size and/or extent of the			
T4	primary tumor			

Table 1-4. Cancer stages

Overall Stage	Description
0	Carcinoma <i>in situ</i> . No metastatic potential.
I-III	Cancer with increasing tumor and nodal extent.
IV	Cancer has metastasized.

Prior to cancer growth, pre-neoplastic lesions (abnormal cell growths) ([Table 1-5](#)) occur due to the presence of growth-promoting stimuli such as genetic changes, hormones and infection ([Figure 1.1](#)) ([Yokota, 2000](#)). If the stimuli cease, the abnormal growths may be reversed ([Ingber, 2008](#)). When genetic mutations accumulate, the lesions can be converted into neoplastic ones (e.g. carcinoma *in situ*) irreversibly ([Kerr, 2001](#)). At the early stage, neoplastic tumors are benign and non-invasive ([Yokota, 2000](#)). Further accumulations of gene mutations convert them into malignant ones that invade locally or even metastasize to distant areas of the body ([Chaffer and Weinberg, 2011](#)). The phenotypic changes acquired during cancer progression are in general defined as the ten **hallmarks of cancer**, which include sustained proliferation, invasion and metastasis, as well as energetic changes ([Figure 1.1](#)) ([Hanahan and Weinberg, 2000, 2011](#)).

Table 1-5. Types of abnormal cell growths

Abnormal cell growths	Description
Hypertrophy	Increase in cell size
Hyperplasia	Increase in cell number
Metaplasia	Change in cell type (to another cell type that is not normally present in the tissue)
Dysplasia	Change in cell appearance (phenotype)
Neoplasia	Formation of new, abnormal growth; Neoplasms can be benign or malignant

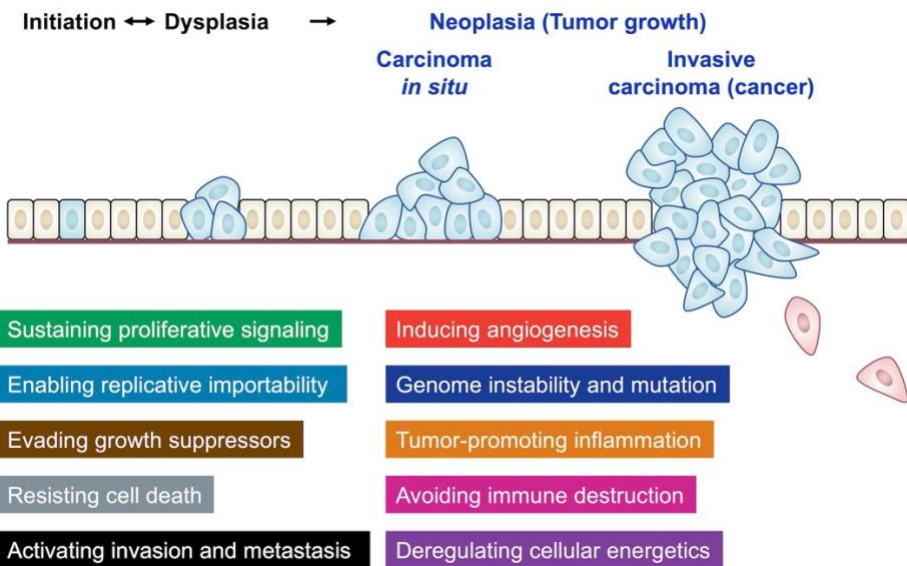


Figure 1.1. Stepwise progression of carcinoma (epithelial cancer)

Abnormal cell growths such as dysplasia may be initiated in epithelial cells (normal cells in pale yellow, abnormal cells in blue) sitting on the basement membrane. Accumulation of irreversible genetic mutations trigger neoplasms where the tumor cells proliferate uncontrollably, disrupt the basement membrane and/or metastasize (cells in red). Texts in boxes are the ten hallmarks of cancer.

1.1.3. Epithelial-to-mesenchymal transition

Metastasis accounts for the majority (at least two-thirds) of cancer mortality (Dillekås et al., 2019). During metastasis, cancer cells execute a series of events known as the invasion-metastasis cascade (**Table 1-6**) (Valastyan and Weinberg, 2011). To initiate metastasis, cancer cells activate a cellular program called epithelial-to-mesenchymal transition (EMT) primarily by mis-expressing EMT transcription factors (EMT-TFs) such as Snail and Twist (Pastushenko and Blanpain, 2019). EMT-TFs repress the transcriptional expression of epithelial markers such as epithelial cadherin (E-cadherin; an adherens junction protein), but upregulate mesenchymal markers like neural cadherin (N-cadherin), Vimentin (an intermediate filament protein) and matrix metalloproteinases (MMPs) (Lamouille et al., 2014). As a result, cancer cells undergoing EMT manifest a switch from cobblestone to spindle-like morphology, cell motility and an ability to degrade basement membrane (Dongre and Weinberg, 2019). After reaching the distant sites, cancer cells resume epithelial properties (mesenchymal-to-epithelial transition, MET) and colonize, showing an EMT/MET plasticity (Tsai and Yang, 2013).

Table 1-6. The invasion-metastasis cascade

Steps	Description
Invasion	Cancer cells from primary tumor activate EMT, lose cell adhesion, increase motility and migrate to the surrounding tissues.
Intravasation	Cancer cells enter the lymph or blood vessels.
Circulation	Cancer cells survive and translocate in the bloodstream.
Extravasation	Cancer cells arrest at distant organs and exit from blood vessels.
Colonization	Cancer cells activate MET, adapt to the foreign environments in distant organs and form secondary tumors.

When dysregulated as a consequence of genetic mutations, several signaling pathways such as Wnt, Notch, PI3K-Akt, RTK-Ras and JNK can cooperate to induce EMT through upregulating EMT-TFs (Dongre and Weinberg, 2019). Recent single-cell transcriptomics analysis of head and neck cancer reveals that cells localized at the leading edge of the primary tumors display a partial EMT (Puram et al., 2017), indicating that environmental factors in addition to cell-intrinsic genetic mutations can contribute to EMT. Intriguingly, accumulating evidence has shown that hyperglycemia (high blood glucose) exacerbates the malignancy of colon cancer (Vasconcelos-Dos-Santos et al., 2017), lung cancer (Kang et al., 2015) and bile duct cancer (Phoomak et al., 2017). However, how excess nutrients promote cancer progression remains elusive.

1.2. Nutrient sensing pathways in cancer

As cancer cells grow and divide, their biomass increases substantially. Experimental results show that large amounts of nutrients and energy including adenosine triphosphate (ATP), acetyl coenzyme A (acetyl-CoA) and amino acids are required for cancer cell proliferation (Keibler et al., 2016). To satisfy the metabolic requirements, cells are constantly sensing nutrients in the surroundings and employing nutrient sensing pathways (Table 1-7) to coordinate cell growth and survival with nutrient availability (Palm and Thompson, 2017). Therefore, nutrients should not be viewed only as substrates for ATP and macromolecular synthesis, but also as **nutrient signaling molecules** (Marshall, 2006). Nutrient sensing pathways have been the proposed links between cancer and metabolic disorders like diabetes (Yang et al., 2017).

Table 1-7. Examples of nutrient sensing pathways

Abbreviations are as follows: AMPK, adenosine monophosphate (AMP)-activated protein kinase; mTORC1, mammalian target of rapamycin complex 1; UDP-GlcNAc, uridine diphosphate *N*-acetylglucosamine; HBP, hexosamine biosynthetic pathway; OGT, O-linked β -*N*-acetylglucosamine transferase; InR, insulin receptor; PI3K, phosphoinositide 3-kinase; SREBP, sterol response element binding protein

Nutrient sensing pathways	Sensing	Description	References
AMPK signaling	Energy	When AMP levels rise (low ATP levels), AMPK is activated, antagonizing mTORC1 functions, promoting catabolism for ATP production and inhibiting ATP-consuming anabolism.	(Hardie et al., 2012)
Hexosamine signaling	Glucose	When glucose levels rise, more UDP-GlcNAc is produced through the HBP. UDP-GlcNAc is used as the nucleotide sugar donor substrate for O-GlcNAcylation by OGT.	(Levine and Walker, 2016)
InR signaling	Insulin (hormone-sensing)	Upon binding of insulin (released in response to high blood glucose levels), InR-PI3K-AKT signaling is activated, stimulating glucose uptake and metabolism and activating mTORC1.	(Haeusler et al., 2018)
mTORC1 signaling	Amino acids	When amino acids are abundant, mTORC1 is activated, promoting protein synthesis (consumption of amino acids) and cell growth.	(González and Hall, 2017)
SREBP signaling	Cholesterol	When cellular cholesterol levels decrease, SREBP undergoes proteolytic cleavage and translocates from endoplasmic reticulum to nucleus to induce expression of lipoprotein receptors and lipogenic enzymes for cholesterol uptake and <i>de novo</i> biosynthesis, respectively.	(Brown and Goldstein, 1997)

1.2.1. The hexosamine biosynthetic pathway and O-GlcNAcylation

The disaccharide sucrose (common table sugar), which is made up of glucose and fructose, is highly abundant in brown sugar, sugar cane and maple syrup (Clemens et al., 2016). Glucose entering glycolysis is broken down into pyruvate, which is further oxidized in the tricarboxylic acid (TCA) cycle (the citric acid cycle) in mitochondria (Fernie et al., 2004). Glucose can also be diverted to other metabolic pathways branching off glycolysis, including the four-step hexosamine biosynthetic pathway (HBP) (Figure 1.2) (Rossetti, 2000). The first and rate-limiting step of the HBP is catalyzed by Glutamine-fructose-6-phosphate aminotransferase (GFAT), converting fructose-6-phosphate (fructose-6P) derived from glucose into glucosamine-6-phosphate (glucosamine-6P) (Obici and Rossetti, 2003). Through additional three enzymatic steps, the end-product, uridine diphosphate-N-acetylglucosamine (UDP-GlcNAc), is formed (Ma and Hart, 2014).

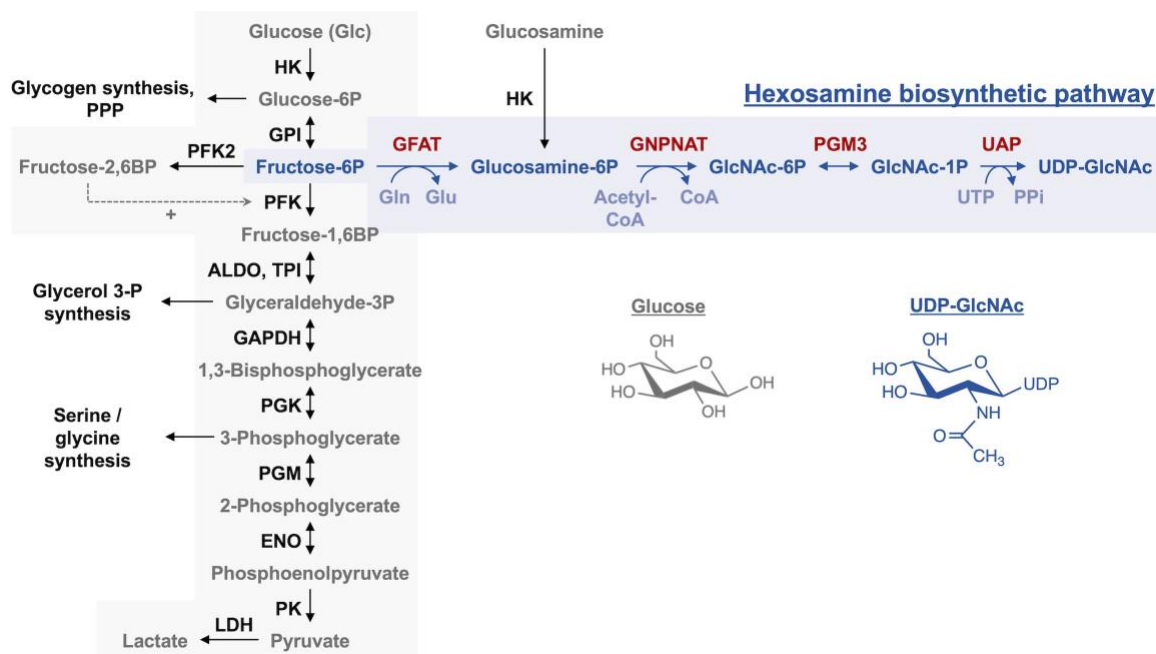


Figure 1.2. Glycolysis and the hexosamine biosynthetic pathway (HBP)

Glycolytic intermediates are shown in grey, enzymes in black. Double-head and single-head arrows refer to reversible and essentially irreversible enzymatic reactions. Fructose-2,6-bisphosphate (fructose-2,6BP) is an allosteric activator (+) of phosphofructokinase (PFK). Metabolic pathways branching off glycolysis including glycogen synthesis, pentose phosphate pathway (PPP) and the HBP. The HBP intermediates are shown in blue, enzymes in red. Glucosamine bypasses the first, rate-limiting step of the HBP. Chemical structures of glucose and UDP-GlcNAc are shown. Hexokinase, HK; Glucose 6-phosphate isomerase,

GPI; Aldolase, ALDO; Triosephosphate isomerase, TPI; Glyceraldehyde 3-phosphate dehydrogenase, GAPDH; Phosphoglycerate kinase, PGK; Phosphoglycerate mutase, PGM; Enolase, ENO; Pyruvate kinase, PK; LDH, Lactate dehydrogenase, LDH; Glutamine, Gln; glutamate, Glu; Glucosamine 6-phosphate *N*-acetyltransferase, GNPNAT; Phosphoacetylglucosamine mutase, PGM3; UDP-N-acetylglucosamine pyrophosphorylase, UAP; In metabolic intermediates, P refers to phosphate and BP refers to bisphosphate.

UDP-GlcNAc serves as the donor substrate for glycosylation mediated by various glycosyltransferases (Ban et al., 2012). Complex *N*-linked and *O*-linked glycosylation reactions of transmembrane proteins, secreted factors and lipids take place in the rough endoplasmic reticulum and Golgi apparatus (Stanley, 2011). More recently appreciated is the dynamic, reversible post-translational modification (PTM) of intracellular proteins by simple monosaccharide *O*-linked *N*-acetylglucosamine (*O*-GlcNAc) (*O*-GlcNAcylation) (Figure 1.3) (Hart, 2014). *O*-GlcNAc transferase (OGT) uses UDP-GlcNAc to catalyze protein *O*-GlcNAcylation, whereas another enzyme, *O*-GlcNAcase (OGA), removes *O*-GlcNAc from proteins by hydrolysis (Yang and Qian, 2017).

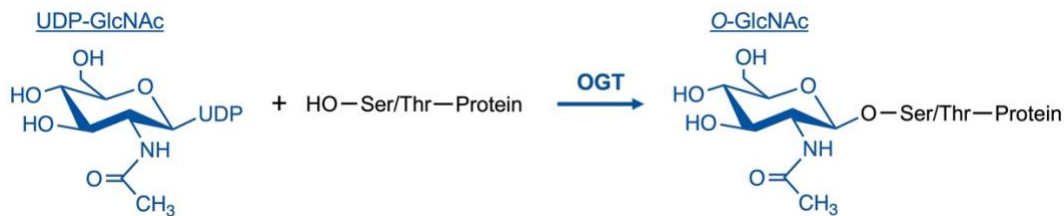


Figure 1.3. *O*-GlcNAcylation by OGT.

Using UDP-GlcNAc as the donor substrate, OGT catalyzes the addition of *O*-GlcNAc onto serine (Ser) and threonine (Thr) residues of proteins, releasing UDP (not shown).

Studies have found that, under normal conditions, only a tiny fraction (0.003-3%) of glucose is used in the HBP, depending on cell types (Marshall et al., 1991; Olson et al., 2020). As glucose levels rise, HBP flux increases, producing more UDP-GlcNAc (Hu et al., 2019). As the donor substrate, UDP-GlcNAc also increases OGT catalytic activity, feeding forward to promote extensive *O*-GlcNAcylation of numerous proteins (Kreppel and Hart, 1999). The list of *O*-GlcNAc modified proteins is growing (Table 1-8), highlighting the importance of direct *O*-GlcNAcylation in the regulation of gene expression, signaling, metabolism and cell behaviors. Thus, *O*-GlcNAc is regarded as a nutrient sensor to fine-tune cellular processes in a nutrient-responsive manner (Hart, 2019). The HBP in combination with *O*-GlcNAcylation is sometimes termed the hexosamine signaling pathway (Hanover et al., 2010).

Table 1-8. Effects of direct O-GlcNAcylation on protein activity

Abbreviations are as follows: Glycogen synthase kinase-3 Beta, GSK3B; nuclear factor kappa B, NF κ B; Pentose phosphate pathway, PPP; Yes-associated protein, YAP; phosphofructokinase, PFK or PFK1; serine, Ser; threonine, Thr

O-GlcNAc modified proteins	Functional O-GlcNAc sites	Effects of direct O-GlcNAcylation on protein activity	References
c-MYC	Thr 58	This O-GlcNAc site is a phosphorylation site mediated by GSK3B. Phosphorylation at Thr 58 promotes c-MYC degradation.	(Chou et al., 1995b; Sears et al., 2000)
NF κ B	Thr 352	This modification is required for NF κ B transcriptional activation.	(Won et al., 2008)
p53	Ser 149	This modification reduces phosphorylation at Thr 155, thus stabilizing p53	(Yang et al., 2006)
PFK	Ser 529	This modification inhibits PFK activity, redirecting glucose flux towards the PPP.	(Yi et al., 2012)
RNA polymerase II	Ser 5 and Ser 7	These modifications in the C-terminal domain (CTD) of RNA polymerase II are required for transcription initiation.	(Ranuncolo et al., 2012)
Snail1	Ser 112	This modification suppresses phosphorylation-mediated degradation, thereby stabilizing Snail1 and increasing its repressor function	(Park et al., 2010)
YAP	Ser 109 and Thr 241	These modifications prevent YAP phosphorylation, promote its translocation into nucleus and its transcriptional activity.	(Peng et al., 2017; X. Zhang et al., 2017)
β -catenin	Thr 41	This modification stabilizes β -catenin through direct competition with phosphorylation.	(Olivier-Van Stichelen et al., 2014)

In cancer, upregulation of OGT and GFAT, and downregulation of OGA are frequently observed, which can account for the elevated O-GlcNAc levels in nearly all cancers examined (Ferrer et al., 2016). As shown in Table 1-8, proteins that are essential to cell functions (e.g. RNA polymerase and PFK) and those that have been implicated in cancer (the rest of the list) are modified by direct O-GlcNAcylation, which likely serve as a molecular link between nutrient signals and various hallmarks of cancer. Indeed, glucose-induced YAP O-GlcNAcylation and activation promote cancer growth in mouse models (Peng et al., 2017). Also, high glucose levels enhance Snail O-GlcNAcylation, which activates Snail for transcriptional repression of E-cadherin (i.e. initiation of EMT) and cell invasion (Park et al., 2010). Therefore, understanding which oncogene proteins and tumor suppressors are O-GlcNAc modified may help develop new cancer treatment strategies (Ferrer et al., 2016).

1.2.2. The InR/AMPK-mTORC1 signaling network

The InR/AMPK-mTORC1 signaling network comprises three signaling pathways that intertwine with each other: (1) InR signaling, (2) AMPK signaling and (3) mTORC1 signaling (Figure 1.4) (Marshall, 2006). In general, each signaling cascade has three major components: (1) **sensors**: nutrient, hormone or energy-sensing proteins, (2) **transducers**: signaling cascades through phosphorylation, translocation and/or change of binding partners, (3) **effectors**: transcription factors that control gene expression programs of various metabolic pathways (Haeusler et al., 2018).

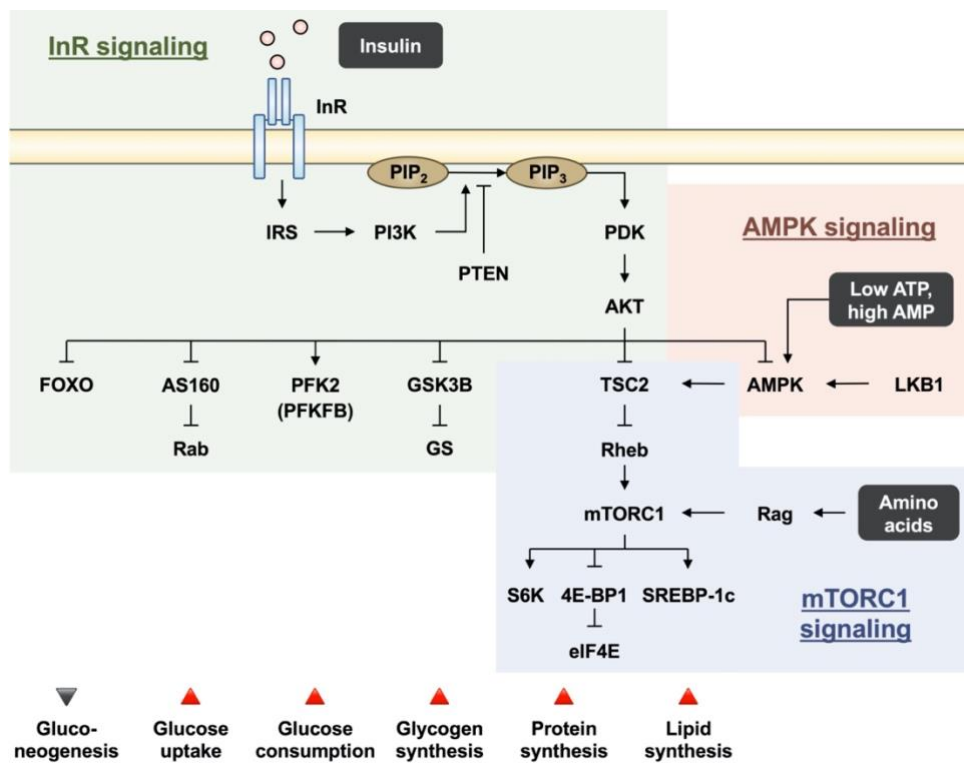


Figure 1.4. The InR/AMPK-mTORC1 signaling network.

(In blue) In mTORC1 signaling, the amino acid-sensing Rag and the TSC2-Rheb axis regulate mTORC1 activity. mTORC1 activates downstream targets including S6K, eIF4E and SREBP-1c. (In green) Upon insulin binding, the receptor tyrosine kinase InR is activated, phosphorylating itself and its substrate (IRS), which activates PI3K. PI3K catalyzes the synthesis of PIP₃ at the plasma membrane. PTEN antagonizes PI3K, converting PIP₃ back to PIP₂. PIP₃ activates PDK, which in turn activates AKT. AKT modulates the activities of several downstream target proteins including FOXO, AS160, PFK2 (also known as PFKFB), GSK3B and TSC2. (In red) Energy-sensing AMPK is activated through allosteric regulation by AMP or through phosphorylation by LKB1. Abbreviations are as follows: Insulin receptor, InR; InR substrate, IRS; Phosphoinositide 3-kinase, PI3K; Phosphatidylinositol 4,5-bisphosphate, PIP₂; Phosphatidylinositol (3,4,5)-trisphosphate, PIP₃; Phosphatase and

tensin homolog, PTEN; Phosphoinositide-dependent kinase-1, PDK, Tuberous sclerosis complex 2, TSC2; Glycogen synthase kinase 3 beta, GSK3B; Glycogen synthase, GS; Akt substrate of 160 kDa, AS160 (also known as TBC1 domain family member 4 (TBC1D4)); Phosphofructokinase 2, PFK2; 6-Phosphofructo-2-Kinase/Fructose-2,6-Biphosphatase, PFKFB; Forkhead box O transcription factor, FOXO; Mammalian (or mechanistic) target of rapamycin complex 1, mTORC1; Ribosomal protein S6 kinase, S6K; Eukaryotic translation initiation factor 4E-binding protein 1, 4E-BP1; Eukaryotic translation initiation factor 4E, eIF4E; Sterol regulatory element-binding protein 1c, SREBP-1c; Adenosine monophosphate, AMP; adenosine triphosphate, ATP; AMP-activated protein kinase, AMPK; Liver kinase B1, LKB1 (also known as Serine/threonine kinase 11 (STK11)).

Mechanistic (or mammalian) target of rapamycin complex I (mTORC1) signaling is well-known for amino acid sensing ([Goberdhan et al., 2016](#)). Amino acids signaling through Rag guanosine triphosphatase (GTPase) activate the serine/threonine kinase complex mTORC1 ([Sancak et al., 2010](#)). mTORC1 is also positively regulated by Rheb GTPase, which is negatively regulated by TSC2 (a GTPase-activating protein GAP) ([Inoki et al., 2003](#)). TSC2 integrates insulin and energy signals from InR and AMPK signaling pathways, respectively (discussed below) ([Marshall, 2006](#)). When mTORC1 is activated, it modulates the activities of downstream targets to promote protein synthesis (consumption of amino acids) and lipid synthesis required for cell growth ([González and Hall, 2017](#)).

Insulin receptor (InR) signaling is activated upon binding of insulin (a hormone secreted in response to high blood glucose levels) ([Röder et al., 2016](#)). InR signaling comprises three major events: **(1)** activation of the receptor tyrosine kinase InR and its substrate, **(2)** activation of the lipid kinase phosphatidylinositol-3-kinase (PI3K) and **(3)** activation of the downstream serine/threonine kinases including AKT (also known as protein kinase B, PKB) ([Haeusler et al., 2018](#)). AKT signals downstream target proteins to inhibit gluconeogenesis and promote glucose uptake and consumption such that the blood glucose levels are restored to normal ([Rui, 2014](#)). AKT also activates mTORC1 through inhibition of TSC2 and the subsequent relief of the inhibitory effect on Rheb ([Inoki et al., 2003, 2002](#)).

Adenosine monophosphate (AMP)-activated protein kinase (AMPK) signaling senses intracellular energy signals ([Garcia and Shaw, 2017](#)). When cellular demand for energy increases or when nutrient availability decreases, the AMP to ATP ratio rises ([Marshall, 2006](#)). AMP allosterically activates the serine/threonine kinase AMPK, inhibiting mTORC1 through the TSC2-Rheb axis such that protein and lipid synthesis

(ATP-consuming anabolism) is reduced and consequently cell growth is restrained ([Hardie et al., 2012](#)). As an upstream kinase, the serine/threonine Liver kinase B1 (LKB1) is required for AMPK activation triggered by other stimuli like AMP ([Woods et al., 2003](#)). The activation of the LKB1-AMPK axis, however, is antagonized by activated AKT such that mTORC1 is not activated and inactivated at the same time ([Hawley et al., 2014](#)). Otherwise, catabolism and anabolism may constitute a futile cycle, wasting energy.

Aberrant nutrient sensing signaling can be caused by gene mutations of the signaling components. Notably, *PIK3CA* (encoding PI3K) ([Samuels and Waldman, 2010](#)) and *AKT* ([Manning and Toker, 2017](#)) are well-characterized oncogenes whereas *TSC2* ([Gao and Pan, 2001](#)), *PTEN* ([Song et al., 2012](#)), *LKB1* ([Zhao and Xu, 2014](#)) and *AMPK* ([Faubert et al., 2013](#)) are tumor suppressor genes (TSGs). As they all converge on the TSC2 complex, their mutations inhibit TSC2, relieving the inhibitory effect of TSC2 on Rheb and thereby activating mTORC1 ([Inoki et al., 2003](#)). Indeed, it is estimated that mTORC1 is constitutively active in more than 70% of cancers ([Rad et al., 2018](#)).

When activated, mTORC1 stimulates the activities of the ribosomal S6 protein kinase (S6K) and eukaryotic translation initiation factor 4E (eIF4E), which function in ribosome biogenesis transcription program ([Chauvin et al., 2014](#)) and the initiation of mRNA translation ([Mamane et al., 2004](#)), respectively. Together, they promote protein synthesis and cell growth ([Goberdhan et al., 2016](#)). In particular, cancer-associated proteins such as cyclin D1 ([Averous et al., 2008](#)), c-MYC ([Csibi et al., 2014](#)), Snail (an EMT-TF) ([Cai et al., 2014](#)), HIF-1 α and VEGF ([Dodd et al., 2015](#)) are regulated at the translational level highly dependent on the mTORC1-S6K/eIF4E signaling ([Mamane et al., 2004](#)).

Thus, nutrient signaling pathways or networks integrate diverse nutrient signals into gene expression programs that confer hallmarks of cancer, providing advantages to cancer progression, especially when nutrients are available ([Torrence and Manning, 2018](#)).

1.3. Metabolic reprogramming

In addition to constantly sensing the nutrient availability, cancer cells often display altered metabolic profiles including aerobic glycolysis, glutamine catabolism and macromolecular biosynthesis (Faubert et al., 2020). Indeed, glucose and glutamine are the two main sources of carbon for cancer cells to meet their metabolic needs, especially when nutrients (and oxygen) become scarce (Lu et al., 2010). Metabolic reprogramming, which is one of the ten main hallmarks of cancer, is further subdivided into six hallmarks (**Table 1-9**) (Pavlova and Thompson, 2016).

Table 1-9. Six hallmarks of cancer metabolism (Pavlova and Thompson, 2016)

Hallmarks	Description / Examples
Increased uptake of glucose and amino acids	Glucose and glutamine are the two main carbon sources. Glutamine also facilitates the import of other amino acids.
Acquisition of nutrients with opportunistic modes	Ras or c-Src cancer cells acquire free amino acids through the lysosomal degradation of extracellular proteins obtained through macropinocytosis.
Use of glycolytic and tricarboxylic acid (TCA) cycle intermediates for biosynthesis of macromolecules	Carbon from glucose and glutamine is used for biosynthesis of fatty acid and cholesterol (from acetyl-CoA/citrate), nucleotides (from pentose), glycans (from hexosamine), glycerol (from glyceraldehyde 3-phosphate) and serine/glycine (from 3-phosphoglycerate).
Increased demand for nitrogen	Glutamine provides the nitrogen source for nucleotide and amino acid metabolism.
Metabolite-driven gene regulation	Metabolites are used as cofactors or substrates of histone modifiers for epigenetic regulation, e.g. acetyl-CoA for histone acetylation.
Interactions with tumor microenvironment	Accumulation of extracellular lactate promotes immunosuppression, angiogenesis and tumor invasiveness.

In the subsequent sections (**Chapters 1.3.1 and 1.3.2**), the contributions of altered glycolytic and mitochondrial metabolism to cancer progression are discussed.

1.3.1. Aerobic glycolysis (the Warburg effect)

Research in cancer metabolism predates the discovery of oncogenes and tumor suppressor genes (TSGs) by around 50 years ([De Berardinis and Chandel, 2016](#)). In the 1920s, Otto Warburg discovered that increased glucose uptake and lactate production are two stereotyped features of cancer cells even in the presence of oxygen, a phenomenon now termed the Warburg effect (aerobic glycolysis) ([Warburg et al., 1927](#)). This discovery has been exploited clinically for 2-deoxy-2-(¹⁸F)fluoro-D-glucose positron emission tomography (FDG-PET) in cancer diagnosis, staging and evaluation of cancer therapy ([Vander Heiden et al., 2009](#)). It has been reported that the specificity and sensitivity of FDG-PET across all oncology applications are nearly 90% ([Zhuang and Codreanu, 2015](#)). Despite the profound influence, our understanding of how the Warburg effect benefits cancer cells remains limited ([Liberti and Locasale, 2016](#)).

Several proposed explanations for the Warburg effect have been put forward (discussed below), including **(1)** rapid metabolic rate, **(2)** macromolecular biosynthesis and **(3)** acid-mediated invasion. Regarding the ATP yield, aerobic glycolysis (2 ATP produced per glucose molecule) is 15-16 fold less efficient than oxidative phosphorylation (OXPHOS) (30-32 ATP produced per glucose molecule), but proceeds at a faster rate ([Lunt and Vander Heiden, 2011](#)). Aerobic glycolysis and OXPHOS in cancer cells therefore yield comparable amounts of ATP over a period of time ([Wu et al., 2016](#)). Yet, cancer cells still opt for increased rate of aerobic glycolysis, which may enable them to outcompete the neighboring cells for glucose especially under nutrient-deprived conditions ([Pfeiffer et al., 2001](#)).

As mentioned earlier ([Chapter 1.2.1](#)), glucose from glycolysis can be diverted to other metabolic pathways such as *de novo* serine or glycine biosynthesis and the pentose phosphate pathway (PPP) ([Figure 1.2](#)). Generated from the PPP, pentose is used in nucleotide synthesis, and NADPH in *de novo* lipid biosynthesis and the protection against oxidative damages ([Patra and Hay, 2014](#)). The rapid uptake of glucose therefore provides cancer cells with anti-oxidant defence and excess carbon for biosynthesis of proteins, lipids and nucleic acids ([Liberti and Locasale, 2016](#)).

In cancer cells, 80-90% of glucose is converted to lactate ([Xie et al., 2014](#)). Lactate formation is necessary for the regeneration of NAD⁺ such that glycolysis

continues unabated (Valvona et al., 2016). When lactate is released extracellularly, the acidic environment produced may facilitate extracellular matrix degradation and tumor invasion, a model known as the acid-mediated tumor invasion hypothesis (Gatenby et al., 2006). Supporting this hypothesis, research findings show that oral administration of sodium bicarbonate inhibits tumor invasion in a mouse tumor model (Estrella et al., 2013). Lactate is recently found to function in histone lysine lactylation and epigenetic regulation of gene expression (Zhang et al., 2019). Whether this type of histone modification plays a role in the high-lactate tumor environments remains unclear.

What causes the Warburg effect in cancer cells has always been the center in the field of cancer metabolism (Lu et al., 2015). Warburg hypothesized that mitochondrial impairment is the cause of aerobic glycolysis and cancer (WARBURG, 1956), which has sparked much controversy among scientists (discussed in **Chapter 1.3.2** (Senyilmaz and Teleman, 2015)). The current, widely-accepted view is that, rather than mitochondrial dysfunction, activation of oncogenes and inactivation of TSGs are key glycolytic inducers through controlling the gene expression program of glycolysis or regulating the glycolytic enzyme activities (**Table 1-10**).

Table 1-10. Well-known glycolytic inducers and their actions.

Oncogenes / TSGs	Effects on aerobic glycolysis
AKT	A serine/threonine kinase that promotes translocation of glucose transporters to the plasma membrane and activates hexokinase and phosphofructokinase-2 (PFK2 or PFKFB) (Robey and Hay, 2009)
c-SRC	A tyrosine kinase that phosphorylates and activates hexokinase and phosphofructokinase-2 (PFK2 or PFKFB) (Ma et al., 2020; J. Zhang et al., 2017)
HIF1α	A transcription factor that activates the gene expression program of glycolysis by direct binding to the glycolytic genes; inactivates pyruvate dehydrogenase (PDH) by upregulating PDH kinase to induce a switch from OXPHOS to aerobic glycolysis (Cai et al., 2013)
MYC	A transcription factor that activates the gene expression program of glycolysis by direct binding to the glycolytic genes (Kim et al., 2004)
p53	A transcriptional factor that represses glycolytic gene expression program; upregulates TP53-induced glycolysis and apoptosis regulator (TIGAR) that reduces the levels of fructose-2,6-bisphosphate (the allosteric activator of phosphofructokinase PFK) (Bensaad et al., 2006; Fischer, 2017)
RAS	A GTPase that induces glycolytic gene expression program through upregulating MYC and HIF1α (Kim and Dang, 2006; Ying et al., 2012)

1.3.2. Mitochondrial metabolism

Mitochondria are the bioenergetic, biosynthetic and signaling hubs that host the tricarboxylic acid (TCA) cycle, the electron transfer chain (ETC or respiratory chain; complexes I-IV), complex V where OXPHOS takes place, metabolic pathways involving amino acids, lipids and nucleotides, and signaling molecules like reactive oxygen species (ROS) ([Vyas et al., 2016](#)). Generated as a by-product of the ETC, ROS including superoxide anion (O_2^-), hydroxyl radical ($\cdot OH$), H_2O_2 , and singlet oxygen ($\cdot O_2$) are scavenged by antioxidant pathways including superoxide dismutase (SOD), catalase, glutathione, thioredoxins and peroxiredoxins ([Birben et al., 2012](#)). Excess ROS causes oxidative damages to lipids, proteins and DNA. For example, H_2O_2 oxidizes and inactivates tumor suppressor PTEN, preventing it from antagonizing the InR-PI3K signaling ([Sullivan and Chandel, 2014](#)). Mitochondria also mediates apoptosis (programmed cell death) as pro-apoptotic stimuli can stimulate the release of cytochrome c from mitochondria to cytosol, thereby activating caspases, the executors of apoptosis ([Redza-Dutordoir and Averill-Bates, 2016](#)).

Since Warburg hypothesized that mitochondrial impairment had been the cause of aerobic glycolysis ([Warburg 1956](#)), extensive research has been conducted to test the hypothesis. In support of his hypothesis, succinate dehydrogenase (SDH) and fumarate hydratase (FH or fumarase), which are mitochondrial enzymes of the TCA cycle, were identified as tumor suppressors ([Gottlieb and Tomlinson, 2005](#); [King et al., 2006](#)). When SDH and FH are inactivated, succinate and fumarate accumulate, respectively, which function as competitive inhibitors of propyl hydroxylase (an enzyme that promotes the degradation of HIF1 α) ([MacKenzie et al., 2007](#)). As a result, accumulation of succinate or fumarate leads to stabilization of HIF1 α that reinforces aerobic glycolysis ([Isaacs et al., 2005](#); [Selak et al., 2005](#)).

However, a growing body of evidence has been found that contradicts Warburg's argument that cancer mitochondria are impaired. For example, in a comparative metabolic profiling of melanoma cell lines, all melanoma cells tested not only exhibit aerobic glycolysis, but also maintain functional TCA cycle activity ([Scott et al., 2011](#)). Analyses of the rates of oxygen consumption (a measure of OXPHOS) and lactate production (a measure of aerobic glycolysis) in a panel of cancer cell lines reveal that some cancer cells rely on OXPHOS heavily and some rely on both OXPHOS and

aerobic glycolysis ([Zu and Guppy, 2004](#)). Thus, unlike aerobic glycolysis that is universal in most cancer cells, cancer mitochondrial metabolism is more heterogeneous and elusive than previously envisioned.

Given the complex, multifaceted functions of mitochondria, it is conceivable that there is no simple answer for the role of mitochondria in cancer progression ([Vyas et al., 2016](#)). Currently, the research on cancer mitochondria seems understudied and lags behind that on the Warburg effect. One notable example is that while FDG-PET is widely applied in clinics, a new probe, 4-[18F]fluorobenzyl-triphenylphosphonium (18F-BnTP), has just been developed recently for PET imaging of OXPHOS-dependent tumors ([Momcilovic et al., 2019](#)). Also, although metformin, a drug used to treat type II diabetes, has been used in more than a dozen of cancer clinical trials and shown promising results because of its inhibitory effect on the respiratory complex I, its molecular mechanism of action remains elusive ([Saraei et al., 2019](#)).

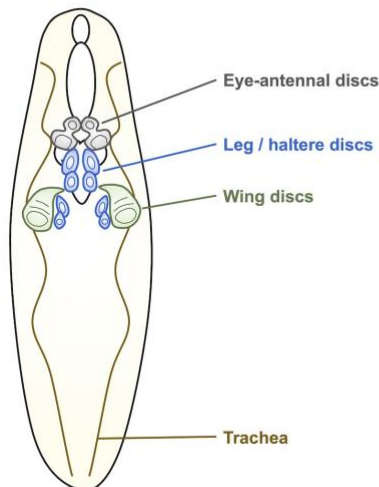
Therefore, tremendous efforts are warranted to gain a better understanding of how mitochondria are linked to cancer such that more therapeutic strategies targeting mitochondria can be developed.

1.4. *Drosophila* as a genetic model of human cancers

Drosophila melanogaster (commonly known a fruit fly or vinegar fly) is extensively used as an *in vivo* genetic model organism to study human cancers, thanks to the high conservation in genes and signaling pathways among fly and human, the reduced genetic redundancy and the rapid life cycle in fly (~ 12 days from embryo to adult at room temperature) (Gonzalez, 2013; Herranz and Cohen, 2017). Examples of fly homologs of human oncogenes and TSGs are shown in **Table 1-2**.

Imaginal epithelia in *Drosophila*, such as wing and eye-antennal imaginal discs, proliferate extensively and are patterned properly during larval development (**Figure 1.5**), and give rise to adult structures after morphogenesis, such as wings and eyes, respectively (McClure and Schubiger, 2005). Carcinomas, which are malignancies of epithelial origin, account for about 90% of all human cancers (Hanahan and Weinberg, 2000). Thus, imaginal discs provide an excellent model to study tumor growth and invasion, as well as to search for novel cancer-associated genes in genetic screens (Herranz et al., 2016). In my thesis, wing imaginal discs are primarily used to model human carcinomas and the wing disc structures are shown in **Figure 1.5**.

Drosophila larva and its imaginal discs



Wing imaginal discs

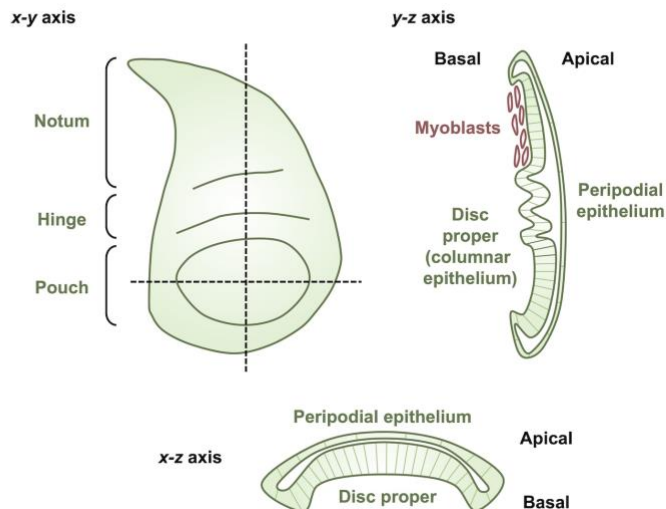


Figure 1.5. Wing imaginal discs.

(Left) A *Drosophila* larva and its eye-antennal, leg/haltere and wing imaginal discs are shown. (Right) Wing disc can be divided into three main regions – notum, hinge and pouch. Wing disc is a sac-like structure consisting of two opposing layers: a peripodial epithelium

(PE) and disc proper (DP; columnar epithelium) that connect to each other. Myoblasts are associated to the basal side of the wing disc in the notum region.

In addition, the development of genetic tools such as the Gal4-UAS (Brand and Perrimon, 1993), FLP-out (Struhl and Basler, 1993), FLP-FRT (Golic and Lindquist, 1989) and MARCM systems (Lee and Luo, 1999) permits the control of gene expression in a spatiotemporal manner (Figure 1.6). Together with large-scale genetic screens, these tools tremendously accelerate the discovery of oncogenes and TSGs and their functional characterization in tumorigenesis (Mirzoyan et al., 2019). The molecular basis of the Gal4-UAS and Flp-out systems, which are employed in my research, are shown in Figure 1.7 and Figure 1.8, respectively.

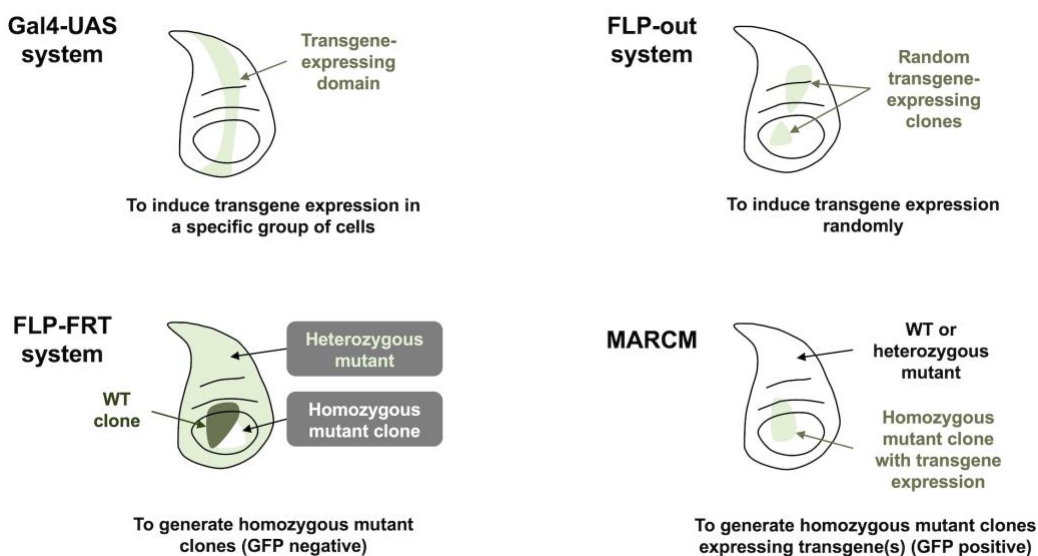


Figure 1.6. Genetic tools to manipulate gene expression.

Various genetic tools are used to manipulate gene expression in larval wing discs. Gal-UAS and FLP-out systems are used to induce expression of transgene(s) in a specific group of cells and in a random manner, respectively. FLP-FRT and MARCM systems are used to generate mutant clones. In the MARCM clones, transgene expression can be additionally induced. Gal4, a transcription activator that regulates galactose-induced gene expression in yeast and binds to UAS in fly Gal4-UAS system; UAS, upstream activating sequence; FLP-out, flip-out; Flp, flippase recombinase; FRT, flippase recognition target; GFP, green fluorescent protein; WT, wild type; MARCM, Mosaic analysis with a repressible cell marker.

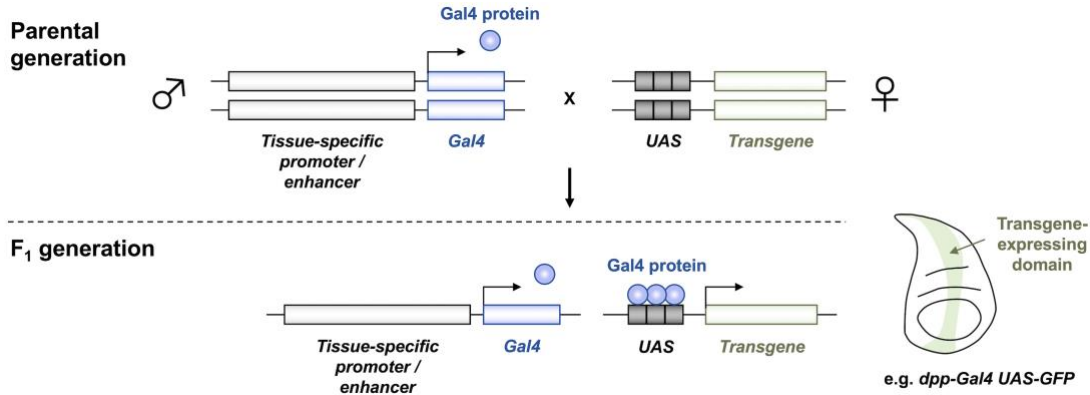


Figure 1.7. The Gal4-UAS system.

One parent fly harboring the tissue-specific Gal4 driver line is crossed to another parent fly harboring the UAS-transgene line. In the progeny, the Gal4 proteins expressed in a tissue-specific manner bind to the UAS sites (which can be arrayed in tandem) and drive transgene expression. The transgene can be double-stranded RNA (dsRNA) and short hairpin RNA (shRNA) for RNA interference (RNAi), guided RNA (gRNA) in CRISPR-Cas9 system, coding DNA (cDNA) for overexpression of wild-type, mutant or fusion proteins, and lacZ (encoding β -galactosidase) or fluorescent protein (e.g. GFP)-based reporters. A *dpp-Gal4 UAS-GFP* (abbreviated as *dpp > GFP*) wing disc is shown with its transgene-expressing (Dpp) domain (in green). CRISPR, clustered regularly interspaced short palindromic repeats

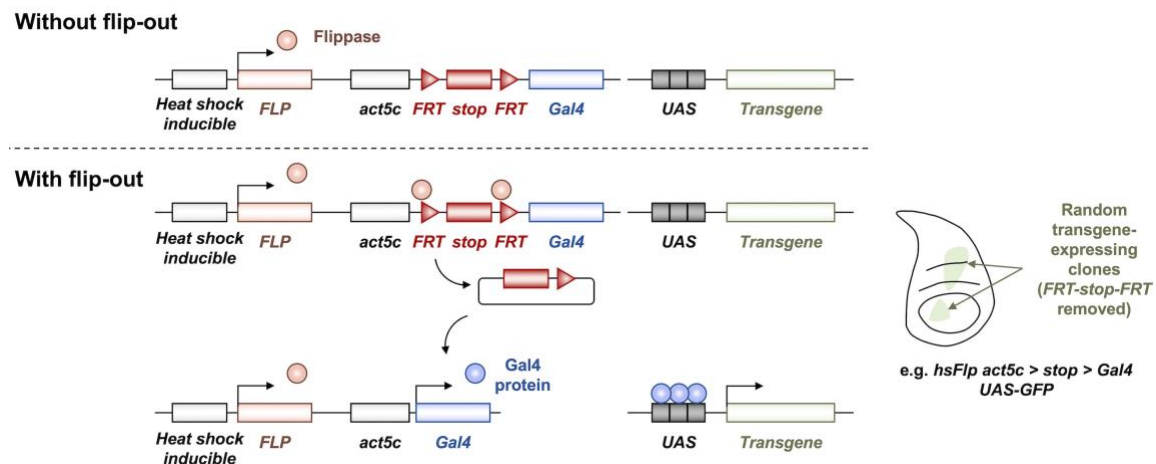


Figure 1.8. The FLP-out system.

Flippase recombinase (Flp) expression is induced by heat shock under the heat shock (*hs*) inducible promoter. If Flp binds to the flippase recognition target sites (FRT) and removes (flips out) the FRT-stop-FRT cassette by recombination, Gal4 proteins will be expressed constitutively under the *act5c* promoter and drive the transgene expression. The flip-out is a random event so that transgene is only induced in clones with the flip-out event. A *hsFlp act5c > stop > Gal4 UAS-GFP* wing disc is shown with transgene-expressing clones generated in a random fashion (in green).

1.4.1. Models of human carcinomas

Numerous fly tumors harboring single mutations of oncogenes or TSGs (**single-hit tumor models**) have been developed, ranging from hyperplasia to malignant neoplasia (**Table 1-11**) (Rudrapatna et al., 2012). These single-hit tumor models at most display local tumor invasion. Using the genetic techniques (discussed in **Chapter 1.4**) to generate **multiple-hit tumor models** such as the well-known *Ras^{V12} scrib* \sim model (Pagliarini and Xu, 2003), enhanced malignancy and metastasis (defined as secondary tumor formation) are more prevalent, mimicking human carcinomas. Transcriptomics analysis of *Ras^{V12} scrib* \sim tumor reveals an oncogenic signaling network integrating JNK, JAK-STAT, MYC and Hippo (Atkins et al., 2016). Also, using this malignant tumor model, researchers have found additional cancer-related phenotypes such as cancer cachexia (peripheral organ wasting) (Figueroa-Clarevega and Bilder, 2015), autophagy in tumor microenvironment (Katheder et al., 2017) and immune responses to cancer (Cordero et al., 2010; Pastor-Pareja et al., 2008).

Intriguingly, emerging evidence suggests that the tissue intrinsic properties render certain regions of a tissue a ‘**tumor hotspot**’. For example, while Notch activation on its own leads to hyperplasia, it interacts with local, endogenous JAK-STAT and JNK in *Drosophila* salivary gland imaginal rings to induce malignant tumorigenesis (Yang et al., 2019). Also, polarity deficient cells (e.g. *scrib* \sim) exploit the local JAK-STAT and cellular architecture in the hinge region of wing disc to cause benign tissue overgrowth (Tamori et al., 2016). These examples demonstrate even single-hit mutations may transform cells into malignant tumors through environment-dependent, cooperative tumorigenesis.

Table 1-11. Hyperplastic or neoplastic (benign or malignant) tumor models.

Abbreviations: Scrib, Scribble; Lgl, Lethal giant larvae; Dlg, Discs large; Wts, Warts; Lats, Large tumor suppressor; Sav, Salvador; Hpo, Hippo; Yki, Yorkie; Yki-S168A, a constitutively active form of Yki; PcG, Polycomb group proteins; Ph, Polyhomeotic-distal and -proximal; Pc, Polycomb; Sce, Sex combs extra; Psc-Su(z)2, Posterior Sex Combs (Psc) and Suppressor of Zeste 2 (Su(z)2); Udp, unpaired; Tsp29Fb, Tetraspanin transmembrane protein; PDGF, Platelet-derived growth factor; VEGF, Vascular endothelial growth factor

Tumor models	Genotypes	Gene / protein functions	Tumor features
Single-hit tumor models			
Activated Ras	<i>Rasv12</i>	<i>Rasv12</i> is an activated form of Ras in the Ras-Raf-MEK-MAPK signaling pathway.	Hyperplasia, increased apoptosis but no disruption in epithelial integrity (Karim and Rubin, 1998).
Hippo inactivation (or Yki activation)	<i>wts</i> \sim or <i>lats</i> \sim or <i>sav</i> \sim or <i>hpo</i> \sim or <i>Yki-S168A</i>	Wts, Lats, Sav and Hpo tumor suppressors and Yki oncogene are components of the Hippo tumor suppressor pathway that controls tissue size.	Hyperplasia, resistance to apoptosis but no disruption in epithelial integrity (Udan et al., 2003)
PcG loss	<i>ph</i> \sim or <i>Pc</i> \sim or <i>Sce</i> \sim or <i>Psc-Su(z)2</i>	Components of PcG are tumor suppressors and repress gene expression of Notch and JAK-STAT signaling components.	Neoplasia, loss of epithelial integrity, invasion into nearby tissues but no metastasis (Classen et al., 2009; Martinez et al., 2009)
Polarity loss	<i>scrib</i> \sim or <i>lgl</i> \sim or <i>dlg</i> \sim	Scrib, Lgl and Dlg are cell polarity proteins and tumor suppressors.	Neoplasia, multi-layering, loss of epithelial integrity (Bilder et al., 2000)
PEGF / VEGF receptor activation	<i>Pvr</i>	A receptor tyrosine kinase that is activated by binding to PDGF or VEGF-related factors	Neoplasia, multi-layering, loss of epithelial integrity (Rosin et al., 2004)
Multiple-hit tumor models			
Activated Ras and polarity loss	<i>Rasv12 scrib</i> \sim (intra-clonal) or <i>Rasv12// scrib</i> \sim (inter-clonal)	Synergy between <i>Rasv12</i> and polarity loss induces JNK-dependent upregulation of Upd (JAK-STAT signaling)	Metastasis (secondary tumor formation) plus local invasion (Pagliarini and Xu, 2003; Wu et al., 2010)
Activated Ras and Wnt	<i>Rasv12 APC</i> \sim	APC is a TSG and a negative regulator of Wnt signaling.	Neoplasia, loss of epithelial integrity, local invasion but no metastasis (Wang et al., 2013)
Activated Ras, Wnt and Snail	<i>Rasv12 APC</i> \sim <i>Snail</i>	Snail is an EMT-TF that activates EMT.	Metastasis (Campbell et al., 2019)
Activated Ras and loss of Tsp29Fb	<i>Rasv12 Tsp29Fb-RNAi</i>	Tsp29Fb is a TSG that inhibits EGFR-Ras signaling and maintains epithelial integrity	Metastasis (Zoranovic et al., 2018)
Activated Ras and c-Src	<i>Rasv12 Src64B Csk</i> \sim	c-SRC is a tyrosine kinase, negatively regulated by Csk	Metastasis (Vidal et al., 2007)
EGFR and psq loss	<i>EGFR psq-RNAi</i>	Psq (pipsqueak) is a chromatin regulator	Metastasis (Herranz et al., 2014)

1.4.2. Models of metabolic reprogramming

In addition to cancer genes and signaling pathways, metabolic enzymes and the regulation of their activities are highly conserved among fly and mammals. For example, *Drosophila* Lactate hydrogenase (LDH) functionally resembles the mammalian homolog LDHA, favoring the reduction of pyruvate to lactate to regenerate NAD⁺ for unabated glycolysis (Rechsteiner, 1970). Also, both mammalian and insect Phosphofructokinase (PFK) proteins have the binding site for fructose 2,6-bisphosphate (F2,6-BP), a metabolite that functions to activate PFK allosterically (Nunes et al., 2016). The high conservation in metabolites and metabolic pathways among fly and human therefore enables us to use *Drosophila* to study cancer metabolism, one of the hallmarks of cancer.

Table 1-12. *Drosophila* tumor models with characterization of metabolic profiles

Features associated with mitochondrial dysfunction are highlighted in light grey.

Tumor models	Aerobic glycolysis	Mitochondrial metabolism	Others	References
Hyperplastic				
Activated Notch	LDH among other glycolytic genes upregulated	Reduced respiration rate	N/A	(Slaninova et al., 2016)
Activated Ras (<i>Rasv12</i>)	LDH upregulated	Little or mild ROS	N/A	(Katheder et al., 2017; Ohsawa et al., 2012; Wang et al., 2016)
Activated Yki	LDH weakly upregulated	Increased mitochondrial fusion; little ROS	N/A	(Katheder et al., 2017; Nagaraj et al., 2012; Wang et al., 2016)
Neoplastic				
Activated Pvr	LDH among other glycolytic genes upregulated	Attenuated OXPHOS; elevated ROS	N/A	(Wang et al., 2016)
<i>EGFR</i> with <i>psq-RNAi</i> (metastatic)	LDH among other glycolytic genes upregulated	N/A	N/A	(Eichenlaub et al., 2018)
Polarity loss (<i>dlg -/-</i> or <i>scrib -/-</i>)	LDH upregulated	Dysfunctional mitochondria; elevated ROS	Active <i>de novo</i> lipid synthesis	(Bunker et al., 2015; Ji et al., 2019; Yadav and Srikrishna, 2019)
Activated Ras with polarity loss (<i>Rasv12 scrib -/-</i>) (metastatic)	Glucose uptake elevated	Damaged mitochondria; elevated ROS	Active amino acid uptake	(Katheder et al., 2017)

Table 1-12 summarizes the fly hyperplastic or neoplastic tumors with characterized metabolic profiles. Regardless of hyperplastic or malignant neoplastic growth, all the characterized tumors acquire increased aerobic glycolysis. Most hyperplasia displays little or mild ROS, indicative of absence of mitochondrial damage, whereas the majority of neoplasia associates with diminished mitochondrial activity and high ROS, supporting Warburg's hypothesis that mitochondrial impairment is the cause of aerobic glycolysis and cancer (WARBURG, 1956).

Details of the individual tumors are discussed below.

In Notch-induced hyperplasia, Notch directly elicits transcriptional upregulation of glycolytic genes including *LDH*, *Glut1* and *Hex-A*, and knockdown of *LDH* or *Hex-A* partially suppresses tissue overgrowth (Slaninova et al., 2016). Notch signaling also reduces oxygen consumption rate (OCR, representing the respiration rate), probably through the repression of TCA cycle genes mediated by the transcription repressor Hairy (Slaninova et al., 2016).

Activated Ras-induced hyperplasia is associated with *LDH* upregulation but its functional relevance is undefined (Wang et al., 2016). The Ras-activated cells display little or mild ROS as revealed by dihydroethidium (DHE) and 2',7'-dichlorofluorescin diacetate (H₂DCFDA) staining (Katheder et al., 2017; Ohsawa et al., 2012). Intriguingly, when mitochondrial dysfunction is introduced in a subset of the Ras-activated tumor cells (inter-clonal *RasV12 mito-/- // RasV12* tumors, where *mito-/-* refers to mitochondrial dysfunction), the Ras-activated benign overgrowth is transformed into malignancy through a signaling cascade of ROS-JNK-Hippo-Udp/Wg (Ohsawa et al., 2012).

In hyperplasia caused by activated Yki, aerobic glycolysis is minimally induced (Wang et al., 2016). Rather, Yki promotes mitochondrial fusion through direct transcriptional induction of genes encoding fusion regulators including mitochondria assembly regulatory factor (Marf) and Optic atrophy 1 (Opa1) (Nagaraj et al., 2012). Inhibition of mitochondrial fusion reduces hyperplastic growth (Nagaraj et al., 2012). Yki-activated hyperplasia has little ROS, suggesting that the mitochondria may remain functional (Katheder et al., 2017).

In tumor with activation of oncogene PDGF- and VEGF-receptor related (Pvr), Ras-Raf-MEK-ERK cooperating with PI3K-Akt-mTORC1 stabilizes HIF1α to induce

aerobic glycolysis (*LDH* upregulation), while Src-JNK signaling attenuates OXPHOS via inhibition of pyruvate dehydrogenase (PHD; which converts pyruvate to acetyl-CoA) (Wang et al., 2016). The consequent mitochondrial dysfunction leads to high ROS production which in turn sustains HIF1 α and Src, feeding forward to reinforce the high glycolysis and low OXPHOS states (Wang et al., 2016). Blocking aerobic glycolysis (*LDH* upregulation) through HIF1 α inhibition has minor effects on suppressing tumor growth (Wang et al., 2016), suggesting mitochondrial dysfunction or other metabolic alterations may play a predominant tumor-promoting role.

In another malignant tumor *EGFR psq-RNAi*, *LDH* along with several other glycolytic genes is upregulated, indicative of increased aerobic glycolysis (Eichenlaub et al., 2018). Notably, *LDH* is necessary for the malignant transformation of *EGFR psq-RNAi* tumor, and is sufficient for transforming EGFR-, Yki- or Notch-induced hyperplastic growth into neoplasm (Eichenlaub et al., 2018).

In tumors with polarity loss (*scrib* $\sim\sim$ or *dlg* $\sim\sim$ tumors), *LDH* is significantly induced (~60-fold increase), although knockdown of *LDH* has no noticeable effect on tumor growth (Bunker et al., 2015). Transcriptomic analyses of *scrib* $\sim\sim$ tumors reveal induction of aerobic glycolysis and downregulation of OXPHOS over time, suggesting a gradual metabolic transition from OXPHOS towards aerobic glycolysis (Ji et al., 2019). Indeed, *scrib-RNAi* tumor cells manifest mitochondrial dysfunction and massive ROS production (Yadav and Srikrishna, 2019). Consistently, *drg* $\sim\sim$ tumors experience high oxidative stress as revealed by high ROS levels and induction of antioxidant genes such as *gstE1* (which encodes Glutathione S transferase E1) (Bunker et al., 2015). In addition, fatty acid synthase (FASN) is elevated, suggesting *de novo* lipid synthesis is active in the tumors cells with polarity loss (Bunker et al., 2015).

In the malignant tumor model with activated Ras and polarity loss (*RasV12 scrib* $\sim\sim$), the tumors cells display increased glucose uptake, high ROS, accumulation of damaged mitochondria (Katheder et al., 2017). While the functional roles of these metabolic changes are unknown, inhibition of amino acid transporter Slimfast (Slif) markedly reduced *RasV12 dlg-RNAi* tumor growth, indicating that this malignant tumor type is highly reliant on active amino acid uptake (Katheder et al., 2017).

1.5. Homeodomain-interacting protein kinases (HIPKs)

In 1998, Homeodomain-interacting protein kinase (HIPKs; HIPK1-4 in vertebrates; Hipk in *Drosophila*; Hpk-1 in *C. elegans*) were discovered as transcriptional co-regulators for homeodomain transcription factors (TFs) (Kim et al., 1998). Since then, emerging evidence shows that HIPKs, especially HIPK2 (the archetypal member of the HIPK family), participate in diverse biological processes by directly phosphorylating and modulating the activities of an ever growing number of TFs, transcriptional co-regulators and other signaling molecules (**Table 1-13**) (discussed further in **Chapter 1.5.1**) (reviewed in (Blaquiere and Verheyen, 2017)).

HIPKs are primarily nuclear (except the cytoplasmic HIPK4), dual serine/threonine and tyrosine kinases, grouped as the HIPK subfamily on the kinase tree (*Superfamily*: CMGC (cyclin-dependent kinases (CDKs), mitogen-activated protein kinases (MAP kinases), glycogen synthase kinases (GSKs) and CDK-like kinases); *Family*: DYRK (dual-specificity tyrosine regulated kinase); *Subfamily*: HIPK) (Aranda et al., 2011). Recent crystal structural analyses confirm that the overall kinase domain of HIPK2 closely resembles the related DYRKs (Agnew et al., 2019). As shown in **Figure 1.9**, human HIPK2 contain a kinase domain, a homeodomain-interacting domain (HID), a PEST sequence (rich in proline P, glutamate E, serine S and threonine T) and a YH domain (rich in tyrosine Y and histidine H). The PEST sequence and YH domain are linked to protein stability (Rogers et al., 1986) and autoinhibition (Gresko et al., 2006; Rui et al., 2004), respectively.

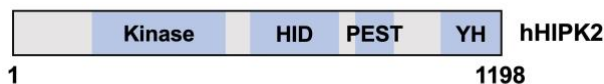


Figure 1.9. Schematic diagram of human HIPK2 (hHIPK2)

hHIPK2 (UniProt: Q9H2X6; amino acid 1-1198 from N- to C-terminal; predicted molecular mass, 131 kilo Dalton) is shown with its kinase domain (192-520; catalytic site Lys (K) 221; activating loop, 352-357), homeodomain-interacting domain (HID; 583-798), PEST sequence (839-934) and YH domain (1076-1198; also known as SQA region rich in serine, glutamine and alanine, which overlaps with the autoinhibitory domain AID (984-1198)).

Table 1-13. Binding partners or protein substrates of HIPKs

Proteins that are directly phosphorylated by HIPKs (confirmed by *in vitro* kinase assays) are highlighted in bold with the phosphorylation sites in brackets, if any.

Binding partners	Molecular functions	Cellular/ physiological roles	References
Transcription factors (TFs)			
AML1 (Ser 249 and Ser 276), p300	HIPK2 complexes with AML1 and p300 (co-activator and histone acetyltransferase HAT) and stimulates their activities in transcription and histone acetylation.	Hematopoiesis, vasculogenesis and angiogenesis	(Aikawa et al., 2006)
ATF1 (Ser 198)	HIPK2 inhibits the repressor function of cyclic AMP-dependent transcription factor ATF-1.	Response to genotoxic stress	(Hailemariam et al., 2010)
CREB (Ser 271)	HIPK2 activates cyclic AMP response element-binding protein (CREB).	Response to genotoxic stress	(Sakamoto et al., 2010)
Hbn (Thr 54, Ser 56, and Thr 399), Ems (Ser 48, Ser 52, Ser 63, Thr 67, and Ser 182), Drop (Thr 147 and Thr 174)	Hipk phosphorylate homeobox TFs including Homeobrain (Hbn), Empty spiracles (Ems), and Drop (or Muscle segment homeobox, Msh). The functional significance is unknown.	Embryonic and brain development	(Steinmetz et al., 2019)
NKx-1.2; NK-1; NK-3; NKx-2.5; HoxC4; HoxD4	HIPKs enhance the DNA binding activity of homeodomain TFs.	Embryonic development, pattern formation and organogenesis	(Kim et al., 1998)
p53 (Ser 46)	HIPK2 activate p53 transcriptional activity.	Apoptotic response to genotoxic stress	(D'Orazi et al., 2002)
Pax6 (Thr 281, Thr 304, Thr 373), Toy (Ser 121, Thr 395, Ser 410, Thr 452), Ey	HIPK2/Hipk activates the Paired box protein 6 (Pax6; Eyeless (Ey) and Twin of eyeless (Toy) in fly) by enhancing Pax6-p300 interaction.	Organogenesis of the eye, nose, pancreas, and central nervous system	(Kim et al., 2006; Steinmetz et al., 2018)
TCF3 (S190)	HIPK2 inhibits the repressor Transcription factor 3 (TCF3) for Wnt signaling activation.	Wnt signalling, body axis specification	(Hikasa et al., 2010)
Transcriptional co-regulators			
CBP (Ser 2361/ 2363/ 2371/ 2376/ 2381)	HIPK2 activates CREB-binding protein (CBP), the co-activator of CREB.	Cell proliferation, differentiation and apoptosis	(Kovács et al., 2015)
CtBP (Ser 422)	HIPK2 promotes the degradation of the co-repressor Carboxyl-terminal binding protein (CtBP).	Apoptotic response to genotoxic stress	(Zhang et al., 2005)
Gro (Ser 297)	Hipk inhibits Groucho (Gro) co-repressor activity.	Notch signaling, <i>Drosophila</i> eye development	(Choi et al., 2005; Lee et al., 2009b)

Yki	Hipk activates the transcriptional co-activator Yorkie (Yki, YAP/TAZ in mammals).	Hippo signaling, tissue/ organ size control	(Chen and Verheyen, 2012)
Other signaling molecules			
Arm, β-catenin (Ser 33, Ser 37)	Hipk/HIPK2 regulates Armadillo (Arm)/ β -catenin protein stability.	Wg/Wnt signaling, wing development in flies; axis duplication in <i>Xenopus</i> embryos	(Kim et al., 2010; Lee et al., 2009b)
Daxx (Ser 669)	HIPK3 phosphorylates the scaffold protein Death-associated protein 6 (Daxx) for ASK1-MKK-JNK-c-Jun activation.	JNK signaling and apoptosis, steroidogenesis	(Lan et al., 2012)
Slimb	Hipk phosphorylates E3 ubiquitin ligases (Slimb in fly; β -TrCP in mammals) to inhibit ubiquitination of proteins like Arm and Ci (Gli in mammals).	Wg and Hedgehog signaling, cell proliferation and cell fate specification	(Swarup and Verheyen, 2011)

1.5.1. Developmental roles of HIPKs

The regulation of homeodomain TFs (which control Homeobox gene expression and tissue patterning) by HIPKs suggests that HIPKs are implicated in the development of organisms (Kim et al., 1998). Indeed, mice lacking both *Hipk1* and *Hipk2* are embryonic lethal, displaying defects in neural tube closure and hematopoiesis, reduced cell proliferation, and decreased responsiveness to the morphogenetic signal Sonic Hedgehog (Aikawa et al., 2006; K. Isono et al., 2006). *Hipk1* or *Hipk2* singly homozygous mutant mice are viable and grossly normal, suggesting a functional redundancy between *Hipk1* and *Hipk2* (K. Isono et al., 2006). In *Drosophila*, loss of *hipk* leads to embryonic lethality (Lee et al., 2009a). On the contrary, in *C. elegans*, *hpk-1* null mutant animals are viable (Raich et al., 2003).

Beyond embryonic development, HIPKs are implicated in a wide range of cellular or physiological processes (see Table 1-13), thanks to the functional versatility of HIPKs to phosphorylate numerous signaling molecules including transcriptional co-regulators which are usually the downstream effectors of developmental signaling pathways. The regulation modes of Notch, Wg, Hedgehog, Hippo, JNK and JAK-STAT by fly Hipk are discussed below.

In *Drosophila*, Hipk antagonizes the global co-repressor Groucho to promote Notch signaling (Lee et al., 2009a). Hipk also functions as a positive regulator of both Wg (Wingless; Wnt in mammals) and Hedgehog signaling by stabilizing Armadillo (β -catenin in mammals) and Cubitus interruptus (Ci; Gli in mammals), respectively (Lee et al., 2009b; Swarup and Verheyen, 2011). In addition, Hipk stimulates the transcriptional activity of Yorkie (Yki; YAP/TAZ in mammals), the effector of the Hippo tumor suppressor pathway (Chen and Verheyen, 2012; Poon et al., 2012). Hipk is also required for JNK (Huang et al., 2011). As for JAK-STAT signaling, Hipk activates the pathway through facilitating the translocation of the transcription factor Signal-transducer and activator of transcription protein at 92E (Stat92E) into the nucleus (Tettweiler et al., 2019).

1.5.2. Regulation of HIPK2 by post-translational modifications

The activity of HIPKs are governed primarily by post-translational modifications (PTMs), which can alter protein stability, activity, localization and protein-protein interactions in response to morphogens, mitogens, genotoxic signals or other cellular stresses ([Figure 1.10](#)) ([reviewed in \(Blaquiere and Verheyen, 2017\)](#)). HIPKs can also be regulated post-transcriptionally by micro-RNAs (e.g. miR-141 and miR-27a) ([Huang et al., 2015; Li et al., 2010](#)), and transcriptionally by the transcription factor Nuclear factor erythroid 2-related factor 2 (NRF2) ([Torrente et al., 2017](#)). Here, the regulation of HIPK2 by PTMs is discussed.

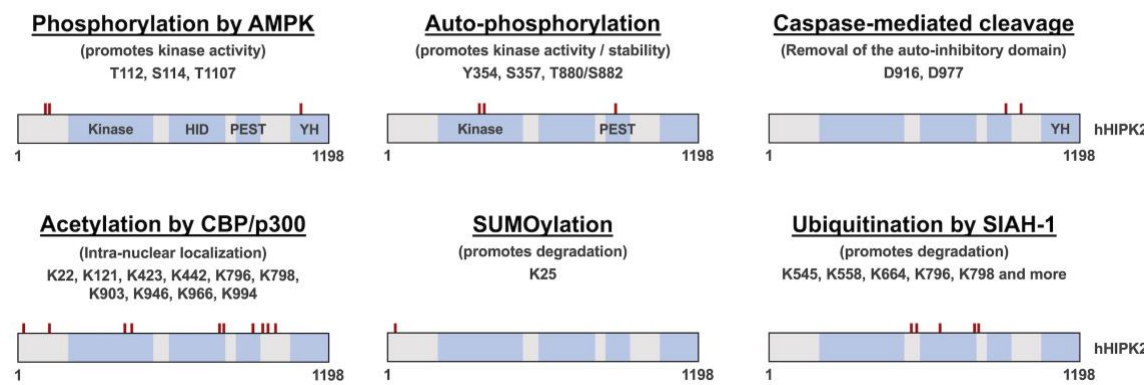


Figure 1.10. Examples of HIPK2 post-translational modifications.

HIPK2 can be phosphorylated by other kinases such as AMP-activated protein kinase (AMPK) ([Choi et al., 2013](#)). HIPK2 proteins can oligomerize and/or (either *cis*- or *trans*-) auto-phosphorylate themselves ([Bitomsky et al., 2013; Saul et al., 2013](#)). Other PTMs include caspase-mediated cleavage ([Gresko et al., 2006](#)), acetylation by acetyltransferases CBP or p300 and deacetylation by HDAC3 ([de la Vega et al., 2012](#)), SUMOylation ([Gresko et al., 2005](#)), and Ubiquitination by SIAH-1 ([Winter et al., 2008](#)). CBP, cAMP response element-binding protein (CREB)-binding protein; HDAC3, Histone deacetylase 3; T, threonine; S, serine; Y, tyrosine; D, aspartate; K, lysine.

Normally, HIPK2 protein expression is maintained at low levels ([Dong et al., 2008](#)). A collection of E3 ubiquitin ligases or their complex components including Seven in absentia homolog-1 (SIAH-1) ([Winter et al., 2008](#)), SIAH-2 ([Calzado et al., 2009](#)), WD40-repeat and suppressor of cytokine signaling (SOCS) box containing-1 (WSB-1) ([Dong et al., 2008](#)), Mouse double minute 2 homolog (MDM2) ([Rinaldo et al., 2007](#)) and F-box only protein 3 (Fbx3) ([Shima et al., 2008](#)) constantly ubiquitinate HIPK2 and promote its degradation by the ubiquitin-proteasome system (UPS).

However, in response to cellular stresses, the interaction between these E3 ubiquitin ligases and HIPK2 may change. For example, upon DNA damage, HIPK2 oligomerizes and auto-phosphorylates at Thr 880/ Ser 882, which serves as a signal to recruit Peptidyl-prolyl cis-trans isomerase (Pin1) (Bitomsky et al., 2013). The formation of HIPK2-Pin1 complex triggers the dissociation of SIAH1/2 from HIPK2 so as to stabilize HIPK2, which then activates p53 and its DNA damage response (cell-cycle arrest, apoptosis, or DNA repair) (Bitomsky et al., 2013; Winter et al., 2008). Intriguingly, activated p53 in turn induces caspase-mediated cleavage of HIPK2 at Asp 916 and Asp 977, which removes the auto-inhibitory domain (AID; overlapping with the YH domain) from HIPK2, forming a positive feedback loop to sustain high p53 activity (Gresko et al., 2006). The binding of Axin to the AID of HIPK2 can also relieve the auto-inhibitory effect of HIPK2 (Rui et al., 2004).

Additional PTMs are summarized in **Figure 1.10**. It is interesting to note that HIPK2 and CBP/p300 are substrates of each other; HIPK2 phosphorylates CBP/p300 and CBP/p300 acetylates HIPK2 (see **Figure 1.10** and **Table 1-13**). Crosstalk of PTMs can occur as well, such as the redox-regulated switch between acetylation and SUMOylation of HIPK2 in response to oxidative stress (de la Vega et al., 2012), providing additional layers of complexity in the dynamic regulation of HIPK2.

1.5.3. Roles of HIPK2 in human diseases

Research has found that dysregulated HIPK2 in humans leads to pathological consequences, including fibrosis and cancer.

HIPK2 is shown to be pro-fibrogenic in kidney ([Jin et al., 2012](#)) and liver fibrosis ([He et al., 2017](#)). In kidney fibrosis, HIPK2 initiates epithelial-mesenchymal transition (EMT), apoptosis and inflammation through a signaling network involving Notch, Wnt, transforming growth factor β (TGF-β)/Smad, p53 and nuclear factor kappa B (NFκB) ([Jin et al., 2012](#)). Similarly, HIPK2 promotes liver fibrosis through the potentiation of TGF-β/Smad signaling ([He et al., 2017](#)). However, fibroblasts in patients with lung fibrosis show lower HIPK2 protein expression, suggesting HIPK2 may play an anti-fibrogenic role that contradicts the role in kidney and liver fibrosis ([Ricci et al., 2013](#)).

Similar confounding observations are made in cancer. On the one hand, HIPK2 is well-known for its tumor-suppressing role in activating the tumor suppressor p53 for its DNA damage response upon ultraviolet irradiation ([D’Orazi et al., 2002; Hofmann et al., 2002](#)). Also, HIPK2 acts as a tumor suppressor upon induction of two-stage skin carcinogenesis ([Wei et al., 2007](#)) or γ-radiation-induced tumorigenesis ([Mao et al., 2012](#)). In further support of the tumor suppressor role, HIPK2 expression is reduced in breast and thyroid carcinomas ([Pierantoni et al., 2002](#)).

On the other hand, HIPK2 promotes the viability of cancer cells challenged with chemotherapeutic drugs through promoting the cytoprotective activity of NRF2 ([Torrente et al., 2017](#)). Elevation of HIPK2 is also associated with human papillomavirus (HPV)-positive tonsillar squamous cell carcinomas (TSCCs) ([Kwon et al., 2017](#)), the malignancy of pilocytic astrocytomas ([H Deshmukh et al., 2008](#)), cervical carcinogenesis ([Al-Beiti and Lu, 2008](#)) and colorectal cancers ([D’Orazi et al., 2006](#)).

Thus, whether HIPK2 is fibrogenic or tumorigenic or not continues to be controversial. Therapeutic interventions simply by activating or inhibiting HIPK2 without the understanding of the context-dependent role may paradoxically exacerbate pathogenesis.

1.6. Aims of the thesis

Given the functional versatility of *Drosophila* Hipk in developmental signaling pathways (**Figure 1.11**), we *hypothesize that* **(1) Hipk plays a positive role in tumor progression**. Thus, the first aim of this thesis is to evaluate the tumorigenic role of Hipk and establish an *in vivo* fly tumor model using Hipk (**Chapter 2**).

In a genetic screen for novel Hipk regulators conducted by our lab members Jessica Blaquiere and Rubia Chung, O-GlcNAc transferase (OGT) and salt-inducible kinase 2 (SIK2) are identified as potential candidates. OGT and SIK2 function in the hexosamine and InR signaling pathways, respectively. Therefore, we *hypothesize that* **(2) Hipk utilizes nutrient-sensing signaling pathways to favor tumor growth under nutrient-rich conditions**. Thus, the second aim of this thesis is to address if Hipk is regulated in a nutrient-responsive manner and if nutrient-sensing pathways cooperate with Hipk to accelerate tumorigenesis (**Chapter 3 and Chapter 4**).

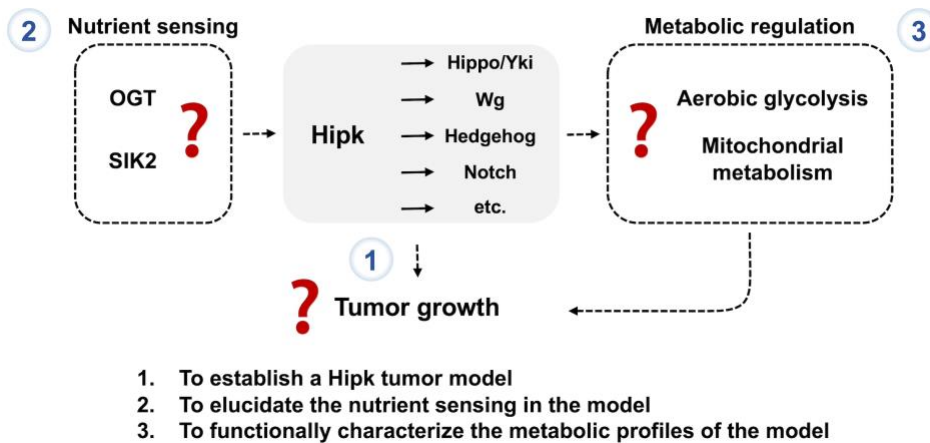


Figure 1.11. Aims of the thesis

Fly Hipk is known for regulating Hippo/Yki, Wg, Hedgehog and Notch signaling. Based on this, we set out to establish a Hipk tumor growth and decode nutrient sensing and metabolic regulation in this model.

As metabolic reprogramming is a hallmark of cancer, we further *hypothesize that* **(3) the Hipk tumor model manifest a switch to an active metabolic profile to fuel tumorigenesis**. Thus, the third aim of this thesis is to characterize the metabolic profiles of the Hipk tumor model with a particular focus on aerobic glycolysis and mitochondrial metabolism (**Chapter 5 and Chapter 6**).

The overarching goals of this thesis are **(1)** to expand our knowledge of the tumorigenic role of *Drosophila* Hipp, **(2)** to understand the integration of nutrient sensing and metabolic regulation with oncogenic signaling during cancer progression, and last but not least **(3)** to identify potential metabolic vulnerabilities or interventions that may be exploited in the prevention and treatment of cancer.

Chapter 2.

Hipk promotes tumorigenesis and metastatic-like cell behavior

Chapter 2 is based off the following published work with modifications.

Jessica A. Blaquier*, **Kenneth Kin Lam Wong***, Stephen D. Kinsey, Jin Wu, and **Esther M. Verheyen**. Homeodomain-interacting protein kinase promotes tumorigenesis and metastatic cell behavior. *Dis Model Mech*. 11: dmm031146 (2018).

*co-first authors

<https://www.ncbi.nlm.nih.gov/pubmed/29208636>

2.1. Contributions to the Chapter

J.A.B., **K.K.L.W.**, E.M.V. Conceptualization; J.A.B., **K.K.L.W.** Methodology; J.A.B., **K.K.L.W.** Validation; J.A.B., **K.K.L.W.**, S.D.K., J.W. Formal analysis; J.A.B., **K.K.L.W.**, S.D.K., J.W. Investigation; J.A.B., **K.K.L.W.**, E.M.V. Writing - original draft; J.A.B., **K.K.L.W.**, S.D.K., E.M.V. Writing - review & editing; J.A.B., **K.K.L.W.**, S.D.K., J.W. Visualization; E.M.V. Supervision; E.M.V. Project administration; E.M.V. Funding acquisition

2.2. Abstract

Aberrations in signaling pathways that regulate tissue growth often lead to tumorigenesis. Homeodomain-interacting protein kinase (Hipk) family members are reported to have distinct and contradictory effects on cell proliferation and tissue growth. Hence, much remains to be learned about the roles of Hipk family protein kinases in proliferation and cell behavior. Previous work has shown that *Drosophila* Hipk is a potent growth regulator, thus we predicted that it could have a role in tumorigenesis. In our study of Hipk-induced phenotypes in larval epithelial imaginal discs, we observed tissue overgrowth, multilayering and severe distortions in tissue morphology. Furthermore, elevated Hipk induces cell invasion and epithelial-to-mesenchymal transition (EMT). Past studies have shown that developmental signaling pathways implicated in cancer and EMT, such as Wg/Wnt, Hippo, Notch and JNK, are regulated by Hipk. We here show that Hipk phenotypes are not likely to arise from activation of a single target, but rather through a cumulative effect on multiple target pathways. Hyperactivating the target pathways further synergize with Hipk to exacerbate tumorigenesis. *In sum, our study presents elevated Hipk as an in vivo tumor model manifesting neoplastic tumor growth, compromised epithelial integrity and at least local cell invasion.*

2.3. Introduction

Developmental signaling pathways are essential for growth of healthy tissues and organs. Genetic aberrations in the pathway components can cause uncontrolled proliferation and tumorigenesis. When further genetic mutations accumulate, mutated cells progressively acquire metastatic potential by initiating epithelial-to-mesenchymal transition (EMT) ([reviewed by \(Thiery et al., 2009\)](#)).

Numerous signaling pathways and cellular processes are highly conserved among mammals and *Drosophila*, which marks a major contributing factor for the discovery of human cancer or disease genes using *Drosophila* as a genetic model organism ([Brumby and Richardson, 2005; Gonzalez, 2013; Potter et al., 2000; Rudrapatna et al., 2012](#)). Indeed, *Drosophila* tumor models manifesting neoplastic growth – hyperproliferation coupled with invasive behaviors – have developed using the power of fly genetics to combine multiple genetic aberrations. The earliest metastasis model developed involves activated Ras in conjunction with loss of the tumor

suppressor *scribble* (Pagliarini and Xu, 2003). Notch pathway activation coupled with alterations in histone epigenetic marks also leads to a *Drosophila* tumor model (Ferres-Marcó et al., 2006). Subsequent studies have identified a growing number of factors involved in both Ras- and Notch-driven tumorigenesis (Doggett et al., 2015; Zoranovic et al., 2018).

Homeodomain-interacting protein kinases (HIPKs; HIPKs in mammals; Hipk in *Drosophila*) are essential proteins for development in flies and mammals (reviewed by (Blaquiere and Verheyen, 2017)). However, opposing effects of HIPKs on cell proliferation and tissue growth have been reported. In *Drosophila*, overexpression of *hipk* causes tissue overgrowth in a dose-dependent manner (Chen and Verheyen, 2012; Lee et al., 2009a; Poon et al., 2012). Mouse embryo fibroblasts (MEFs) from *Hipk2* \sim knockout mice show reduced proliferation in one study (Trapasso et al., 2009), whereas another study claimed that such cells proliferated more than control (Wei et al., 2007). Regarding the roles of HIPKs in cancer, HIPK2 (the best characterized member of the HIPK family) acts as a tumor suppressor in the context of p53-mediated cell death after lethal DNA damage (Hofmann et al., 2013), and reduced Hipk is seen in several cancer types including thyroid carcinomas (Lavra et al., 2011; Pierantoni et al., 2002), breast carcinomas (Pierantoni et al., 2002) and bladder cancer metastasis (Tan et al., 2014). In contrast, elevated Hipk2 is associated with cervical cancer progression (Al-Beiti and Lu, 2008), colorectal cancers of patients with familial adenomatous polyposis (D’Orazi et al., 2006) and pilocytic astrocytomas (H. Deshmukh et al., 2008). From these conflicting studies, it is clear that much remains to be learned about the tumorigenic roles of HIPKs.

HIPKs regulate numerous signaling pathways required for the development of healthy tissues (**Figure 2.1**) (reviewed by (Blaquiere and Verheyen, 2017)). Both *Drosophila* and vertebrate HIPKs can modulate Wnt signaling through more than one mechanism (Hikasa et al., 2010; Hikasa and Sokol, 2011; Lee et al., 2009b; Louie et al., 2009; Shimizu et al., 2014; Swarup and Verheyen, 2011). Yorkie (Yki; YAP/TAZ in vertebrates) activity of the Hippo pathway requires Hipk, as *hipk* loss of function suppresses the growth-promoting effects of the constitutively active Yki (Yki-S168A) (Chen and Verheyen, 2012; Poon et al., 2012). HIPKs have also been shown to regulate Jun N-terminal kinase (JNK) signaling (Hofmann et al., 2003; Huang et al., 2011; Lan et

al., 2007). Hipk is required for attaining the full effect of JAK/STAT signaling, as loss of *hipk* impedes the signaling output (Tettweiler et al., 2019).

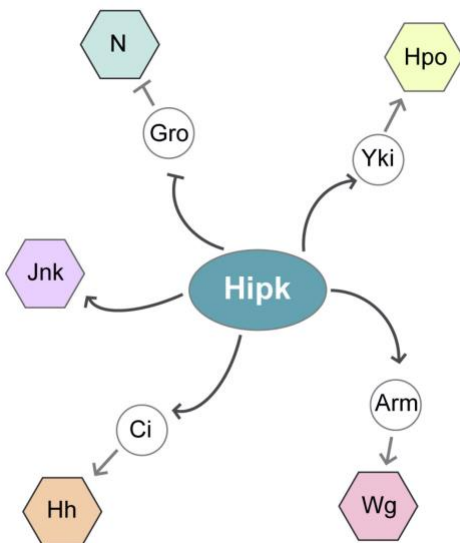


Figure 2.1. Hipk regulates numerous signaling pathways.

A schematic diagram depicting Hipk's known relationships with many of the conserved signaling pathways.

Although previous findings showed that *Drosophila* Hipk is a strong inducer of tissue growth and enhances cell proliferation as revealed by increased phosphohistone 3 (PH3) staining (hyperplasia) (Chen and Verheyen, 2012), its role in tumorigenesis (neoplastic growth) remains unknown. Here, we provide evidence that elevated Hipk leads to neoplasia characterized by cell invasiveness, cellular changes reminiscent of the hallmarks of EMT, including loss of E-cadherin, induction of metalloproteinase 1 (MMP1) and disruption in basement membrane. Unlike the previously described models of invasive neoplasia established by more than one genetic aberration, our work demonstrates that Hipk alone can promote cell proliferation and invasion. We propose that *Drosophila* Hipk exerts its tumorigenic effects through concurrent perturbations of its target pathways.

2.4. Results

2.4.1. Elevated Hipk causes tumorous growths

To study the tumorigenic implications of elevated Hipk, we used the GAL4-UAS system to overexpress *hipk* in a variety of tissues. GFP was co-expressed to mark the transgene-expressing cells such that we could visualize the cell behaviors. Compared with the control eye-antennal and wing imaginal discs (*dpp > GFP*) (Figure 2.2 A-B), overexpression of two copies of *hipk* transgene at 25°C (*dpp > HA-hipk^{1M} + HA-hipk^{3M} + GFP*) caused significant tissue overgrowth, characterized by tissue folds and protrusions (Figure 2.2 D-E).

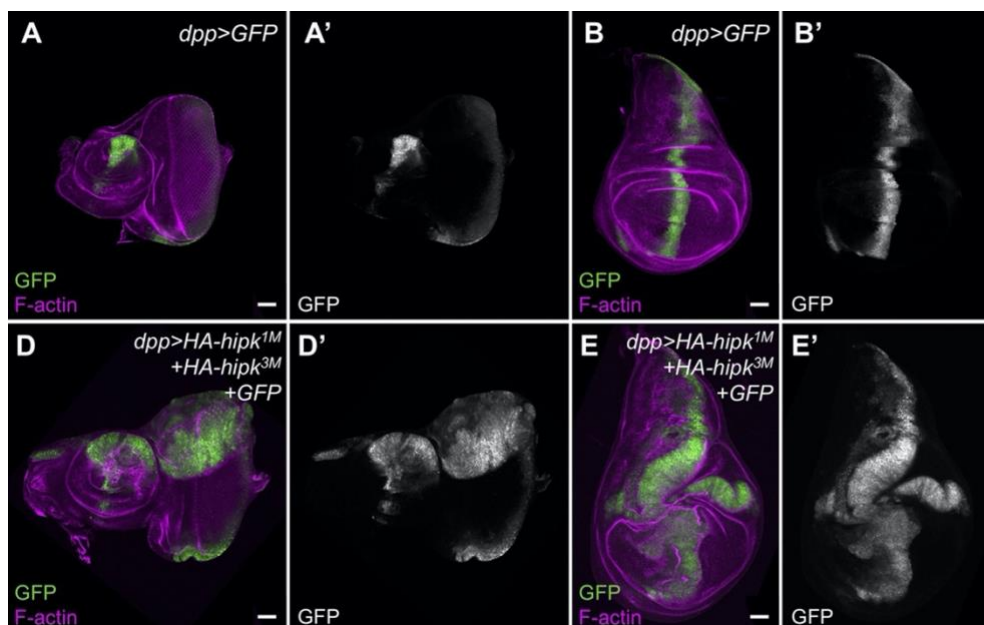


Figure 2.2. Hipk induces overgrowths in larval imaginal discs.

(A-B) Control eye-antennal (A) and wing (B) imaginal discs stained for actin (in magenta) to reveal tissue morphology. GFP expression (green in A, B, D, E; grey in A', B', D', E') marks the transgene-expressing domain. (D-E) Expression of two copies of *HA-hipk* transgene (*HA-hipk^{3M}* and *HA-hipk^{1M}*) within the Dpp domain leads to overgrown eye-antennal (D) and wing (E) imaginal discs. Flies were raised at 25°C. Scale bars: 50 μm.

When the animals were raised at 29°C, the potency of the GAL4 transcription driver increased, leading to more UAS transgene expression. At 29°C, overexpression of one copy of *hipk* (*dpp > HA-hipk^{3M} + GFP*) was sufficient to cause an overgrowth phenotype (Figure 2.3 I-J). We also observed robust staining of cleaved caspase 3

(Casp3), an activated form of caspase 3, in the *hipk*-overexpressing discs (**Figure 2.3 G-H**), suggesting that cell death is induced. When *P35* was co-expressed to block caspase-dependent cell death in the *hipk*-overexpressing discs (*dpp > HA-hipk^{3M} + P35 + GFP*), the transgene-expressing domain expanded considerably and almost occupied the entire disc (**Figure 2.3 K**). Overexpression of *P35* alone had no effect in this context (**Figure 2.3 L**). Together, our data imply that elevated *Hipk* induces both cell hyperproliferation and caspase-dependent cell death.

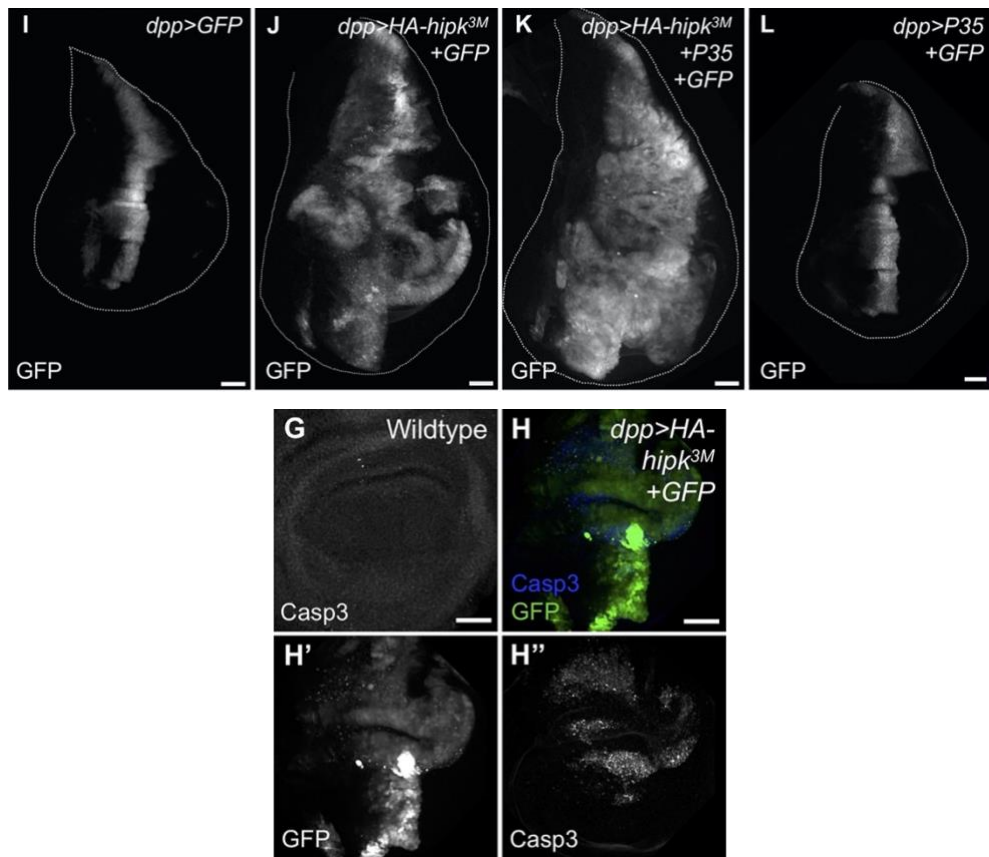


Figure 2.3. Hipk induces hyperproliferation, Caspase 3 activation and cell death.

(I) A control wing imaginal disc (*dpp > GFP*). **(J)** A wing disc overexpressing *hipk* (*dpp > HA-hipk^{3M} + GFP*) displays an overgrowth phenotype. **(K)** Blocking cell death by *P35* overexpression in a *hipk*-overexpressing wing disc (*dpp > HA-hipk^{3M} + GFP + P35*) worsens *Hipk*-induced overgrowths. **(L)** A wing disc overexpressing *P35* (*dpp > GFP + P35*) appears normal. **(G)** A control wing disc pouch stained for Casp3 (in grey). **(H)** A wing disc overexpressing *hipk* (*dpp > HA-hipk^{3M} + GFP*) shows robust Casp3 upregulation (blue in H, grey in H''). GFP expression (grey in I-L, H'; green in H) reveals the transgene-expressing domain. Flies were raised at 29°C. Scale bars: 50 µm.

2.4.2. Elevated Hipk induces cell invasive behaviors

In addition to increased cell proliferation and cell death, we observed cell invasion behaviors upon *hipk* overexpression. In the control wing disc, the anterior-posterior (A/P) boundary is well-defined, as shown by the staining of Cubitus interruptus (Ci) and Engrailed (En) which mark the anterior and posterior compartments, respectively (**Figure 2.4 A-B**). Dpp domain (marked by GFP) is restricted within the anterior (Ci positive) compartment. In contrast, in the *hipk*-overexpressing wing disc (*dpp> HA-hipk^{3M} + GFP*), individual *hipk*-overexpressing cells or cell clusters (marked by GFP) were found outside the Dpp domain (**Figure 2.4 C white arrowheads**). Some *hipk*-overexpressing cells expressed Ci and En simultaneously (**Figure 2.4 C yellow arrowheads**). It is possible that these cells have either lost their ability to interpret A/P positional cues from the tissue or are in a period of fate transition.

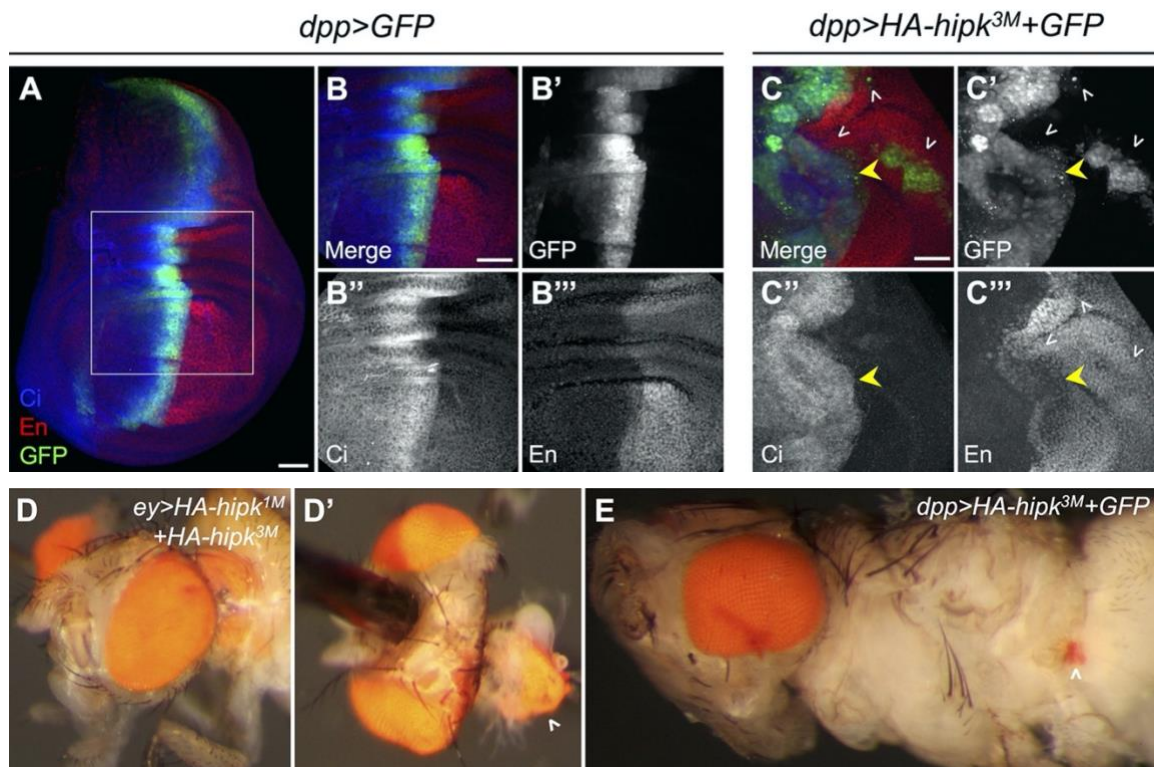


Figure 2.4. Elevated Hipk induces cell invasion and metastatic behaviors.

(A-B) A control wing disc (*dpp > GFP*) stained for Ci (blue in A; grey in B'') and En (red in A; grey in B'''). (C) In a *hipk*-overexpressing wing disc (*dpp > HA-hipk^{3M} + GFP*), *hipk*-overexpressing cells are found in the posterior wing compartment (arrowheads). Flies were raised at 29°C. Scale bars: 50 μm. (D) An ectopic eye seen within the thorax of an *ey > HA-hipk^{1M} + HA-hipk^{3M}* fly (frequency 1%, $n = 100$). (D') Dissection reveals the size of the ectopic

eye (arrowhead). (**E**) A smaller ectopic eye is seen in the abdominal region of a *dpp > HA-hipk_{3M} + GFP* fly (arrowhead; frequency 2%, $n = 100$).

Another phenotype associated with metastasis in *Drosophila* is the migration of retinal tissue into the body of the fly (Ferres-Marco et al., 2006; Pallavi et al., 2012). When *hipk* was expressed in the eye disc using *eyeless-GAL4* (*ey-GAL4*), a large cluster of pigmented retinal cells was observed in the thorax of the adult fly (at a frequency of 1%, $n = 100$) (**Figure 2.4 D** arrowhead). The endogenous eyes were fully intact, which suggests this was not likely to have been a disc eversion defect, but rather a metastatic event where retinal tissue migrated away from the eye disc and lodged into the thorax. This phenotype also occurred in *hipk*-overexpressing (*dpp > HA-hipk_{3M} + GFP*) flies, in which ectopic pigmented eye cells were occasionally observed in the abdomen (at a frequency of 2%, $n = 100$) (**Figure 2.4 E**), indicating that *hipk*-overexpressing eye disc cells *have the potential to migrate and proliferate in distant areas of the body*.

2.4.3. Elevated Hipk causes MMP1 induction and disruption in the basement membrane

As metastasis initiates, cells extrude from the main epithelium through various mechanisms, including the degradation of basement membrane by matrix metalloproteinases (MMPs) (Beaucher et al., 2007; Page-McCaw et al., 2003; Srivastava et al., 2007). We observed that overexpression of *hipk* led to robust MMP1 upregulation (Figure 2.5 A-B). We examined the basement membrane by staining wing imaginal discs for Nidogen (Ndg), an extracellular matrix component (Wolfstetter et al., 2009). In contrast to the uniform Ndg expression on the basal side of the control wing disc (Figure 2.5 A), elevated Hipk caused disruptions in the Ndg pattern as observed in the cross-sections of wing discs (Figure 2.5 B). Specifically, the location of the MMP1 induction in the *hipk*-overexpressing cells coincided with disruptions in Ndg (Figure 2.5 B), suggesting that elevated Hipk induces MMP1 which in turn promotes degradation of the basal membrane. This mechanism may facilitate the *hipk*-overexpressing cells to migrate through the holes in the basement membrane.

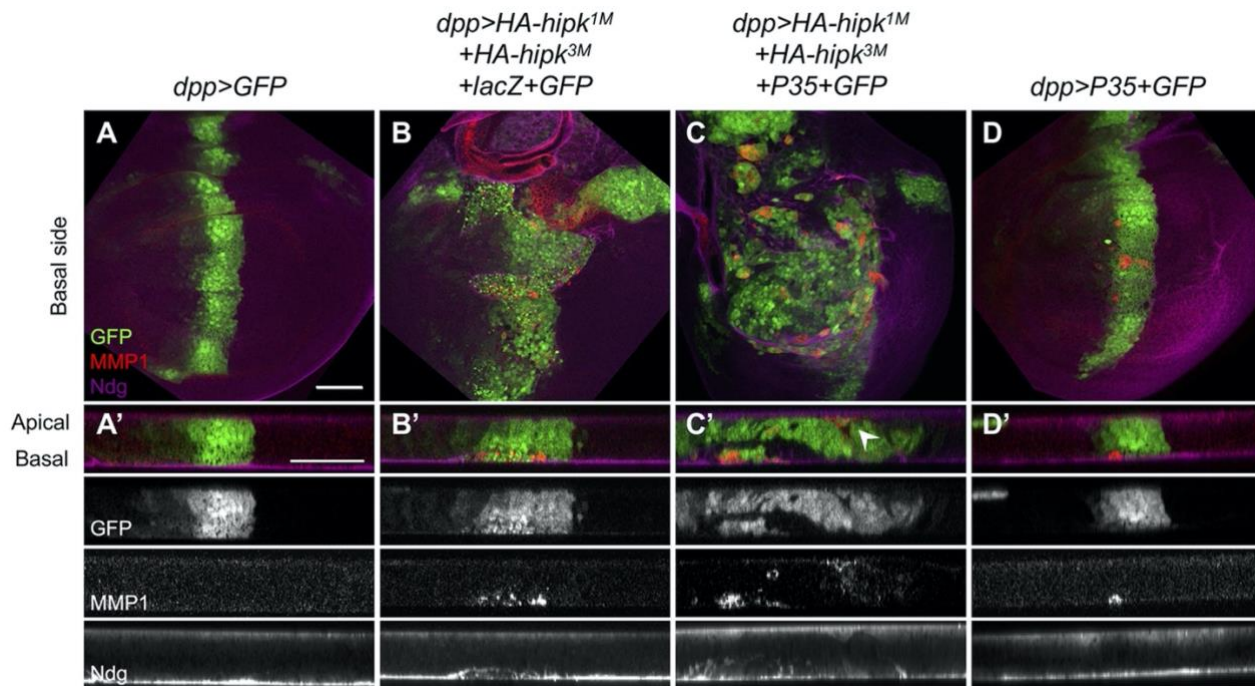


Figure 2.5. Elevated Hipk induces MMP1 upregulation and disruption of basement membrane.

(A) A control wing disc (*dpp > GFP*), (B) a wing disc overexpressing two copies of *hipk* transgene (*dpp > HA-hipk^{1M} + HA-hipk^{3M} + LacZ + GFP*) were stained for Mmp1 (red in A-B;

grey in **A'-B'** third row) and Ndg (purple in **A-B**; grey in **A'-B'** last row). Cross-sections of the corresponding wing discs are shown in **A'-B'**. Flies were raised at 25°C. Scale bars: 50 µm.

To distinguish whether the *hipk*-overexpressing cells are undergoing cell death or cell migration, we introduced *P35* co-expression to block caspase-dependent cell death. Co-expression of *P35* with *hipk* potentiated the abnormalities in disc morphology, with multiple folds and cell layers (**Figure 2.5 C**). In this context with inhibition of cell death, the *hipk*-overexpressing cells were observed breaking through the disc surface at both the apical and basal surfaces (**Figure 2.5 C'**), suggestive of active migration rather than cell death. Alterations in MMP1 and Ndg (**Figure 2.5 C**) were seen in disc sections. *P35* overexpression alone was capable of inducing MMP1, as reported previously (Rudrapatna et al., 2013), but no defects in Ndg integrity were seen (**Figure 2.5 D**).

2.4.4. Elevated Hipk alters expression levels of additional EMT markers including E-cadherin and Twist

In addition to MMPs, we examined other EMT markers to address if elevated Hipk triggers the EMT program. In control wing discs, E-cad was enriched on the apical side of the epithelium (**Figure 2.6 I**). When *hipk* was overexpressed, the E-cad levels were drastically reduced, especially in those *hipk*-overexpressing cells that were dissociating from the original Dpp domain (**Figure 2.6 J yellow arrowheads in the insets**).

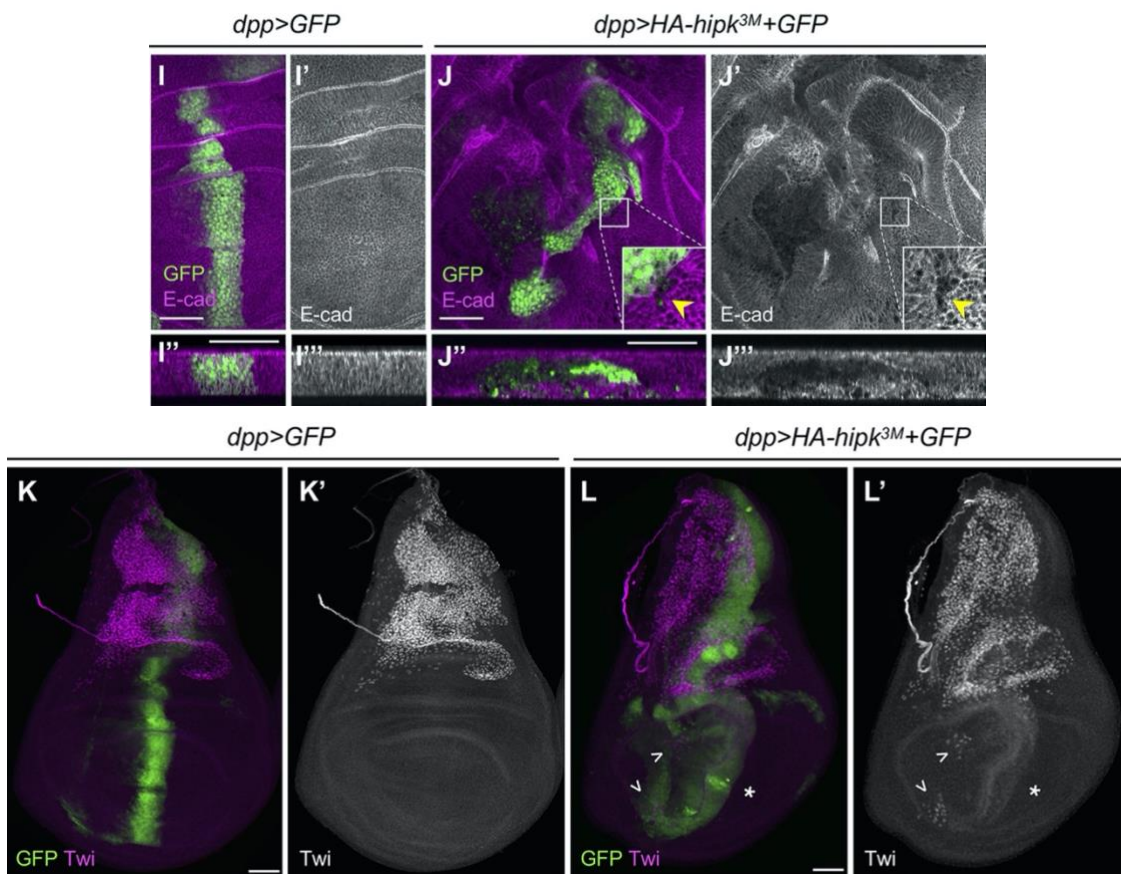


Figure 2.6. Elevated Hipk leads to downregulation of E-cadherin and upregulation of Twist.

(**I-J**) A control (*dpp > GFP*) wing disc (**I**) and a *hipk*-overexpressing wing disc (*dpp > HA-hipk^{3M} + GFP*) (**J**) were stained for E-cad (magenta in **I-J** and **I''-J''**, grey in **I'-J'** and **I'''-J'''**). Transgene-expressing cells were marked by GFP (green). **I''-J''** and **I'''-J'''** are the cross-sections of the wing discs. (**K**) Twist (magenta in **K**, grey in **K'**) is expressed in the myoblasts, located in the notum region of a control wing disc (*dpp > GFP*). (**L**) Twist-positive (magenta in **L**, grey in **L'**) mesenchymal cells are present in the wing pouch region of a *hipk*-overexpressing wing disc (*dpp > HA-hipk^{3M} + GFP*) (arrowheads), and Twist is mildly induced

in a swathe of cells along the Dpp domain (asterisk). Flies were raised at 29°C. Scale bars: 50 µm.

Twist, an EMT transcription factor (EMT-TF), is normally expressed within mesenchymal cells found within the notum region of a control wing disc (**Figure 2.6 K**) (Herranz et al., 2014). When *hipk* was overexpressed, Twist expression was mildly induced along the Dpp domain (**Figure 2.6 L asterisk**), and multiple cells within the wing pouch displayed ectopic expression of Twist (**Figure 2.6 L arrowheads**).

Altogether, our findings suggest that *elevated Hipk activates EMT at least in part through upregulation of the EMT-TF Twist, thus promoting tumorigenesis (neoplasia) coupled with cell invasion or even metastasis.*

2.4.5. Hipk-mediated tumorigenic phenotypes cannot be attributed to a single targeted pathway

We further investigated the molecular mechanisms underlying Hipk-mediated tumorigenesis. Earlier studies have demonstrated that Hipk is a versatile regulator of numerous signaling pathways. If Hipk-mediated tumorigenesis is through dysregulation of one single signaling pathway, we would expect to see a rescue in the cell proliferation or migration phenotypes when the signaling pathway is perturbed. To test whether the Hipk phenotypes could be reverted, we first used *hipk-RNAi* to knock down *hipk* and found that it completely rescued the tumorigenic activities seen in *hipk*-overexpressing discs (Figure 2.7 A-B).

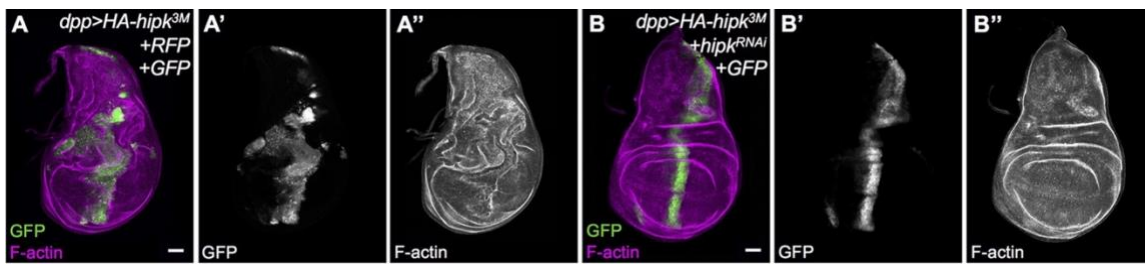


Figure 2.7. Hipk-mediated tumorigenic phenotypes are completely rescued by co-expression of *hipk-RNAi*.

We assessed the ability of knockdown of the activity of individual pathways to suppress the tumorigenic phenotypes induced by elevated Hipk, by F-actin staining (magenta in A, B; grey in A'', B'') to reveal morphology and GFP (green in A, B; grey in A', B') to indicate cells in which genotypes were manipulated. (A-B) As proof of concept, *hipk-RNAi* (B) suppressed effects seen in *dpp > HA-hipk^{3M}* wing discs (A).

Then, we tested the effects of inhibition of Wg signaling by either knockdown of *pangolin/TCF* (Figure 2.8 C) or overexpression of the negative regulator Axin (Figure 2.8 D). We noticed that *hipk*-overexpressing discs with loss of *pan* (*TCF*) still displayed the invasive phenotype and even some overgrowth in the notum region. Likewise, expression of Axin failed to suppress the *hipk* overexpression phenotypes. Wing discs co-expressing a dominant negative form of epidermal growth factor receptor (*Egfr-DN*) (Figure 2.8 E) or a dominant negative form of basket (*basket-DN*) (*Drosophila JNK*) (Figure 2.8 F) with *hipk* were phenotypically indistinguishable from discs overexpressing *hipk* alone. Knockdown of *yki* reduced the overgrowth effect to some degree, consistent with the effect of Hipk on the Hippo signaling, but the discs still showed ectopic cell migration (Figure 2.8 G). Expression of dominant negative Delta (*DI-DN*) did not

appreciably modify the *hipk* overexpression phenotype (**Figure 2.8 H**). Interestingly, after inhibition of the Hedgehog pathway through expression of the repressor form of Ci (*Ci-REP*) (**Figure 2.8 I**), the cell spreading phenotype seemed suppressed and the discs displayed only an enlarged Dpp domain. We also noticed relatively weak GFP expression in the discs, which is most likely to be attributable to the repression of *dpp-Gal4* expression, because Hh controls *dpp* transcription (Basler and Struhl, 1994). Reduction of JAK/STAT signaling through knockdown of *hopscotch* (*hop*) (Drosophila JAK) (**Figure 2.8 J**) or knockdown of one of the unpaired ligands, Upd3 (**Figure 2.8 K**), failed to rescue the *hipk* overexpression phenotypes.

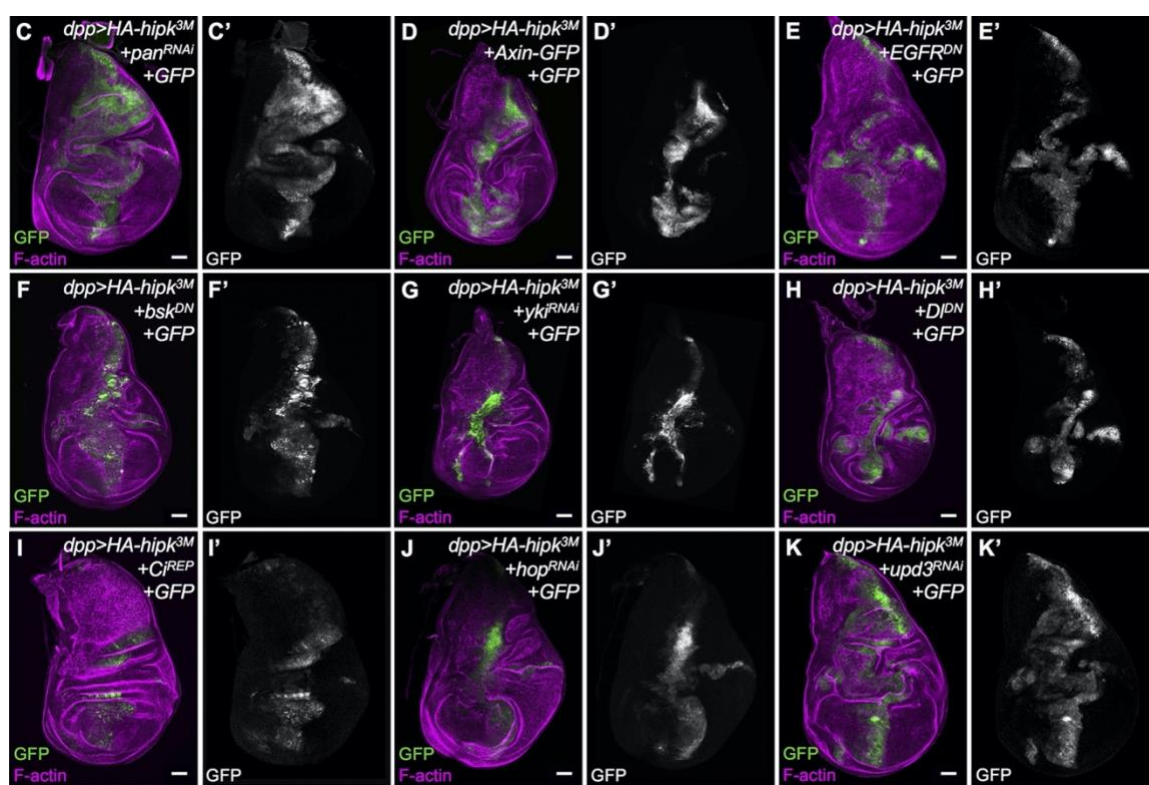


Figure 2.8. Loss of individual signaling pathway components cannot suppress the Hipk tumorigenic phenotypes.

The following pathways were targeted with the indicated transgenes: Wg, using (**C**) *UAS-panRNAi* [dTcf] and (**D**) *UAS-Axin-GFP*; Egfr, using (**E**) *UAS-Egfr^{DN}*; JNK, using (**F**) *UAS-bsk^{DN}*; Hippo, using (**G**) *UAS-yki^{RNAi}*; Notch, using (**H**) *UAS-Dld^{DN}*; Hedgehog, using (**I**) *UAS-Ci^{Rep}*; JAK/STAT using (**J**) *UAS-hop^{RNAi}* and (**K**) *UAS-upd3^{RNAi}*. All crosses were done at 29°C. Scale bars: 50 μm.

The effects caused by each transgene on the Hipk-induced tumorigenic phenotypes (cell proliferation and cell invasion) were quantified by measuring area of the transgene-expressing domain (GFP positive) relative to total disc area and by assigning a ‘relative degree of invasiveness’ score to each disc (**Figure 2.9**). Each transgene used in this assay was validated by assaying the targets or downstream events specific to each pathway (**Figure 2.10**). The effects of expressing the transgene in the absence of *hipk* overexpression on the wing discs were also evaluated (**Figure 2.11**).

Together, our genetic data show that *interfering with individual signaling pathways using RNAi or dominant negative forms of the corresponding key effectors could not effectively suppress Hipk-induced tumorigenic activities.*

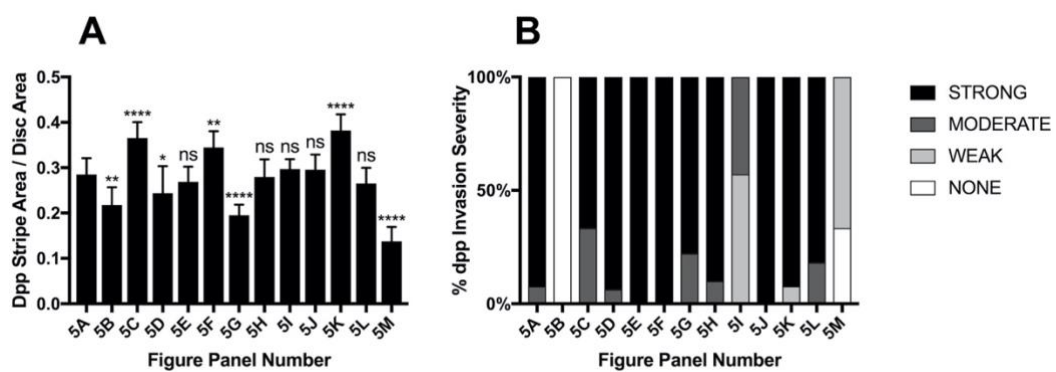


Figure 2.9. Quantification of proliferative areas in wing discs and the degree of invasiveness.

Imaginal disc size measurements and invasiveness scoring were performed as described in methods and materials. 5A-B refer to **Figure 2.7 A-B**. 5C-K refer to **Figure 2.8 C-K**. 5L-M refer to **Figure 2.12 L-M**. The genotypes in the charts are listed in **Table 2-1**.

Table 2-1. Genotypes of flies used in the panels of Figure 2.9 for the quantification of the proliferative and invasive indexes.

Panels	Genotypes	Panels	Genotypes
A-B	(5A-G) <i>dpp > GFP + HA-hipk_{3M} +</i>	A-B	(5H-J) <i>dpp > GFP + HA-hipk_{3M} +</i>
5A	<i>RFP</i>	5H	<i>DI-DN</i>
5B	<i>hipk-RNAi</i>	5I	<i>Ci-REP</i>
5C	<i>pan-RNAi</i>	5J	<i>hop-RNAi</i>
5D	<i>Axin-GFP</i>	5L	<i>upd3-RNAi</i>
5E	<i>EGFR-DN</i>	5M	<i>dpp > HA-hipk_{3M}</i>
5F	<i>bsk-DN</i>		+ <i>yki-RNAi + bsk-Dn</i>
5G	<i>yki-RNAi</i>		

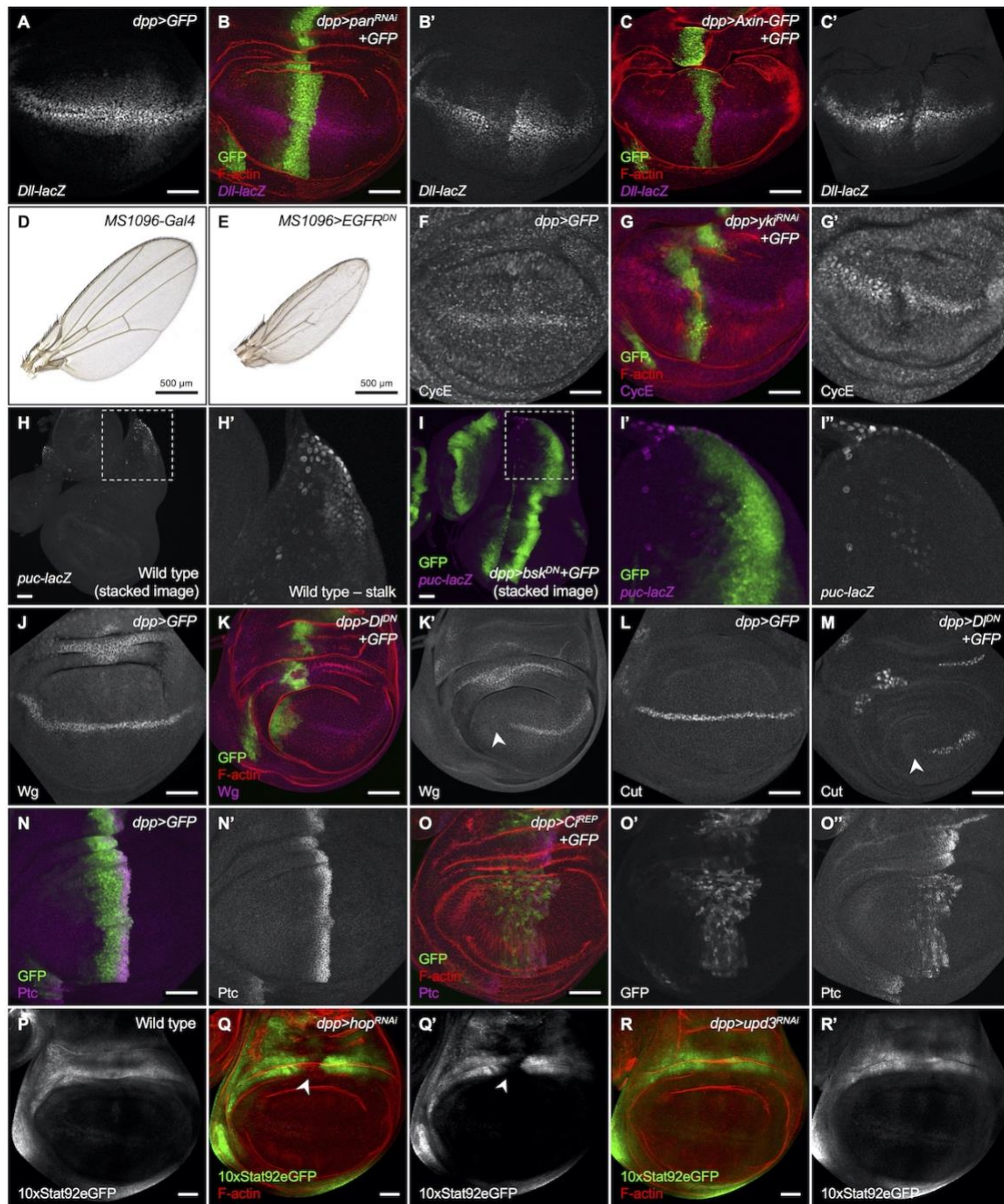


Figure 2.10. Validation of signaling pathway disruptions by reagents used in study.

To validate that all transgenes used in the study targeted their respective pathways, we examined either phenotypes or changes in target genes following GAL4-driven expression of either GFP or the indicated transgenes. GFP (green in B-C, G, I, K, N-O; grey in O') marks the transgene expressing cells. F-actin staining (red in B-C, G, K, O, Q-R) reveals disc morphology. (A) control, (B) *pan* [dTCF]-*RNAi* or (C) *Axin*-GFP expressing wing discs stained for Wg target *Dll-lacZ*. (D) MS1096-GAL4 control adult wing. (E) *EGFR-DN*

expressing adult wing showing typical EGFR loss of function vein loss phenotype. **(F)** Control (*dpp > GFP*), **(G)** *yki-RNAi* expressing wing discs stained for Hippo downstream target gene cyclin E (CycE). **(H)** Control wing disc stained for JNK signaling reporter *puc-lacZ*. **(H')** Inset shows expression in stalk of disc. **(I)** *bsk-DN* expressing wing disc stained for JNK signaling reporter *puc-lacZ*. **(J)** Control and **(K)** *DI-DN* wing discs stained for the Notch target Wg. **(L)** Control and **(M)** *DI-DN* wing discs stained for the Notch target Cut. **(N)** Control and **(O)** *Ci-Rep* stained for Hedgehog target Ptc. **(P)** Control, **(Q)** *hop-RNAi* and **(R)** *upd3-RNAi* expressing wing discs harboring 10xStat92EGFP reporter for JAK/STAT signaling.

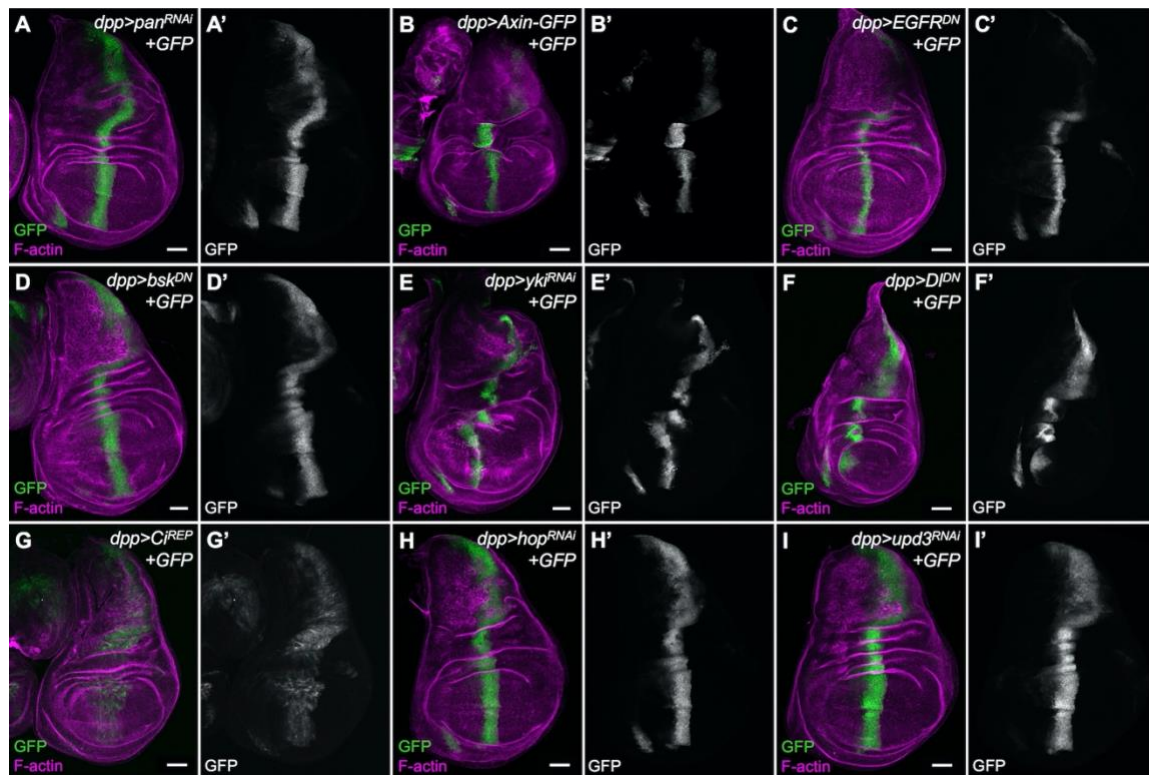


Figure 2.11. Phenotypes of signaling pathway disruptors used in study.

GFP (green in **A-I**; grey in **A-I'**) marks the transgene expressing domain. F-actin staining (magenta in **A-I**) reveals tissue morphology. The following pathways were targeted with the indicated transgenes: Wg, using **(A)** *pan* [dT_{CF}]-*RNAi* and **(B)** *Axin-GFP*; EGFR, using **(C)** *EGFR-DN*; JNK, using **(D)** *bsk-DN*; Hippo, using **(E)** *yki-RNAi*; Notch, using **(F)** *DI-DN*; Hedgehog, using **(G)** *Ci-REP*; JAK/STAT using **(H)** *hop-RNAi* and **(I)** *upd3-RNAi*.

2.4.6. Hipk-mediated tumorigenic phenotypes are attributed to at least Hippo-Yki and JNK signaling pathways.

To test whether the Hipk-mediated tumorigenic phenotypes are attributable to more than one pathway, we simultaneously interfered with the activity of Yki and Bsk by co-expressing *yki-RNAi* with *bsk-DN* in a *dpp>HA-hipk^{3M}* background.

Overexpression of Hipk induces over-proliferation of the *dpp*-expressing cells, which could be seen by staining for Hipk in *dpp > HA-hipk^{3M}* (**Figure 2.12 L**). After inhibition of Yki and Bsk, the area of the transgene-expressing domain was drastically reduced, and little cell spreading was observed (**Figure 2.12 M**). In the absence of hipk overexpression, co-expression of *yki-RNAi* with *bsk-DN* caused a mild tissue distortion in the wing discs (**Figure 2.12 N**), indicating the Hippo and JNK signaling pathways are essential for normal wing disc development.

Thus, our data highlight the *Hipk-mediated tumorigenic phenotypes are at least mediated by Hippo-Yki and JNK signaling pathways*.

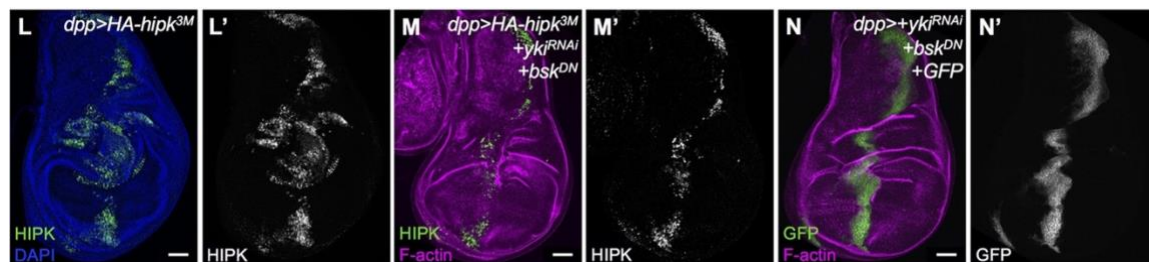


Figure 2.12. Hipk-mediated tumorigenic phenotypes are largely mediated by Hippo and JNK signaling pathways.

(**L**) *dpp > HA-hipk^{3M}* wing disc stained for nuclei (DAPI) (blue in **L**) and Hipk (green in **L**; grey in **L'**). (**M**) Expression of *dpp > HA-hipk^{3M} + yki^{RNAi} + bsk^{DN}* stained for Hipk (green in **M**; grey in **M'**) and F-actin (magenta in **M**). (**N**) *dpp > yki^{RNAi} + bsk^{DN}* stained for F-actin (magenta in **N**) GFP (green in **N**; grey in **N'**) marks the transgene expressing domain. All crosses were done at 29°C. Scale bars: 50 μm.

2.4.7. Perturbing signaling pathways individually does not phenocopy Hipk-induced phenotypes

We next examined whether perturbations in developmental pathways that are regulated by Hipk, or that have been shown to be implicated in tumorigenesis, can induce similar phenotypes to those caused by elevated Hipk ([Figure 2.13 A](#)). This might inform us if certain pathways may play a more dominant role in propagating the Hipk signal for tumorigenesis.

We used various UAS-transgene targeting signaling components to mimic the gain-of-function signaling outputs ([Table 2-2](#)). Wing discs expressing the degradation-resistant Arm-S10 (i.e. hyperactive form; β -catenin) to promote Wg signaling ([Figure 2.13 B](#)) displayed ectopic wing pouch-like structure in the notum, yet the Dpp stripe appeared relatively normal. Overexpression of Stat92E to elevate JAK/STAT signaling led to oversized discs ([Figure 2.13 C](#)). Wing discs expressing oncogenic Ras to promote Ras-ERK signaling showed robust overgrowths ([Figure 2.13 D](#)). Stimulation of the JNK pathway using *eiger* expression primarily caused invasive phenotypes but had little effect on proliferation ([Figure 2.13 E](#)). Inactivation of Hippo signaling by expression of constitutively active Yki (Yki-S168A) led to widening of the Dpp domain, and smooth, curved edges along the domain ([Figure 2.13 F](#)). Activated Notch signaling (N-act) ([Figure 2.13 G](#)) and ectopic Ci ([Figure 2.13 H](#)), which promotes Hh, both induced very dramatic and unique cellular effects. Wing discs of *dpp* > *N-act* resemble those previously seen with expression of *dpp* > *DI* ([Ferres-Marcos et al., 2006](#)).

Overall, this assay reveals that the effects of individually perturbed signaling pathways on proliferation and migration bear some, but not all, resemblance to Hipk elevation. Altogether, we favor the model that *Hipk-induced phenotypes are likely to arise as a cumulative effect of stimulating the activity of multiple pathways at least including Yki and JNK activities*.

Table 2-2. Signaling pathway reagents used in this study.

Cell signaling	Loss of function	Gain of function
Wingless	UAS-pan (TCF)-RNAi UAS-axin	UAS-arm-S10
EGFR/Ras	UAS-egfr-DN	UAS-ras-act
JNK	UAS-bsk-DN	UAS-eiger
Hippo	UAS-yki-S168A	UAS-yki-RNAi
Notch	UAS-delta-DN	UAS-Notch-act
Hedgehog	UAS-Ci-REP	UAS-Ci-5M
JAK-STAT	UAS-hop-RNAi UAS-upd3-RNAi	UAS-stat92E

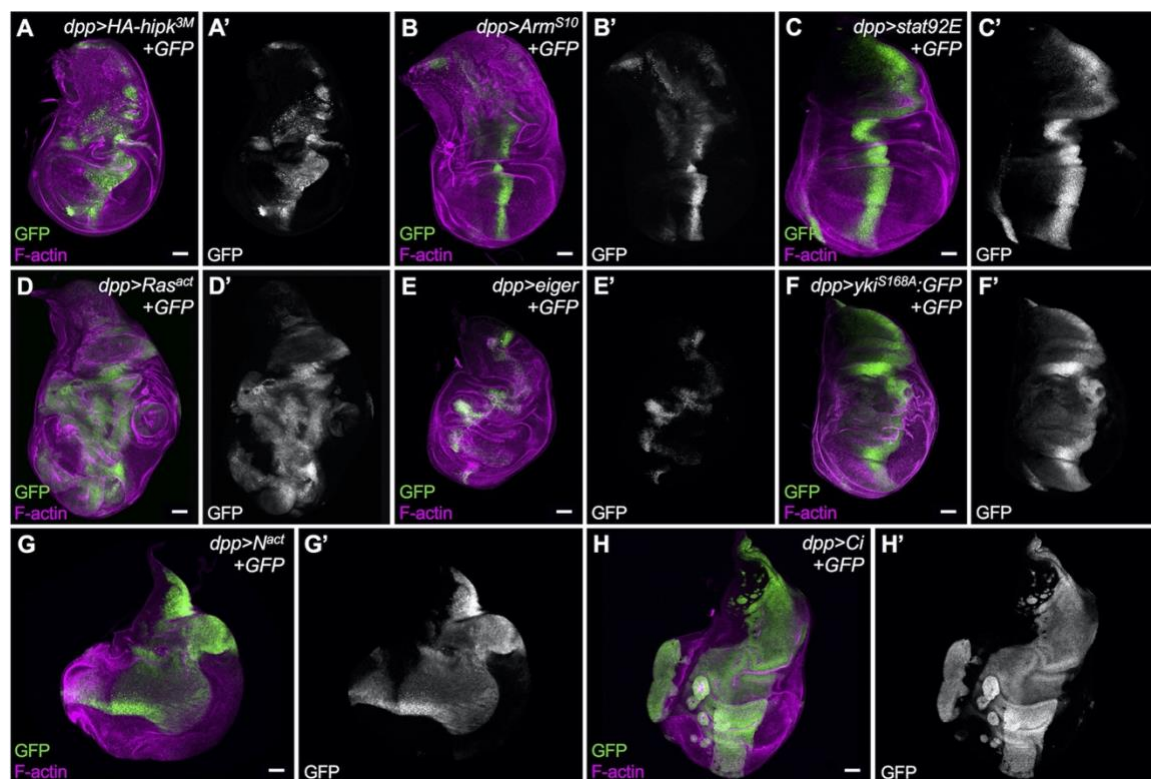


Figure 2.13. Overexpression of individual signaling pathway components does not phenocopy the tumorigenic phenotypes induced by elevated Hipk.

(A) A third instar wing imaginal disc with *HA-hipk^{3M}*+GFP expressed along the *dpp* domain serves as the baseline phenotype/control disc. Individual pathway activators were expressed using *dpp-Gal4*, *UAS-GFP*, namely: (B) *UAS-Arms¹⁰*, (C) *UAS-Stat92E*, (D) *UAS-Ras^{act}*, (E) *UAS-eiger*, (F) constitutively active *UAS-yki^{S168A}*, (G) *UAS-N^{act}* and (H) *UAS-Ci*. Discs were stained for F-actin (magenta) to reveal tissue morphology and for GFP (green, white) to mark cells in which transgenes were ectopically expressed using *dpp-Gal4*. Scale bars: 50 μ m. All crosses were done at 29°C.

2.4.8. Hipk synergizes with perturbed signaling pathways to exacerbate tumor progression

Finally, we assessed whether Hipk expression could synergize with perturbed signaling pathways in *Drosophila* wing discs. We co-expressed Hipk with the same gain of function UAS-transgenes used in the previous section (**Table 2-2**) and assayed proliferation and cell invasion phenotypes. The phenotype of *dpp* > *Arm-S10* alone was enhanced upon co-expressing *HA-hipk_{3M}*; notably, the effect was much more pronounced in the notum region of the disc (**Figure 2.14 B**). Co-expression of *stat92E* and *hipk* resulted in invasive phenotypes (**Figure 2.14 C**), whereas discs expressing *stat92E* alone did not (**Figure 2.13 C**). In stark contrast to the phenotype in *eiger*-expressing discs (**Figure 2.13 E**), Hipk cooperated with Eiger to cause a significant increase in migrating cells (**Figure 2.14 E**). Despite being smaller than *dpp* > *yki-S168A* discs, *dpp* > *hipk* + *yki-S168A* discs acquired noticeable cell spreading properties (**Figure 2.14 F**). Ras-act (**Figure 2.14 D**) and Notch-act (**Figure 2.14 G**) both showed a strong synergistic effect with ectopic Hipk, compared with phenotypes seen with either one alone, shown in **Figure 2.13**. The strongest synergy was seen with Ci (**Figure 2.14 H**). Thus, elevated Hipk synergize with perturbed signaling pathways to exacerbate tumor progression, supporting its oncogenic properties.

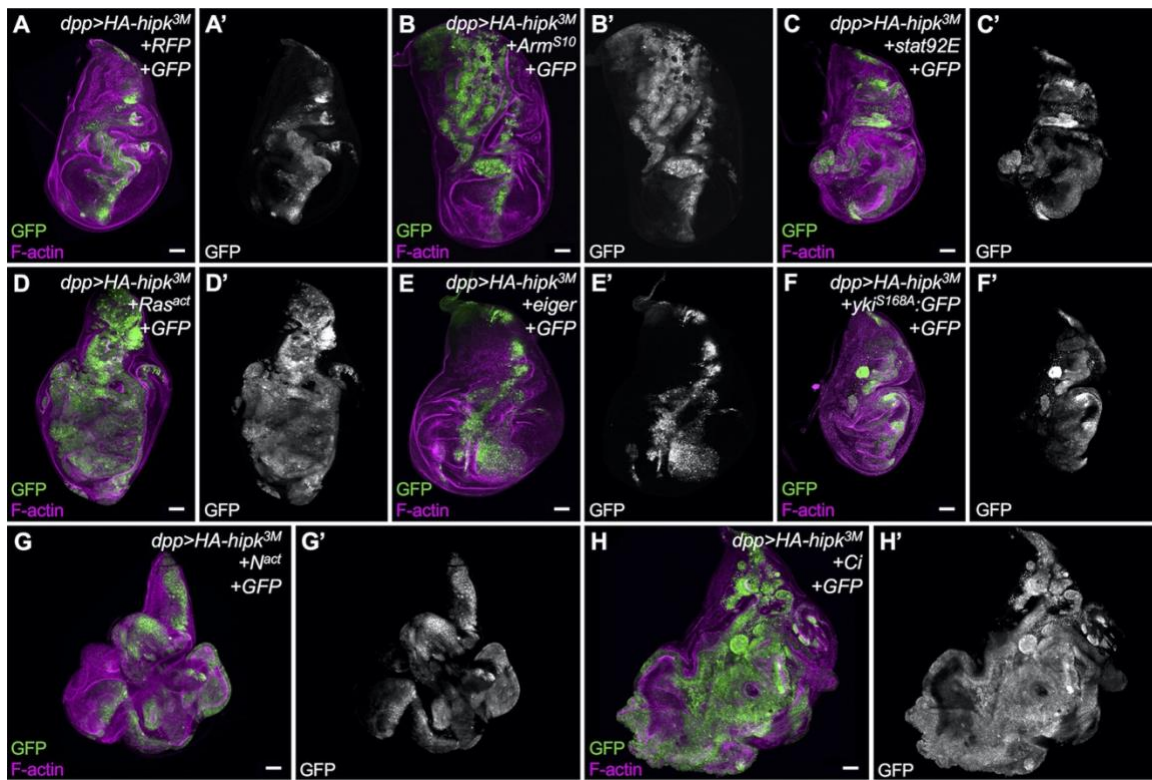


Figure 2.14. Hipk synergizes with other tumor models to exacerbate tumor progression

Individual pathway activators were expressed by crossing to *dpp-Gal4*, *UAS-GFP*; *UAS-HA-*hipk*^{3M/TM6B}*, namely: (A) Gal4 titration control crossed to *UAS-RFP*, (B) *UAS-Arms₁₀*, (C) *UAS-Stat92E*, (D) *UAS-Ras_{act}*, (E) *UAS-eiger*, (F) constitutively active *UAS-yki^{S168A}:GFP*, (G) *UAS-Nact* and (H) *UAS-Ci*. Discs were stained for F-actin (magenta) to reveal tissue morphology and for GFP (green, white) to mark cells in which transgenes were ectopically expressed using *dpp-Gal4*. Scale bars: 50 μ m. All crosses were done at 29°C.

2.5. Discussion

2.5.1. Elevated Hipk as an *in vivo* tumor model featuring neoplastic growth with invasion

A body of accumulating evidence has strongly indicated that mammalian HIPKs are implicated in various diseases including cancer (reviewed by (Blaquiere and Verheyen, 2017)). However, whether HIPKs act as oncogenes or tumor suppressor genes remains ambiguous, possibly in part because of the genetic heterogeneity among cancer types. Given the diverse expression patterns, distinct subcellular localization and potential functional redundancy of HIPKs, considerable efforts are needed to identify the roles of individual isoforms in each cell context, not to mention in unstressed or stressed conditions (for example, ultraviolet induction or hypoxia) (Schmitz et al., 2014). In light of these complications, we decided to use *Drosophila*, a simpler genetic model organism containing only one well-conserved Hipk, in our studies to unravel the roles of Hipk in tumorigenesis.

Our work reveals that elevated expression of a single gene, *hipk*, in *Drosophila* tissues is sufficient to produce features of transformed tumors. We provide evidence that Hipk induces hyperplasia in imaginal discs, leading to massive tissue growth (Figure 2.2). More importantly, cells with elevated Hipk display protruding shapes and gain the metastatic potential to spread away from their primary site of origin, manifesting neoplastic growth with invasion (Figure 2.4). Furthermore, our evidence suggests that Hipk induces basal invasion through the induction of EMT (Figure 2.5, Figure 2.6).

Our studies uncover previously unrecognized functions of *Drosophila* Hipk in mediating metastasis. Our conclusions are in agreement with some studies reporting that HIPK2 induces EMT markers in kidney fibrosis (Jin et al., 2012). Moreover, certain human cancers display elevated levels of HIPK2 (Al-Beiti and Lu, 2008; H Deshmukh et al., 2008; Jacob et al., 2009). We infer that *Drosophila* Hipk mimics human HIPK2 in these fibrosis and cancer types. In contrast, another study found that in bladder cancer metastasis, downregulation of HIPK2 induced EMT and cell invasion (Tan et al., 2014). The cues for the switch of roles of HIPKs between EMT promotion and EMT suppression require further investigation.

2.5.2. Hipk tumor growth likely arises from a cumulative effect of perturbations in multiple signaling pathways

To elucidate the molecular mechanism by which Hipk confers both proliferative and metastatic properties, we examined the genetic interactions between Hipk and developmental signaling pathways that are known, or proposed, to be regulated by Hipk. First, we noticed that interfering with the activity of an individual signaling pathway is not sufficient to suppress both Hipk-mediated cell proliferation and invasion phenotypes ([Figure 2.7](#), [Figure 2.8](#)). Second, stimulation of single pathways fails to recapitulate all the phenotypes induced by *hipk* overexpression ([Figure 2.13](#)). Of note, we were able to observe that the simultaneous inactivation of Yki and Bsk (JNK) ameliorated most Hipk phenotypes ([Figure 2.12](#)). We therefore propose that elevation of a single protein kinase, Hipk, even without accumulation of additional mutations, is likely to be potent enough to perturb multiple signaling pathways and, ultimately, have a cumulative effect of oversized, proliferative and invasion phenotypes. This mechanism, in effect, mimics tumor initiation attributable to multiple activating mutations in distinct pathways. Consistent with our proposed mechanism, HIPK2 has been proposed to activate TGF β , Wnt and Notch to drive EMT ([Jin et al., 2012](#)). We believe that, in the future, profiling the transcriptome, the protein-protein and protein-DNA interactions in HIPK mis-expressing cells will give us an unbiased and thorough analysis the roles of HIPKs in the alterations of signaling networks.

Also, we notice that *Drosophila* Hipk synergizes with other perturbed signaling pathways, probably in both additive and synergistic manners ([Figure 2.14](#)). This implies that Hipk itself may elicit tumor-like transformations during the early phases of tumorigenesis. During the later phases, when multiple genetic alterations occur, the synergy greatly accelerates tumor progression and metastasis.

The versatility of HIPK functions raises concerns regarding how we can block HIPK-induced phenotypes effectively. Although inhibition of multiple downstream effectors of HIPK might be an option, we notice that impeding *Drosophila* Hipk expression through *hipk-RNAi* can strongly reverse the overgrowth and cell spreading phenotypes ([Figure 2.7](#)). In line with our suggestion, a previous study proposed that exogenous overexpression of *miR-141*, which targets the 3'UTR of HIPK2, represented a potential approach to hinder HIPK2-mediated EMT ([Huang et al., 2015](#)). Also, given

the large roles of post-translational modifications (PTMs) in HIPK protein turnover and localization ([reviewed by \(Saul and Schmitz, 2013\)](#)), we consider that mutations in other genes encoding HIPK regulators might also contribute to tumorigenesis even in the absence of HIPK gene mutations or changes in HIPK transcript levels. Thus, *revealing the regulation of HIPK activity and identifying the upstream regulators may facilitate the development of promising therapeutic interventions for HIPK-related disorders* ([see Chapter 3 and Chapter 4](#)).

Chapter 3.

The nutrient sensor OGT regulates Hipk stability and tumorigenic activity

Chapter 3 is based off the following published work with modifications.

Kenneth Kin Lam Wong, Ta-Wei Liu, Jessica M. Parker, Donald A.R. Sinclair, Yi Yun Chen, Kay-Hooi Khoo, David J. Vocadlo, and **Esther M. Verheyen**. The nutrient sensor OGT regulates Hipk stability and tumorigenic-like activities in *Drosophila*. *Proc. Natl. Acad. Sci. U.S.A.* 117: 2004-213 (2020).

<https://www.ncbi.nlm.nih.gov/pubmed/31932432>

3.1. Contributions to the Chapter

K.K.L.W., T.-W.L., Y.-Y.C., K.-H.K., D.J.V., and E.M.V. designed research; **K.K.L.W.**, T.-W.L., J.M.P., and Y.-Y.C. performed research; D.A.R.S. contributed new reagents/analytic tools; **K.K.L.W.**, T.-W.L., J.M.P., D.A.R.S., Y.-Y.C., K.-H.K., D.J.V., and E.M.V. analyzed data; and **K.K.L.W.**, T.-W.L., D.J.V., and E.M.V. wrote the paper.

3.2. Abstract

Environmental cues such as nutrients alter cellular behaviors by acting on a wide array of molecular sensors inside cells. Of emerging interest is the link observed between effects of dietary sugars on cancer proliferation. Here, we identify the requirements of hexosamine biosynthetic pathway (HBP) and O-GlcNAc transferase (OGT) for *Drosophila* homeodomain-interacting protein kinase (Hipk)-induced growth abnormalities in response to a high sugar diet. On a normal diet, OGT is both necessary and sufficient for inducing Hipk-mediated tumor growth. We further show that OGT maintains Hipk protein stability by blocking its proteasomal degradation and that Hipk is O-GlcNAcylated by OGT. In mammalian cells, human HIPK2 proteins accumulate post-transcriptionally upon OGT overexpression. Mass spectrometry analyses reveal that HIPK2 is at least O-GlcNAc modified at S852, T1009, and S1147 residues. Mutations of these residues reduce HIPK2 O-GlcNAcylation and stability. Together, our data demonstrate a conserved role of OGT in positively regulating the protein stability of HIPKs (fly Hipk and human HIPK2), which likely permits the nutritional responsiveness of HIPKs.

3.3. Introduction

Nutrients such as glucose, amino acids, and fatty acids are metabolic fuels that provide energy to cells (Marshall, 2006). They also function as signaling molecules in various nutrient signaling pathways (Marshall, 2006), allowing coordination between nutrient sensing and cellular behaviors like cell growth (Yuan et al., 2013).

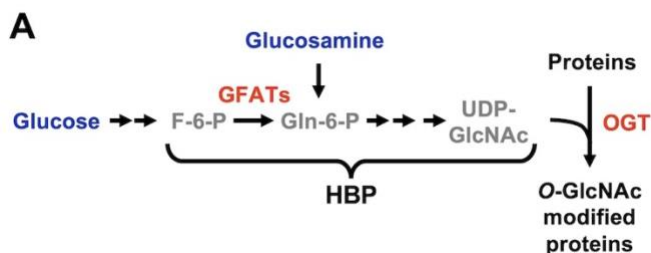


Figure 3.1. The hexosamine biosynthetic pathway HBP

Schematic diagram of the HBP. Dietary glucose and glucosamine are shown in blue, metabolites in gray, enzymes in red.

One emerging nutrient signaling pathway is the hexosamine biosynthetic pathway (HBP) (Love and Hanover, 2005). In the HBP, glutamine:fructose-6-phosphate amidotransferases (GFATs) catalyze the first and rate-limiting step that converts glucose-derived fructose-6-phosphate into glucosamine-6-phosphate (Figure 3.1) (Love and Hanover, 2005). The end product of the HBP is UDP-GlcNAc, the donor nucleotide sugar substrate for various glycosyltransferases, including nucleocytoplasmic O-GlcNAc transferase (OGT) (Bond and Hanover, 2015). OGT is the only known enzyme that catalyzes the addition of O-GlcNAc to serine and threonine residues of hundreds of target proteins in a UDP-GlcNAc-dependent manner (Hardivillé and Hart, 2014). Notably, O-GlcNAcase (OGA) removes O-GlcNAc from proteins, making O-GlcNAc a dynamic and reversible post-translational modification (PTM) (Yang and Qian, 2017). In this way, cellular UDP-GlcNAc levels and global O-GlcNAcylation are coordinated and are highly responsive to glucose availability, making O-GlcNAc well suited to serve as a nutrient-sensing mechanism (Liu et al., 2000; Walgren et al., 2003).

Pathologically, O-GlcNAc has been implicated in cancers. For instance, hyper-O-GlcNAcylation, high levels of OGT or GFAT2, or low OGA levels are positively correlated with poor prognosis of patients with prostate or breast cancers (Kamigaito et al., 2014; Onodera et al., 2014), aggressiveness of bladder tumors (Rozanski et al., 2012), or tumor recurrence of liver cancer (Zhu et al., 2012). Also, many oncoproteins and tumor suppressors such as c-MYC (Chou et al., 1995a), p53 (Yang et al., 2006), and YAP (Peng et al., 2017; X. Zhang et al., 2017) are O-GlcNAc modified. These observations link O-GlcNAc with multiple hallmarks of cancer, including sustaining proliferative signals and deregulating cellular energetics. Cancer cells are usually metabolically active. In particular they often sustain high rates of glucose uptake, a phenomenon commonly known as the Warburg effect, which is a preferential reliance on aerobic glycolysis to obtain energy (Hsu and Sabatini, 2008). How elevated uptake of glucose triggers O-GlcNAc modification of cancer-related proteins and controls their activities is accordingly a topic of growing interest.

Homeodomain-interacting protein kinases (HIPKs; HIPK1-4 in mammals and Hipk in *Drosophila* [fruit fly]) are protein kinases involved in the regulation of signal transduction (Chen and Verheyen, 2012; Lee et al., 2009b, 2009a; Swarup and Verheyen, 2011), cell proliferation and differentiation (Hattangadi et al., 2010; Rinaldo et al., 2012), apoptosis (D’Orazi et al., 2002), stress response (Torrente et al., 2017),

embryonic development (Kyoichi Isono et al., 2006), angiogenesis (Shang et al., 2013), adipogenesis (Sjolund et al., 2014), as well as immune homeostasis (Cao et al., 2019). The activity of HIPK2 (the most studied member of the mammalian HIPK family) is governed by multiple strategies depending on the environments. HIPK2 is normally maintained at low levels by proteasomal degradation involving various ubiquitin E3 ligases such as Siah1 and Siah2 (Calzado et al., 2009; Winter et al., 2008). During hypoxia, HIPK2 degradation is facilitated by the increased association between HIPK2 and Siah2 (Calzado et al., 2009). DNA damage, on the other hand, disrupts the HIPK2-Siah1 interaction, protecting HIPK2 from degradation (Winter et al., 2008). Furthermore, high oxidative stresses modulate HIPK2 SUMOylation and acetylation states, which influence HIPK2 localization (de la Vega et al., 2012). Given the capacity for HIPK2 to respond to environmental cues and the growing recognition that nutrient sensing through OGT is a key regulator of cellular homeostasis, we were intrigued by the potential for O-GlcNAc modification to serve as a nutritional regulator of HIPK(s).

Our previous work has established that elevated Hipk in *Drosophila* promotes tissue growth abnormalities and several neoplastic tumor-like features, including metabolic reprogramming, cell invasion-like behaviors, and cellular changes reminiscent of epithelial-to-mesenchymal transition, including up-regulation of Twist and Matrix metalloproteinase 1 (MMP1) and down-regulation of E-cadherin (Blaquiere et al., 2018; Chen and Verheyen, 2012; Wong et al., 2019). Using this *in vivo* tumor model, we show that OGT is not only necessary for Hipk-mediated tissue growth abnormalities, but also sufficient to synergize with mild levels of Hipk to produce tumor phenotypes. Furthermore, we find that HIPKs (both fly Hipk and human HIPK2) are O-GlcNAc-modified proteins. Elevated OGT results in the buildup of HIPK proteins in a posttranscriptional manner. In particular, we identify that HIPK2 O-GlcNAcylation at residues S852, T1009, and S1147 are responsible for OGT-mediated stabilization.

3.4. Results

3.4.1. High dietary sugar potentiates Hipk-induced tissue growth abnormalities

In *Drosophila*, Hipk promotes tissue growth in a dose-dependent manner (Chen and Verheyen, 2012). Using the Gal4-UAS system (Brand and Perrimon, 1993) in flies grown at different temperatures, which affects the extent of Gal4-driven transgene expression, we can generate a range of *hipk* overexpression phenotypes that can be used to examine genetic and environmental interactions with Hipk (Figure 3.2). Using the *dpp-Gal4* driver to induce *UAS-hipk* expression in a subset of cells in larval leg imaginal discs that give rise to adult leg appendages, we observed distinct effects at 25°C or 29°C.

Compared with control flies (Figure 3.2 A, G left), flies overexpressing *hipk* at 25°C (full genotype: *dpp-Gal4 > UAS-hipk*, abbreviated as *dpp > hipk*) usually displayed a wild-type (WT) slender leg phenotype (Figure 3.2 B, Figure 3.3 B white arrowheads) and rarely had one or two mildly disfigured legs (Figure 3.2 B black arrowheads, Figure 3.3 B black arrowhead, Figure 3.3 E). We define this phenotype as *mild leg malformation* (Figure 3.2 G Middle). In contrast, the same genotype grown at 29°C led to a *severe leg malformation* phenotype characterized by significant distortion of pharate adult legs and loss of segmentation (Figure 3.2 C, G Right). Because of such severe growth abnormalities, these flies usually failed to eclose from their pupal cases. The same severe phenotype was seen when overexpressing two copies of *hipk* transgenes at 25°C (Figure 3.2 D), which is associated with the previously reported cell hyperproliferation phenotypes observed in two other larval imaginal discs, wing and eye-antennal discs (Blaquiere et al., 2018).

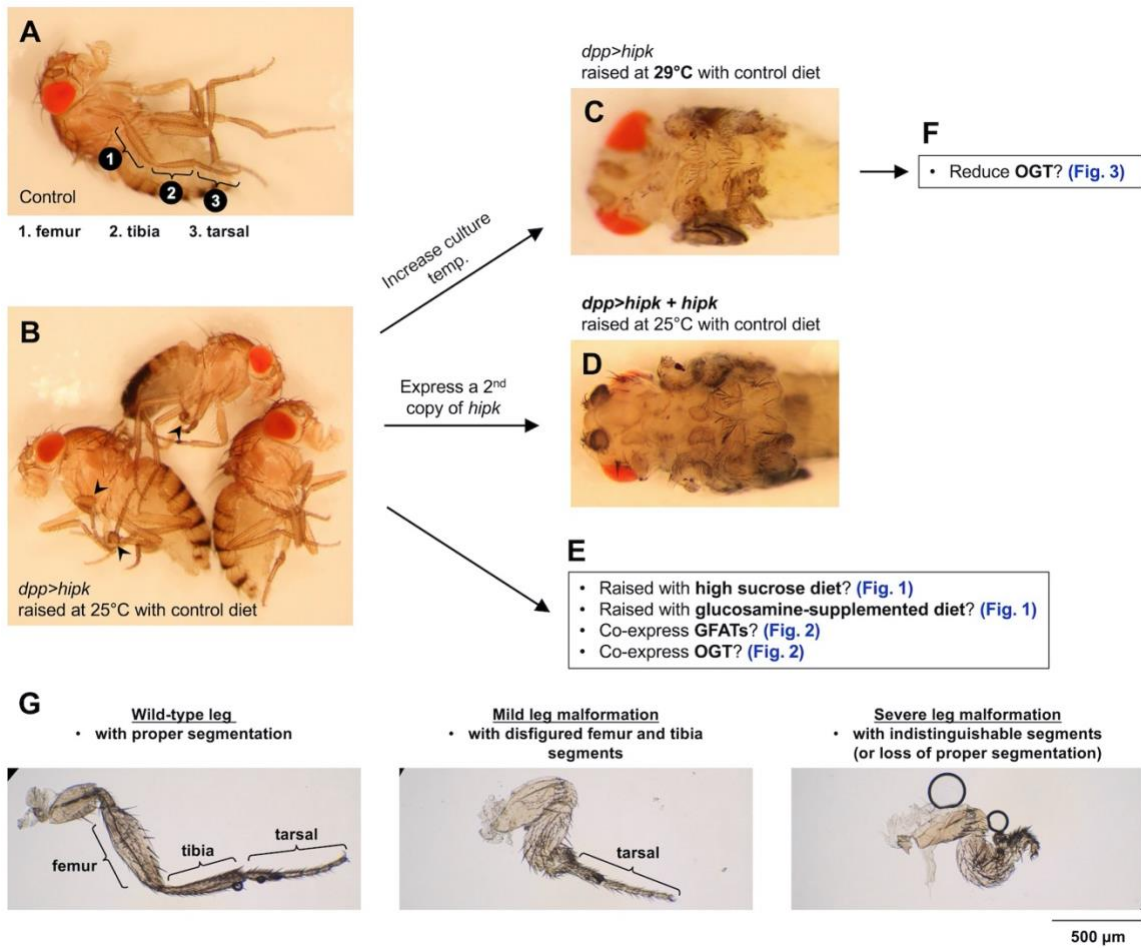


Figure 3.2. We used a sensitized Hipk genetic background to investigate potential modifiers of Hipk.

(A) A control fly without *hipk* overexpression (raised at 25°C with control diet) is shown. The adult legs are slender with proper segmentation. Three major segments, femur, tibia and tarsal, are indicated. **(B)** Raised at 25°C with control diet, flies overexpressing *hipk* (*dpp > hipk*) usually had a wild-type slender leg phenotype. Occasionally, the flies had one or two legs with deformed segments (black arrowheads). We refer this phenotype as *mild leg malformation*. **(C-D)** Using the sensitized Hipk genetic background described in **(B)**, we further increased Hipk levels by either raising the culture temperature to 29°C (which increases the potency of Gal4 driver thus leading to more transgene expression) **(C)** or expressing a second copy of *hipk* transgene at 25°C **(D)**. High/elevated expression of *hipk* led to formation of legs without proper segmentation. We refer this phenotype as *severe leg malformation*. **(E)** Using the mild leg malformation indicative of moderate *hipk* expression levels **(B)**, we set out to investigate whether Hipk could sense and respond to nutrient signals like high dietary sucrose or glucosamine. FIG 1 refers to **Figure 3.3**. Then, we examined the genetic interactions between Hipk with regulatory enzymes of the hexosamine biosynthetic pathway and O-GlcNAcylation, namely GFATs and OGT respectively. FIG 2 refers to **Figure 3.8**. **(F)** Using the severe leg malformation indicative of high *hipk* expression levels, we set out to investigate whether OGT is required for Hipk activity. FIG 3 refers to **Figure 3.13**. **(G)** Definitions of the leg phenotypes used in this study. A wild-type leg with proper segmentation is shown **(left)**. Mild leg malformation refers to the formation of legs

with some distorted segments (**middle**). Severe leg malformation refers to the formation of legs with significant loss of segmentation (**right**). Scale bar, 500 μ m.

The Hipk phenotype seen at 25°C indicates that when *hipk*-overexpressing flies were raised and fed a normal diet (0.15 M sucrose), Hipk expression levels remained close to, yet still below, the threshold required to cause significant growth abnormalities (**Figure 3.3 B**). We took advantage of the sensitized background of the mild Hipk overexpression phenotype to interrogate whether dietary sugar alters Hipk function in controlling tissue growth. Strikingly, we found that a high sucrose diet (HSD; 1 M sucrose) enhanced the abnormal leg phenotype in *hipk*-overexpressing flies such that nearly all legs were malformed (**Figure 3.3 C black arrowheads, E**).

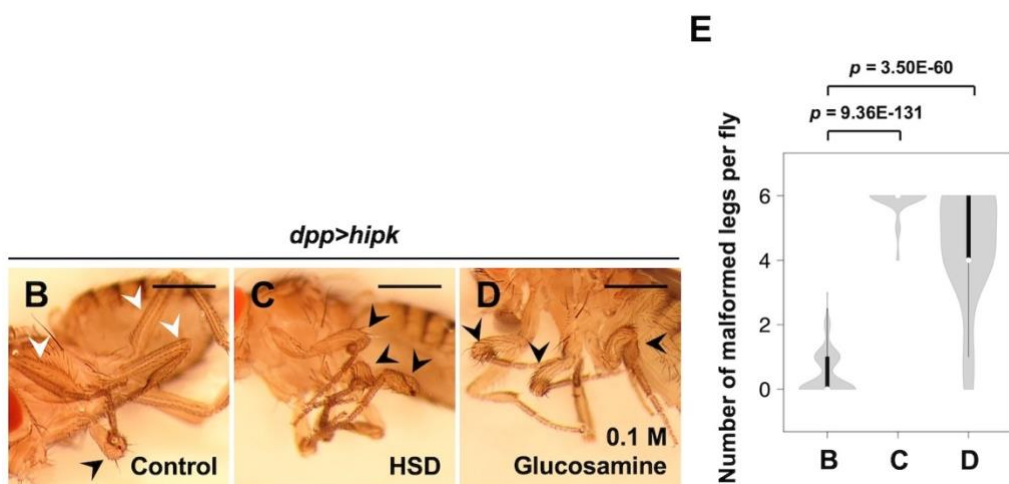


Figure 3.3. High dietary sugar potentiates Hipk-induced growth abnormalities.

(B-D) Adult legs of *hipk*-overexpressing animals (*dpp > hipk*) which were fed a control diet (0.15 M sucrose) (B), a HSD (1 M sucrose) (C), or a glucosamine-supplemented diet (D) from embryo hatch. White arrowheads mark the WT-like, slender leg phenotype. Black arrowheads mark the mild leg malformation phenotype. (E) A violin plot showing the malformed leg phenotype of the *dpp > hipk* flies raised on different diets. The letters B-D refer to the flies shown in **Figure 3.3 B-D**. Numbers of flies counted N: (B) 173, (C) 52, and (D) 37. *p* values were calculated using unpaired two-tailed Student's *t*-test. Scale bars, 500 μ m.

Similarly, we observed that eye-antennal discs from HSD-fed *hipk*-overexpressing larvae showed an enlarged Decapentaplegic (Dpp) domain (marked by Hipk immunoreactivity) (**Figure 3.4 C-D**), indicative of augmented Hipk activities and enhanced cell proliferation.

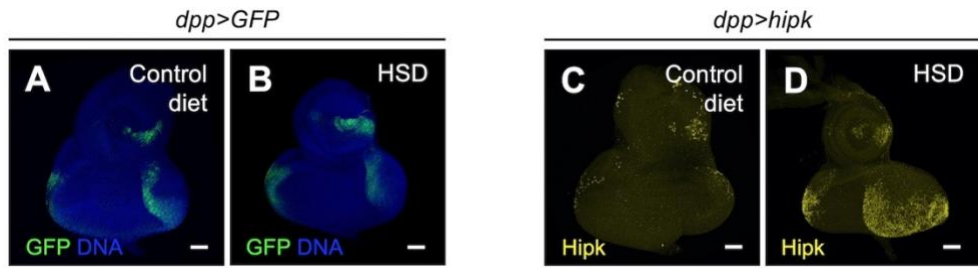


Figure 3.4. High sugar promotes cell proliferation in *hipk*-overexpressing eye discs.

Flies were raised at 25°C with the indicated diets. **(A-B)** Eye discs expressing GFP (green) in larvae (*dpp > GFP*) fed with either control diet (0.15 M sucrose) **(A)** or high-sucrose diet (HSD, 1 M sucrose) **(B)**. DAPI staining for DNA (blue) shows the overall tissue morphology. **(C-D)** Eye discs overexpressing *hipk* in larvae (*dpp > hipk*) fed with either control diet **(C)** or HSD **(D)**. Eye discs were stained for Hipk (yellow). Scale bars, 50 µm.

To test if dietary sugar modulates Hipk tissue growth through the HBP flux, we added glucosamine to the fly culture media. Glucosamine bypasses the rate-limiting step governed by GFAT enzymes and directly enters the HBP (Figure 3.1) (Love and Hanover, 2005). We found that supplementing the normal diet (0.15 M sucrose) with glucosamine (0.1 M glucosamine) also potentiated the mild leg malformation phenotype in *hipk*-overexpressing flies (Figure 3.3 **D** black arrowheads, **E**) in a similar manner as feeding with a high sucrose diet. Under either feeding conditions, flies without overexpression of *hipk* did not show any malformed leg phenotypes (Figure 3.5) or increased cell proliferation (Figure 3.4 **A-B**).

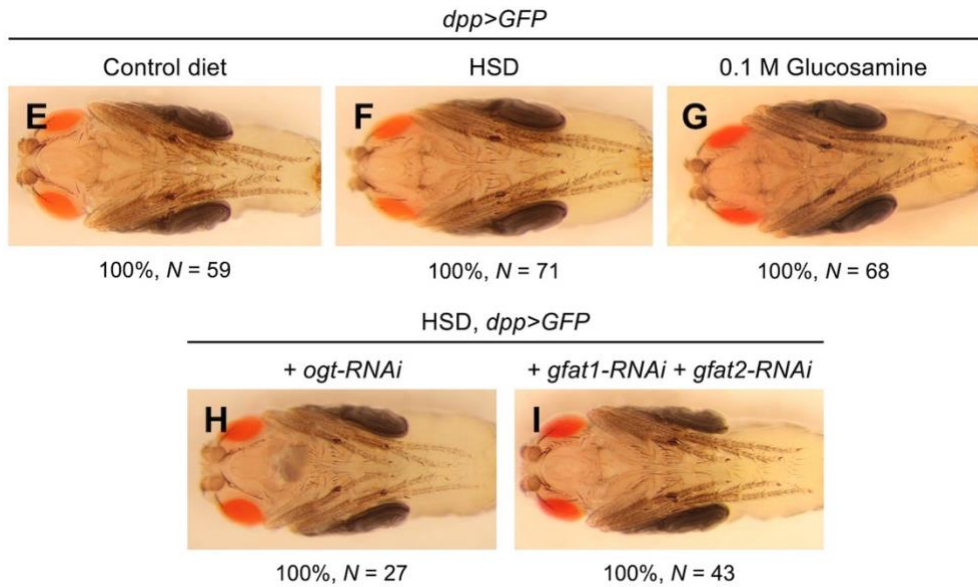


Figure 3.5. High sugar does not induce any tissue growth abnormalities in the absence of *hipk* overexpression.

(E-G) No abnormal leg phenotypes (as a readout of Hipk activity) were found on control flies (*dpp > GFP*) fed with control diet (E), HSD (F) or glucosamine-supplemented diet (G) since hatching. (H-I) No abnormal leg phenotypes were found on flies with genetic inhibition of OGT (*dpp > GFP + ogt-RNAi*) (H) or GFATs (*dpp > GFP + gfat1-RNAi + gfat2-RNAi*) (I). Percentages show the phenotype penetrance. N is the number of flies counted.

3.4.2. The high sugar effect on Hipk activity depends on the HBP and OGT

Next, we used RNA interference (RNAi) to knock down the rate-limiting enzymes in the HBP, GFATs, which are encoded in flies by *gfat1* and *gfat2*. Notably, simultaneous knockdown of *gfat1* and *gfat2* suppressed the effect of high sugar on Hipk-induced malformed leg phenotypes (**Figure 3.6 F, G, J**).

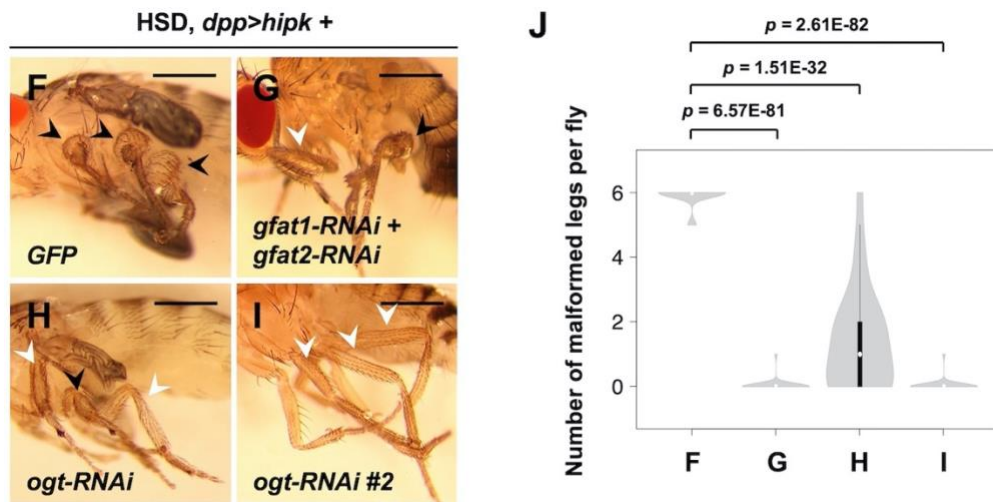


Figure 3.6. High sugar potentiates Hipk activity through GFATs and OGT.

(F-I) Adult legs of *dpp > hipk + GFP* (**F**), *dpp > hipk + gfat1-RNAi + gfat2-RNAi* (**G**), *dpp > hipk + ogt-RNAi* (**H**), and *dpp > hipk + ogt-RNAi #2* (**I**) flies which were fed an HSD from embryo hatch. Black arrowheads mark the disfigured legs. White arrowheads mark the WT-like legs. **(J)** A violin plot showing the malformed leg phenotype of the indicated animals fed a HSD. The letters **F-I** refer to the flies shown in **Figure 3.6 F-I**. Numbers of flies counted *N*: (**F**) 53, (**G**) 28, (**H**) 25, and (**I**) 29. *p* values were calculated using unpaired two-tailed Student's *t*-test. Flies were raised at 25°C. Scale bars, 500 μm.

To examine if OGT downstream of the HBP is required for the stimulatory effect of high sucrose on Hipk-mediated tissue growth phenotypes, we investigated the effects of genetic inhibition of OGT. Using two independent RNAi fly lines, we found that knockdown of *ogt* (also known as *super sex combs* (*sxc*) in *Drosophila* ([Gambetta et al., 2009](#); [Sinclair et al., 2009](#))) partly rescued the leg phenotype seen after high sucrose feeding (**Figure 3.6 H-J**). We confirmed the knockdown efficiency of the RNAi lines used in this study by qRT-PCR, Western blotting, and/or immunofluorescence (IF) analyses (**Figure 3.7**).

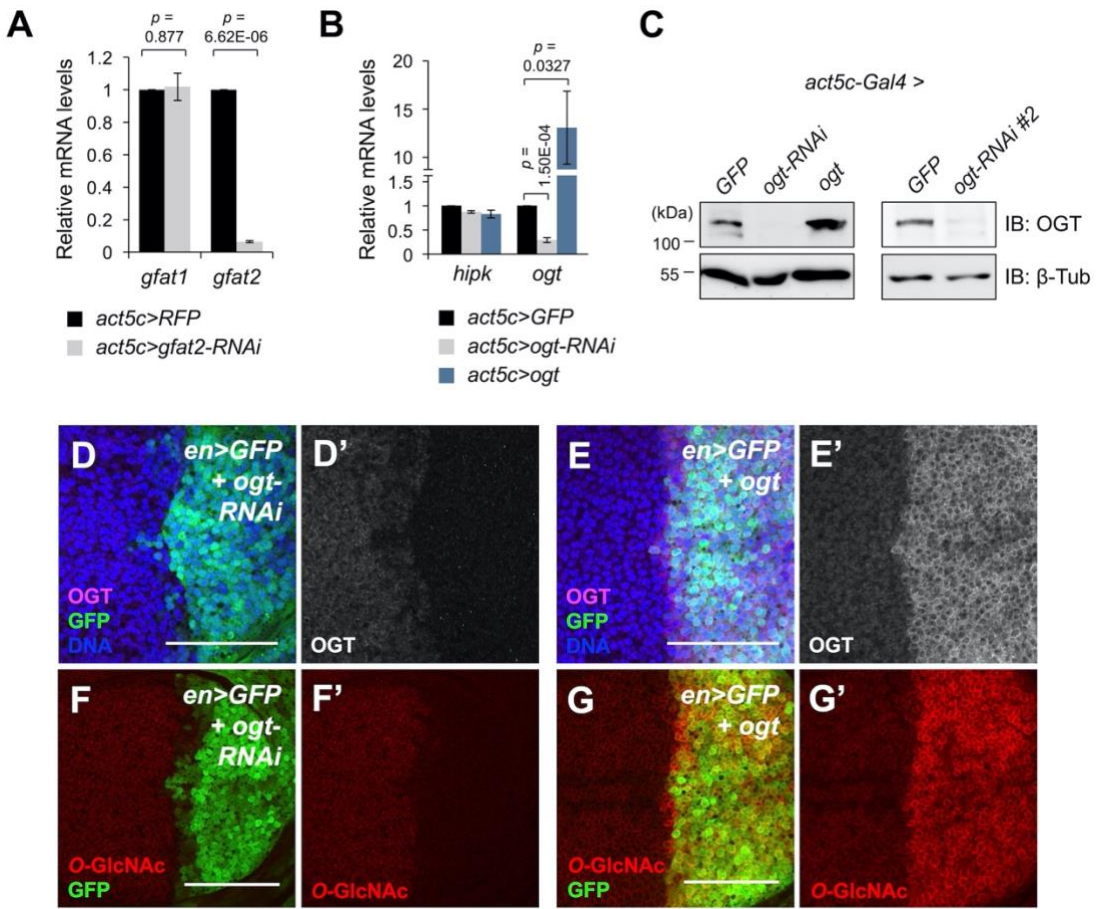


Figure 3.7. Validation of tools used in this study to modulate GFAT and OGT expression levels.

Flies were raised at 25°C with control diet. **(A)** qRT-PCR analyses of *gfat1* and *gfat2* mRNA levels in control (*act5c > RFP*) and *gfat2* knockdown (*act5c > gfat2-RNAi*) larvae. The knockdown efficiency of the *gfat1-RNAi* line was not evaluated as *act5c > gfat1-RNAi* animals could not survive to larval stage. **(B)** qRT-PCR analyses of *hipk* and *ogt* mRNA levels in control (*act5c > GFP*), *ogt* knockdown (*act5c > ogt-RNAi*), and *ogt*-overexpressing (*act5c > ogt*) larvae. **(C)** Western-Blot analyses of OGT protein levels in control (*act5c > GFP*), *ogt* knockdown (*act5c > ogt-RNAi*), *ogt* knockdown #2 (*act5c > ogt-RNAi #2*) and *ogt*-overexpressing (*act5c > ogt*) larvae. β -Tubulin was used as a loading control. **(D-G)** Immunofluorescence staining of OGT (magenta in **D**, **E**; grey in **D'**, **E'**) and O-GlcNAc (**F-G** red) in larval wing imaginal discs. *en-Gal4* driver induces *UAS-ogt-RNAi* (**D**, **F**) or *UAS-ogt* (**E**, **G**) expression in the posterior compartments (marked by GFP). DAPI was used to stain DNA (blue). Scale bars, 50 μ m.

Further supporting a link to the HBP and OGT, we also found that simultaneous overexpression of *gfat1* and *gfat2* (Figure 3.8 C, E) or overexpression of *ogt* (Figure 3.8 D, E) in a *dpp > hipk* genetic background at 25°C was sufficient to produce leg malformations reminiscent of Hipk hyperactivation (Figure 3.8 B, E) even under normal dietary conditions. Altogether, using the leg malformation phenotypes as a readout for Hipk activity, our genetic interaction studies indicate that *high dietary sugar promotes Hipk activity at least in part through the HBP and OGT*.

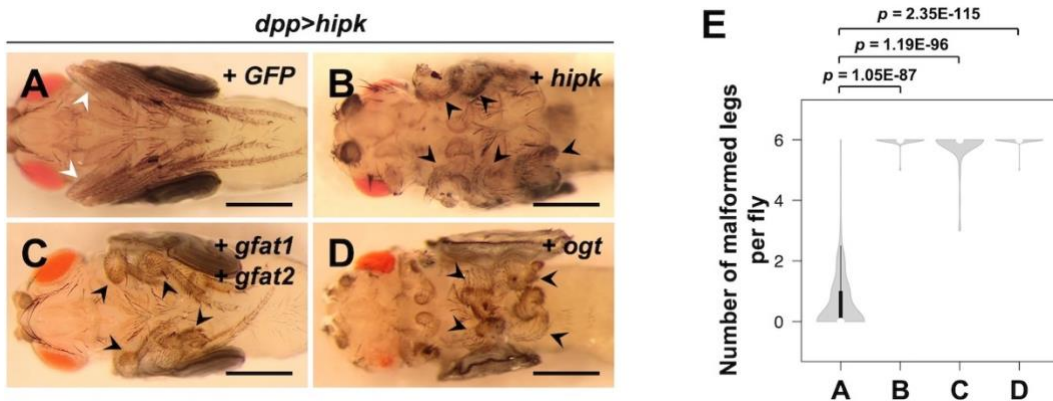


Figure 3.8. GFATs and OGT potentiate Hipk-mediated growth abnormalities under normal diet conditions.

(A-D) Adult legs of *dpp > hipk + GFP* (A), *dpp > hipk + hipk* (B), *dpp > hipk + gfat1 + gfat2* (C), and *dpp > hipk + ogt* (D) flies. White arrowheads mark the WT-like slender leg phenotype. Black arrowheads mark the malformed legs. Scale bars, 500 µm. (E) A violin plot showing the malformed leg phenotype of the indicated animals. The letters A-D refer to the flies shown in Figure 3.8 A-D. Numbers of flies counted N: (A) 141, (B) 47, (C) 64, and (D) 76. p values shown were calculated using unpaired two-tailed Student's t-test.

3.4.3. OGT synergizes with Hipk to drive tumor growth

As stated in the introduction, we previously established an *in vivo* fly tumor model with elevation of *hipk* (overexpression of two copies of *hipk*) using wing imaginal discs in larvae raised at 25°C (Blaquiere et al., 2018). Given the genetic interactions between Hipk and OGT observed in the adult legs (Figure 3.8 D), we next asked whether OGT plays a role in Hipk-mediated tissue growth effects in larval wing and eye discs.

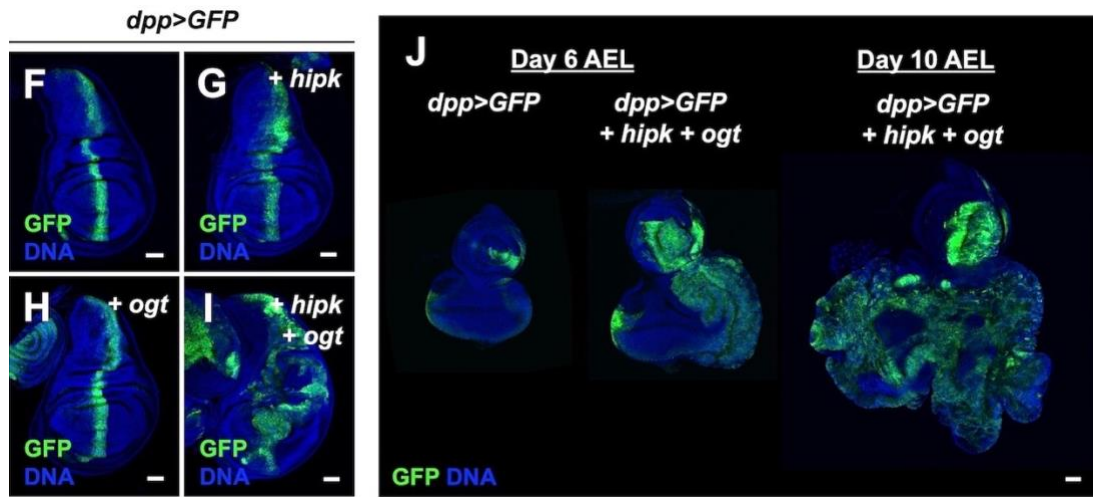


Figure 3.9. OGT synergizes with Hipk to drive tumor growth.

(F-I) Wing discs of *dpp > GFP* (F), *dpp > GFP + hipk* (G), *dpp > GFP + ogt* (H), and *dpp > GFP + hipk + ogt* (I) larvae. GFP (green) marks the transgene-expressing cells. (J) Eye-antennal discs of *dpp > GFP* (Left) and *dpp > GFP + hipk + ogt* (Middle) larvae dissected 6 d after egg laying (AEL). *dpp > GFP + hipk + ogt* animals experienced an extended larval phase, and their eye disc (dissected 10 d AEL) is shown (Right). GFP (green) marks the transgene-expressing cells. Scale bars, 50 μm.

We found that in larval wing imaginal discs at 25 °C, overexpression of either *hipk* (single copy) (Figure 3.9 G) or *ogt* (Figure 3.9 H) on their own did not cause any abnormal phenotypes. Co-expression of *ogt* with *hipk*, however, resulted in profound tissue overgrowth (Figure 3.9 I), suggesting that they drive tumor-like growth in a synergistic manner. Co-expression of *hipk* and *ogt* also resulted in a delay in timing of pupariation (Figure 3.10), a phenotype commonly seen when tumor burden is present in larvae (Menut et al., 2007).

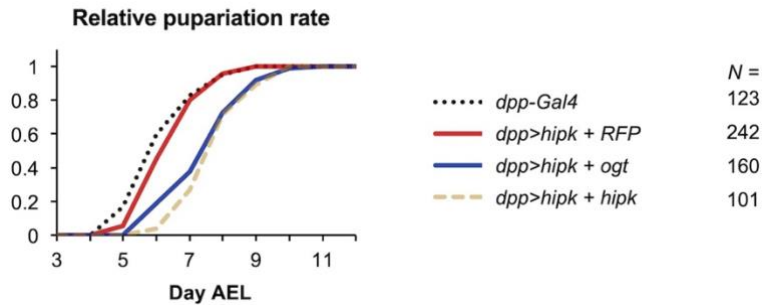


Figure 3.10. Co-expression of *hipk* and *OGT* causes a developmental delay in the timing of pupariation.

Flies were raised at 25°C with control diet. Relative pupariation rate of the flies of indicated genotypes revealing a developmental delay in larvae driven by a synergistic effect between Hipk and OGT, an effect mimicking that when two copies of *hipk* are expressed. N, number of pupae counted. AEL, after egg laying.

A comparable synergy was also seen in larval eye-antennal discs ([Figure 3.9 J](#), [Figure 3.11](#), [Figure 3.12](#)) and, in the developmentally delayed larvae, *hipk* and *ogt* co-expressing tissues grew in size continuously ([Figure 3.9 J](#)). Furthermore, we found that the cells co-expressing *hipk* and *ogt* were characterized by an enrichment in phosphohistone H3 (PH3, a mitotic marker), up-regulation of cyclin E (CycE), matrix metalloproteinase 1 (MMP1), and dMyc (MYC in vertebrates), as well as loss of E-cadherin (E-cad) ([Figure 3.11](#)), which are all established markers associated with extensive cancerous growth. These data indicate that *OGT* is capable of augmenting the tumorigenic potential of Hipk even though Hipk is mildly expressed in this system.

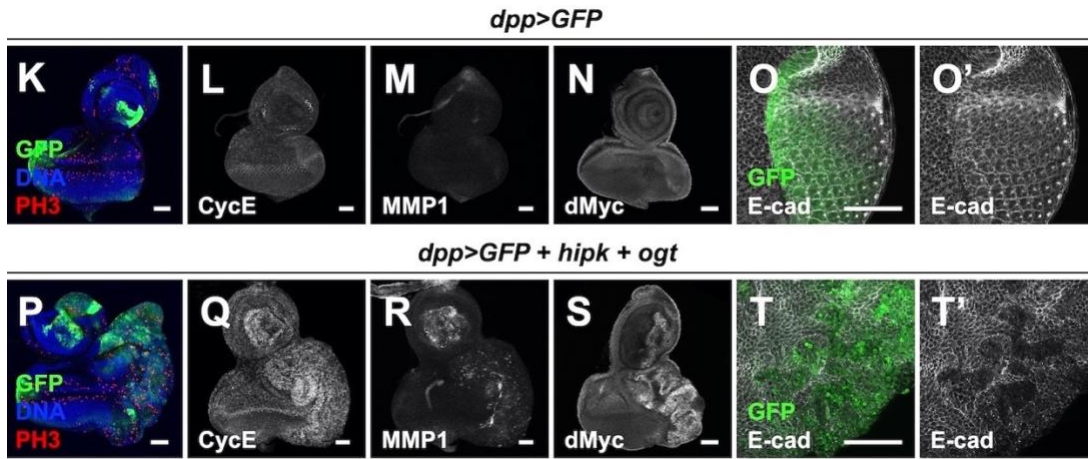


Figure 3.11. Tissues co-expressing *hipk* and *OGT* display changes in markers associated with cancer growth.

(K-O) Control eye discs (*dpp > GFP*) stained for PH3 (red in K), CycE (gray in L), MMP1 (gray in M), dMyc (gray in N), and E-cad (gray in O and O'). (P-T) *hipk* and *ogt* co-expressing eye discs (*dpp > GFP + hipk + ogt*) stained for PH3 (red in P), CycE (gray in Q), MMP1 (gray in R), dMyc (gray in S), and E-cad (gray in T and T'). DAPI staining for DNA (blue) reveals tissue morphology. Flies were raised at 25°C with control diet. Scale bars, 50 µm.

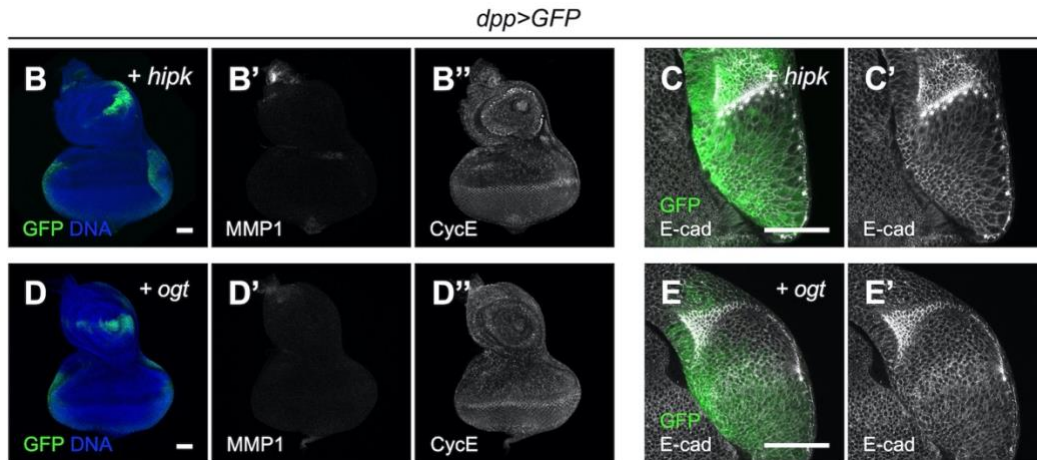


Figure 3.12. Tissues overexpressing *hipk* or *OGT* alone do not show any abnormal phenotypes.

(B-E) Staining of MMP1, CycE and E-cad in *hipk*-expressing eye-antennal discs (*dpp>GFP + hipk*) (B-C) and *ogt*-expressing discs (*dpp>GFP + ogt*) (D-E). No noticeable changes in MMP1, CycE or E-cad levels were observed when compared with control discs (Figure 3.11 K-O). DAPI was used to stain DNA (blue). Scale bars, 50 µm.

3.4.4. OGT is necessary for Hipk-induced tissue growth abnormalities.

Next, we set out to evaluate the requirement of OGT for Hipk activity using the leg malformation phenotypes. We shifted the fly culture temperature from 25°C to 29°C such that Gal4 activity was increased to drive greater Hipk expression to reach a level sufficient to cause severe growth abnormalities (**Figure 3.13 B black arrowheads, E**). Co-expression of *ogt-RNAi* with *hipk* partially rescued the severe leg malformation phenotype caused by excess Hipk as the leg segmentation was partly restored (**Figure 3.13 C black arrowheads, E**). Expression of *ogt-RNAi* alone did not cause any abnormal leg phenotypes (**Figure 3.13 D**).

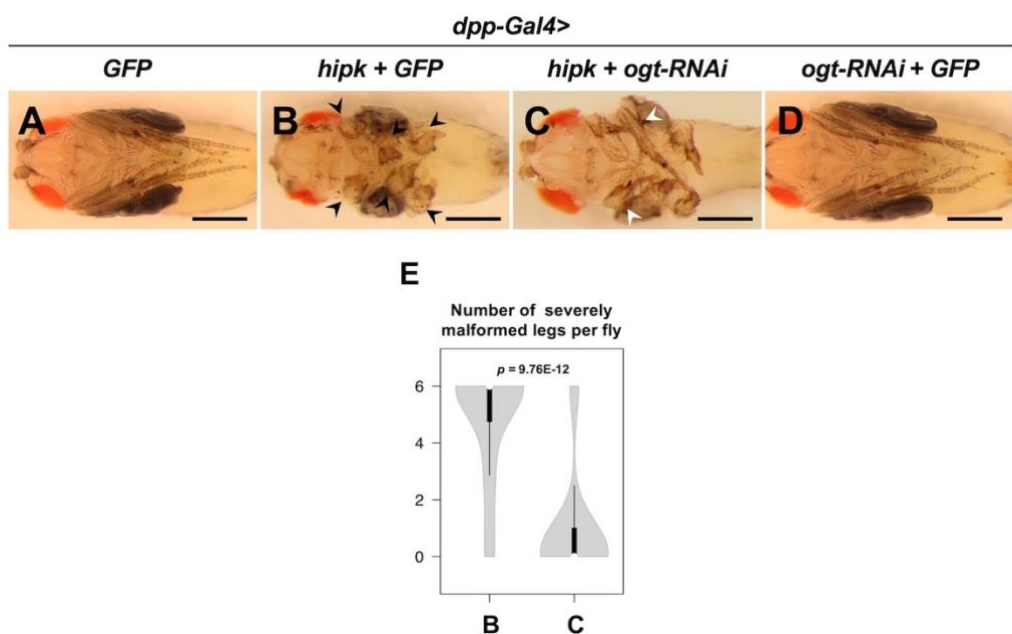


Figure 3.13. OGT is necessary for Hipk-induced severe leg malformation phenotype.

(A-D) Adult legs of *dpp > GFP* (A), *dpp > hipk + GFP* (B), *dpp > hipk + ogt-RNAi* (C), and *dpp > ogt-RNAi + GFP* (D) flies. Black arrowheads in B mark the legs with severe malformation. White arrowheads in C mark the legs with mild malformation. (E) Quantification of the severe leg malformation phenotype of the indicated animals. The letters B-C refer to the flies shown in **Figure 3.13 B-C**. Numbers of flies counted N: B: 36. C: 28. p value shown was calculated using unpaired two-tailed Student's *t*-test. Scale bars, 500 μ m.

We then examined the requirement of OGT for Hipk-induced tumor growth in wing discs. Compared with the control wing discs (**Figure 3.14 E**), elevated Hipk

(overexpression of one copy of *hipk* at 29°C) induced significant abnormal overgrowth (**Figure 3.14 F**). When *ogt* was knocked down in *hipk*-overexpressing cells, the overgrowth induced by elevated Hipk was largely suppressed, though mild tissue distortions remained (**Figure 3.14 G**). We also used *ogt* mutant alleles, *sxc[6]* and *sxc[7]*, which possess a point mutation at a splice acceptor site and a nonsense mutation, respectively (Gambetta et al., 2009; Sinclair et al., 2009), to generate an *ogt* null genetic background. Similar to the effects of *ogt* knockdown, the proliferative potential of the cells with elevated Hipk was largely reduced in the *ogt* mutant background (**Figure 3.14 I**). Altogether, our data illustrate a requirement for OGT in *Hipk*-induced tissue growth abnormalities, and the requirement is general to all tissues examined.

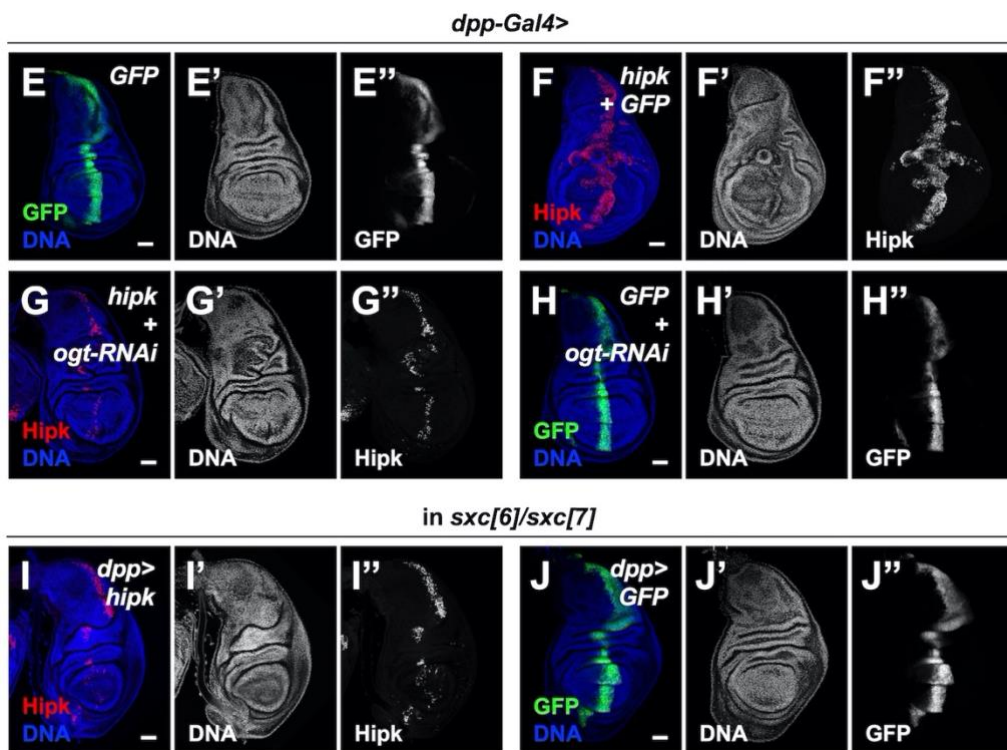


Figure 3.14. OGT is required for Hipk-induced tumor growth.

(E-H) Wing discs of *dpp > GFP* (E), *dpp > hipk + GFP* (F), *dpp > hipk + ogt-RNAi* (G), and *dpp > ogt-RNAi + GFP* (H) larvae. The transgene-expressing domain was marked by GFP (green in E and H; gray in E'' and H'') or Hipk staining (red in F and G; gray in F'' and G''). (I-J) In an *ogt* mutant background (*sxc[6]/sxc[7]*), wing discs of *dpp > hipk* (I) and *dpp > GFP* (J) larvae are shown. The transgene-expressing domain is marked by Hipk staining (red in I; gray in I'') or GFP (green in J; gray in J''). Flies were raised at 29°C with control diet. DAPI staining for DNA (blue; gray in E'-J'') reveals tissue morphology. Scale bars, 50 μm.

3.4.5. Depletion of OGT or GFAT reduces Hipk protein levels.

Given these results, we considered mechanisms by which OGT might influence Hipk activity. Using immunofluorescence staining experiments, we found that loss of OGT caused a robust reduction in the exogenous Hipk immunoreactivity (**Figure 3.14 F, G, I**). Compared with a control genetic background (**Figure 3.15 A**), fewer *hipk*-expressing cells were detected and Hipk expression levels were lower in the *ogt* null (*sxc[6]/sxc[7]*) (**Figure 3.15 B**) or knockdown backgrounds (**Figure 3.15 C**). A comparable result was obtained using additional *ogt* mutant alleles, *sxc[4]* and *sxc[5]* (**Figure 3.15 D-E**), which encode catalytically inactive forms of OGT (OGT-N948I and OGT-Δ1031 to 1059, respectively (Gambetta et al., 2009; Sinclair et al., 2009). We also examined another larval epithelial tissue, salivary glands, because their large cell size facilitates imaging. Knockdown of *ogt* in salivary gland cells caused drastic reductions in Hipk protein levels (**Figure 3.15 F-G**). Using immunoblotting, we confirmed that depletion of OGT led to down-regulation of the exogenous Hipk protein levels (**Figure 3.15 H-I**).

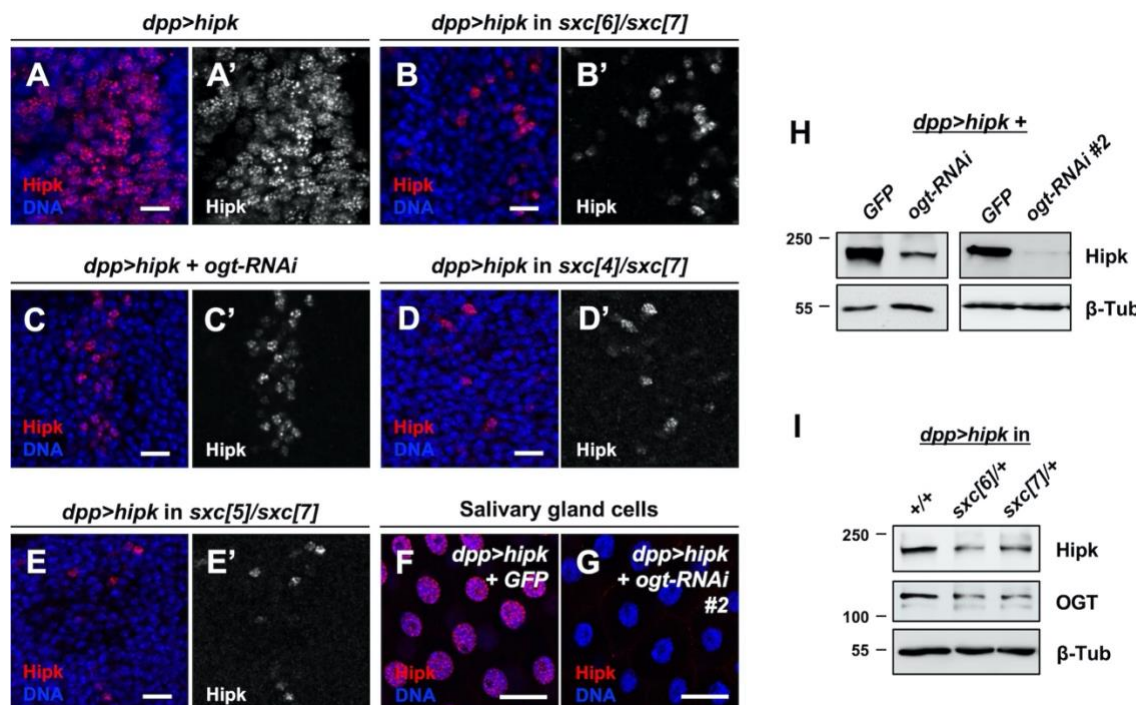


Figure 3.15. Depletion of OGT reduces Hipk protein levels.

(A-B) Wing discs overexpressing *hipk* (*dpp > hipk*) in a WT background (A), in an *ogt* mutant background (*sxc[6]/sxc[7]*) (B), with co-expression of *ogt-RNAi* (C), in *sxc[4]/sxc[7]* mutant

background (**D**), or in *sxc[5]/sxc[7]* mutant background (**E**) were stained for Hipk using anti-Hipk antibodies (red in **A-E**; gray in **A'-E'**). Scale bars, 10 μ m. (**F-G**) *hipk*-overexpressing salivary glands without (*dpp > hipk + GFP*) (**F**) or with *ogt* knockdown (*dpp > hipk + ogt-RNAi #2*) (**G**) were stained for Hipk using anti-Hipk antibodies (red). DAPI was used to stain DNA (blue). Scale bars, 50 μ m. (**H**) Western blot analyses of the exogenous Hipk protein levels in the larval head extracts (which included imaginal discs and salivary glands) obtained from *dpp > hipk + GFP*, *dpp > hipk + ogt-RNAi* and *dpp > hipk + ogt-RNAi #2* animals. (**I**) Western blot analyses showing that loss of one copy of the wild type *ogt* (*sxc*) alleles led to reduced Hipk and OGT protein levels. β -Tubulin was used as a loading control. Flies were raised at 29 °C with control diet.

We also investigated the role of HBP upstream of OGT in modulating Hipk protein levels. We found that knockdown of *gfat1* mildly decreased Hipk protein levels (**Figure 3.16 C, E**), whereas *gfat2* knockdown had no noticeable effect (**Figure 3.16 D, E**). Such a discrepancy could be possibly due to a difference in knockdown efficiency or imply that GFAT1 plays a more important role than GFAT2 in controlling Hipk protein levels. Strikingly, when *gfat1* and *gfat2* were simultaneously knocked down, the exogenous Hipk protein levels were markedly reduced (**Figure 3.16 B, E**), indicating GFAT1 and GFAT2 are functionally redundant.

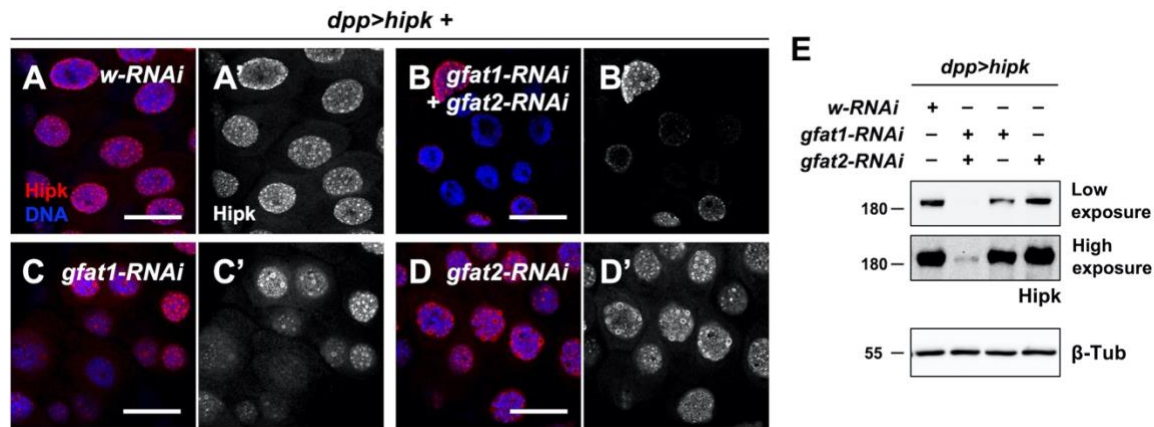


Figure 3.16. Depletion of GFAT reduces Hipk protein levels.

(**A-D**) *hipk*-overexpressing salivary glands with *white* knockdown (*dpp > hipk + w-RNAi*) (Control) (**A**), *gfat1* and *gfat2* double knockdown (*dpp > hipk + gfat1-RNAi + gfat2-RNAi*) (**B**), *gfat1* knockdown (**C**) or *gfat2* knockdown (**D**) were stained for Hipk using anti-Hipk antibodies (red in **A-D**, gray in **A'-D'**). DAPI was used to stain DNA (blue). Scale bars, 50 μ m. (**E**) Western blot analyses of the exogenous Hipk protein levels in the larval head extracts obtained from *dpp > hipk + w-RNAi*, *dpp > hipk + gfat1-RNAi + gfat2-RNAi*, *dpp > hipk + gfat1-RNAi* and *dpp > hipk + gfat2-RNAi* animals. β -Tubulin was used as a loading control. Flies were raised at 29 °C with control diet.

Hipk was predominantly nuclear regardless of OGT or GFAT levels (**Figure 3.15 A-G**, **Figure 3.16 A-D**), indicating that OGT or GFAT is not involved in the regulation of Hipk subcellular localization. We also noted that OGT depletion did not cause loss of *dpp-Gal4* expression (**Figure 3.14 E, H, J**). Thus, OGT depletion does not reduce Hipk protein levels by repressing *UAS-hipk* transcription. Also, reductions in OGT levels had little effects on the transcriptional levels of endogenous *hipk* (**Figure 3.7 B**). Taken together, our data imply that the HBP-OGT axis regulates Hipk protein levels. Specifically, *the catalytic activity of OGT is required to sustain Hipk protein levels post-transcriptionally*.

3.4.6. OGT stabilizes Hipk by preventing Hipk from proteasome degradation.

Given the dependence of Hipk protein levels on catalytically active OGT, we asked whether OGT controls Hipk protein stability. Using a cycloheximide (CHX) chase assay to observe protein stability in the absence of translation, we found that while Hipk levels dropped slightly in control cells, Hipk levels dropped precipitously when *ogt* was knocked down (Figure 3.17 A). To impair proteasomal degradation, we knocked down *rpn2*, which encodes a component of the 26S proteasome (Rosenzweig et al., 2012), and this restored Hipk protein levels (Figure 3.17 B) as well as the tumor growth in the *ogt*-depleted background (Figure 3.17 C-E).

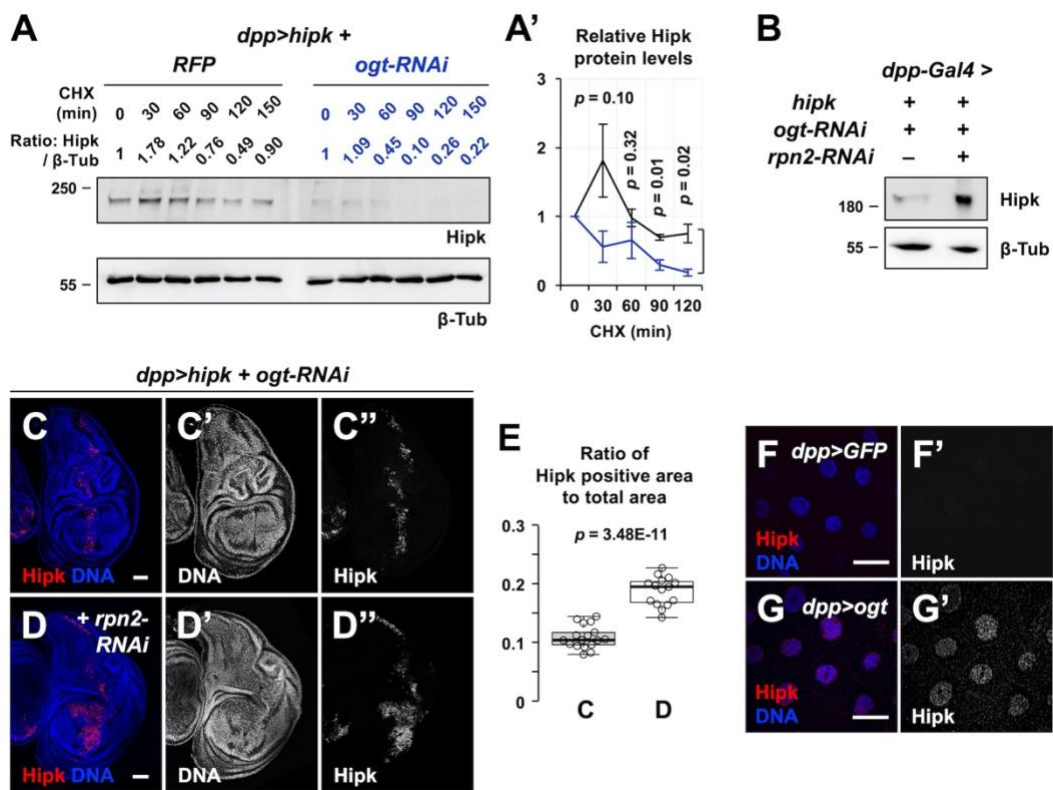


Figure 3.17. OGT stabilizes Hipk by preventing Hipk from proteasomal degradation.

Flies were raised at 29 °C with control diet. (A-A') Dissected larval heads from *dpp > hipk + RFP* and *dpp > hipk + ogt-RNAi* larvae were cultured in insect media and exposed to 200 µg/mL CHX for the indicated times, followed by western blot analyses of the exogenous Hipk protein levels. β-Tubulin was used as a loading control. Numeric values above the Hipk blot show the relative Hipk protein levels, which are set as 1 at 0 min of CHX treatment. (A') Quantification of the relative Hipk protein levels in *dpp > hipk + RFP* (black line) and *dpp >*

hipk + ogt-RNAi (blue line) larval head extracts in the CHX chase assay. Data are mean \pm SEM and pooled from three biological replicates. At each time point, the *p* value shown is calculated using unpaired two-tailed Student's *t*-test. (B) Western blot analyses of the exogenous Hipk protein levels in the larval heads extracted from *dpp > hipk + ogt-RNAi* and *dpp > hipk + ogt-RNAi + rpn2-RNAi* animals. β -Tubulin was used as a loading control. (C-E) Wing discs of *dpp > hipk + ogt-RNAi* (C) and *dpp > hipk + ogt-RNAi + rpn2-RNAi* (D) larvae are shown. The transgene-expressing domain is marked by Hipk staining (red; gray in C'' and D''). DAPI staining for DNA (blue; gray in C' and D') reveals tissue morphology. Scale bars, 50 μ m. (E) A box and whisker plot showing the ratio of Hipk-positive area to total area of the *dpp > hipk + ogt-RNAi* wing discs without or with *rpn2* knockdown. The letters C and D refer to the fly genotypes shown in Figure 3.17 C-D. *p* value is calculated using unpaired two-tailed Student's *t*-test. (F-G) Control (*dpp > GFP*) (F) and *ogt*-overexpressing (*dpp > ogt*) (G) salivary glands were stained for Hipk (red; gray in F' and G'). DAPI was used to stain DNA (blue). Scale bars, 50 μ m.

Endogenous Hipk proteins were scarce and hardly detectable (Figure 3.17 F). However, overexpression of *ogt* was sufficient to induce accumulation of endogenous Hipk proteins (Figure 3.17 G). Using immunoblotting, we confirmed that OGT upregulates endogenous Hipk protein levels (Figure 3.18 C-D). Together, our results suggest that OGT activity positively regulates Hipk protein stability by reducing proteasomal degradation of Hipk.

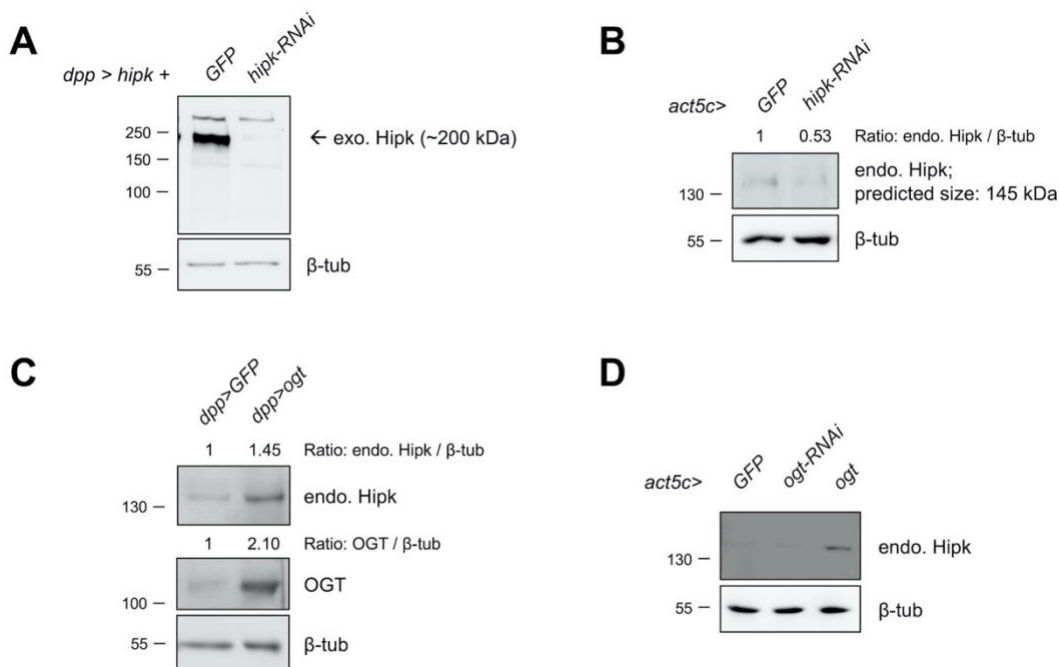


Figure 3.18. Elevated OGT increases protein levels of endogenous Hipk.

(A) Validation of the anti-Hipk antibodies in the detection of exogenous Hipk proteins. Western-blots analyses using anti-Hipk antibodies to show exogenous Hipk proteins (at a molecular size of approximate 200 kDa) in protein lysates extracted from *dpp > hipk + GFP*

and $dpp > hipk + hipk-RNAi$ larval heads. **(B)** Validation of the anti-Hipk antibodies in the detection of endogenous Hipk proteins. Western blot analyses using anti-Hipk antibodies to show endogenous Hipk proteins (predicted molecular size: 145 kDa) in protein lysates extracted from control ($act5c > GFP$) and *hipk* knockdown ($act5c > hipk-RNAi$) larvae. **(C)** Western-blot analyses using anti-Hipk antibodies to show endogenous Hipk proteins in protein lysates extracted from control ($dpp > GFP$) and *ogt*-overexpressing ($dpp > ogt$) larval heads. **(D)** Western-blot analyses using anti-Hipk antibodies to show endogenous Hipk proteins in protein lysates extracted from control ($act5c > GFP$), *ogt* knockdown ($act5c > ogt-RNAi$) and *ogt* overexpressing ($act5c > ogt$) larvae. β -Tubulin was used as a loading control.

3.4.7. OGT binds to and O-GlcNAcylates Hipk.

To test if Hipk and OGT physically interact with each other, we performed coimmunoprecipitation (co-IP) experiments. Using protein extracts from larval tissues expressing both proteins (*dpp > hipk + ogt-flag*), we found that Hipk and OGT could be reciprocally co-immunoprecipitated (Figure 3.19), indicating the two proteins can bind to each other.

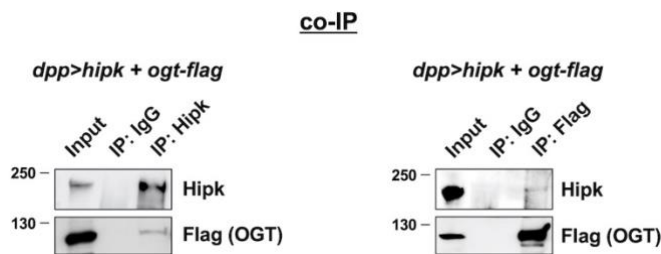


Figure 3.19. OGT binds to Hipk.

Flies were raised at 25°C with control diet. Protein lysates extracted from *dpp > hipk + ogt-flag* larval heads were incubated with either IgG or anti-Hipk antibodies, followed by co-immunoprecipitation (co-IP). Western blot analyses using anti-Hipk and anti-Flag antibodies showing that flag-tagged OGT coimmunoprecipitated with Hipk proteins (Left). Reciprocal IP showing that Hipk coimmunoprecipitated with flag-tagged OGT (Right).

A physical interaction suggested to us that Hipk may be an OGT substrate. To test whether Hipk is O-GlcNAc modified, we employed a chemoenzymatic approach (Figure 3.20 B) (Khidel et al., 2003) . Using a mutant β-1,4-galactosyltransferase (Y289L GALT), we labeled O-GlcNAc-modified proteins with N-azidoacetylgalactosamine (GalNAz). GalNAz-labeled proteins were then biotinylated using click chemistry in combination with a biotin-alkyne probe, followed by precipitation using streptavidin resin. Subsequent immunoblot analyses of the precipitated proteins using antibodies against Hipk revealed marked Hipk O-GlcNAcylation when *ogt* was co-expressed (Figure 3.20 B). We validated the selectivity of the ligation chemistry during labeling by showing Hipk was undetectable in the precipitates when GALT was excluded from the chemoenzymatic labeling step (Figure 3.21).

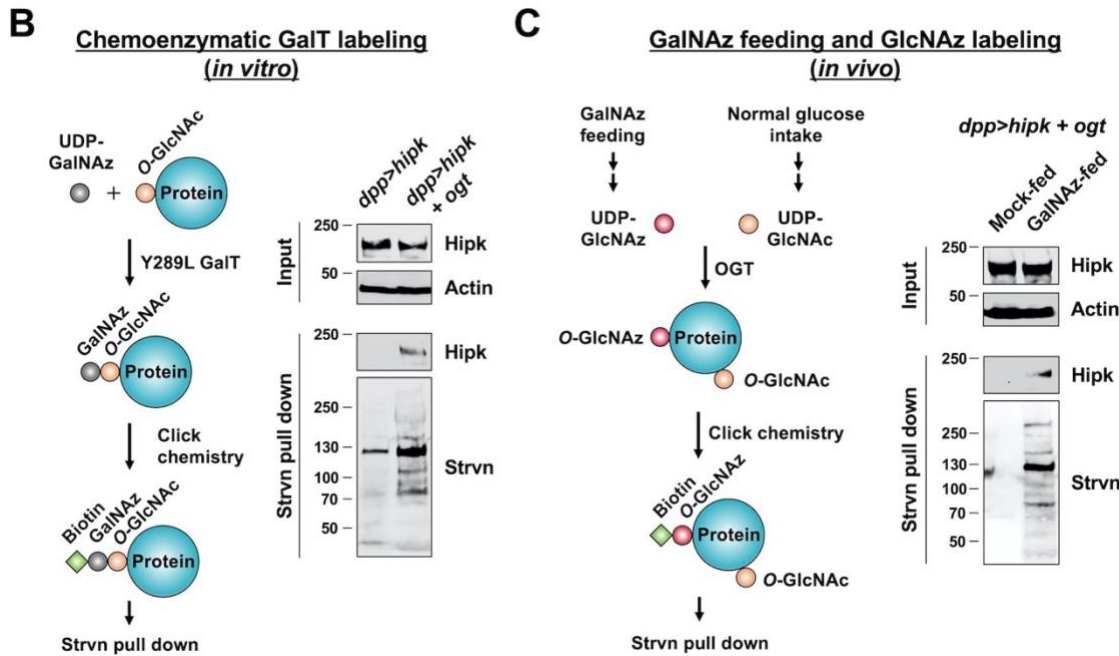


Figure 3.20. OGT O-GlcNAcylates Hipk.

Flies were raised at 25°C with control diet (**B**) or the indicated diets (**C**). (**B**) Detection of O-GlcNAc modified Hipk by chemoenzymatic GalT labeling (schematic diagram shown on the left). Protein lysates extracted from *dpp > hipk* and *dpp > hipk + ogt* larval heads were incubated with UDP-GalNAz and the enzyme Y289L GalT, followed by coupling with a biotin-alkyne probe by click chemistry, streptavidin (Strvn) pull-down, and western blot analyses using anti-Hipk antibodies and fluorescently labeled streptavidin to detect O-GlcNAc Hipk and O-GlcNAc modified proteins, respectively. Actin was used as a loading control. (**C**) Detection of O-GlcNAc-modified Hipk by GalNAz feeding and GlcNAz labeling (schematic diagram shown on the Left). Click chemistry was performed in protein lysates extracted from mock-fed or GalNAz-fed *dpp > hipk + ogt* larvae, followed by streptavidin (Strvn) pull-down and western blot analyses using anti-Hipk antibodies and fluorescently labeled streptavidin to detect O-GlcNAc/O-GlcNAz Hipk and O-GlcNAc/O-GlcNAz modified proteins, respectively. Actin was used as a loading control.

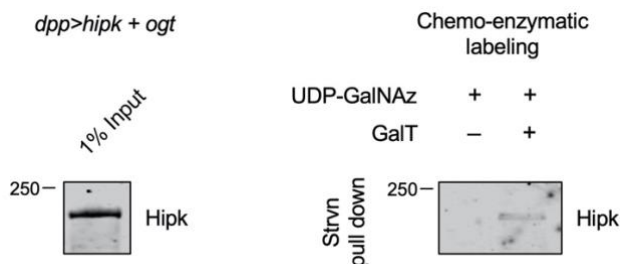


Figure 3.21. GalT selectively labels Hipk with UDP-GalNAz.

Western blot analyses of Hipk following chemoenzymatic labeling with or without GalT, and streptavidin (Strvn) precipitation using protein lysates from larvae co-expressing *hipk* and *ogt* (*dpp > hipk + ogt*) (input).

To corroborate the Galt labeling result, we adopted a metabolic feeding strategy (**Figure 3.20 C**) (Liu et al., 2017). Larvae co-expressing *hipk* and *ogt* were raised on food supplemented with either DMSO (control) or *N*-azidoacetylgalactosamine-tetraacylated (Ac₄GalNAz). After feeding, the precursor Ac₄GalNAz is converted *in vivo* through metabolism into UDP-GlcNAz (Boyce et al., 2011). As UDP-GlcNAz is a close analog of UDP-GlcNAc, OGT can use this substrate to transfer GlcNAz onto proteins, to generate O-GlcNAz (Boyce et al., 2011; Vocadlo et al., 2003). O-GlcNAz-modified proteins in the larval extracts were then chemoselectively coupled with a biotin-alkyne probe. Streptavidin pull-down followed by immunoblot analyses showed that Hipk was only present among the proteins precipitated from GalNAz-fed animals (**Figure 3.20 C**), further supporting Hipk being a substrate for OGT and being O-GlcNAc modified *in vivo*. Thus, our biochemical analyses confirm that *fly Hipk is an O-GlcNAc-modified protein*.

3.4.8. Elevated Hipk may activate the HBP-OGT metabolic pathway, forming a positive feedback loop

While OGT acts an upstream regulator of Hipk, governing Hipk's protein stability, O-GlcNAcylation and tumorigenic activity, we were also intrigued if OGT is a downstream target of Hipk to drive tumor growth. Interestingly, we observed a very mild upregulation of OGT in the *hipk*-overexpressing tumor cells (**Figure 3.22 C white arrowheads**), inferring that OGT may be a downstream target of Hipk. Recently, we reported that the Hipk tumor cells display elevated aerobic glycolysis driven by upregulation of Myc ([Wong et al., 2019](#)) (see **Chapter 5**). It is therefore tempting to speculate that the increased glucose metabolism could stimulate HBP flux and generate more UDP-GlcNAc for O-GlcNAcylation. Indeed, we observed robust O-GlcNAc signals in the Hipk tumor cells (**Figure 3.22 G white arrowhead**), indicative of stimulated flux in the HBP or activation of OGT. Depletion of OGT or Myc by RNAi markedly suppressed the O-GlcNAc robustness in the tumor cells as well as tumor growth (**Figure 3.22 H-I white arrowheads**).

Therefore, our data suggest that elevated Hipk promotes O-GlcNAcylation of intracellular proteins, likely through Myc-dependent increased glucose metabolism, mild OGT upregulation, or the combined effects. The upregulated OGT or O-GlcNAc may feedforward to sustain high Hipk protein levels and reinforce tumor growth.

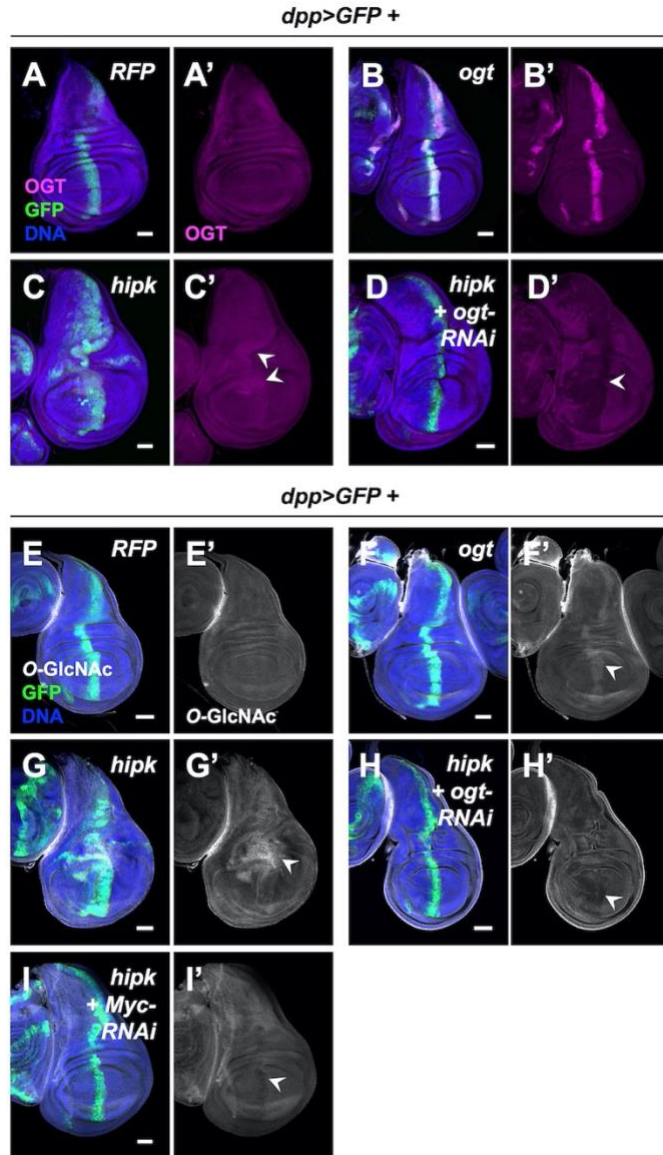


Figure 3.22. Hipk tumor cells display mild OGT upregulation and robust O-GlcNAc signals.

(A-D) Control (*dpp > GFP + RFP*) (A), *ogt*-overexpressing (*dpp > GFP + ogt*) (B), *hipk*-overexpressing (*dpp > GFP + hipk*) (C), *hipk* and *ogt*-*RNAi* co-expressing (*dpp > GFP + hipk + ogt-RNAi*) (D) wing discs stained for OGT (magenta). (E-I) Control (*dpp > GFP + RFP*) (E), *ogt*-overexpressing (*dpp > GFP + ogt*) (F), *hipk*-overexpressing (*dpp > GFP + hipk*) (G), *hipk* and *ogt*-*RNAi* co-expressing (*dpp > GFP + hipk + ogt-RNAi*) (H) and *hipk* and *Myc*-*RNAi* co-expressing (*dpp > GFP + hipk + Myc-RNAi*) (I) wing discs stained for O-GlcNAc (gray). (C) White arrowheads mark the relatively small increases in OGT levels in *hipk*-overexpressing cells. (D) White arrowhead marks a significant loss of OGT in *hipk* and *ogt*-*RNAi* co-expressing cells. (F-G) White arrowheads point to increases in O-GlcNAc levels. (H-I) White arrowheads point to decreases in O-GlcNAc levels. GFP (green) marks the transgene-expressing cells. DAPI staining for DNA (blue) shows the tissue morphology. Scale bars, 50 μ m.

3.4.9. HIPK2 O-GlcNAcylation by OGT promotes HIPK2 protein stability.

Our observations in *Drosophila* indicate that Hipk is a direct target protein for OGT and that OGT is required to modulate Hipk protein stability and Hipk-induced tissue growth abnormalities. To see whether the regulation of Hipk by OGT is conserved across species, we extended our analyses to human HIPK2 using cultured mammalian cells.

We transfected human embryonic kidney (HEK) 293 cells with OGT and found accumulation of exogenous HIPK2 proteins (**Figure 3.23 A**). Comparable results were obtained in MCF7 breast adenocarcinoma cells and mouse embryonic fibroblasts (MEFs), independent of the tags used to label the exogenous HIPK2. Next, using an MEF cell line where OGT knockout can be induced by administration of 4-hydroxytamoxifen (4HT) (Kazemi et al., 2010), we found that loss of OGT correlated with loss of HIPK2 (**Figure 3.23 B**). Notably, no statistically significant changes in endogenous HIPK2 mRNA levels were found in HEK293 and MEF cells upon genetic manipulation of OGT levels (**Figure 3.24 A, C**). In MCF7 cells, however, OGT induced HIPK2 transcriptional up-regulation (**Figure 3.24 B**). Together, our data suggest that, whereas OGT generally promotes HIPK2 protein buildup post-transcriptionally, the transcriptional response of HIPK2 to OGT seems to be cell-type specific.

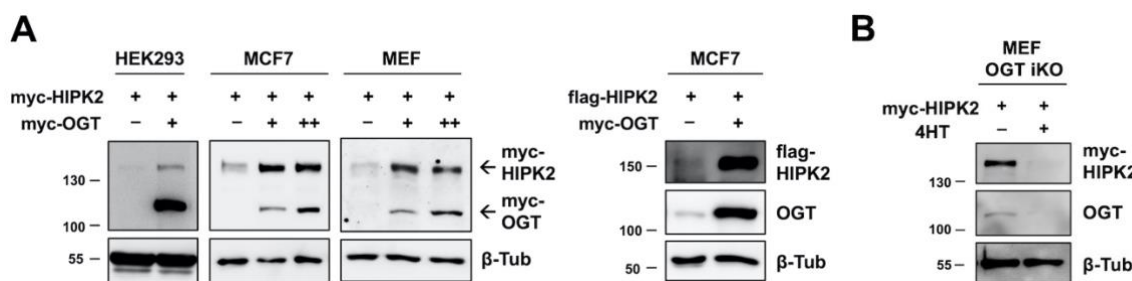


Figure 3.23. OGT modulates HIPK2 protein levels in mammalian cells.

(A) Increasing amounts of myc-tagged OGT were co-transfected with myc- or flag-tagged HIPK2 in HEK293, MCF7, and/or MEF cell lines. 48 hours after transfection, protein levels of HIPK2 and OGT were analyzed by Western blotting using anti-myc antibodies, anti-flag antibodies and anti-OGT antibodies. β-Tubulin was used as a loading control. (B) myc-tagged HIPK2 was transfected in mock (methanol)-treated or 4-hydroxytamoxifen (4HT)-treated MEF cells (an OGT inducible knockout [iKO] strain). 48 hours after transfection, protein levels of myc-tagged HIPK2 were analyzed by Western blotting using anti-myc

antibodies. OGT knockout efficiency was evaluated by examining the endogenous OGT levels. β -Tubulin was used as a loading control.

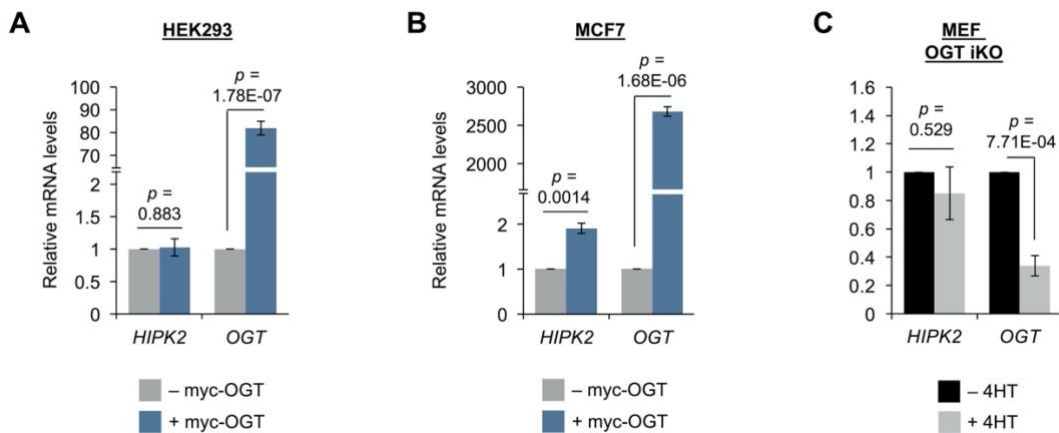


Figure 3.24. Effects of OGT on the HIPK2 transcript levels.

(A) qRT-PCR analyses of *HIPK2* and *OGT* mRNA levels in HEK293 cells transfected with mock or myc-OGT. **(B)** qRT-PCR analyses of *HIPK2* and *OGT* mRNA levels in MCF7 cells transfected with mock or myc-OGT. **(C)** qRT-PCR analyses of *HIPK2* and *OGT* mRNA levels in an MEF OGT inducible knockout (iKO) cell line treated with mock or 4HT. *p* values were calculated using unpaired two-tailed Student's *t*-test.

We next mapped the positions of O-GlcNAc modification on HIPK2 purified from transfected HEK293 cells, which were treated with Thiamet-G, an OGA selective inhibitor (Yuzwa et al., 2008), to stabilize O-GlcNAc modifications and facilitate mapping sites of modification. By using higher energy collision dissociation (HCD) product-ion triggered electron transfer/higher energy collision dissociation (EThcD) tandem mass spectrometry (MS/MS) analyses, we identified three O-GlcNAc-modified peptides containing five putative OGT target sites (S852, T853, S1008, T1009, and S1147) (Figure 3.25, Figure 3.26). Subsequent analyses confirmed that S852, T1009, and S1147 are O-GlcNAc modified (Figure 3.26 B-D). All of the sites identified are located outside of the kinase domain (Figure 3.25). S852 and T853 are within a conserved PEST region implicated in protein stability and S1147 within the YH protein interaction domain (sometimes referred to as an auto-inhibitory region AID) (Blaquiere and Verheyen, 2017). Notably, these sites are conserved among mammals (Figure 3.27).

Peptide 1 (S852/T853): CAMVHSSPACS**TSVTCGWDVASSSTTR**
Peptide 2 (S1008/T1009): SSSNVT**STSGHSSGSSSGAITYR**
Peptide 3 (S1147): HTVQHTAYPASIVHQVPVS**MGPR**

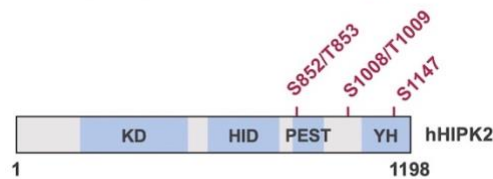


Figure 3.25. O-GlcNAc sites in human HIPK2.

Mass spectrometry analyses revealed three O-GlcNAc-modified peptides of HIPK2. O-GlcNAc sites identified by MS are shown in dark red. Schematic diagram of the human HIPK2 protein (amino acids 1 to 1198) with its domains. KD, kinase domain; HID, homeobox-interacting domain; PEST, proline, glutamic acid, serine, and threonine-rich domain; YH, tyrosine, histidine-rich domain (also known as auto-inhibitory domain [AID]).

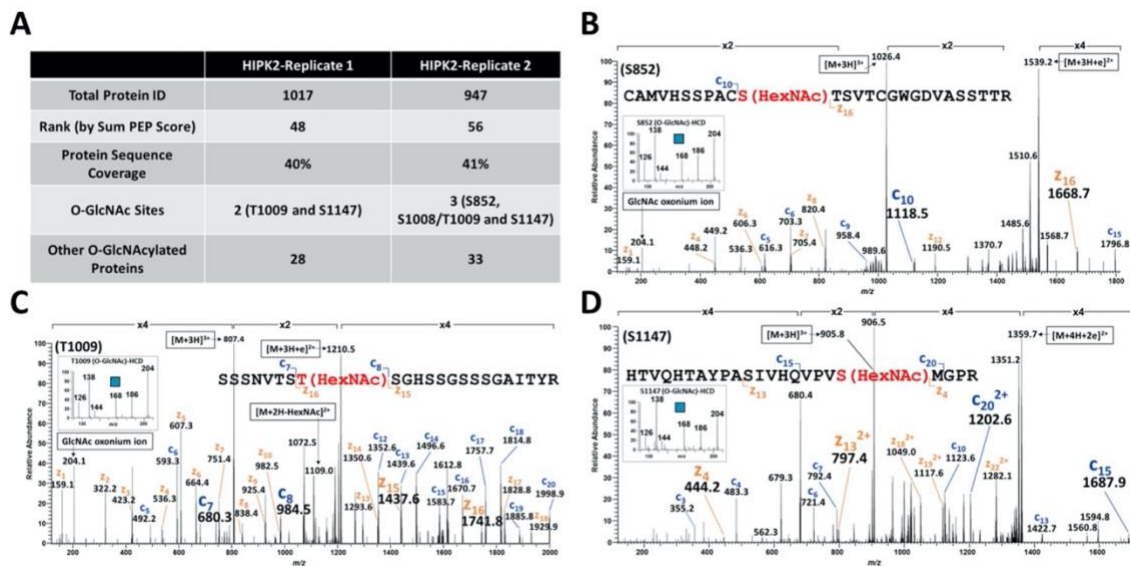


Figure 3.26. HIPK2 is O-GlcNAcylated at multiple serine and threonine residues.

(A) Summary of the mass spectrometry results showing protein coverage and identification of O-GlcNAc sites (S852/T853, S1008/T1009 and S1147) obtained from two biological samples of purified HIPK2. **(B-D)** Representative EThcD MS/MS spectra for the three different O-GlcNAc modified HIPK2 peptides identified. The accompanying HCD MS/MS data each afforded the low mass characteristic ions that further identified the HexNAc as GlcNAc (insets).

Entry	Species	Peptide 1 (S852, T853)	Peptide 2 (S1008, T1009)	Peptide 3 (S1147)
Q9H2X6	Human	CAMVHSSPAC S TSGCGWGDVASSTR	SSSNVT S TGHSSGSSSSGA I TYR	HTVQHTAYPASIVHQVPV S MGPR
Q9QZ5	Mouse	CAMVHSSPAC S TSGCGWGDVASSTR	SSST V T S TGHSSGSSSSGA I YR	HTVQHTAYPASIVHQVPV S MGPR
Q9WUM7	Golden hamster	CAMVHSSPAC S TSGCGWGDVASSTR	SSST V T S TGHSSGSSSSGA I YR	HTVQHTAYPASIVHQVPV S MGPR
D3ZN85	Rat	CAMVHSSPAC S T L TGCGWGD G ASSTR	SSST V T S TGHSSGSSSSGA I YR	HTVQHTAYPASIVHQVPV S MGPR
H2QVH2	Chimpanzee	CAMVHSSPAC S TSGCGWGDVASSTR	SSSNVT S TGHSSGSSSSGA I TYR	HTVQHTAYPASIVHQVPV S MGPR
F1PR67	Dog	CALVHSSPAC S SSVTCGWD G ASSTR	SSSNVT S TGHSSGSSSSGA I YR	HTVQHTAYPASIVHQVPV S MGPR
F6XB80	Horse	CALVHSSPAC S SSVTCGWD G ASSTAR	SSSNVT S TGHSSGSSSSGA V YR	HTVQHTAYPASIVHQVPV S MGPR
H0VQ0	Guinea pig	CAMAHSSPAC S AVTCGWD G ASSTR	SSSNVT S TGHSSGSSSSGA I YR	HTVQHTAYPASIVHQVPV S MGPR
S6BAK9	Zebrafish	No similar peptides found	No similar peptides found	HAVQHASYPPGIVHQVPV S MGHR
Q9W0Q1	Fruit fly	No similar peptides found	No similar peptides found	PPLQVPPQQYVNVPVPV S MVEP

Figure 3.27. The O-GlcNAc sites in HIPK2 are highly conserved in mammals.

Searches and alignments of the O-GlcNAc sites (S852/T853, S1008/T1009 and S1147) in human HIPK2 with other species. The O-GlcNAc sites are labeled in red. In simpler organisms like zebrafish and fruit fly, only S1147 seems conserved. Conserved residues are labeled in grey, and non-conserved residues in brown.

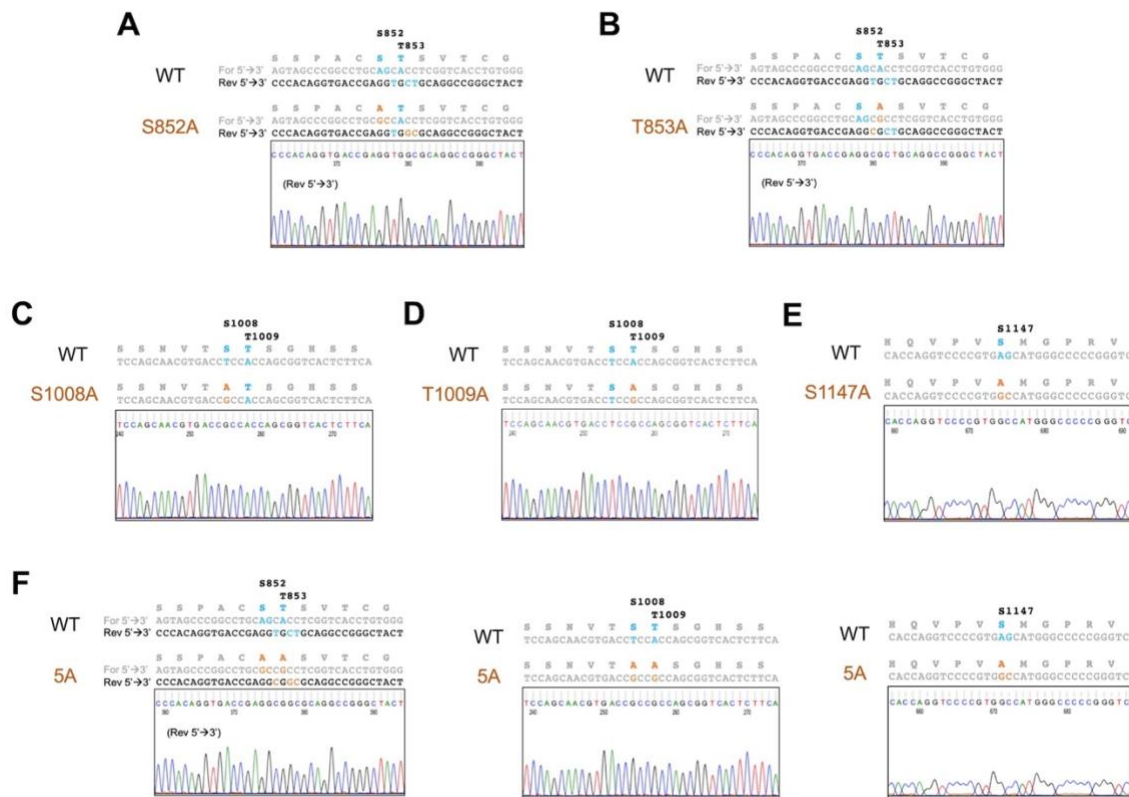


Figure 3.28. Replacements of HIPK2 O-GlcNAc sites by alanine are confirmed by sequencing.

Sequencing data confirm the replacements of O-GlcNAc modified serine and threonine sites by alanine residues in individual single alanine mutants (**A-E**) and a quintuplet alanine (**5A**) mutant (**F**). Wild-type O-GlcNAc modified residues and the corresponding nucleotides are shown in light blue; replaced residues/mutated nucleotides in brown.

To assess the functional relevance of HIPK2 O-GlcNAcylation, we replaced these serine and threonine residues with alanine by site-directed mutagenesis. Since we could not definitively rule out that all five residues are targets of OGT, we mutated the three confirmed (S852, T1009, and S1147) and two adjacent sites (T853 and S1008) to alanine to address the possibility of these sites being modified. Individual single alanine mutants and a quintuplet alanine (5A) mutant were generated (Figure 3.28). WT HIPK and the mutants would be expressed under the control of the same promoter. We found that while WT HIPK2 was weakly expressed (Figure 3.29 D lane 1), the mutants were expressed below detectable limits (Figure 3.29 D lanes 2-7). Even in the presence of MG132 (used to impair proteasomal degradation), the mutants were expressed at reduced levels when compared with WT HIPK2 (Figure 3.29 D lanes 8-14).

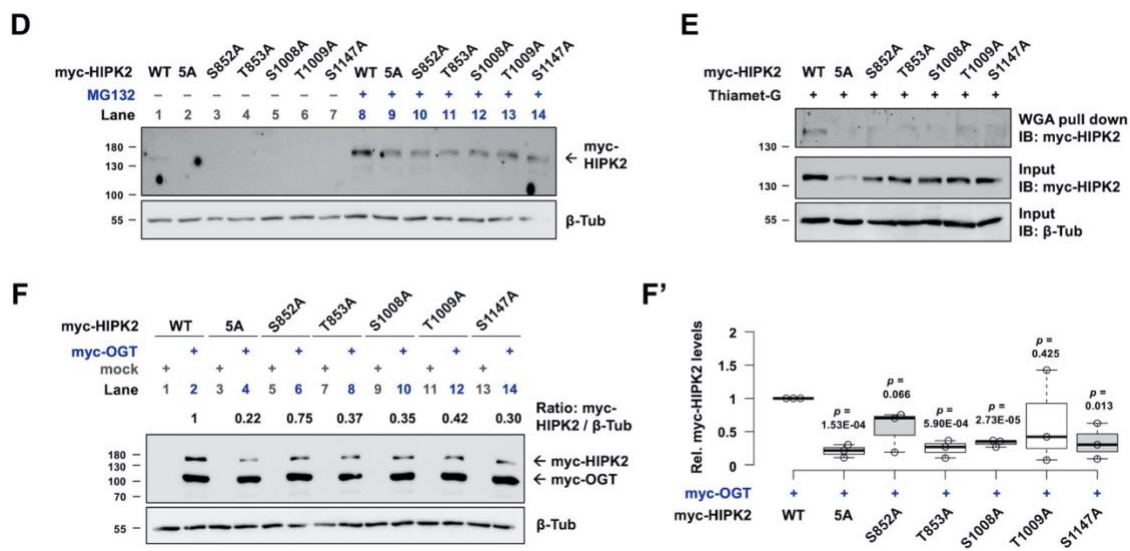


Figure 3.29. HIPK2 O-GlcNAcylation by OGT promotes HIPK2 protein stability.

(D) WT or alanine mutant variants of myc-tagged HIPK2 were transfected in HEK293 cells. 24 hours after transfection, indicated cells were treated with MG132. 48 hours after transfection, protein levels of myc-tagged HIPK2 were analyzed by western blotting using anti-myc antibodies. β-Tubulin was used as a loading control. (E) Detection of O-GlcNAc levels of HIPK2. HEK293 cells were transfected with WT or alanine mutant variants of myc-tagged HIPK2 and treated with Thiamet-G. O-GlcNAc-modified proteins were pulled down by WGA-conjugated beads. myc-tagged HIPK2 in the precipitates and in the input were analyzed by western blotting. β-Tubulin was used as a loading control. (F-F') WT or alanine mutant variants of myc-tagged HIPK2 were co-transfected with mock or myc-tagged OGT as indicated. 48 hours after transfection, protein levels of myc-tagged HIPK2 and OGT were analyzed by Western blotting using anti-myc antibodies. β-Tubulin was used as a loading control. (F') A box and whisker plot showing the relative protein levels of the WT or alanine mutant variants of myc-tagged HIPK2 in the presence of myc-OGT co-transfection. Data are pooled from three biological replicates. *p* values showing the significant differences between

the WT and the mutant protein levels were calculated using unpaired two-tailed Student's *t*-test.

To determine the O-GlcNAc states of WT HIPK2 and the mutants, we used higher concentrations of plasmids for transfection, combined with Thiamet-G treatment to prevent the removal of O-GlcNAc modifications. Using wheat germ agglutinin (WGA) to selectively pull down O-GlcNAc-modified proteins, we found that WT HIPK2, unlike the alanine mutants, was readily detectable in the precipitates (**Figure 3.29 E**), indicating that the serine and threonine residues identified by MS can be O-GlcNAc modified and losses of these residues rendered HIPK2 more resistant to O-GlcNAcylation.

If the O-GlcNAc sites identified are responsible for maintaining HIPK2 protein stability through OGT, we would expect the mutants to be less responsive to OGT-mediated stabilization. Strikingly, OGT overexpression had much reduced effects on the stabilization of the mutants when compared with WT HIPK2 (**Figure 3.29 F even-numbered lanes, F'**). Nevertheless, all mutant variants, like WT HIPK2, could be stabilized to some extent by OGT (**Figure 3.29 F compare even- with odd-numbered lanes**), suggesting the presence of additional, not yet identified, OGT-mediated mechanisms contributing to HIPK2 stability. These data point to the importance of *direct O-GlcNAcylation of HIPK2 in the positive regulation of HIPK2 protein stability by OGT*.

3.5. Discussion

Cancer cells often vigorously consume glucose, aided by metabolic reprogramming involving multiple processes, for example, elevated expression of glucose transporters (Hsu and Sabatini, 2008). Notably, an ample supply of glucose not only facilitates aerobic glycolysis within tumors, but also drives increased flux through parallel pathways, including the HBP (Ma and Vosseller, 2014). As a consequence, increased levels of UDP-GlcNAc and subsequent hyper-O-GlcNAcylation are found in nearly all cancers examined, including breast, prostate, colon, lung, liver, pancreatic, and leukemias (Ferrer et al., 2016). Indeed, global O-GlcNAcylation is emerging as a node linking glucose availability and cancer progression (Ferrer et al., 2016).

The link between dietary sugar and increased tumorigenesis is found to be conserved in *Drosophila* (Eichenlaub et al., 2018; Hirabayashi et al., 2013; Hirabayashi and Cagan, 2015). Using various fly cancer models, researchers have shown that excess sugar intake affects cancer progression through multiple pathways. For example, high dietary sugar has been shown to drive the malignancy of Ras/Src tumors and neoplasia of EGFR-driven tumors through evasion of insulin resistance and aerobic glycolysis, respectively (Eichenlaub et al., 2018; Hirabayashi et al., 2013; Hirabayashi and Cagan, 2015). The involvement of hexosamine signaling in fly tumorigenesis, however, has not been explored. Here we report that the activity of Hipk, a proliferation-promoting protein in flies, is controlled by the HBP-OGT axis in response to metabolic nutrients (Figure 3.3, Figure 3.6). Using the fly Hipk tumor-like model, we demonstrate that OGT is both necessary and sufficient for Hipk-induced growth abnormalities (Figure 3.8, Figure 3.9, Figure 3.11, Figure 3.13, Figure 3.14). Thus, our work defines the HBP-OGT axis as a glucose-dependent mechanism regulating Hipk-mediated growth control. This is consistent with several mammalian studies of O-GlcNAc-dependent regulation of growth-promoting proteins such as YAP (Peng et al., 2017; X. Zhang et al., 2017).

Although Hipk proteins are proposed to be maintained at low levels through degradation by the proteasomal machinery, minimal amounts of Hipk are indispensable for normal growth and development as flies homozygous mutant for *hipk* are not viable (Lee et al., 2009a). This hints at the existence of cellular mechanisms that oppose Hipk protein degradation. Our work demonstrates that OGT stabilizes both endogenous and

exogenous Hipk and protects Hipk from proteasomal degradation ([Figure 3.15](#), [Figure 3.17](#), [Figure 3.18](#)). We confirm that fly Hipk is an O-GlcNAc-modified protein ([Figure 3.20](#)). While the fly Hipk O-GlcNAc motifs and their roles remain unknown, we show that OGT-mediated stabilization of human HIPK2 relies on direct O-GlcNAcylation of HIPK2 at residues S852/T853, S1008/T1009, and S1147 ([Figure 3.25](#), [Figure 3.26](#)). Our report describes HIPK2 O-GlcNAcylation as a molecular mechanism that controls HIPK2 protein stability ([Figure 3.29](#)). Given the nutrient-sensing nature of O-GlcNAc, it is conceivable that HIPK2 O-GlcNAcylation might contribute to the nutrient sensitivity of HIPK2 abundance. Intriguingly, a study shows that HIPK2 protein levels increased in a mouse model of diabetes, and the authors attributed the effect to down-regulation of the E3 ubiquitin ligase SIAH-1 ([Oh et al., 2016](#)). Hence, the nutritional regulation of HIPK2 might be achieved by multiple strategies like direct O-GlcNAcylation and impairment of proteasome system, or their cooperative effects.

In summary, our work illustrates the conserved regulation of HIPK (fly Hipk and human HIPK2) protein stability by OGT and demonstrates the functional consequences of this regulation in tumor-like events using an *in vivo* fly model. The roles of human HIPK2 in cancers are context dependent and yet to be fully understood. On the one hand, HIPK2 activates the tumor suppressor p53 after UV irradiation ([D’Orazi et al., 2002](#); [Hofmann et al., 2002](#)). Also, HIPK2 acts as a tumor suppressor upon induction of two-stage skin carcinogenesis ([Wei et al., 2007](#)) or γ -radiation-induced tumorigenesis ([Mao et al., 2012](#)). On the other hand, HIPK2 promotes cytoprotection in cancer cells when challenged with chemotherapeutic drugs ([Torrente et al., 2017](#)). Elevation of HIPK2 is also associated with malignancy of pilocytic astrocytomas ([H Deshmukh et al., 2008](#)) and cervical carcinogenesis ([Al-Beiti and Lu, 2008](#)). These results raise concerns that targeting HIPK2 may have paradoxical effects. Elevated HIPK2 is also implicated in fibrosis in kidney ([Jin et al., 2012](#)), lung ([Ricci et al., 2013](#)), and liver ([He et al., 2017](#)). Thus, depending on the context, we believe that the dynamic control of HIPK2 abundance by O-GlcNAc modification reported in our study can be of great interest and exploited in the treatment of HIPK2-related disorders with the use of dietary control or metabolic drugs targeting the HBP-OGT axis.

Chapter 4.

Insulin-InR-SIK2 signaling regulates Hipk phosphorylation and tumorigenic activity.

The work shown in **Chapter 4** is unpublished.

4.1. Contributions to the Chapter

SIK2 is identified as a potential Hipk regulator through an *RNAi* screen conducted by Jessica Blaquiere and Rubia Chung. Further investigations were done by Kenneth Kin Lam Wong and Jessica Parker, and the analysis of data by Landiso Madonsela and Devon Chohan.

4.2. Abstract

Feeding *Drosophila* with a high sucrose diet leads to hyperglycemia and hyperinsulinemia. Our previous work demonstrates that this nutrient-rich condition enhances Hipk activity to induce tissue growth abnormalities, and that the nutrient sensor O-GlcNAc transferase (OGT) directly modifies Hipk with O-GlcNAc and synergizes with Hipk to induce tumorigenesis. Here, we find a distinct mode of nutritional regulation of Hipk – phosphorylation and activation of Hipk through the insulin-sensing signaling involving the insulin receptor (InR) and salt-inducible kinase 2 (SIK2). Acute and chronic stimulation of insulin/InR causes Hipk hyper-phosphorylation in a SIK2 kinase activity-dependent manner. InR-SIK2 signaling synergizes with Hipk, accelerating tumor progression. Notably, Hipk in turn upregulates InR transcriptionally and activates InR signaling, forming a positive feedback loop that may evade insulin insensitivity. Further studies will analyze how SIK3, another SIK protein kinase, interacts with SIK2 in modulating the nutritional regulation of Hipk.

4.3. Introduction

Obesity is becoming more prevalent worldwide, increasing a person's risks of developing type 2 diabetes as well as several types of cancers ([Giovannucci et al., 2010](#)). However, the mechanisms that link obesity and tumorigenesis remain poorly understood. *Drosophila* fed with high sucrose diet (HSD) displays features reminiscent of an obese person, such as hyperglycemia and hyperinsulinemia ([Musselman et al., 2011](#)). Thus, *Drosophila* is an effective tool to examine the influence of diet on animal physiology.

SIK is a serine/threonine protein kinase belonging to the adenosine monophosphate (AMP)-activated protein kinase (AMPK) family ([Wang et al., 1999](#)). Mammals have SIK1-3; in flies, only SIK2 (mammalian ortholog of SIK1 and SIK2) and SIK3 are present ([Okamoto et al., 2004](#)). The activities of SIKs are under hormonal control. Under fed conditions, stimulated insulin receptor phosphorylates downstream kinase AKT, which activates SIKs ([Wang et al., 2011, 2008](#)). Conversely, during starvation, glucagon signals through a G-protein coupled receptor and protein kinase A (PKA), inhibiting SIKs ([Wang et al., 2011, 2008](#)). Downstream of SIKs, effectors mediate expression of metabolic programs, including gluconeogenesis, glycogen and fat storage

(Wang et al., 2011, 2008). In addition to metabolic roles, SIKs are found to be negative modulators of Hippo signaling pathway (Wehr et al., 2013). Phosphorylation of Salvador (Sav) by SIKs leads to dissociation of the Hippo/Warts core kinases complex, activating the downstream transcriptional effector, Yorkie (Yki) (Wehr et al., 2013).

Previously, our lab conducted *in vivo* RNAi screens in *Drosophila* to search for novel regulators of Homeodomain-interacting protein kinase (Hipk) and identified SIK2 as a potential Hipk regulator (Jessica Blaquiere and Rubia Chung, unpublished). We previously reported that a high sucrose diet potentiates Hipk activity and the nutrient responsiveness of Hipk is mediated by the hexosamine biosynthetic pathway (HBP) and the downstream O-GlcNAc transferase (OGT) (Wong et al., 2020) (see Chapter 3). These findings prompt us to ask is SIK2 functions as an additional nutrient sensor for Hipk activity.

4.4. Results

4.4.1. The high sugar effect on Hipk activity depends on InR and SIKs

The use of a high sucrose diet (HSD) is a well-established *Drosophila* model for type 2 diabetes, featuring chronic hyperglycemia as well as hyperinsulinemia (Musselman et al., 2011). Previously, we found that a high sucrose diet enhances Hipk activity through the HBP and OGT (see Chapter 3). Given that hyperinsulinemia is one of the characteristics of type II diabetes, we asked whether InR-SIK signaling is involved in mediating the high sugar effects on Hipk activity.

Interestingly, silencing of *SIK2* using RNAi strongly suppressed the sugar effect on Hipk-mediated malformed leg phenotype (Figure 4.1 A-B). Knockdown of *SIK3* using *SIK3-RNAi* (II) only weakly reversed the severity of the high sugar diet-induced malformed leg phenotype in *hipk*-overexpressing flies (Figure 4.1 C). Co-expression of an independent RNAi targeting *SIK3* (*SIK3-RNAi* (III)), on the other hand, moderately suppressed the sugar effect (Figure 4.1 D). The variation could possibly be due to a difference in the knockdown efficiency of the two RNAi lines. Knockdown of *InR* in *hipk*-expressing cells partially abolished the effects of high sucrose on Hipk-mediated leg phenotype (Figure 4.1 F), phenocopying the effect of *SIK3-RNAi* (III). Surprisingly, double knockdown using a single RNAi line targeting both *SIK2* and *SIK3* (*SIK2/3-RNAi*) in the *hipk*-overexpressing flies fed with HSD led to a higher frequency of severe leg malformation phenotype, indicative of enhanced Hipk activity (Figure 4.1 E). Quantifications of the malformed leg phenotype were performed by scoring the number of malformed legs per fly (Figure 4.1 G) and the severity of the malformed leg phenotype (Figure 4.1 H). Together, our data imply that *the high sugar effect on Hipk-induced leg malformation can be modulated by the InR-SIK signaling*.

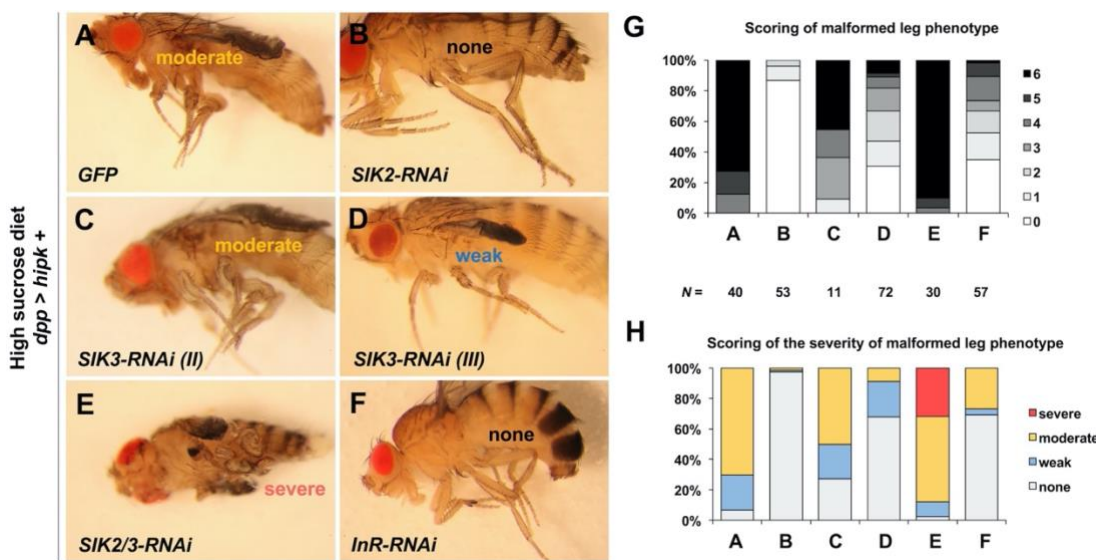


Figure 4.1. High dietary sugar modulates Hipk-mediated leg malformation phenotype through InR and SIKs.

Adults of the indicated genotypes were raised on high sucrose diet (HSD, 1 M sucrose) at 25°C since birth. Transgenes were expressed under the control of *dpp-Gal4* driver. **(A)** Adult legs of *hipk*-overexpressing flies with co-expression of *GFP* (**A**), *SIK2-RNAi* (**B**), *SIK3-RNAi (II)* (**C**), *SIK3-RNAi (III)* (**D**), *SIK2/3-RNAi* (**E**) or *InR-RNAi* (**F**). **(G)** Quantification of the leg malformation phenotype by counting the number of malformed legs per fly. **(H)** Quantification of the leg malformation by scoring the severity of the malformation leg phenotype. *N* refers to the numbers of flies counted in the corresponding genotypes.

4.4.2. Insulin-InR signaling induces Hipk hyper-phosphorylation

Next, we hypothesized that the enhanced Hipk activity induced by high sucrose diet is due to high insulin levels. To ask whether Hipk could respond to insulin stimulation, we used an *ex vivo* culture approach. Larval tissues including imaginal discs and salivary glands were dissected from *hipk*-overexpressing larvae (*dpp* > *hipk*) and cultured in media supplemented with recombinant human insulin. Upon the insulin treatment, we detected robust phosphorylated AKT S505 (p-AKT) signals in western blotting ([Figure 4.2 A-B compare lane 1 with the other lanes in p-AKT blots](#)). tGPH is an *in vivo* GFP-based reporter for PI3K activity by encoding a GFP-PH fusion protein under the control of *tubulin* promoter ([Britton et al., 2002](#)). When activated PI3K converts PIP₂ to PIP₃, PIP₃ recruits tGPH to the plasma membrane by binding to its PH domain. In our *ex vivo* culture assay, we observed the insulin treatment caused a re-distribution of tGPH from cytosol or nucleus to the plasma membrane, indicative of elevated PI3K activity ([Figure 4.3](#)). Together, these two readouts (p-AKT and tGPH) confirmed that the recombinant human insulin is capable of activating InR-PI3K-AKT signaling in fly tissues.

More importantly, when insulin (1 μM) was added to the cultured media, we found Hipk proteins migrated slower during electrophoresis and manifested mobility upshift over time ([Figure 4.2 A](#)). At 0 μM, the majority of the Hipk proteins remained unshifted ([Figure 4.2 A-B lane 1](#)). An increase in the insulin concentration led to an increase in the fraction of upshifted Hipk proteins ([Figure 4.2 B lanes 2-6](#)). Lambda phosphatase (λ Ppase) treatment confirmed that the Hipk protein band shift was due to Hipk hyper-phosphorylation upon insulin stimulation ([Figure 4.2 C](#)). Therefore, the insulin-dependent gradual change in the shifting migration pattern ([Figure 4.2 B lanes 2-6](#)) implies the presence of more than one phosphorylation site on Hipk. The prominent AKT phosphorylation preceded Hipk protein upshift in both assays ([Figure 4.2 A-B](#)), suggesting that the two events may have different kinetics and/or that phosphorylation of Hipk is a downstream event of AKT phosphorylation.

To mimic the stimulation of insulin, we used fly genetics to activate InR signaling to evaluate its effects on Hipk activity. We found that co-expression of a constitutively active form of InR (InR-CA, also known as InR-A1325D) in *hipk*-expressing cells also led to Hipk protein mobility upshift, which could be reversed by the λ Ppase treatment ([Figure](#)

4.2 D). Thus, our data indicate that both insulin stimulation and activated InR signaling can induce Hipk hyper-phosphorylation.

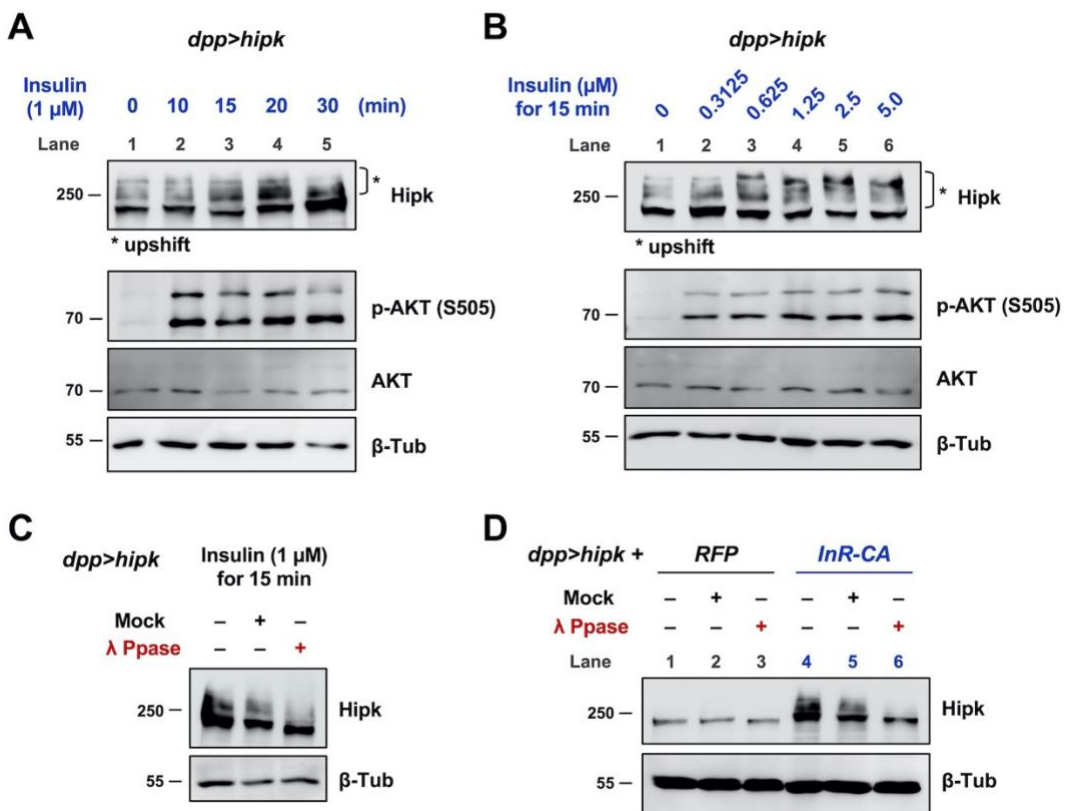


Figure 4.2. Insulin and InR signaling induce Hipk hyper-phosphorylation.

(A) Western blot analyses of Hipk, p-AKT (S505), AKT and β-Tubulin (β-Tub) in dissected larval tissues overexpressing *hipk* (*dpp > hipk*) treated with recombinant human insulin at 1 μM for the indicated times. **(B)** Western blot analyses of Hipk, p-AKT, AKT and β-Tub in dissected larval tissues overexpressing *hipk* (*dpp > hipk*) treated with insulin at the indicated concentrations for 15 minutes. **(C)** Western blot analyses of Hipk and β-Tub from untreated, mock (buffer only)-, Lambda phosphatase (λ Ppase)-treated cell lysates obtained from larval head tissues overexpressing *hipk* (*dpp > hipk*) treated with insulin at 1 μM for 15 minutes. **(D)** Western blot analyses of Hipk and β-Tub from untreated, mock-, λ Ppase-treated cell lysates obtained from *dpp > hipk + RFP* and *dpp > hipk + InR-CA* larval head tissues.

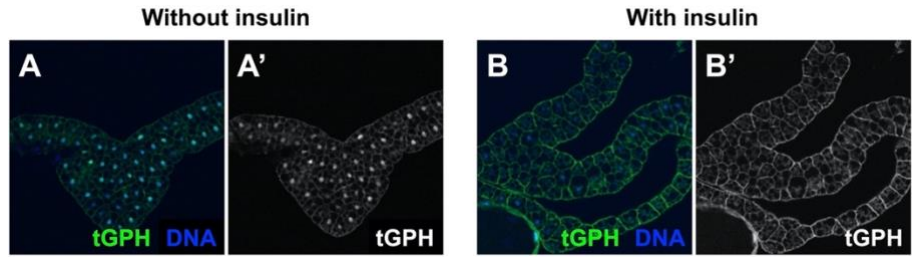


Figure 4.3. Recombinant human insulin causes the recruitment of tGPH to the plasma membrane.

Wild-type larval fat tissues were dissected and cultured in media without (**A**) or with insulin treatment (**B**). The tissues harbor a reporter for PI3K activity, tGPH (green in **A-B**; grey in **A'-B'**). DAPI staining for DNA (blue) marks the nuclei.

4.4.3. The insulin-InR effect on Hipk phosphorylation is SIK2-dependent

Given that SIK activities can be modulated by InR signaling, we tested whether SIK2 is required for Hipk hyper-phosphorylation induced by insulin-InR signaling.

Using the *ex vivo* culture approach, we found that, whereas insulin induced Hipk protein mobility upshift (**Figure 4.4 A lanes 1-2**), the shift is abolished when *SIK2-RNAi* (VDRC) was co-expressed (**Figure 4.4 A compare lane 4 with lane 2**). A comparable result was observed when another independent RNAi line (*SIK2-RNAi* (BL)) was co-expressed; the majority of Hipk proteins remained unshifted even in the presence of insulin stimulation (**Figure 4.4 B compare lane 4 with lane 2**). Thus, the reverse in the mobility shift upon *SIK2-RNAi* co-expression is unlikely due to off-target effects of the RNAi lines used. Similarly, activation of InR signaling failed to cause the Hipk protein mobility upshift when *sik2-RNAi* was co-expressed (**Figure 4.4 C**).

Together, our data suggest that insulin-InR-SIK2 may serve as a module to regulate Hipk phosphorylation states in response to the metabolic states in flies.

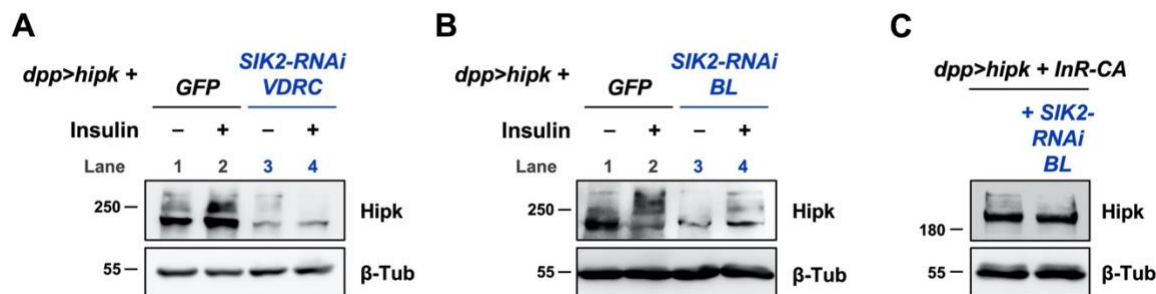


Figure 4.4. The insulin-InR effect on Hipk phosphorylation is SIK2-dependent.

Flies were raised at 25°C. **(A)** Western blot analyses of Hipk and β-Tub in dissected larval tissues overexpressing *hipk* without (*dpp > hipk + GFP*) or with SIK2 knockdown (*dpp > hipk + SIK2-RNAi* VDRC #26497) treated with mock (PBS) or insulin at 1 μM for 15 minutes. **(B)** Western blot analyses of Hipk and β-Tub in dissected larval tissues overexpressing *hipk* without (*dpp > hipk + GFP*) or with SIK2 knockdown (*dpp > hipk + SIK2-RNAi* BL #55880) treated with mock (PBS) or insulin at 1 μM for 15 minutes. **(C)** Western blot analyses of Hipk and β-Tub in dissected larval tissues co-expressing *hipk* and *InR-CA* without (*dpp > hipk + InR-CA*) or with SIK2 knockdown (*dpp > hipk + InR-CA + SIK2-RNAi* BL #55880).

4.4.4. SIK2 binds to Hipk and induces Hipk hyper-phosphorylation

Using co-immunoprecipitation (co-IP) assays, we found that Hipk immunoprecipitated with myc-tagged SIK2 in protein extracts collected from larvae co-expressing *hipk* and *myc-SIK2-WT* (*dpp > hipk + myc-SIK2-WT*) (Figure 4.5 A). A reciprocal co-IP confirmed a physical interaction between Hipk and SIK2 (Figure 4.5 B).

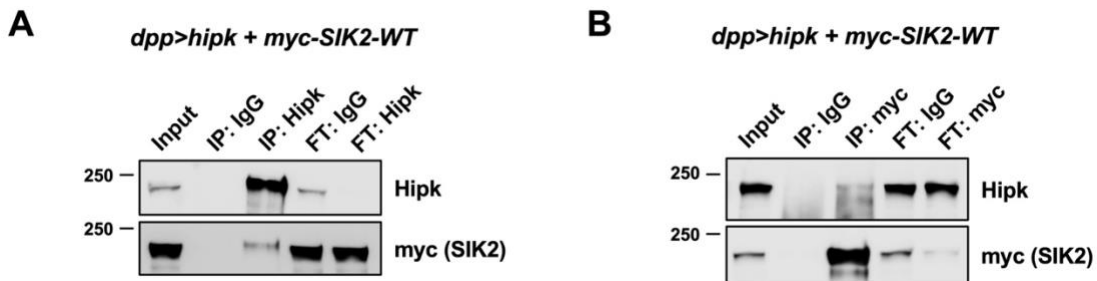


Figure 4.5. SIK2 physically interacts with Hipk.

Flies were raised at 25°C. (A-B) Protein lysates extracted from *dpp > hipk + myc-SIK2-WT* larval heads were incubated with either IgG or anti-Hipk antibodies, followed by co-immunoprecipitation (co-IP). Western blot analyses using anti-Hipk and anti-myc antibodies showing that Hipk coimmunoprecipitated with myc-tagged SIK2 proteins (A). Reciprocal IP showing that myc-tagged SIK2 coimmunoprecipitated with Hipk (B). FT: flow-through.

Next, we addressed if SIK2 could induce Hipk hyperphosphorylation. Overexpression of the wild-type SIK2 (SIK2-WT), but not the kinase-dead form (SIK2-KD, also known as SIK2-K170M), led to Hipk protein mobility upshift (Figure 4.6 C). Notably, sodium fluoride (NaF), which is a serine and/or threonine phosphatase inhibitor (Shenolikar and Nairn, 1991), enhanced the intensity of the Hipk band upshift in the larval extracts co-expressing *hipk* and SIK2-CA (a constitutively active form of SIK2, also known as SIK2-S1032A) (Figure 4.6 D compare lane 4 with lane 1), whereas λ Ppase treatment abolished the upshift (Figure 4.6 D compare lane 6 with lane 5). This demonstrates that the band shift is due to phosphorylation events. Together, our data suggest that SIK2, either directly or indirectly, modulates Hipk phosphorylation and this effect is dependent on SIK2 kinase activity.

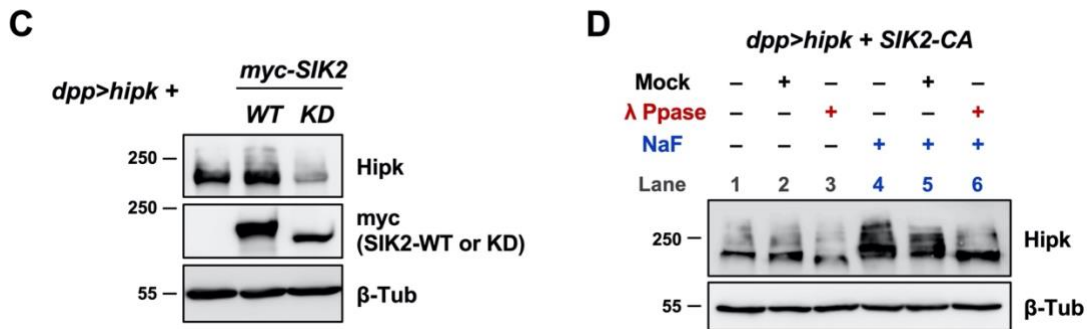


Figure 4.6. SIK2 induces Hipk hyper-phosphorylation.

Flies were raised at 25°C. **(C)** Western blot analyses of Hipk, myc-tagged SIK2 (WT or KD) and β -Tub in dissected larval tissues of the indicated genotypes: *dpp > hipk + GFP*, *dpp > hipk + myc-SIK2-WT* and *dpp > hipk + myc-SIK2-KD*. **(D)** Western blot analyses of Hipk and β -Tub from untreated, mock-, λ Ppase-treated cell lysates obtained from *dpp > hipk + SIK2-CA* larval head tissues.

4.4.5. InR-SIK2 signaling synergizes with Hipk to drive tumor growth

So far, we gathered evidence that high sugar enhanced Hipk activity at least in part through InR-SIK signaling (**Figure 4.1**) and that insulin-InR-SIK2 signaling induces Hipk hyper-phosphorylation (**Figure 4.2**, **Figure 4.4**, **Figure 4.6**).

We next evaluated if Hipk genetically interacts with InR-SIK2 signaling in larval wing discs under normal diet conditions. Transgene-expressing domains were marked by GFP. All larvae were raised at 25°C such that the exogenous Hipk levels (*dpp > GFP + hipk*) remained below the threshold to cause any tissue growth abnormalities (**Figure 4.7 A-B**). Overexpression of the constitutively active form of InR on its own (*dpp > GFP + InR-CA*) led to an expansion of the transgene expressing domain as well as enlarged wing discs (**Figure 4.7 C**). Co-expression of *hipk* and *InR-CA* (*dpp > GFP + hipk + InR-CA*) caused significant tissue overgrowths and severe distortions in the tissue architecture (**Figure 4.7 D**), indicating Hipk can synergize with activated InR signaling to promote tumor growth. Notably, knockdown of *SIK2* in the *hipk* and *InR* co-expressing wing discs (*dpp > GFP + hipk + InR-CA + SIK2-RNAi*) potently reduced the tumor growth (**Figure 4.7 E**). Intriguingly, the knockdown disc (*dpp > GFP + hipk + InR + SIK2-RNAi*) was morphologically comparable to the *InR*-overexpressing disc (*dpp > GFP + InR*), suggesting the SIK2 is required for the synergistic effect between Hipk and InR signaling.

While overexpression of *SIK2-CA* on its own led a wing disc with a wild type-like morphology (**Figure 4.7 F**), co-expression of *SIK2-CA* and *hipk* induced profound tumor growth (**Figure 4.7 G**). Such a synergy was not observed between Hipk and SIK2-KD (**Figure 4.7 I**), indicating the SIK2 kinase activity is critical to drive synergistic tumor growth.

Together, our data demonstrate that InR-SIK2 signaling triggers Hipk hyper-phosphorylation and potentiates Hipk tumorigenic activity.

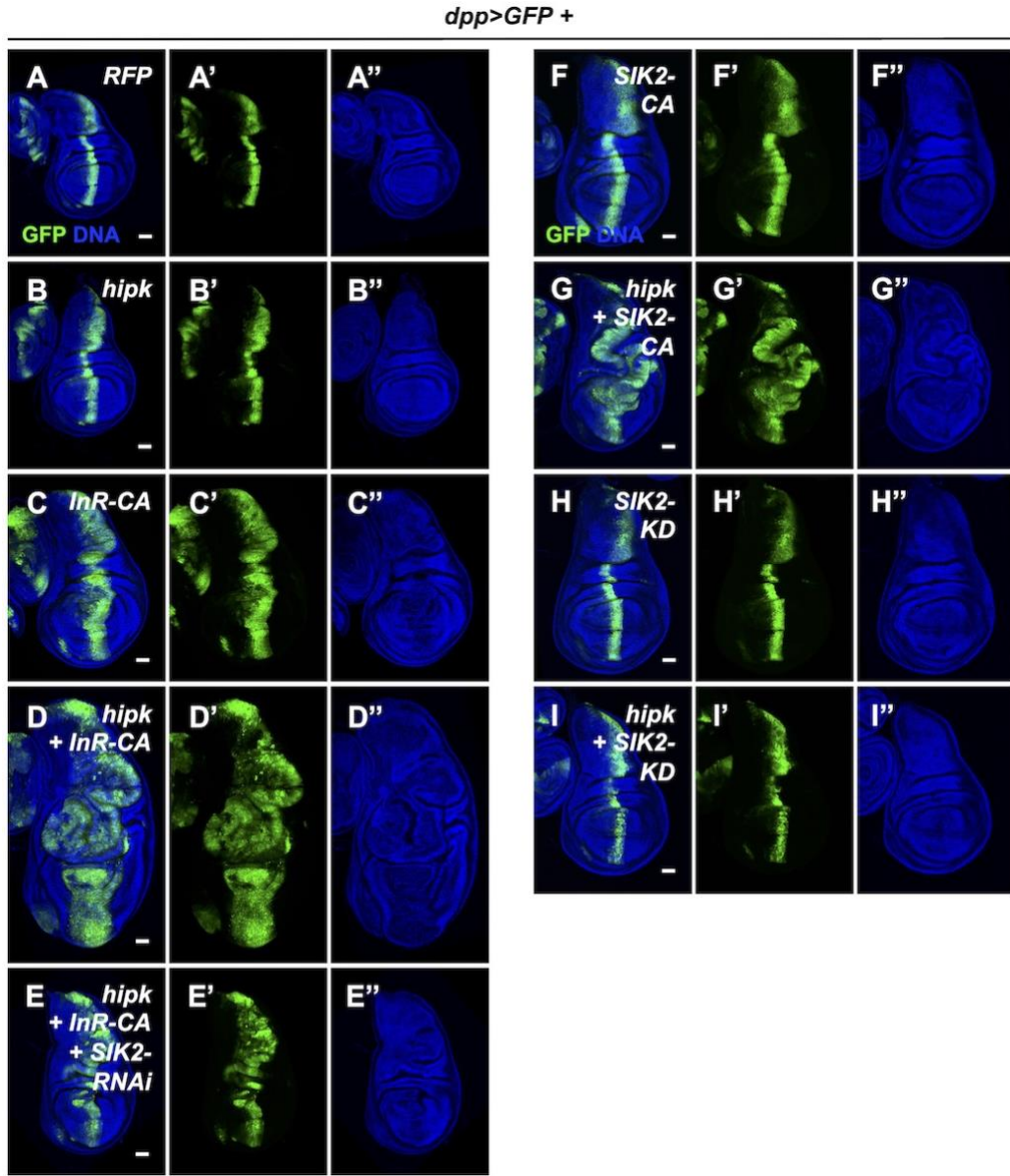


Figure 4.7. InR-SIK2 signaling synergizes with Hipk to drive tumor growth

Larvae were raised at 25°C. (A-I) Wing discs of *dpp > GFP + RFP* (A), *dpp > GFP + hipk* (B), *dpp > GFP + InR-CA* (C), *dpp > GFP + hipk + InR-CA* (D), *dpp > GFP + hipk + InR-CA + SIK2-RNAi* (BL #55880) (E), *dpp > GFP + SIK2-CA* (F), *dpp > GFP + hipk + SIK2-CA* (G), *dpp > GFP + myc-SIK2-KD* (H) and *dpp > GFP + hipk + myc-SIK2-KD* (I) larvae. GFP (green) marks the transgene-expressing cells. DAPI staining for DNA (blue) reveals tissue morphologies. Scale bars, 50 µm.

4.4.6. Loss of SIK2 reduces exogenous Hipk protein levels

To further elucidate the roles of SIK2 in the regulation of Hipk activity, we used RNAi to knock down SIK2. Strikingly, SIK2 knockdown caused a drastic reduction in the exogenous Hipk protein levels (**Figure 4.8 A** compare lane 3 with lane 1). *SIK2Δ41* is a null mutant allele harboring a deletion of the region including the translation start site and the encoding ATP-binding site of the SIK2 kinase domain (Choi et al., 2011). Intriguingly, when *hipk* was overexpressed in the *SIK2* hemizygous mutant background (*SIK2Δ41/Y*) (**Figure 4.8 B**), Hipk protein levels were reduced. This suggests that SIK2-KD may serve as a dominant negative form of SIK2. More importantly, our data suggest that the kinase activity of SIK2 may be required for the protein stability of the exogenous Hipk.

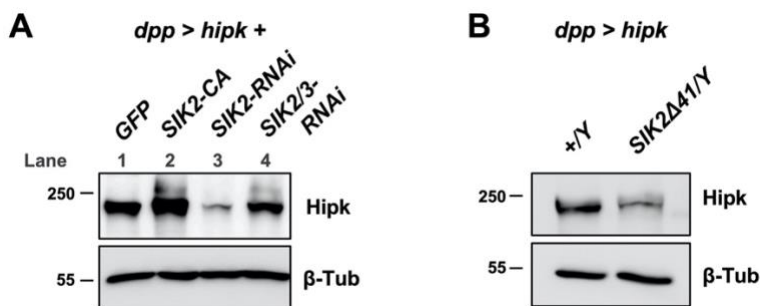


Figure 4.8. Loss of SIK2 reduces the exogenous Hipk protein levels.

Flies were raised at 25°C. **(A)** Western blot analyses of Hipk and β-Tub in dissected larval tissues overexpressing *hipk* with co-expression of *GFP*, *SIK2-CA*, *SIK2-RNAi* (VDRC #26497) or *SIK2/3-RNAi*. **(B)** Western blot analyses of Hipk and β-Tub in dissected larval tissues overexpressing *hipk* in a wild-type background (+/Y) or the *SIK2* hemizygous mutant background (*SIK2Δ41/Y*).

Using a RNAi targeting both *SIK2* and *SIK3* (*SIK2/3-RNAi*), we found that depletion of SIK2 and SIK3 together caused a partial Hipk protein mobility upshift (**Figure 4.8 D** lane 4), mimicking the effect of *SIK2-CA* co-expression (**Figure 4.8 D** lane 2). This hints at additional, unknown kinases responsible for phosphorylating Hipk when SIK2 and SIK3 are both depleted. Further analyses are required to confirm this.

4.4.7. Hipk-6A is a hyper-phosphorylated and constitutively active form

We hypothesized that SIK2 might act on Hipk by direct phosphorylation and activation. Using the known SIK consensus target motif ($\Phi x[HKR]xx[ST]xxx\Phi$) (Horike et al., 2003), we found that Hipk has a total of six putative SIK target sites (Figure 4.9). By site-directed mutagenesis, we mutated all the putative sites to alanine and generated a *UAS-HA-hipk-6A* (abbreviated as *hipk-6A*) transgenic fly. The replacement of the putative target sites with alanine was confirmed by sequencing (Figure 4.10).

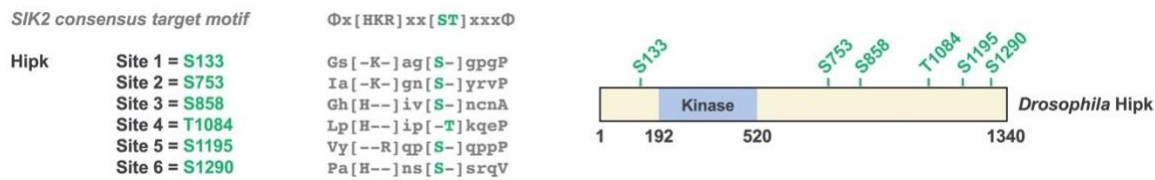


Figure 4.9. Putative SIK2 target sites in *Drosophila* Hipk.

(Left) SIK2 consensus target motif and the 6 putative SIK2 target sites (green) in Hipk are shown. (Right) Schematic diagram of the *Drosophila* Hipk protein (amino acids 1 to 1340) with its kinase domain (amino acids 192 to 520) and the putative SIK2 target sites (green).

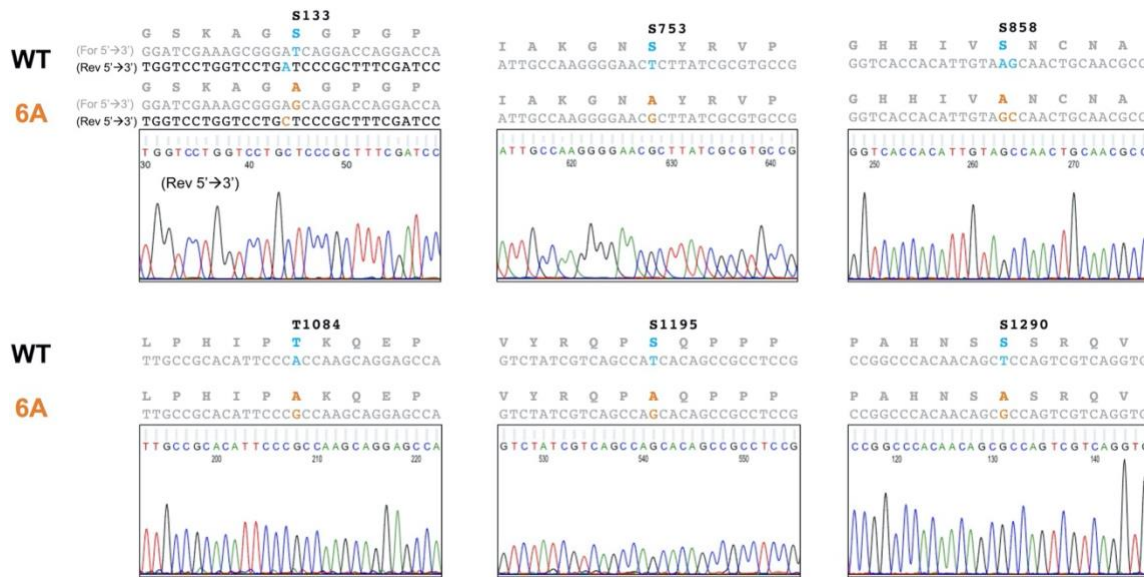


Figure 4.10. Replacements of the six putative SIK target sites in *Drosophila* Hipk by alanine are confirmed by sequencing.

Sequencing data confirm the replacements of the six putative SIK target sites (S133, S753, S858, T1084, S1195 and S1290) by alanine in the *Hipk-6A* mutant. Wild-type (WT) putative

SIK targets sites and the corresponding nucleotides are shown in light blue; replaced sites/nucleotides in orange.

We anticipated that wild-type Hipk proteins (Hipk-WT) (**Figure 4.11 A lanes 1-2**), but not the mutant, would respond to insulin and display the mobility upshift (indicative of hyper-phosphorylation). Contrary to our expectations, instead of being unshifted, the Hipk mutant proteins already manifested mobility upshift even in the absence of insulin treatment (**Figure 4.11 A lanes 3-4**). Notably, the stimulation with insulin apparently failed to cause any further increase in the fraction of the shifted Hipk-6A proteins (**Figure 4.11 A lanes 3-4**), suggesting that Hipk-6A, despite being hyper-phosphorylated, is less responsive to insulin and that the six sites are essential for the responsiveness to insulin. We previously showed that loss of SIK2 reduces Hipk protein levels (**Figure 4.8**). However, the protein levels of both the WT and the mutant was comparable (**Figure 4.11 A compare lane 3 with 1**), implying the 6A mutant is not more susceptible to degradation. In line with the upshift, we found that the 6A mutant acted like a constitutively active form of Hipk as its overexpression induced significant overgrowth and tissue distortions (**Figure 4.11 C**), whereas expression levels of the WT Hipk remained below the threshold to cause any abnormal overgrowth under the same conditions (**Figure 4.11 B**). Both the WT and mutant Hipk proteins are primarily located in the nucleus (**Figure 4.11 D-E**), indicating the 6 serine/threonine sites are dispensable for the regulation of Hipk subcellular localization.

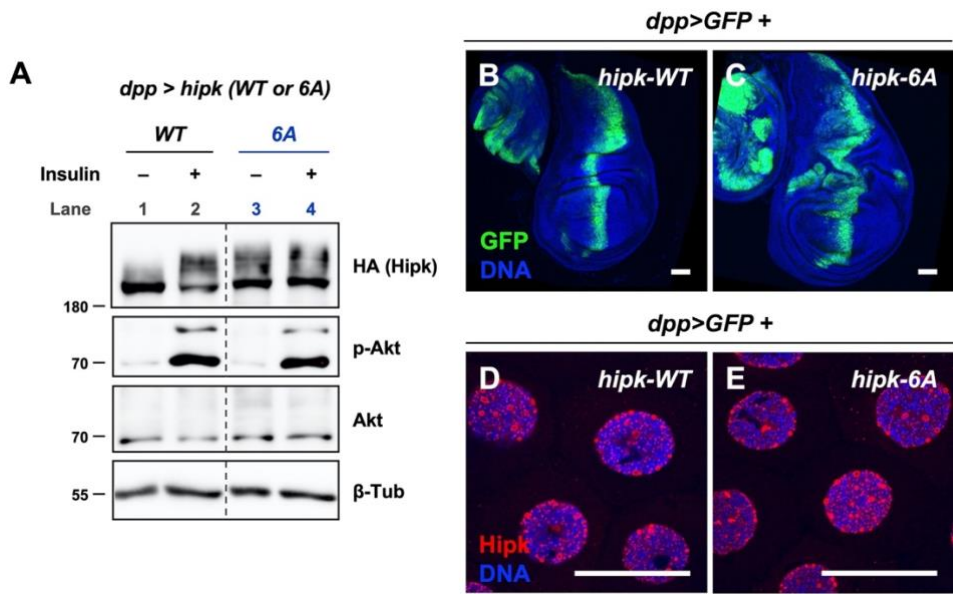


Figure 4.11. Hipk-6A is a hyper-phosphorylated and constitutively active form.

Flies were raised at 25°C. **(A)** Western blot analyses of HA (Hipk), p-AKT, AKT and β-Tub in dissected larval tissues overexpressing the wild-type Hipk (*dpp > hipk-WT*) or the 6A mutant (*dpp > hipk-6A*) treated with (+) or without (-) insulin at 1 μM for 15 minutes. **(B-C)** A wing disc overexpressing *hipk-WT* (*dpp > GFP + hipk-WT*) **(B)** or *hipk-6A* (*dpp > GFP + hipk-6A*) **(C)**. GFP (in green) marks the transgene-expressing domain. DAPI staining for DNA (blue) shows the overall tissue morphology. **(D-E)** Larval salivary gland cells overexpressing *hipk-WT* **(D)** or *hipk-6A* **(E)** stained against anti-Hipk antibodies (red). DAPI staining for DNA (blue) shows the nuclear localization of both Hipk-WT and Hipk-6A. Scale bars, 50 μm.

4.4.8. Elevated Hipk drives InR upregulation, forming a positive feedback loop

Finally, we asked if elevated Hipk influences InR signaling using the GFP-based reporter of PI3K activity, tGPH.

When an activated form of PI3K (PI3K-CAAX) was expressed in the posterior compartment of wing discs under the control of *engrailed* (*en*) Gal4 driver, we observed intense enhancement of tGPH fluorescent signals at the plasma membrane (PM), validating the PI3K reporter. Clones overexpressing *hipk* (marked by RFP) showed mild accumulation of tGPH at the PM, indicative of activation of InR signaling ([Figure 4.12 C-D](#)). By western blot analyses, we observed that overexpression of *hipk* increased AKT phosphorylation (p-AKT), mimicking effect of *InR-CA* (constitutively active) overexpression ([Figure 4.12 E](#)). Furthermore, *InR* transcript levels were significantly upregulated in *hipk*-overexpressing discs ([Figure 4.12 F](#)), suggesting that elevated Hipk promotes insulin sensitivity by induction of *InR* expression. Notably, the robust PM localization of tGPH in *hipk*-expressing cells was suppressed when *InR* was knocked down.

Altogether, the results suggest elevated Hipk can activate InR signaling at least in part through *InR* upregulation, forming a positive feedback loop to sustain Hipk tumorigenic activity.

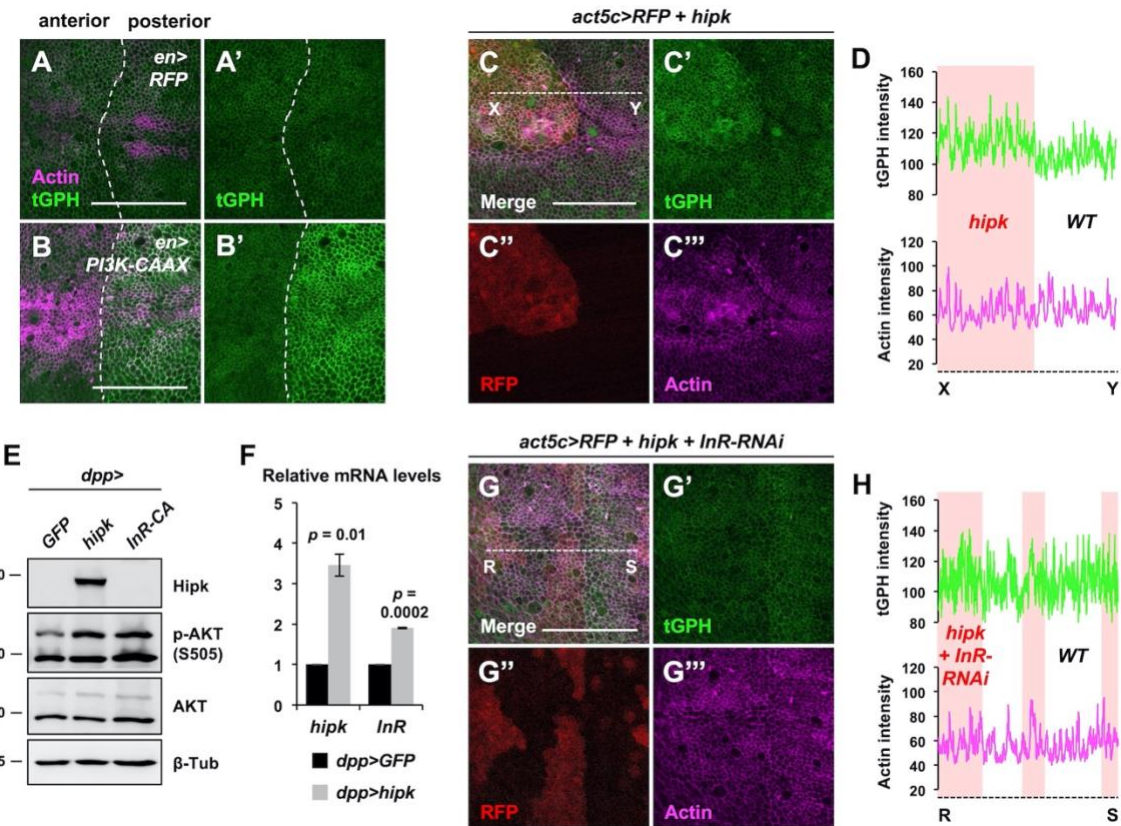


Figure 4.12. Elevated Hipk potentiates InR signaling at least through *InR* upregulation

(A) A control wing disc (*en* > *RFP*) harboring a PI3K activity reporter, tGPH (green). The *en*-*Gal4* driver induces transgene expression in the posterior compartment of the wing disc. **(B)** A PI3K-CAAX overexpressing wing disc (*en* > *PI3K-CAAX*) harboring tGPH (green). **(C, G)** tGPH signals (green) in flip-out clones expressing *hipk* without (**C**) or with *InR* knockdown (*InR-RNAi*) (**G**) under the control of *actin-Gal4*. RFP (red) marks the transgene-expressing clones. **(D, H)** Quantifications of the tGPH (green) and actin (magenta) intensities in the dashed lines XY and RS in the *hipk*-overexpressing (**C**) and *hipk* and *InR-RNAi* co-expressing clones (**G**), respectively. Shaded areas (in pink) refer to the clones expressing *hipk* (**C**) or co-expressing *hipk* and *InR-RNAi* (**G**). Unshaded areas refer to the neighboring wild-type cells. F-actin staining is shown in magenta. Scale bars, 50 μ m. **(E)** Western blot analyses of *Hipk*, p-AKT, AKT and β -Tub of control (*dpp* > *GFP*), *hipk*-overexpressing (*dpp* > *hipk*) and *InR-CA*-overexpressing (*dpp* > *InR-CA*) larval head tissues. **(F)** qRT-PCR analysis of *hipk* and *InR* expression in *hipk*-expressing discs (*dpp* > *hipk*) relative to control discs (*dpp* > *GFP*). Data are mean \pm sem. $n = 2$ biological sample sets. Each set is pooled from 10 to 20 wing discs per genotype. Exact *p* values are shown and calculated using unpaired two-tailed *t*-test.

4.5. Discussion

4.5.1. Two modes of nutrient sensing PTMs of Hipk – Phosphorylation and O-GlcNAcylation

Here, we describe a new mode of insulin-sensing post-translational modification (PTM) of Hipk. First, we find that InR -SIK2 signaling pathway mediates the high sugar effect on Hipk activity ([Figure 4.1](#)), suggesting that Hipk may respond to extracellular insulin levels. Indeed, both acute stimulation of insulin and chronic activation of InR signaling pathway promote Hipk hyper-phosphorylation in a SIK2 kinase activity-dependent manner ([Figure 4.2](#), [Figure 4.4](#), [Figure 4.6](#)).

We previously reported that Hipk activity is regulated by the glucose-sensing hexosamine biosynthetic pathway (HBP) in conjunction with O-GlcNAc transferase (OGT) ([Wong et al., 2020](#)). Thus, it is likely that Hipk activity is governed by two modes of nutritional regulation: one mediated through phosphorylation in response to high glucose by the insulin-sensing InR-SIK2 pathway, and another through O-GlcNAcylation by the glucose-sensing HBP-OGT axis. When we evaluated the functional relevance of the regulation of Hipk by OGT or InR-SIK2, we find that activation of either one is sufficient to synergize with Hipk to drive profound tumor growth ([\(Figure 4.7\)](#) and ([Wong et al., 2020](#))). These results suggest that Hipk renders the tumor cells sensitive to the availability of both nutrient cues – glucose and insulin – to support growth.

It is also tempting to speculate that the two PTMs may interact to regulate Hipk activity, given that phosphate and O-GlcNAc can reciprocally modify the same or structurally proximal serine/threonine amino acids ([Hart et al., 2011](#)). In addition, accumulating studies reveal that InR signaling is regulated by OGT as the major InR signaling components including insulin receptor substrate (IRS), PI3K, PDK and AKT are O-GlcNAc modified proteins ([Yang et al., 2008](#)). It has been shown that increased O-GlcNAc alters their phosphorylation states, binding affinities for their upstream/downstream partners, and thereby their activities, desensitizing InR signaling and conferring insulin resistance ([Whelan et al., 2010; Yang et al., 2008](#)). Indeed, we noticed that the hyperplasia induced by activated InR can be suppressed by overexpression of OGT (not shown; unpublished). Hence, this complex, antagonizing

effect of OGT exerting on InR signaling may be exploited; simultaneous activation of both may counterintuitively suppress Hipp tumor growth.

4.5.2. Regulation of Hipk by a tight balance of SIK2 and SIK3 activities

Our work reveals that SIK2 mediates effects of InR signaling on Hipk ([Figure 4.4](#), [Figure 4.7](#)). Furthermore, SIK2 physically binds to Hipk and activated SIK2 is sufficient to cause Hipk phosphorylation and augment Hipk tumorigenic activity ([Figure 4.5](#), [Figure 4.6](#), [Figure 4.7](#)). Loss of SIK2 results in a reduction in Hipk protein expression levels ([Figure 4.8](#)) and suppression of Hipk tumor growth in an activated InR background ([Figure 4.7](#)).

Surprisingly, when both SIK2 and SIK3 are knocked down simultaneously, rather than a further decrease in expression levels, Hipk proteins are relatively stable and manifest a mobility upshift suggestive of phosphorylation events ([Figure 4.8](#)). This suggests that while SIK2 promotes Hipk hyper-phosphorylation, SIK3 counteracts with SIK2 to maintain a balance of Hipk phosphorylation state, leading to hypo-phosphorylation in the SIK2-deficient background. Furthermore, we find that the Hipk 6A mutant proteins seem to be refractory to insulin stimulation and show the mobility upshift, recapitulating the effects of the double knockdown ([Figure 4.11](#)).

Hence, these experiments inform us that the regulation of Hipk by SIKs is likely sensitive to slight fluctuations in the balance of SIK2 and SIK3 activity. Further studies examining Hipk activity in the singly and doubly mutant backgrounds are warranted due to the potential issue regarding the knockdown efficiency of RNAi. Also, it will be interesting to address why Hipk becomes activated under a SIK2 and SIK3 double deficient background. Does this mean Hipk will turn to additional, yet unidentified nutrient-sensing phosphorylation mechanisms in order to sustain Hipk tumor growth? Intriguingly, mammalian HIPK2 has been found to be phosphorylated by AMPK at Thr 112, Ser 114 and Thr 1107, which are required for HIPK2 kinase activity ([see also Chapter 1.5.1](#)) ([Choi et al., 2013](#)). The AMPK consensus motif (LxRxx(S/T)) ([Ducommun et al., 2015](#)) share some features with the SIK2 one. Future work will involve the functional characterization of interactions between Hipk and AMPK signaling. Nevertheless, our work highlights the phosphorylation of Hipk is mediated in a nutrient-responsive manner, likely mediated by more than one kinase.

Chapter 5.

A positive feedback loop between Myc and aerobic glycolysis sustains tumor growth in the Hipp tumor model

Chapter 5 is based off the following published work with modifications.

Kenneth Kin Lam Wong, Jenny Zhe Liao, and **Esther M Verheyen**. A positive feedback loop between Myc and aerobic glycolysis sustains tumor growth in a *Drosophila* tumor model. *eLife* 8 (July). **eLife**. 8: e46315 (2019).

<https://www.ncbi.nlm.nih.gov/pubmed/31259690>

5.1. Contributions to the Chapter

K.K.L.W. Conceptualization, Data curation, Formal analysis, Investigation, Visualization, Writing-original draft, Writing-review and editing; **J.Z.L.** Formal analysis, Investigation, Visualization, Writing-review and editing; **E.M.V.** Conceptualization, Formal analysis, Supervision, Funding acquisition, Project administration, Writing-review and editing

5.2. Abstract

Cancer cells usually exhibit aberrant cell signaling and metabolic reprogramming. However, mechanisms of crosstalk between these processes remain elusive. Here, we show that in an *in vivo* tumor model expressing oncogenic *Drosophila* Homeodomain-interacting protein kinase (Hipk), tumor cells display elevated aerobic glycolysis. Mechanistically, elevated Hipk drives transcriptional upregulation of *Drosophila* Myc (dMyc; MYC in vertebrates) likely through convergence of multiple perturbed signaling cascades. dMyc induces robust expression of *pfk2* (encoding 6-Phosphofructo-2-kinase/fructose-2,6-bisphosphatase; PFKFB in vertebrates) among other glycolytic genes. Pfk2 catalyzes the synthesis of fructose-2,6-bisphosphate, which acts as a potent allosteric activator of Phosphofructokinase (Pfk) and thus stimulates glycolysis. Pfk2 and Pfk in turn are required to sustain dMyc protein accumulation post-transcriptionally, establishing a positive feedback loop. Disruption of the loop abrogates tumorous growth. Together, our study demonstrates a reciprocal stimulation of Myc and aerobic glycolysis and identifies the Pfk2-Pfk governed committed step of glycolysis as a metabolic vulnerability during tumorigenesis.

5.3. Introduction

In the 1920s, Otto Warburg first discovered that cancer cells vigorously take up glucose and preferentially produce lactate even in the presence of oxygen, a phenomenon now widely termed the Warburg effect or aerobic glycolysis (Warburg et al., 1927). Despite his pioneering work, the Warburg effect was largely disregarded for the subsequent decades (Koppenol et al., 2011; Liberti and Locasale, 2016). After the discoveries of oncogenes and tumor suppressor genes, cancers are generally considered as genetic diseases rather than metabolic ones (Seyfried et al., 2014; Wishart, 2015). Not until the 1980s did the revisiting of the Warburg effect in connection with oncogenes spark substantial research in cancer metabolism (Koppenol et al., 2011), laying the foundation for 2-deoxy-2-(¹⁸F)fluoro-D-glucose (¹⁸F-FDG) positron emission tomography (PET) in clinical cancer diagnosis (Ben-Haim and Ell, 2008; Vander Heiden et al., 2009), recognition of metabolic reprogramming as a hallmark of cancer (Hanahan and Weinberg, 2011; Ward and Thompson, 2012) and development of

anti-cancer agents targeting aerobic glycolysis ([Ganapathy-Kanniappan and Geschwind, 2013](#); [Granchi and Minutolo, 2012](#); [Pelicano et al., 2006](#)).

How the Warburg effect arises and contributes to tumor progression have always been the center in the field of cancer metabolism ([Lu et al., 2015](#)). Warburg hypothesized that mitochondrial impairment is the cause of aerobic glycolysis and cancer ([WARBURG, 1956](#)), which has sparked much controversy among scientists ([Senyilmaz and Teleman, 2015](#)). Contrary to his idea, the current, widely-accepted view is that oncogenic drivers such as RAS, MYC, Hypoxia-inducible factors (HIFs) and Steroid receptor coactivators (SRCs) promote cancer cell proliferation and directly stimulate aerobic glycolysis through regulating transcriptional expression or catalytic activities of metabolic enzymes ([Koppenol et al., 2011](#)). Several explanations for the Warburg effect have been put forward, including rapid adenosine triphosphate (ATP) production and *de novo* biosynthesis of macromolecules ([Liberti and Locasale, 2016](#)). Recently, Warburg effect functions are being re-evaluated as a growing body of evidence shows that metabolic rewiring in cancers impacts cell signaling and epigenetics ([Liberti and Locasale, 2016](#); [Lu and Thompson, 2012](#)).

Drosophila has proven to be a powerful genetic model organism for studying tumorigenesis *in vivo* largely due to high conservation of genes and signaling cascades between human and flies and reduced genetic redundancy ([Table 5-1](#)) ([Gonzalez, 2013](#); [Herranz and Cohen, 2017](#)). In a recent study, we showed that elevation of *Drosophila* Hipk causes an *in vivo* tumor model characterized by tissue overgrowth, loss of epithelial integrity and invasion-like behaviors ([Blaquiere et al., 2018](#)). The tumorigenic roles of *Drosophila* Hipk seem to be conserved in mammals as the four members of the HIPK family (HIPK1-4) are also implicated in certain cancers (Reviewed in ([Blaquiere and Verheyen, 2017](#))). For example, HIPK1 is highly expressed in breast cancer cell lines, colorectal cancer samples and oncogenically-transformed mouse embryo fibroblasts ([Kondo et al., 2003](#); [Rey et al., 2013](#)). Also, HIPK2 is elevated in certain cancers including cervical cancers, pilocytic astrocytomas, colorectal cancer cells and in other proliferative diseases, such as thyroid follicular hyperplasia ([Al-Beiti and Lu, 2008](#); [Cheng et al., 2012](#); [D’Orazi et al., 2006](#); [H Deshmukh et al., 2008](#); [Lavra et al., 2011](#); [Saul and Schmitz, 2013](#); [Yu et al., 2009](#)). To gain a better understanding of cancer metabolism, we set out to use the fly Hipk tumor model to investigate whether and how cellular metabolism is altered in tumor cells. We find that Hipk-induced tumorous growth

is accompanied by elevated aerobic glycolysis. Furthermore, we identify novel feedback mechanisms leading to prolonged dMyc expression and hence tumorigenesis. Our study reveals potential metabolic vulnerabilities that could be exploited to suppress tumor growth.

Table 5-1. A list of *Drosophila* genes studied in this work with their human homologs.

<i>Drosophila</i> genes	Fly annotation symbol	Human homolog(s)	Description
Glycolysis			
<i>glut1</i>	CG43946	<i>SLC2A3, SLC2A1, SLC2A4, SLC2A14, SLC2A2</i>	Glucose transporter
<i>hex-A</i>	CG3001	<i>GCK, HK1, HK2, HK3, HKDC1</i>	Hexokinase
<i>hex-C</i>	CG8094	<i>GCK, HK1, HK2, HK3, HKDC1</i>	Hexokinase
<i>pgi</i>	CG8251	<i>GPI</i>	Glucose-6-phosphate isomerase
<i>pfk</i>	CG4001	<i>PFKM, PFKP, PFKL</i>	Phosphofructokinase
<i>pfk2</i> (or <i>pfrx</i>)	CG3400	<i>PFKFB3, PFKFB1, PFKFB2, PFKFB4</i>	6-Phosphofructo-2-kinase/fructose-2,6-bisphosphatase
<i>ald</i> (or <i>ald1</i>)	CG6058	<i>ALDOA, ALDOC, ALDOB</i>	Aldolase
<i>tpi</i>	CG2171	<i>TPI1</i>	Triosephosphate isomerase
<i>gapdh1</i>	CG12055	<i>GAPDH, GAPDHS</i>	Glyceraldehyde-3-phosphate dehydrogenase
<i>gapdh2</i>	CG8893	<i>GAPDH, GAPDHS</i>	Glyceraldehyde-3-phosphate dehydrogenase
<i>pgk</i>	CG3127	<i>PGK1, PGK2</i>	Phosphoglycerate kinase
<i>pglym78</i>	CG1721	<i>PGAM1, PGAM2, PGAM4</i>	Phosphoglycerate mutase
<i>eno</i>	CG17654	<i>ENO1, ENO2, ENO3</i>	Enolase
<i>pyk</i>	CG7070	<i>PKM, PKLR</i>	Pyruvate kinase
<i>Ldh</i> (or <i>impl3</i>)	CG10160	<i>LDHA, LDHB, LDHAL6A, LDHC, LDHAL6B</i>	Lactate dehydrogenase
Cell signaling			
<i>dMyc</i>	CG10798	<i>MYC, MYCL, MYCN</i>	Transcription factor, cell growth, cell competition and regenerative proliferation
<i>sima</i>	CG45051	<i>HIF1A, HIF2A, HIF3A</i>	Hypoxia-inducible factors
<i>yki</i>	CG4005	<i>YAP1, WWTR1 (TAZ)</i>	Effectors of the Hippo tumor suppressor pathway
<i>arm</i>	CG11579	<i>CTNNB1 (β-catenin), JUP (γ-catenin)</i>	Cell adhesion and Wingless signaling
<i>ci</i>	CG2125	<i>GLI3, GLI2, GLI1</i>	Effectors of Hedgehog signaling
<i>N</i>	CG3936	<i>NOTCH1, NOTCH2, NOTCH3, NOTCH4</i>	Notch receptors in Notch signaling
<i>ex</i>	CG4114	<i>FRMD1, FRMD6</i>	A FERM-domain containing protein, target gene and positive regulator of the Hippo signaling

5.4. Results

5.4.1. Hipk tumor cells exhibit elevated glucose uptake

Larval imaginal epithelia such as wing and eye-antennal imaginal discs, which give rise to wing and eye structures in adult flies, respectively, are extensively used as tumor models to study human carcinomas (Herranz et al., 2016). To generate the Hipk tumor model, we used the Gal4-UAS system (Brand and Perrimon, 1993) to induce overexpression of *hipk* in larval wing discs (full genotype: *dpp-Gal4 > UAS-RFP + UAS-hipk*, abbreviated as *dpp > RFP + hipk*) (Figure 5.1 c-d). Fluorescent proteins, for example red fluorescent proteins (RFP) or green fluorescent proteins (GFP), were co-expressed to label the transgene-expressing cells. As previously reported (Blaquiere et al., 2018), in contrast to control discs (*dpp > RFP*) (Figure 5.1 a-b), tumorous growth and severe tissue distortions were evident in *hipk*-expressing discs (*dpp > RFP + hipk*) (Figure 5.1 c-d).

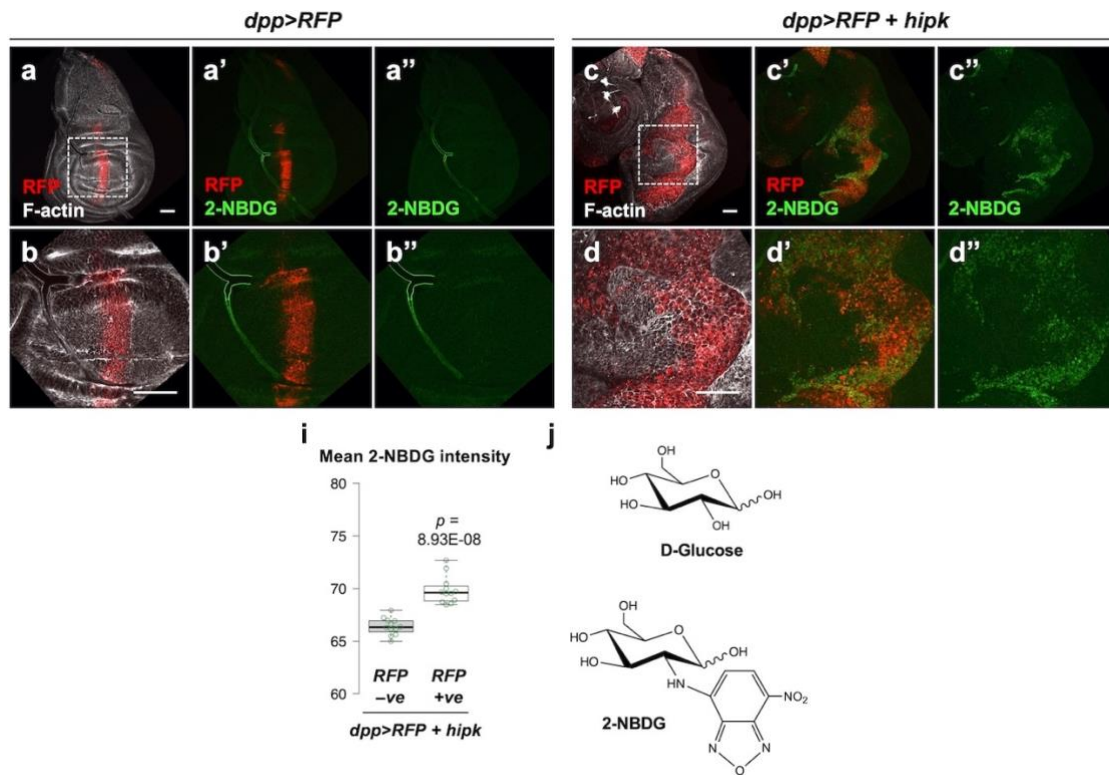


Figure 5.1. Hipk tumor cells exhibit elevated glucose uptake.

(a-d) Incorporation of 2-NBDG (green) in control (*dpp > RFP*) (a-b) and *hipk*-expressing (*dpp > RFP + hipk*) wing discs (c-d). Insets (dashed line) in a and c are magnified in b and d,

respectively. RFP (red) marks the transgene-expressing cells. F-actin (gray) staining shows the overall tissue morphology. **(i)** Quantification of mean 2-NBDG intensity in *hipk*-expressing cells (RFP positive) and the neighboring wild-type cells (RFP negative) in *hipk*-expressing wing discs (*dpp > RFP + hipk*) ($N = 12$ wing discs). **(j)** Chemical structures of D-glucose (top) and 2-NBDG (bottom). Scale bars, 50 μm . Exact p values are shown and calculated using unpaired two-tailed t -test.

To ask if elevated Hipk alters cellular metabolism, we first used a fluorescently labeled glucose analogue, 2-deoxy-2-[(7-nitro-2,1,3-benzoxadiazol-4-yl)amino]-D-glucose (2-NBDG) ([Figure 5.1 i](#)). Like D-glucose, 2-NBDG is transported into cells through glucose transporters and phosphorylated by hexokinases ([O’Neil et al., 2005](#); [Yoshioka et al., 1996](#)). However, due to the presence of the fluorescent amino group at the C-2 position, 2-NBDG-6-phosphate cannot proceed further through glycolysis and is consequently trapped within the cells, rendering it a probe for monitoring glucose uptake ([O’Neil et al., 2005](#)). 2-NBDG is often used in *Drosophila* to measure glucose uptake. For example, overexpression of *glut1* (encoding Glucose transporter 1) is sufficient to promote the accumulation in 2-NBDG ([Niccoli et al., 2016](#)). Increased import of 2-NBDG is also found in *dMyc*-expressing cells ([de la Cova et al., 2014](#)) and *RasV12scrib-/-* tumor cells ([Kathedder et al., 2017](#)), indicating that such cells acquire enhanced glucose metabolism.

Similarly, we found that cells with elevated Hipk (RFP positive) in *hipk*-expressing wing discs (*dpp > RFP + hipk*) exhibited statistically significant 2-NBDG accumulation when compared with the neighboring wild-type cells (RFP negative) ([Figure 5.1 c-d, i](#)) or cells (either RFP positive or negative) in control discs (*dpp > RFP*) ([Figure 5.1 a-b](#)). A comparable phenomenon was seen in larval eye-antennal discs ([Figure 5.2 a-b](#)).

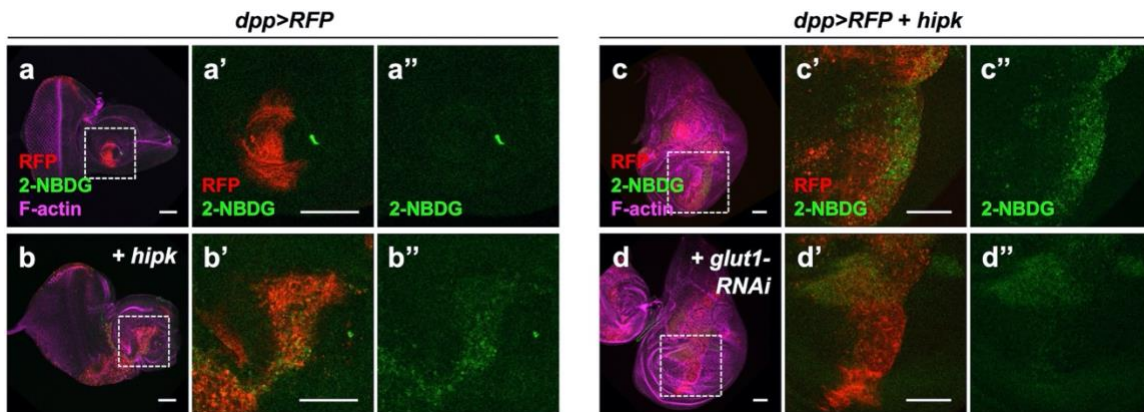


Figure 5.2. Elevated Hipk stimulates 2-NBDG uptake in a Glut1-dependent manner.

(a-b) Incorporation of 2-NBDG (green) in control (*dpp > RFP*) **(a)** and *hipk*-expressing eye-antennal discs (*dpp > RFP + hipk*) **(b)**. Insets (dashed line) in **a** and **b** are magnified in **a'-a''** and **b'-b''**, respectively. **(c-d)** Incorporation of 2-NBDG (green) in *hipk*-expressing wing discs without (*dpp > RFP + hipk*) **(c)** or with co-expression of *glut1-RNAi* (*dpp > RFP + hipk + glut1-RNAi*) **(d)**. Insets (dashed line) in **c** and **d** are magnified in **c'-c''** and **d'-d''**, respectively. RFP (red) marks the transgene-expressing cells. F-actin (magenta) staining shows the overall tissue morphology. Scale bars, 50 μ m.

Furthermore, we detected a mild upregulation of *glut1* (1.6-fold) in *hipk*-expressing discs by quantitative real-time PCR (qRT-PCR) (Figure 5.5 a). Knockdown of *glut1* using RNA interference (RNAi) moderately reduced 2-NBDG incorporation in Hipk tumor cells (Figure 5.2 c-d). The knockdown efficiency of *glut1-RNAi* was tested using a ubiquitous Gal4 driver, *act5c-Gal4* (Figure 5.3 a). Together, these results suggest that elevated *Hipk* facilitates the import of glucose into cells at least in part through augmenting *Glut1* expression.

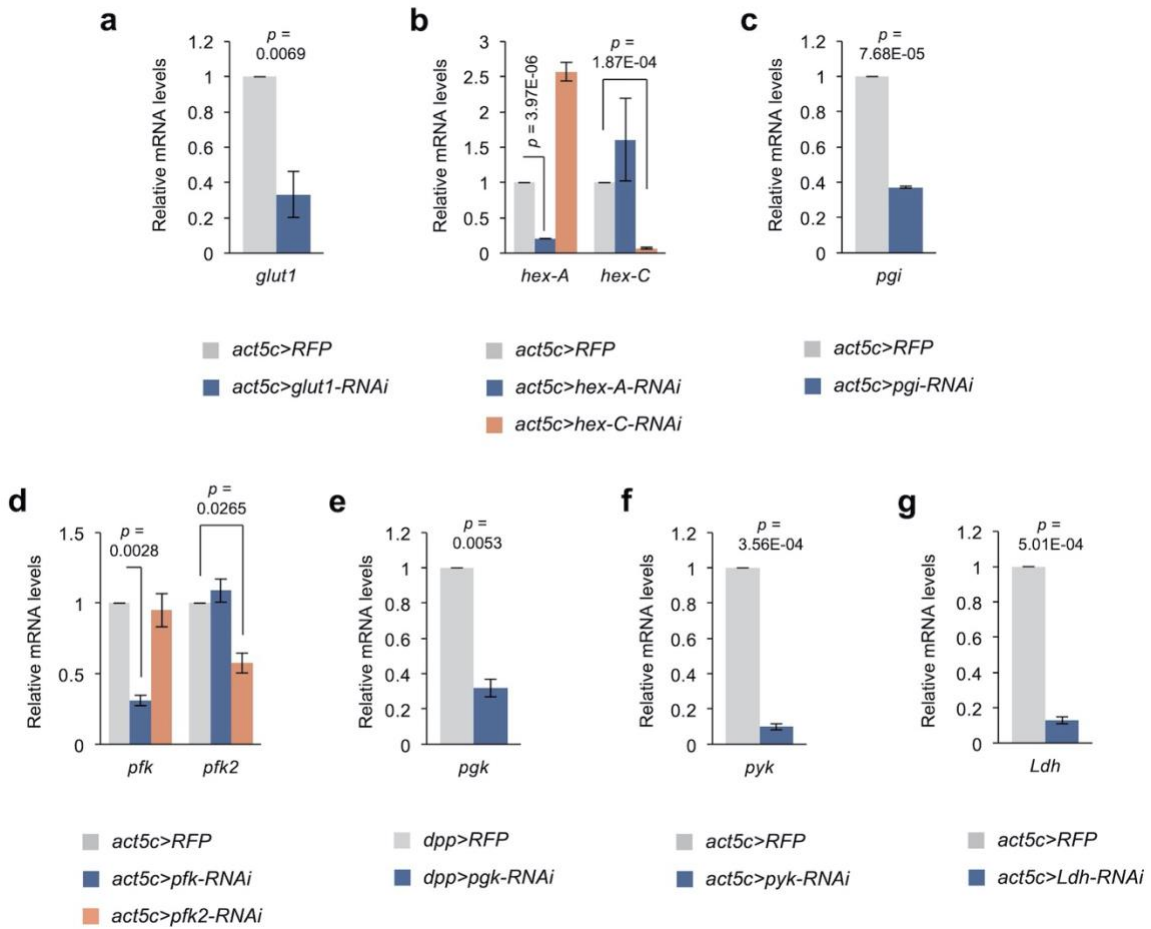


Figure 5.3. Knockdown efficiencies of the RNAi lines targeting glycolytic genes.

(a) qRT-PCR analysis of *glut1* expression in control (*act5c > RFP*) and *glut1* knockdown (*act5c > glut1-RNAi*) pupae. **(b)** qRT-PCR analyses of *hex-A* and *hex-C* expression in control (*act5c > RFP*), *hex-A* knockdown (*act5c > hex A-RNAi*) and *hex-C* knockdown (*act5c > hex C-RNAi*) pupae. **(c)** qRT-PCR analysis of *pgi* expression in control (*act5c > RFP*) and *pgi* knockdown (*act5c > pgi-RNAi*) pupae. **(d)** qRT-PCR analyses of *pfk* and *pfk2* expression in control (*act5c > RFP*), *pfk* knockdown (*act5c > pfk-RNAi*) and *pfk2* knockdown (*act5c > pfk2-RNAi*) larvae. **(e)** qRT-PCR analysis of *pgk* expression in control (*dpp > RFP*) and *pgk* knockdown (*dpp > pgk-RNAi*) larval salivary gland cells. **(f)** qRT-PCR analysis of *pyk* expression in control (*act5c>RFP*) and *pyk* knockdown (*act5c > pyk-RNAi*) larvae. **(g)** qRT-PCR analysis of *Ldh* expression in control (*act5c > RFP*) and *Ldh* knockdown (*act5c > Ldh-RNAi*) pupae. Data are mean \pm sem. At least $n = 2$ independent experiments with samples pooled from approximately 10 larvae or pupae. Exact p values are shown and calculated using unpaired two-tailed *t*-test.

5.4.2. Hipk tumor cells exhibit low intracellular glucose levels.

Next, we evaluated the intracellular glucose levels using a FRET (Förster resonance energy transfer)-based glucose sensor, which is composed of a glucose-binding domain (GBD) fused with cyan fluorescent protein (CFP) and yellow fluorescent protein (YFP) (**Figure 5.4 I**) (Fehr et al., 2003; Volkenhoff et al., 2018). The binding of glucose to GBD induces conformational changes, leading to increased FRET efficiency (the ratio of FRET to CFP). Intriguingly, a lower FRET/CFP ratio indicative of reduced glucose concentration was observed in *hipk*-expressing cells (**Figure 5.4 g-h, k**) when compared with control discs (**Figure 5.4 e-f, k**). This implies that despite enhanced glucose uptake (**Figure 5.1**), glucose is substantially utilized in the rapidly proliferating Hipk tumor cells.

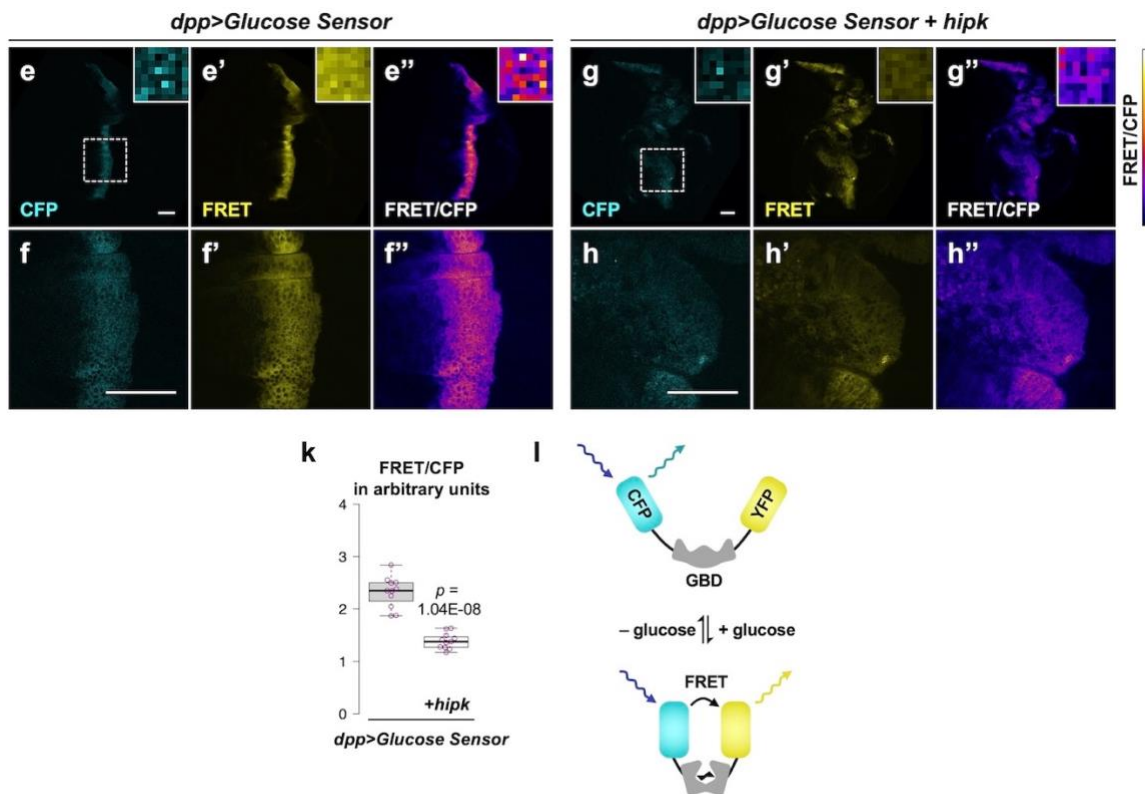


Figure 5.4. Hipk tumor cells display low intracellular glucose levels.

(e-h) Intracellular glucose FRET efficiency (FRET/CFP) (colored using Fire Lookup Table) in control (*dpp > Glucose Sensor*) (e-f) and *hipk*-expressing (*dpp > Glucose Sensor + hipk*) wing discs (g-h). Individual CFP and FRET channels are shown in cyan and yellow, respectively. Insets (dashed line) in e and g are magnified in f and h, respectively. Insets (solid line) at the upper right corners in e-e'' and g-g'' show the corresponding signals at

single pixel level. **(k)** Quantification of glucose FRET efficiency in control (*dpp > Glucose Sensor*) and *hipk*-expressing (*dpp > Glucose Sensor + hipk*) wing discs ($N = 11$ wing discs per genotype). **(l)** Schematic diagram of the FRET-based glucose sensor. Glucose binding induces conformational changes of glucose-binding domain (GBD) such that FRET occurs and YFP emission increases. Scale bars, 50 μm . Exact p values are shown and calculated using unpaired two-tailed t -test.

5.4.3. Elevated Hipk induces robust expression of a subset of glycolytic genes

Glycolysis is a catabolic process that breaks down glucose into pyruvate via multiple enzymatic steps. To ask if glycolysis is upregulated, we examined the expression profile of glycolytic genes by qRT-PCR and changes greater than 1.5-fold were considered significant. We isolated RNA from whole wing discs expressing either GFP (control) or *hipk* under the *dpp-Gal4* driver control. qRT-PCR analyses revealed that genes encoding Hexokinases (Hex-A and Hex-C, 2.2-fold and 4.3-fold respectively), Phosphoglucose isomerase (Pgi, 2.4-fold), Phosphofructokinase 2 (Pfk2, also known as Pfrx, 2.7-fold) and Lactate dehydrogenase (Ldh, also known as Impl3, 3.4-fold) are significantly upregulated in *hipk*-expressing discs (Figure 5.5 a-b). Expression of other glycolytic genes, on the other hand, remained relatively unchanged.

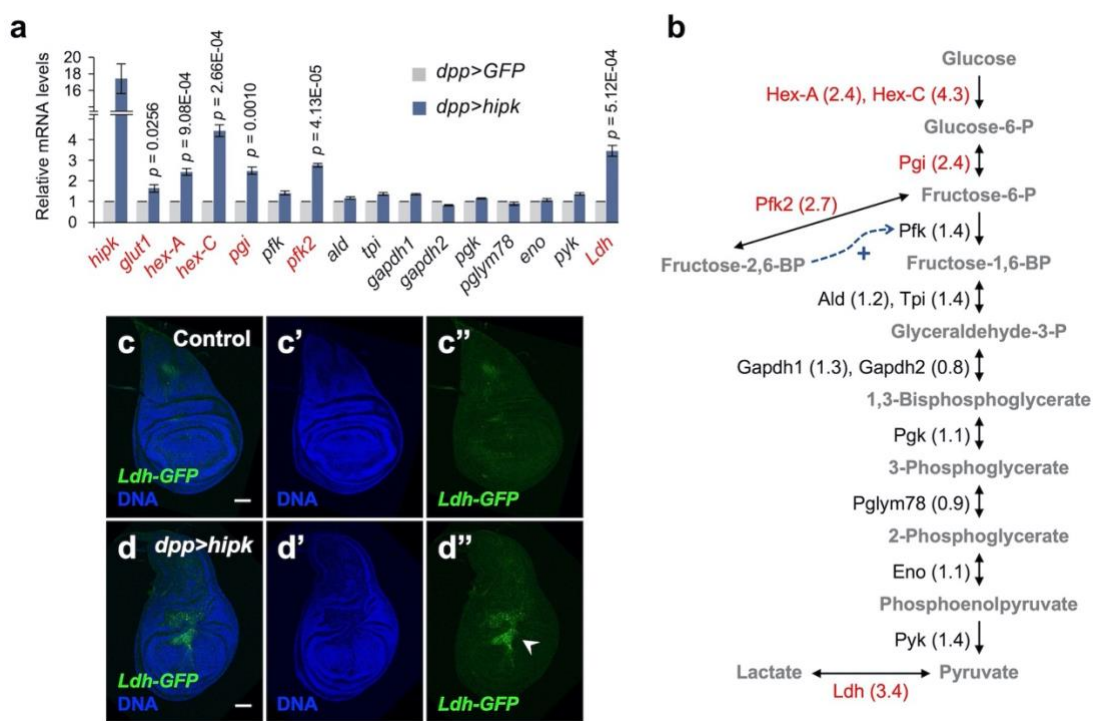


Figure 5.5. Elevated Hipk induces robust expression of a subset of glycolytic genes.

(a-b) qRT-PCR analysis of glycolytic gene expression in *hipk*-expressing discs (*dpp > hipk*) relative to control discs (*dpp > GFP*) (a). Data are mean \pm sem. $n = 3$ independent experiments with samples pooled from 10 to 20 wing discs per genotype. Schematic diagram of glycolysis (b). Fold changes are shown in brackets. Glycolytic enzymes with more than 1.5-fold transcriptional upregulation in *hipk*-expressing discs are marked in red. Bi- and uni-directional arrows indicate the reversible and essentially irreversible steps in glycolysis,

respectively. Dashed arrow (blue) shows the positive allosteric regulation of Pfk by fructose-2,6-BP. Full names of the glycolytic genes are provided in **Table 5-1**. Exact *p* values are shown and calculated using unpaired two-tailed *t*-test. (**c-d**) Expression of *Ldh-GFP* (green), an enhancer trap to monitor *Ldh* expression, in control (genotype: *Ldh-GFP/+*) (**c**) and *hipk*-expressing wing discs (genotype: *Ldh-GFP/dpp > hipk*) (**d**). DAPI staining for DNA (blue) reveals tissue morphology. White arrowhead in **d**'' indicates marked induction of *Ldh* expression. Scale bars, 50 μ m.

As the Dpp domain comprises 10-20% of the wing disc, the glycolytic gene upregulation within *hipk*-expressing cells is likely understated. In light of such a limitation, we used a GFP-based enhancer trap to monitor *Ldh* transcription in vivo (*Ldh-GFP*) (Quinones-Coello et al., 2006). In control wing discs, little *Ldh-GFP* was detected (**Figure 5.5 c**), indicating that *Ldh* is minimally expressed under physiological conditions as previously described (Wang et al., 2016). On the contrary, we observed robust *Ldh-GFP* expression in *hipk*-expressing wing discs (**Figure 5.5 d**), confirming that elevated Hipk induces *Ldh* expression.

Hexokinases phosphorylate glucose to form glucose-6-phosphate (G6P), which is the first essentially irreversible step in glycolysis (**Figure 5.5 b**). Pgi catalyzes the reversible conversion of G6P and fructose-6-phosphate. Pfk2 is a bifunctional enzyme that synthesizes fructose-2,6-bisphosphate (F2,6-BP). F2,6-BP is a potent allosteric activator of Pfk, which governs the committed, second irreversible step in glycolysis. Ldh, similar to LDHA in vertebrates (Rechsteiner, 1970), favors the reduction of pyruvate to lactate, regenerating nicotinamide adenine dinucleotide (NAD⁺) such that glycolysis continues unabated (Valvona et al., 2016). The robust upregulation of these glycolytic enzymes in *hipk*-expressing discs is in agreement with previous data implying that glucose consumption is stimulated. Taken together, the results support the hypothesis that *Hipk tumor cells exhibited elevated glycolytic activities, resembling the Warburg effect seen in cancers.*

5.4.4. Elevated Hipk drives dMyc upregulation in a region-specific manner

To elucidate the underlying mechanisms for the metabolic alterations in the Hipk tumors, we examined gene expression of dMyc and Sima (HIF1- α in vertebrates) since these two transcription factors are well-known inducers of glycolysis in cancer cells (Marín-Hernández et al., 2009; D. M. Miller et al., 2012). qRT-PCR analyses showed that *dMyc* was upregulated in *hipk*-expressing discs whereas *sima* expression remained unchanged (Figure 5.6 a).

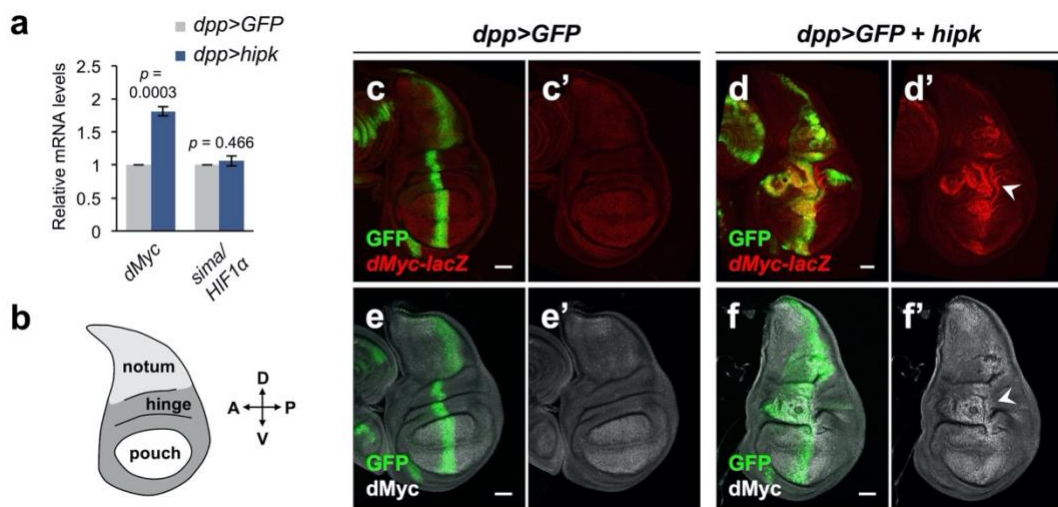


Figure 5.6. Elevated Hipk drives dMyc upregulation in a region-specific manner.

(a) qRT-PCR analysis of *dMyc* and *sima* expression in *hipk*-expressing discs (*dpp > hipk*) relative to control discs (*dpp > GFP*). Data are mean \pm sem. $n = 3$ independent experiments with samples pooled from 10 to 20 wing discs per genotype. Exact *p* values are shown and calculated using unpaired two-tailed *t*-test. (b) Schematic diagram of a larval wing imaginal disc, with notum, hinge and pouch in light gray, dark gray and white, respectively. (c-d) β -galactosidase staining (red) in control (*dpp > GFP*) (c) and *hipk*-expressing (*dpp > GFP + hipk*) (d) wing discs harboring a *lacZ* reporter to monitor the transcriptional induction of *dMyc* (*dMyc-lacZ*). White arrowhead in (d') indicates robust upregulation of *dMyc* in the wing hinge. (e-f) *dMyc* staining (gray) in control (*dpp>GFP*) (e) and *hipk*-expressing (*dpp>GFP + hipk*) (f) wing discs. White arrowhead in f' indicates *dMyc* accumulation in the wing hinge. GFP (green) marks the transgene-expressing cells. Scale bars, 50 μ m.

Larval wing discs are mainly composed of three regions known as the notum, hinge and pouch, corresponding to the adult structures they give rise to (Figure 5.6 b). Using a *dMyc-lacZ* enhancer trap (encoding β -galactosidase (β -gal)) to monitor the transcriptional control of *dMyc* *in vivo*, we observed that *dMyc* was expressed at high

levels in the pouch region of control discs (**Figure 5.6 c**). In the hinge and notum areas of control discs, *dMyc* was minimally and weakly expressed, respectively.

In *hipk*-expressing discs, we found intense β -galactosidase staining, confirming that *Hipk* cell-autonomously drives transcriptional upregulation of *dMyc* (**Figure 5.6 d**). Interestingly, the increase in the β -gal signal intensity appeared to be the largest in the wing hinge where the tumor cells proliferated most rapidly, while the intensity faded when moving away from the hinge region.

The variability in *Hipk*-induced *dMyc* accumulation suggests a potential region-specificity in *dMyc* upregulation. To assess this, we generated random flip-out clones of *hipk*-expressing cells. The clones were marked by RFP. We observed that *hipk*-expressing clones located in the dorsal hinge (**Figure 5.7 c-d**), the lateral hinge (**Figure 5.7 e**) as well as the epithelium on the peripodial side (**Figure 5.7 f**) exhibited marked *dMyc* accumulation. On the contrary, when *hipk*-expressing clones were located in the wing pouch, *dMyc* levels appeared unchanged (**Figure 5.7 g**). Altogether, our data imply that elevated *Hipk* drives *dMyc* upregulation in a region-specific manner.

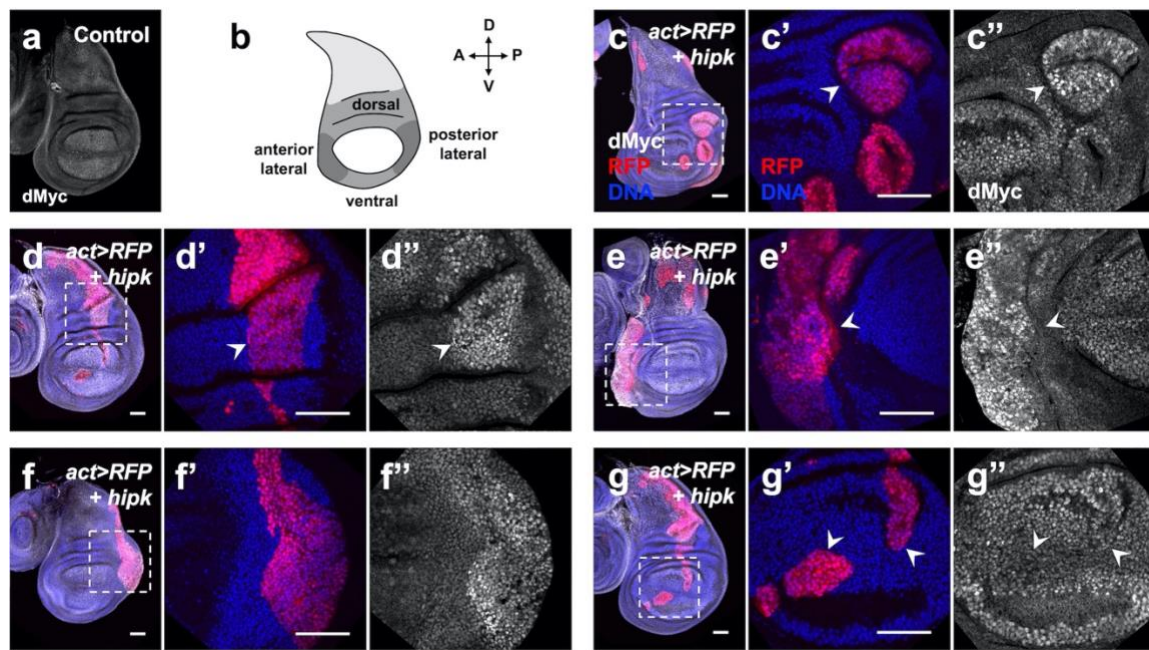


Figure 5.7. Elevated Hipk induces *dMyc* accumulation in the wing hinge region.

(a) *dMyc* staining (gray) in a control wing disc. (b) Schematic diagram of a larval wing imaginal disc. The hinge region can be divided into dorsal, lateral and ventral compartments. (c) *dMyc* staining (gray) in flip-out clones expressing *hipk* located in the dorsal hinge region

(c-d), in the lateral hinge region **(e)**, on the peripodial side **(f)** and in the pouch region **(g)** under the control *actin-Gal4*. RFP (red) marks the transgene-expressing clones. DAPI staining for DNA (blue) reveals tissue morphology. **c'**, **c''-g'**, **g''** are magnified images of the insets (dashed lines) in **c-g**. **(c-e)** White arrowheads indicate dMyc accumulation in *hipk*-expressing clones. **(g)** White arrowheads indicate unchanged dMyc protein levels in *hipk*-expressing clones. Scale bars, 50 μ m.

5.4.5. Elevated Hipk upregulates dMyc likely through convergence of multiple perturbed signaling cascades

We further investigated the molecular mechanisms underlying the upregulation of dMyc in Hipk tumor cells. Earlier studies have demonstrated that Hipk is a versatile regulator of numerous signaling pathways. For example, Hipk stimulates the transcriptional activity of Yorkie (Yki, a *Drosophila* orthologue of YAP/TAZ), the effector of the Hippo tumor suppressor pathway (Chen and Verheyen, 2012; Poon et al., 2012). Hipk also functions as a positive regulator of both Wnt/Wingless (Wg) and Hedgehog signaling by stabilizing Armadillo (β -catenin in vertebrates) and Cubitus interruptus (Ci; Gli in vertebrates), respectively (Lee et al., 2009b; Swarup and Verheyen, 2011). In addition, Hipk has been found to antagonize Groucho, a global co-repressor, to promote Notch signal transduction (Lee et al., 2009a). If Hipk-induced dMyc upregulation is through deregulation of multiple signaling pathways, we would expect to see dMyc accumulation when the signaling pathways are perturbed. We first focused on the dorsal hinge area since ectopic dMyc expression and tumor growth are most striking in such region in *hipk*-expressing discs.

Flip-out clones expressing a constitutively active form of Yki (Yki-S168A) to inactivate the Hippo pathway were usually round and most of them in the dorsal hinge displayed dMyc upregulation (Figure 5.8 d white arrowheads). Wing discs with flip-out clones expressing an active form of Arm (Arm-S10) featured an expansion in the hinge area and some dMyc accumulated at the interface between the clone and the neighboring wild-type cells (Figure 5.8 e white arrowheads) but not at the center of the clone. Flip-out clones expressing Ci to activate Hedgehog signaling in the hinge region were round or irregular in shape and exhibited elevated levels of dMyc (Figure 5.8 f white arrowheads). Consistent with previous findings (Djiane et al., 2013), expression of activated Notch appeared to induce dMyc accumulation in both cell and non-cell autonomous fashions in the hinge area likely involving a signaling relay (Figure 5.8 g white arrowheads). Therefore, individual perturbation of signaling pathways that have been previously shown to be regulated by Hipk was sufficient to trigger ectopic dMyc expression in the wing hinge region.

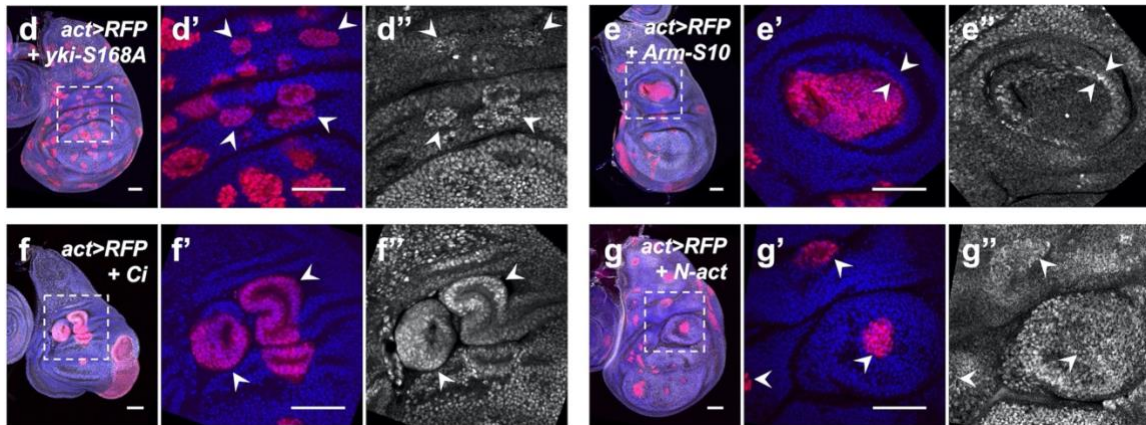


Figure 5.8. Perturbations in cell signaling induce dMyc accumulation in the wing hinge region.

(d-g) dMyc staining (gray) in flip-out clones expressing *yki-S168A* (d), *Arm-S10* (e), *Ci* (f) or *N-act* (g) under the control of *actin-Gal4*. RFP (red) marks the transgene-expressing clones. DAPI staining for DNA (blue) reveals tissue morphology. d', d''-g', g'' are magnified images of the insets (dashed lines) in d-g. (d) White arrowheads indicate *yki-S168A*-expressing clones with dMyc accumulation. (e) White arrowheads indicate ectopic dMyc expression at the boundary of the *Arm-S10*-expressing clone and the neighboring wild-type cells. (f) White arrowheads indicate dMyc upregulation in *Ci*-expressing clones. (g) White arrowheads indicate dMyc accumulation in *N-act*-expressing clones and the adjacent wild-type cells. Scale bars, 50 μ m.

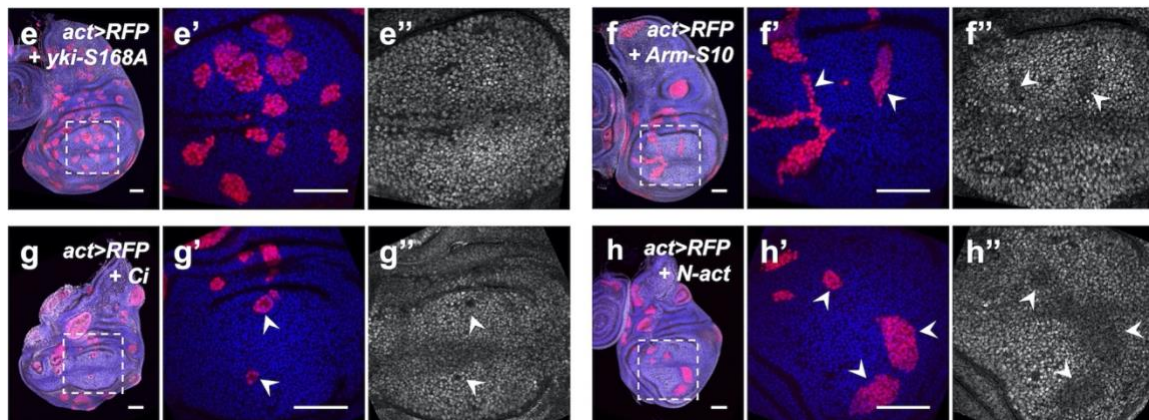


Figure 5.9. dMyc protein levels upon perturbations in cell signaling in the wing pouch region.

(e-h) dMyc staining (gray) in flip-out clones expressing *yki-S168A* (e), *Arm-S10* (f), *Ci* (g) or *N-act* (h) under the control of *actin-Gal4*. RFP (red) marks the transgene-expressing clones. DAPI staining for DNA (blue) reveals tissue morphology. (e', e''-h', h'') are magnified images of the insets (dashed lines) in (e-h). Scale bars, 50 μ m.

In the wing pouch region, activation of Yki failed to cause any dMyc upregulation (**Figure 5.9 e**). This is in contrast to previous findings that overexpression of Yki increased dMyc protein levels in both hinge and pouch regions (Ziosi et al., 2010). Such discrepancy could be due to the different expression levels of the *UAS-Yki* constructs. Flip-out clones expressing Arm-S10 (**Figure 5.9 f**) or activated Notch (**Figure 5.9 g**) displayed reduced dMyc expression, which is consistent with earlier studies showing that Wg and Notch signaling negatively regulate dMyc expression in the pouch region (Duman-Scheel et al., 2004; Herranz et al., 2008). Clones with *Ci* overexpression were few and tiny in the wing pouch and the dMyc levels in the clones seemed comparable to those in the neighboring wild-type cells (**Figure 5.9 g**). Our data suggest that the region specificity in dMyc upregulation applies to not only Hipk tumor cells, but also cells with other tumorigenic stimuli.

In summary, our data show that *in the wing hinge region where Hipk tumor growth is most prominent, dMyc protein markedly accumulates*. Individual perturbations in signaling pathways that have been shown to be regulated by Hipk also result in ectopic dMyc expression in the same region. Hence, it is likely that in the rapidly proliferating Hipk tumor cells, aberrant signals propagate and converge at the transcriptional control of dMyc. In other words, *the modulation of dMyc levels by Hipk seems to be a cumulative effect of alterations in multiple signaling outputs*.

5.4.6. Hipk-induced dMyc governs aerobic glycolysis and tumor growth

In addition to growth control, dMyc/MYC plays a conserved role in upregulating glycolysis in vertebrates and *Drosophila* during normal development and in cancers (de la Cova et al., 2014; Gallant, 2013). As expected and previously reported (de la Cova et al., 2014), overexpression of *dMyc* caused marked 2-NBDG uptake (Figure 5.10 a, d) and promoted glycolytic gene expression (Figure 5.10 e). More importantly, knockdown of *dMyc* by RNAi in hipk-expressing discs reversed the 2-NBDG accumulation (Figure 5.10 c, d) and moderately suppressed glycolytic gene upregulation (Figure 5.10 e), suggesting that dMyc is essential for the enhanced glycolysis in Hipk tumor cells.

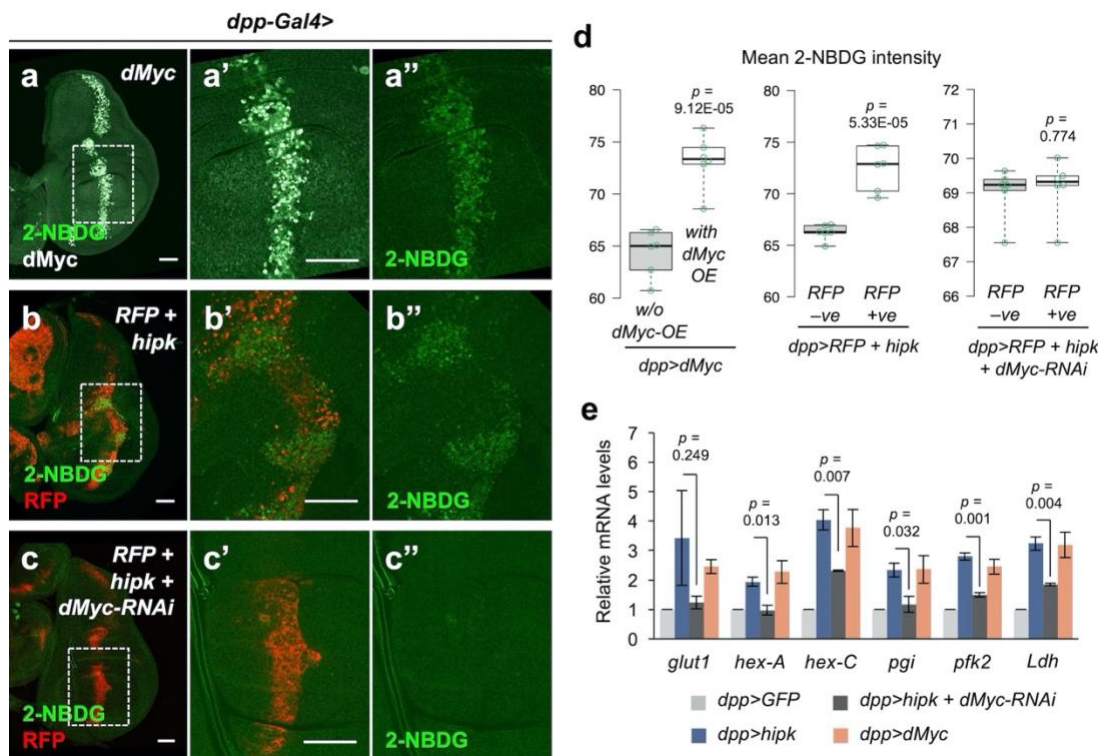


Figure 5.10. dMyc is required for Hipk-induced aerobic glycolysis.

(a-c) Incorporation of 2-NBDG (green) in *dMyc*-expressing wing disc (*dpp > dMyc*) (a), *hipk*-expressing wing disc (*dpp > RFP + hipk*) (b), and *hipk*-expressing wing disc with *dMyc* knockdown (*dpp > RFP + hipk + dMyc-RNAi*) (c). Insets (dashed line) in a, b and c are magnified in a'-a'', b'-b'' and c'-c'', respectively. *dMyc* staining (gray) in a marks the *dMyc*-overexpressing cells. *RFP* (red) in b and c marks the transgene-expressing cells. **(d)** Quantification of mean 2-NBDG intensity in *dMyc*-expressing cells and the neighboring wild-type cells in *dMyc*-expressing wing discs (*dpp > dMyc*) (left), in *hipk*-

expressing cells (RFP positive) and the neighboring wild-type cells (RFP negative) in *hipk*-expressing discs (*dpp > RFP + hipk*) (**middle**) and, in *hipk*, dMyc-RNAi co-expressing cells (RFP positive) and the neighboring wild-type cells (RFP negative) in *hipk*-expressing discs with dMyc knockdown (*dpp > RFP + hipk + dMyc-RNAi*) (**right**). $n = 6$ discs per genotype. (**e**) qRT-PCR analysis of expression of a set of glycolytic genes in *hipk*-expressing wing discs (*dpp > hipk*), *hipk*-expressing discs with dMyc knockdown (*dpp > hipk + dMyc-RNAi*), and dMyc-expressing discs relative to control discs (*dpp > GFP*). Data are mean \pm sem. $n = 3$ independent experiments with samples pooled from 10 to 20 wing discs per genotype. Exact p values are shown and calculated using unpaired two-tailed t -test.

Additionally, knockdown of dMyc significantly suppressed the tumorous growth and tissue distortions in *hipk*-expressing discs, as seen by the decrease in GFP positive cells (**Figure 5.11 f-g**). Using an independent RNAi construct targeting dMyc (dMyc-RNAi #2), we observed a similar effect upon silencing of dMyc (**Figure 5.11 h**). dMyc immunofluorescent staining showed the efficient knockdown when dMyc-RNAi constructs were expressed (**Figure 5.11 g-i**). Wing discs with dMyc knockdown alone appeared wild type (**Figure 5.11 i**). Altogether, our results imply that the dMyc-induced glycolysis may be a key driver for Hipk tumor growth. Intriguingly, overexpression of dMyc alone (**Figure 5.10 a**), despite the enhanced glycolysis, failed to reproduce the tumorous phenotypes observed in *hipk*-expressing discs (**Figure 5.11 f**). Thus, while upregulation of dMyc is indispensable for Hipk-induced glycolysis and tumor growth, additional mechanisms are involved in the Hipk tumors to trigger the tumorigenesis.

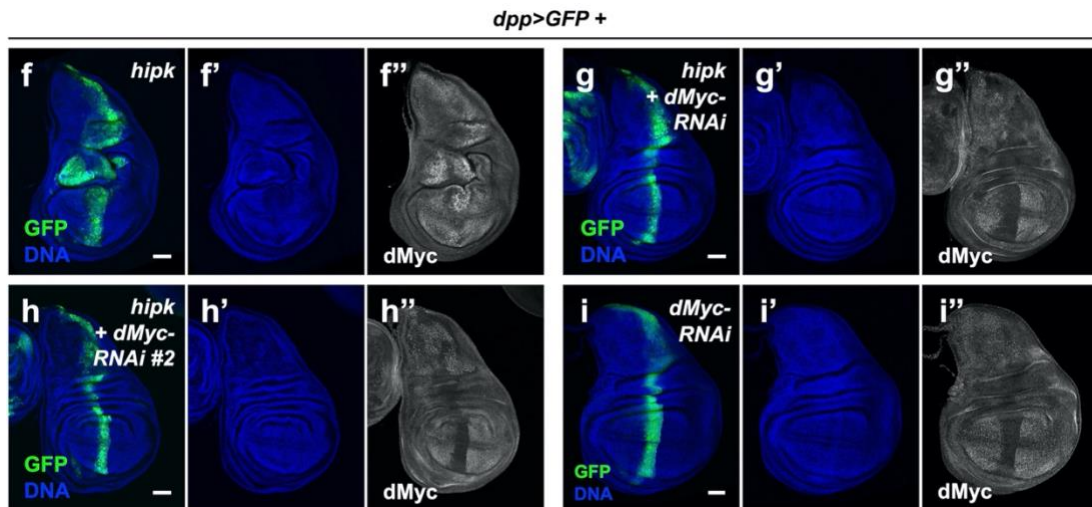


Figure 5.11. dMyc is required for Hipk tumor growth.

(**f-i**) dMyc staining (gray in **f''-i''**) in *hipk*-expressing disc (*dpp > GFP + hipk*) (**f**), *hipk* and dMyc-RNAi co-expressing disc (*dpp > GFP + hipk + dMyc-RNAi*) (**g**), *hipk* and dMyc-RNAi #2 co-expressing disc (*dpp > GFP + hipk + dMyc-RNAi #2*) (**h**)

and *dMyc* knockdown disc (*dpp > GFP + dMyc-RNAi*) (i). GFP (green) marks the transgene-expressing cells. DAPI staining for DNA (blue) reveals tissue morphology. Scale bars 50 μ m.

5.4.7. Aerobic glycolysis (the Warburg effect) is essential to tumor growth through sustaining ectopic *dMyc* expression

Earlier studies have shown that flies incompetent at glycolysis displayed reduced viability as deletion or ubiquitous knockdown of the glycolytic genes *pfk*, *ald*, *pgk*, *pglym78*, *eno* or *pyk* resulted in lethality (Gerber et al., 2006; D. Miller et al., 2012; Tennessen et al., 2011; Volkenhoff et al., 2015). Likewise, we observed that flies ubiquitously depleted of *Pgk* (*act5c > pgk-RNAi*) failed to reach the larval stage. Flies lacking *Pfk* (*act5c > pfk-RNAi*) or *Pyk* (*act5c > pyk-RNAi*) reached the larval stage but could not pupariate. Flies with reduced *Pfk2* (*act5c > pfk2-RNAi*) died at the early pupal stage but did not differentiate further to become late pupae. Most flies lacking *Glut1* (*act5c > glut1-RNAi*) or *Pgi* (*act5c > pgi-RNAi*) succeeded in emerging as adults. The timing of lethality following knockdown targeting glycolytic genes could presumably be influenced by maternal contribution, knockdown efficiency or the importance of the glycolytic step which the particular enzyme controls.

To confirm the regulatory roles of *Pfk* and *Pfk2* in glycolytic flux, we measured the relative pyruvate content in the knockdown larvae. Consistent with previous work (Li et al., 2018), knockdown of *pfk* significantly decreased pyruvate levels (Figure 5.12). Similarly, knockdown of *pfk2* induced an approximately 60% drop in the pyruvate content. The knockdown efficiencies of all RNAi constructs used in this study to silence glycolytic genes were evaluated by qRT-PCR analyses (Figure 5.3).

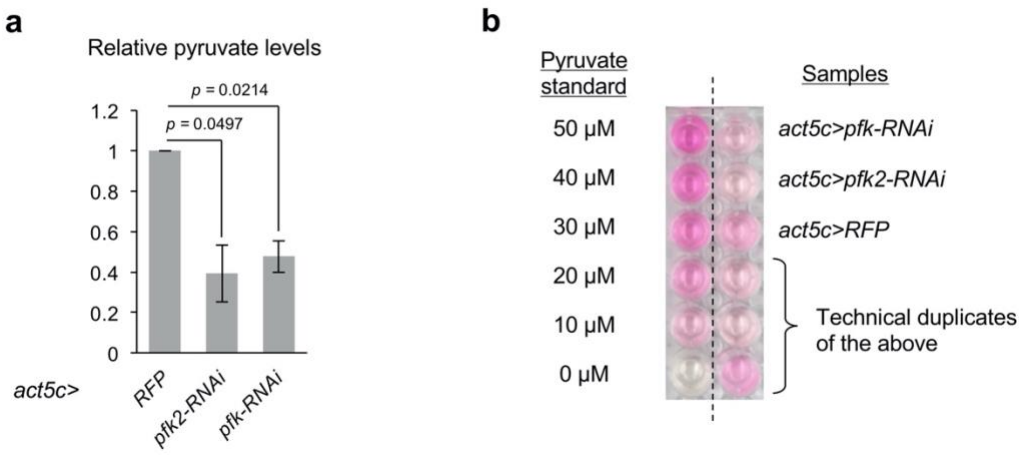


Figure 5.12. Knockdown of *pfk2* or *pfk* causes decreases in the pyruvate levels.

(a) Relative pyruvate levels in control (*act5c > RFP*), *pfk2* knockdown (*act5c > pfk2-RNAi*) and *pfk* knockdown (*act5c > pfk-RNAi*) larvae. Data are mean \pm sem and pooled from two biological replicates. Exact *p* values are shown and calculated using unpaired two-tailed *t*-test. **(b)** The representative result of the colorimetric assay for pyruvate measurement from one set of biological samples. The left column shows the pyruvate standards. The right column shows the biological samples with the indicated genotypes.

To examine the roles of glycolytic activation in Hipk tumor cells, we used RNAi to deplete key glycolytic genes. Knockdown of *hex-A* or *hex-C* had negligible effects on Hipk tumor growth; as did *hex-A* and *hex-C* double knockdown (Figure 5.13). Similarly, knockdown of *glut1* or *pgi* failed to block Hipk-induced tumorigenesis (Figure 5.14 a-b). Knockdown of *pgk*, *pyk* or *Ldh* appeared to slightly restrict Hipk tumor growth but the tissue morphology remained distorted (Figure 5.14 c-d, Figure 5.15 d).

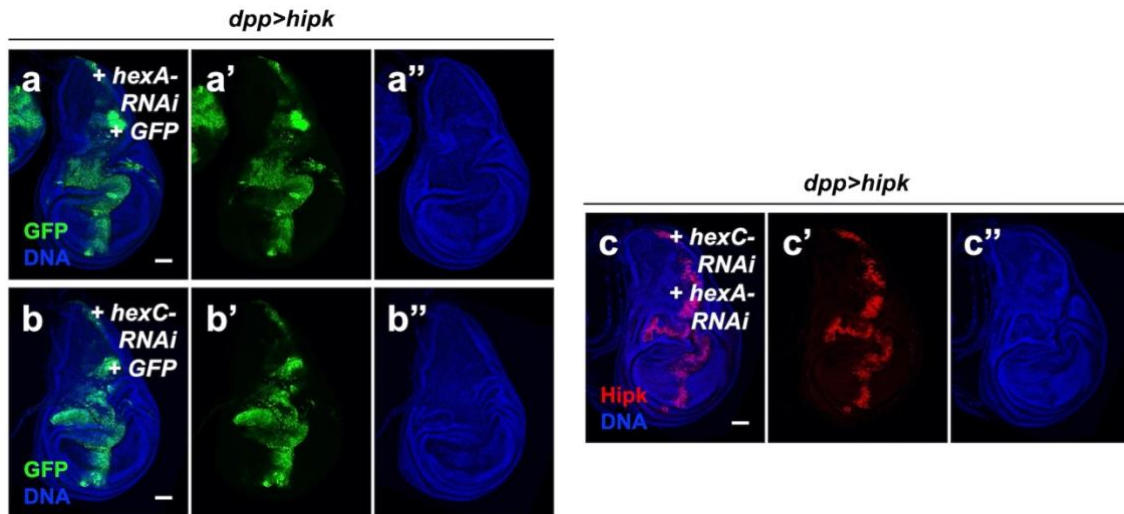


Figure 5.13. Knockdown of *hex-A* and *hex-C* fail to suppress Hipk tumor growth.

(a-b) *hipk*-expressing wing disc with *hex-A* knockdown (a) or *hex-C* knockdown (b). GFP (green) marks the transgene-expressing cells. (c) *hipk*-expressing wing disc with *hex-A* and *hex-C* double knockdown. Hipk staining (red) marks the transgene-expressing cells. DAPI staining for DNA (blue) reveals tissue morphology. Scale bars, 50 μ m.

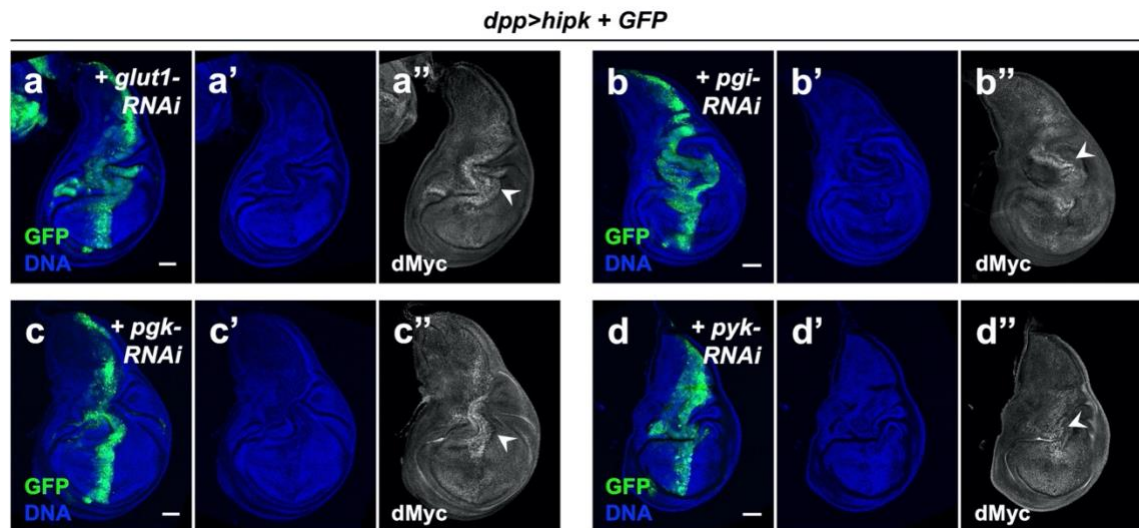


Figure 5.14. Non-targeted inhibition of glycolysis is not sufficient to prevent tumor growth nor dMyc accumulation.

(a-d) dMyc staining (gray) in *hipk* and *glut1-RNAi* co-expressing disc (*dpp > GFP + hipk + glut1-RNAi*) (a), *hipk* and *pgi-RNAi* co-expressing disc (*dpp > GFP + hipk + pgi-RNAi*) (b), *hipk* and *pgk-RNAi* co-expressing disc (*dpp > GFP + hipk + pgk-RNAi*) (c) and *hipk* and *pyk-RNAi* co-expressing disc (*dpp > GFP + hipk + pyk-RNAi*) (d). GFP (green) marks the transgene-expressing cells. DAPI staining for DNA (blue) reveals tissue morphology. Scale bars, 50 μ m.

Knockdown of *pfk2*, on the contrary, markedly prevented tumor growth and restored tissue architecture in *hipk*-expressing discs (**Figure 5.15 b**), suggesting that the committed step of glycolysis determines *Hipk* tumorigenesis. Indeed, the effect of *pfk* knockdown was comparable to that of *pfk2* knockdown (**Figure 5.15 c**), even though we did not detect significant *pfk* upregulation (<1.5 fold) in *hipk*-expressing discs (**Figure 5.5 a-b**).

We also examined dMyc expression in *Hipk* tumor cells when glycolysis was inhibited. Intriguingly, dMyc accumulation was largely abolished in *hipk*-expressing discs when *pfk2* or *pfk* was knocked down (**Figure 5.15 a-c**). In the absence of *hipk* overexpression, neither knockdown of *pfk* nor *pfk2* affected the normal dMyc expression pattern nor led to defects in tissue growth (**Figure 5.16**). Knockdown of *glut1*, *pgi*, *pgk*, *pyk* or *Ldh* in *Hipk* tumor cells did not rescue dMyc upregulation (**Figure 5.14**, **Figure 5.15 d**). Together, our results suggest that *dMyc accumulation and the associated Hipk tumor growth are most sensitive to the committed step of glycolysis governed by Pfk2-Pfk*.

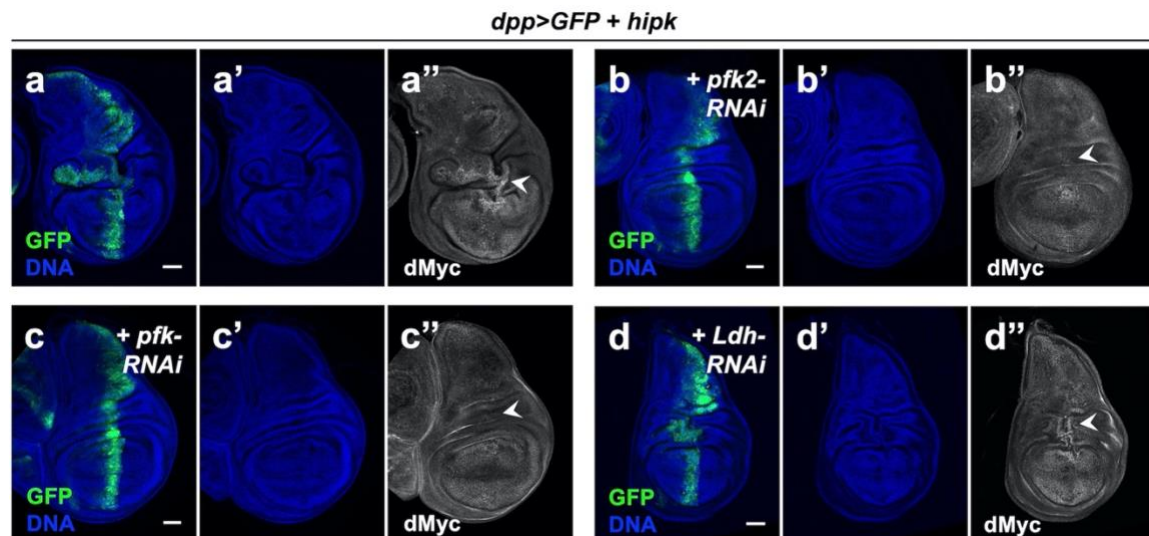


Figure 5.15. Pfk2 and Pfk sustain dMyc accumulation and Hipk tumor growth.

(a-d) dMyc staining (gray) in *hipk*-expressing wing disc (*dpp > GFP + hipk*)
(a), *hipk* and *pfk2-RNAi* co-expressing disc (*dpp > GFP + hipk + pfk2-RNAi*)
(b), *hipk* and *pfk-RNAi* co-expressing disc (*dpp > GFP + hipk + pfk-RNAi*) **(c)** and *hipk* and *Ldh-RNAi* co-expressing disc (*dpp > GFP + hipk + Ldh-RNAi*) **(d)**. GFP (green) marks the transgene-expressing cells. DAPI staining for DNA (blue) reveals tissue morphology. Scale bars, 50 μ m.

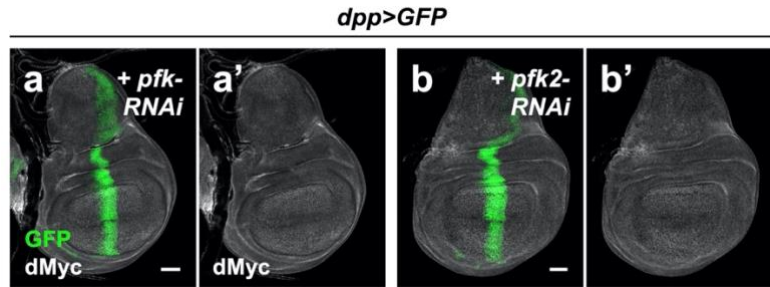


Figure 5.16, Pfk2 and Pfk do not affect dMyc expression in the absence of *hipk* overexpression.

(a-b) dMyc staining (gray) in *pfk* knockdown discs (*dpp > GFP + pfk-RNAi*) (a) and *pfk2* knockdown discs (*dpp > GFP + pfk2-RNAi*) (b). GFP (green) marks the transgene-expressing cells. Scale bars, 50 μ m.

Using the *dMyc-lacZ* reporter, we found that dMyc transcriptional activation remained robust when *pfk2* or *pfk* was depleted in Hipk tumor cells even though the tumor growth was reduced (Figure 5.17) and dMyc protein levels were reduced (Figure 5.15 a-c). Thus, our data indicate that *Pfk2* and *Pfk* are required to sustain ectopic dMyc expression specifically in Hipk tumor cells through post-transcriptional regulation.

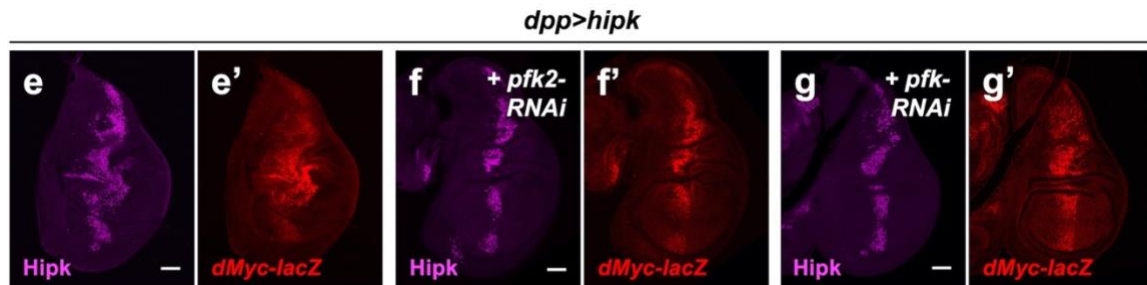


Figure 5.17. Knockdown of *pfk2* or *pfk* does not affect the transcriptional induction of dMyc by Hipk.

(e-g) Hipk staining (magenta) and β -galactosidase staining (red) in *hipk*-expressing disc (*dpp > hipk*) (e), *hipk* and *pfk2-RNAi* co-expressing disc (*dpp > hipk + pfk2-RNAi*) (f), *hipk* and *pfk-RNAi* co-expressing disc (*dpp > hipk + pfk-RNAi*) (g). All wing discs harbor a *lacZ* reporter to monitor the transcriptional induction of *dMyc* (*dMyc-lacZ*). Scale bars, 50 μ m.

The control of Hipk tumor growth by Pfk2 or Pfk seemed not to be a consequence of altered Hipk protein stability or functions because of the following reasons. First, we did not detect a noticeable change in Hipk protein levels in discs depleted of Pfk2 or Pfk when compared with discs expressing *hipk* alone (Figure 5.17), indicating that blocking glycolysis does not trigger Hipk protein degradation. Second, the

robust stimulation of the *dMyc-lacZ* reporter in *hipk*-overexpressing discs with *pfk2* or *pfk* knockdown suggests that Hipk activities remain intact. Indeed, when we examined other signaling targets downstream of Hipk as readouts for Hipk activity, we found that Hipk-mediated stabilization of Armadillo (Wnt/Wg signaling), and induction of Cyclin E or expanded-lacZ (Hippo signaling) remained unaffected by knockdown of *pfk2* or *pfk* in a *hipk*-overexpression background, indicating Hipk is still functional (**Figure 5.18**).

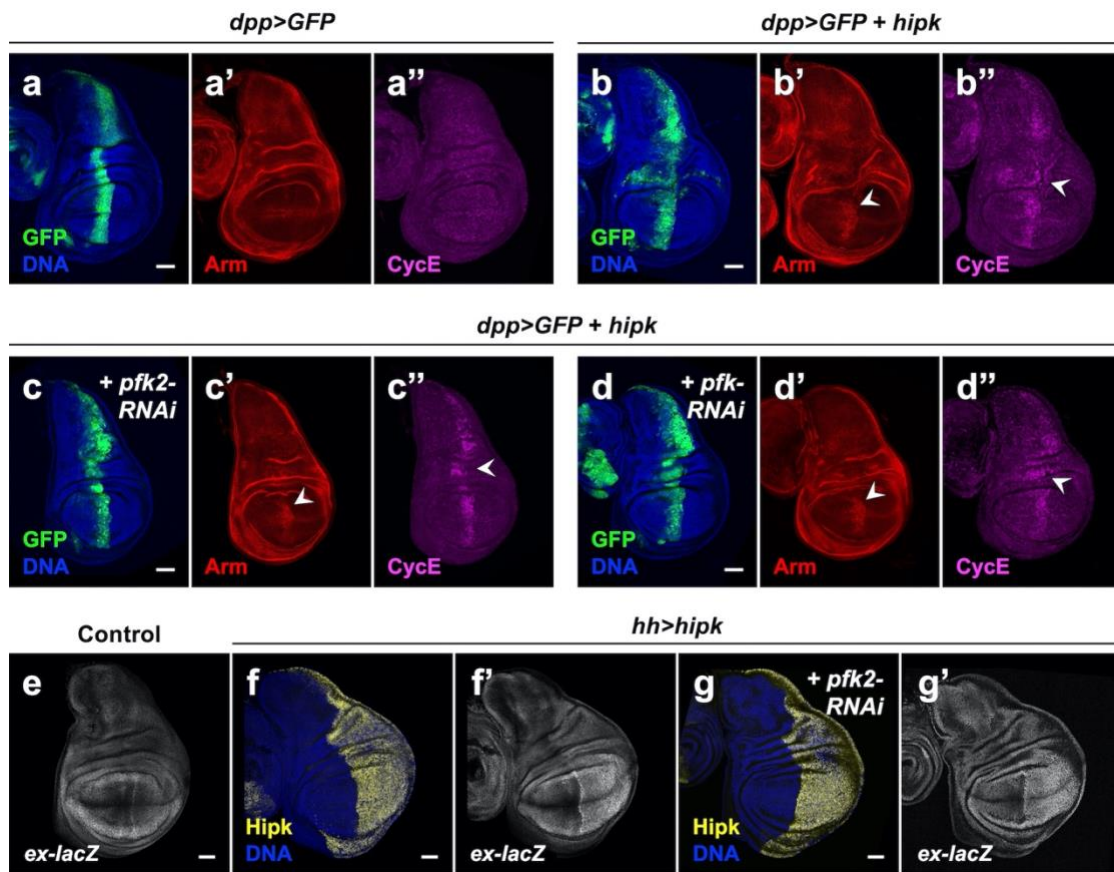


Figure 5.18. Knockdown of *pfk2* or *pfk* does not affect Hipk activities.

(a-b) Armadillo (Arm, red) and Cyclin E (CycE, magenta) in control discs (*dpp > GFP*) (a), *hipk*-expressing discs (*dpp > GFP + hipk*) (b), *hipk*-expressing discs with *pfk2* knockdown (*dpp > GFP + hipk + pfk2-RNAi*) (c), *hipk*-expressing discs with *pfk* knockdown (*dpp > GFP + hipk + pfk-RNAi*) (d). White arrowheads in b', c' and d' indicate stabilization of Arm in the pouch region. White arrowheads in b'', c'' and d'' indicate CycE induction along the anterior/posterior boundary of the wing discs. GFP (green) marks the transgene-expressing cells. (e-g) β -galactosidase staining (gray) in control disc (*hh-Gal4*) (e), *hipk*-expressing disc (*hh > hipk*) (f) and *hipk*-expressing disc with *pfk2* knockdown (*hh > hipk + pfk2-RNAi*) (g). *Hh-Gal4* drives transgenic expression in the posterior compartment of wing discs (left half of the discs). All wing discs harboring a *lacZ* reporter to monitor the transcriptional induction of *expanded* (*ex-lacZ*). *Hipk* staining (yellow) in f and g marks the transgene-expressing cells (posterior compartment). Scale bars, 50 μ m.

Altogether, our data suggest that *while dMyc upregulation promotes glycolytic activities, the upregulation of Pfk2, along with subsequent F2,6-BP biosynthesis and Pfk activation, is required to foster the accumulation of dMyc proteins*. In other words, a positive feedback loop between dMyc and aerobic glycolysis is formed, coordinating growth signals with metabolic states to reinforce tumor progression.

5.5. Discussion

5.5.1. dMyc-driven aerobic glycolysis in the Hipk tumor model

Multiple approaches and tools have been developed to measure glycolysis including measurement of the extracellular acidification rate (ECAR), fluorescent probes, biosensors, fluorescent/colorimetric assays and mass spectrometry (Bittner et al., 2010; Tennessen et al., 2014; TeSlaa and Teitell, 2014). In the Hipk tumor model, the tumor cells are surrounded by wild-type cells. Our study primarily used fluorescence imaging such that we could examine changes in metabolite levels, gene and protein expression between tumor cells and the adjacent wild-type cells. Our work delineates the causes and significance of metabolic changes in tumor cells.

Drosophila tumor models frequently acquire metabolic changes, especially the Warburg effect. For instance, epidermal growth factor receptor (EGFR)-driven tumors, tumors with activated platelet-derived growth factor (PDGF)/vascular endothelial growth factor (VEGF) receptor (Pvr) and tumors with polarity loss (such as *scrib* or *dlg* mutant tumors) feature robust upregulation of *Ldh* among other glycolytic genes (Bunker et al., 2015; Eichenlaub et al., 2018; Wang et al., 2016). Depletion of *Ldh* was shown to reduce growth of EGFR-driven tumors but not tumors with polarity loss (Bunker et al., 2015; Eichenlaub et al., 2018). In *RasV12scrib*^{-/-} tumors, elevated glucose uptake was evident, but its significance was not evaluated (Katheder et al., 2017). Similar to the previously described models, Hipk tumor cells exhibited elevated glucose metabolism (**Figure 5.1**, **Figure 5.4**, **Figure 5.5**). Metabolic reprogramming was driven by dMyc upregulation (**Figure 5.6**, **Figure 5.7**, **Figure 5.10**). Although the transcript levels of another glycolytic inducer Sima (HIF-1 α) remained unchanged (**Figure 5.6 a**), we could not eliminate the possibility that Sima protein levels are altered in the tumor cells. Thus, whether Sima is involved in the tumor growth warrants further studies. Genetical inhibition of Pfk or Pfk2 was sufficient to block Hipk-induced tumorigenesis whereas depletion of Pgk, Pyk or Ldh at most slightly reduced tumor growth (**Figure 5.14**, **Figure 5.15**). Therefore, our data suggest that targeted but not generic inhibition of glycolysis is required to abrogate tumor growth.

5.5.2. A feedback loop between dMyc and aerobic glycolysis as a metabolic vulnerability in tumor cells

Although MYC functions in cancer metabolism are widely recognized, MYC is generally considered ‘undruggable’ largely due to its nuclear localization, lack of an enzymatic ‘active site’, and indispensable roles during normal development (Soucek and Evan, 2010). Hence, limited therapeutic strategies have been developed, and identification of the ‘druggable’ regulatory proteins of MYC becomes critical.

Our study reveals two modes of dysregulation of endogenous dMyc specifically during Hipp-induced tumorigenesis. The first mode is transcriptional stimulation of dMyc likely as a consequence of convergence of multiple signaling outputs (Figure 5.8, Figure 5.9). In our previous study, we found that genetically targeting individual signaling cascades failed to restrain Hipp tumor growth (Blaquiere et al., 2018). This is likely due to the redundancy of signaling cascades in inducing dMyc upregulation. It is also interesting to note that dMyc upregulation and the associated tumor growth are most striking in the wing hinge (Figure 5.6, Figure 5.7). The pouch region, however, seems more refractory to such alterations. We also observed the lowest intracellular glucose levels (Figure 5.4) and robust Ldh upregulation (Figure 5.5) in the hinge area. dMyc-dependent glucose uptake (Figure 5.10), on the other hand, was enhanced in both hinge and pouch regions even though dMyc protein buildup is undetectable in the wing pouch, suggesting that glucose uptake is particularly sensitive to changes in dMyc levels. Our data therefore imply that the Warburg effect and the tumor growth phenotype may be linked to the dMyc levels being induced. The region-specific susceptibility to tumorigenic stimuli has been previously described and the hinge region was coined a ‘tumor hotspot’ because of its unique epithelial cell architectures and high endogenous JAK/STAT signaling (Tamori et al., 2016). It is possible that such features in the hinge region also contribute to the sensitivity of dMyc upregulation by elevated Hipp and other signaling pathways. Further studies are required to verify this proposition.

The second mode of dMyc regulation is the metabolic control of dMyc protein levels by aerobic glycolysis. Specifically, we found that the rate-limiting enzymes Pfk2 and Pfk are required to perpetuate dMyc buildup in tumor cells in a post-transcriptional manner (Figure 5.15, Figure 5.17). Similar to the effects on tumor growth, while *pfk2* or *pfk* knockdown prevented dMyc accumulation, knockdown of other glycolytic enzymes

had little effect on sustaining dMyc accumulation. Such a disparity could possibly be explained by the potency of the glycolytic enzymes in controlling glycolytic flux. While Pfk2 and Pfk govern the rate-limiting, committed step of glycolysis, RNAi targeting other glycolytic genes may fail to render the corresponding steps rate-limiting, especially in tumors with elevated aerobic glycolysis. In other words, knockdown of other glycolytic enzymes may not reach the threshold that would restrict glycolytic flux as potently as *pfk2* or *pfk* knockdown. Given that Pfk2 is mis-expressed in tumor cells but not in normal cells (**Figure 5.5**) and that dMyc accumulation is most sensitive to the Pfk2-Pfk mediated committed step of glycolysis specifically in tumor cells (**Figure 5.15**), targeting Pfk2 may be a favorable, selective metabolic strategy in the treatment of cancers, especially those displaying ectopic MYC expression.

5.5.3. Potential pro-tumorigenic roles of the Pfk and Pfk2 in addition to their core biochemical role in glycolysis

The human homologs of fly Pfk and Pfk2 are PFK and PFK-2/FBPase (PFKFB), respectively. The functions of mammalian PFK and PFKFB in controlling glycolytic flux are well-defined. The allosteric regulation of PFK by F2,6-BP seems to be conserved among mammals and insects as F2,6-BP is able to activate insect Pfk, likely due to the conserved amino acid residues for F2,6-BP binding ([Nunes et al., 2016](#)). This suggests that Pfk2 can induce Pfk activation and hence glycolytic flux through biosynthesizing F2,6-BP. A previous report shows that flies lacking Pfk2 exhibited levels of circulating glucose and reduced sugar tolerance, providing a functional link between Pfk2 and glucose metabolism ([Havula et al., 2013](#)). We provide evidence that both *pfk2* and *pfk* knockdown larvae exhibited significant decreases in pyruvate contents ([Figure 5.12](#)), confirming a conserved role of Pfk2 in regulating glycolytic flux.

Recently, the roles of PFK and PFKFB in the regulation of transcription factors or cofactors have drawn considerable attention. For example, vertebrate PFK was shown to physically interact with TEAD factors to stimulate YAP/TAZ activity, thus promoting proliferation and malignancy in cancer cells ([Enzo et al., 2015](#)). PFKFB4 (an isoform of PFK2) phosphorylates and activates oncogenic SRC-3 to promote breast cancers through stimulating purine synthesis ([Dasgupta et al., 2018](#)). These studies point to the fact that PFK and PFKFB functions are not restricted to metabolic regulation. Thus, it is tempting to speculate that Pfk2/Pfk may sustain ectopic dMyc through a direct interaction with or even phosphorylation of dMyc. That being said, as knockdown of *pfk2* or *pfk* had no effects on dMyc protein levels under normal conditions ([Figure 5.16](#)), we tend to believe that a tumorigenic environment with active aerobic glycolysis is necessary for the metabolic control of dMyc in particular through the committed step governed by Pfk2/Pfk.

In summary, we and others show that glycolytic enzymes Pfk and Pfk2, likely through their core biochemical role in stimulating glycolytic flux, glycolysis-independent actions or both, act as key players in coupling metabolic demands with growth signals to achieve cancer progression.

Chapter 6.

Pdsw (NDUFB10) of Respiratory Complex I as a metabolic vulnerability in the Hipk tumor model

The work shown in **Chapter 6** is unpublished.

Kenneth Kin Lam Wong, Jenny Zhe Liao, Claire R. Y. Shih, Nicholas Harden and **Esther M. Verheyen**. Pdsw (NDUFB10) of Respiratory Complex I as a metabolic vulnerability in a *Drosophila* tumor model. *Unpublished* (2020).

6.1. Contributions to the Chapter

K.K.L.W. Conceptualization, Data curation, Formal analysis, Investigation, Visualization, Writing-original draft, Writing-review and editing; **J.Z.L.** Formal analysis, Investigation, Visualization, Writing-review and editing; **C.R.Y.S** Formal analysis, Investigation; **N.H.** Supervision, Project administration, Writing-review and editing; **E.M.V.** Conceptualization, Formal analysis, Supervision, Funding acquisition, Project administration, Writing-review and editing

6.2. Abstract

Both functional and dysfunctional mitochondria have been, paradoxically, shown to underlie cancer progression. This observation poses challenges to targeting mitochondria for cancer therapy. Here, we show that, in an *in vivo* tumor model established by elevation of oncogenic *Drosophila* Homeodomain-interacting protein kinase (Hipk), tumor cells are rich in highly fused, active mitochondria and do not accumulate reactive oxygen species (ROS). Suppression of the mitochondrial fusion phenotype is insufficient to prevent Hipk tumor growth. Inhibition of respiratory complex subunits produces Hipk tumors with high ROS and activation of c-Jun N-terminal kinase (JNK), likely accelerating tumor invasion. A notable exception is that knockdown of Pdsw (NDUFB10 in mammals, a Pd subunit of complex I) abrogates Hipk tumor growth and causes only moderate ROS. Furthermore, the tumor mitochondrial changes are downstream of a positive feedback loop between Myc and aerobic glycolysis. Altogether, we report a tumor model characterized by active mitochondrial metabolism and the complex I subunit-dependent, opposing effects on tumor progression.

6.3. Introduction

In the 1920s, Otto Warburg observed that cancer cells take up glucose and produce lactate vigorously even in the presence of oxygen, a phenomenon now termed the Warburg effect or aerobic glycolysis ([Warburg et al., 1927](#)). Warburg hypothesized that mitochondrial dysfunction is the cause of aerobic glycolysis and cancers ([WARBURG, 1956](#)), which remains highly debated today. In support of his hypothesis, succinate dehydrogenase (SDH) and fumarate hydratase (FH or fumarase), which are mitochondrial enzymes of the tricarboxylic acid (TCA) cycle, are identified as tumor suppressors ([Gottlieb and Tomlinson, 2005; King et al., 2006](#)). Mutations in SDH or FH cause cancers by stabilizing hypoxia-inducible factor 1-alpha (HIF1 α) and activating of a pseudo-hypoxic response ([Isaacs et al., 2005; Selak et al., 2005](#)). Meanwhile, a growing body of evidence has been found that contradicts Warburg's hypothesis. For example, in a comparative metabolic profiling of melanoma cell lines, all melanoma cells tested not only exhibit the Warburg effect, but also maintain functional TCA cycle activity ([Scott et al., 2011](#)). Also, a collection of data reveals that, despite high glycolytic rates, many cancer cells generate the majority of ATP through oxidative phosphorylation (OXPHOS)

(summarized in (Zu and Guppy, 2004)). All these data indicate that cancer mitochondrial metabolism is more heterogeneous than previously thought, posing great challenges in devising therapeutic strategies targeting mitochondria.

Drosophila has been extensively used to model human cancers largely due to the high conservation between human and fly genes (Sonoshita and Cagan, 2017). Interestingly, most, if not all, previously described fly tumor models are characterized by mitochondrial dysfunction. For example, the well-known *Rasv12scribble*^{-/-} tumors harbor damaged mitochondria with reduced respiratory capacity and high levels of reactive oxygen species (ROS) (Katheder et al., 2017). In tumors with activated platelet-derived growth factor (PDGF)- and vascular endothelial growth factor (VEGF)-receptor related (Pvr), pyruvate dehydrogenase is inactivated, attenuating mitochondrial flux and causing high ROS (Wang et al., 2016). Nonetheless, growing evidence points to the importance of functional mitochondria in fly tumorigenesis. For instance, larval brain tumor growths caused by loss of Brain tumor (Brat) or Notch gain-of-function can be reduced by inhibition of respiratory complex subunits (Lee et al., 2013; Van Den Ameele and Brand, 2019). Also, blocking mitochondrial fusion reduces overgrowths induced by activated Yorkie (Yki; Yes-associated protein, YAP in vertebrates) (Nagaraj et al., 2012). However, the respiratory profiles of these tumor models have not been clearly characterized. A tumor model with functional mitochondria is as yet not reported.

Homeodomain-interacting protein kinases (Hipk in fly, HIPK1-4 in vertebrates) are transcriptional co-regulators and regulators of multiple cellular signaling pathways (Chen and Verheyen, 2012; Kim et al., 1998; Lee et al., 2009b; Swarup and Verheyen, 2011; Tettweiler et al., 2019). Dysregulation of HIPKs have been implicated in certain diseases and cancers (reviewed in (Blaquiere and Verheyen, 2017)). Previously, we established elevation of *Drosophila* Hipk as an *in vivo* tumor model characterized by neoplastic overgrowth, cell invasion behaviors, cellular changes reminiscent of epithelial-to-mesenchymal transition, including induction of matrix metalloproteinase 1 (Mmp1) and loss of E-cadherin (Blaquiere et al., 2018; Chen and Verheyen, 2012). Also, Hipk has been shown to synergize with a wide array of proteins implicated in cancers to promote tumor progression (Blaquiere et al., 2018; Wong et al., 2020). Moreover, Hipk tumor cells exhibit Myc-driven aerobic glycolysis, which in turn functions to sustain accumulation of the Myc oncogene, forming a positive feedback loop (Wong et al., 2019). Here, we continue characterizing the metabolic profile of the Hipk tumor model,

with a particular focus on mitochondrial metabolism. Probing the mitochondrial morphology, membrane potential ($\Delta\psi_m$) and ROS levels, we show that the tumor cells display active mitochondrial metabolism, which is downstream of the Myc-aerobic glycolysis feedback loop. Our work identifies Pdsw (NDUFB10 in mammals), a Pd subunit of respiratory complex I (NADH:ubiquinone oxidoreductase), but not other subunits, as a metabolic vulnerability in the Hipk tumor model that could be exploited to suppress tumor growth.

6.4. Results

6.4.1. Elevated Hipk promotes mitochondrial fusion and branching

To generate the *Drosophila* Hipk tumor model, we used Gal4-UAS system (Brand and Perrimon, 1993) to induce *UAS-hipk* transgene overexpression under the control of *dpp-Gal4* driver in wing discs of developing larvae. Wing discs are epithelial tissues that give rise to wing structures in adult flies, and are commonly used to model human carcinomas (Herranz et al., 2016). The full genotype of the Hipk tumor model is *dpp-Gal4 > UAS-hipk*, abbreviated as *dpp > hipk*. Fluorescent proteins were co-expressed to mark the transgene-expressing control or tumor cells.

To assess mitochondrial energy metabolism in Hipk tumor cells, we first examined the mitochondrial morphology using a mitochondrially targeted GFP, UAS-mito-GFP (Pilling et al., 2006). In control wing discs (*dpp > mito-GFP*), mitochondria appear as puncta around the nuclei (Figure 6.1 a-a''). As previously reported (Blaquiere et al., 2018; Wong et al., 2020, 2019), when *hipk* was overexpressed (*dpp > mito-GFP + hipk*), profound expansion of the transgene-expressing domain and severe tissue distortions were evident (Figure 6.1 b), indicative of tumorous growth. More importantly, in Hipk tumor cells, patches of fused mitochondria accumulated around the nuclei, in addition to the presence of the dot-like mitochondria (Figure 6.1 b'-b'').

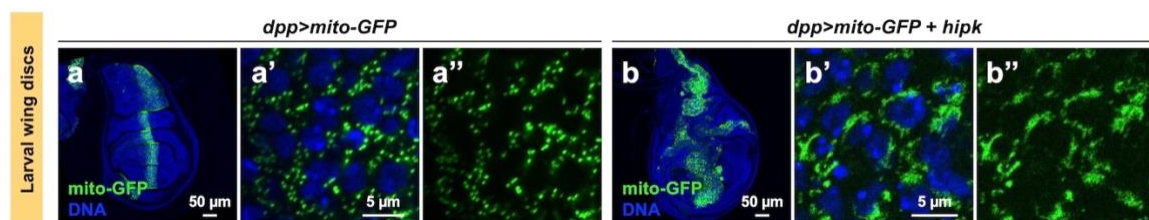


Figure 6.1. Elevated Hipk promotes tumorous growth and mitochondrial fusion.

(a-b) Control (*dpp > mito-GFP*) (a) and *hipk*-overexpressing (*dpp > mito-GFP + hipk*) (b) wing discs expressing mito-GFP (marking mitochondria in green) under the control of *dpp-Gal4*. Mitochondrial morphologies in control (a'-a'') and *hipk*-overexpressing (b'-b'') disc proper (columnar epithelial) cells of wing discs. DAPI staining for DNA (blue) shows the overall tissue morphologies and nuclei. Scale bars are shown as indicated.

We also examined two other larval tissues, muscle walls and salivary glands, because their large cell size facilitates imaging. In control muscle cells where *mito-GFP*

was expressed under a muscle-specific Gal4 driver *mef2* (*mef2 > mito-GFP*), mitochondria were abundant, and they appeared rod-shaped and tubular (**Figure 6.2 c**). Upon *hipk* overexpression (*mef2 > mito-GFP + hipk*), mitochondria were highly convoluted (**Figure 6.2 d**). In larval salivary gland cells, mitochondria appeared punctate in control cells (*dpp > mito-GFP*) (**Figure 6.2 e**). Upon *hipk* overexpression, elongated and branched mitochondria were observed, in addition to punctate mitochondria (**Figure 6.2 f**). Quantitative analyses of the single-plane images (**Figure 6.2 e'', f''**) using the Mitochondrial Network Analysis (MiNA) toolset (Valente et al., 2017) showed significant increases in the numbers of mitochondrial individuals and networks, length and branching upon *hipk* overexpression (**Figure 6.3**), revealing that Hipk promotes mitochondrial abundance as well as fusion. Three-dimensional (3D) imaging acquired by Airyscan super-resolution microscopy revealed individual mitochondria of various sizes and shapes (including punctate, rod-like, round, network and irregular) in control cells (**Figure 6.2 g**) in contrast to meshes of mitochondria with extensive, fine branches in *hipk*-overexpressing cells (**Figure 6.2 h**).

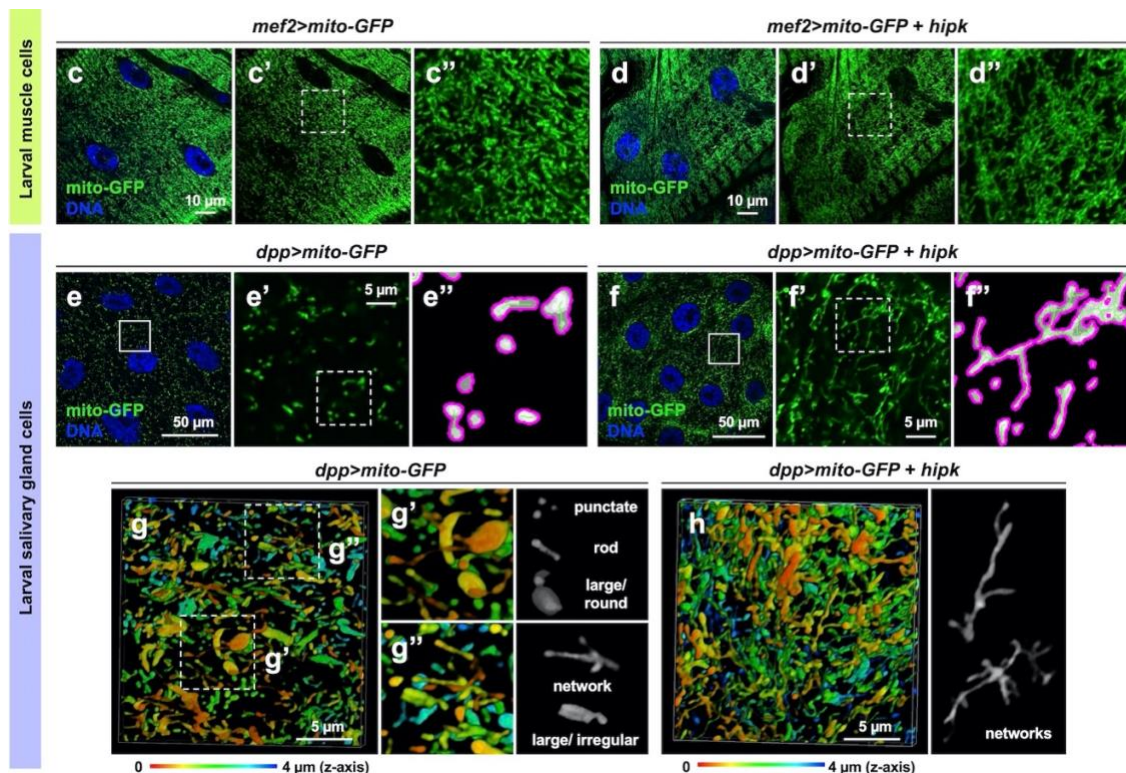


Figure 6.2. Elevated Hipk promotes mitochondrial fusion and branching.

(c-d) Muscle cells expressing *mito-GFP* (green) without (*mef2 > mito-GFP*) (c) or with *hipk* overexpression (*mef2 > mito-GFP + hipk*) (d) under the control of *mef2-Gal4*. Insets (dashed

line) in **c'** and **d'** are magnified in **c''** and **d''**, respectively. (**e-f**) Salivary gland cells expressing *mito-GFP* (green) without (*dpp > mito-GFP*) (**e**) or with *hipk* overexpression (*dpp > mito-GFP + hipk*) (**f**). Insets (solid line) in **e** and **f** are magnified in **e'** and **f'**, respectively. Insets (dashed line) in **e'** and **f'** are magnified in **e''** and **f''**, respectively, and processed by the MiNA algorithm for mitochondrial network feature analysis. In **e''** and **f''**, mitochondrial outline is shown in magenta and skeleton in green. (**g-h**) 3D images of mitochondria (marked by *mito-GFP*, color-coded for depth) in control (*dpp > mito-GFP*) (**g**) and *hipk*-overexpressing (*dpp > mito-GFP + hipk*) salivary gland cells (**h**). Insets (dashed line) in **g** are magnified in **g'** and **g''**. Selected mitochondria of various shapes are highlighted and shown in grey. DNA was stained with DAPI (blue). Scale bars are shown as indicated.

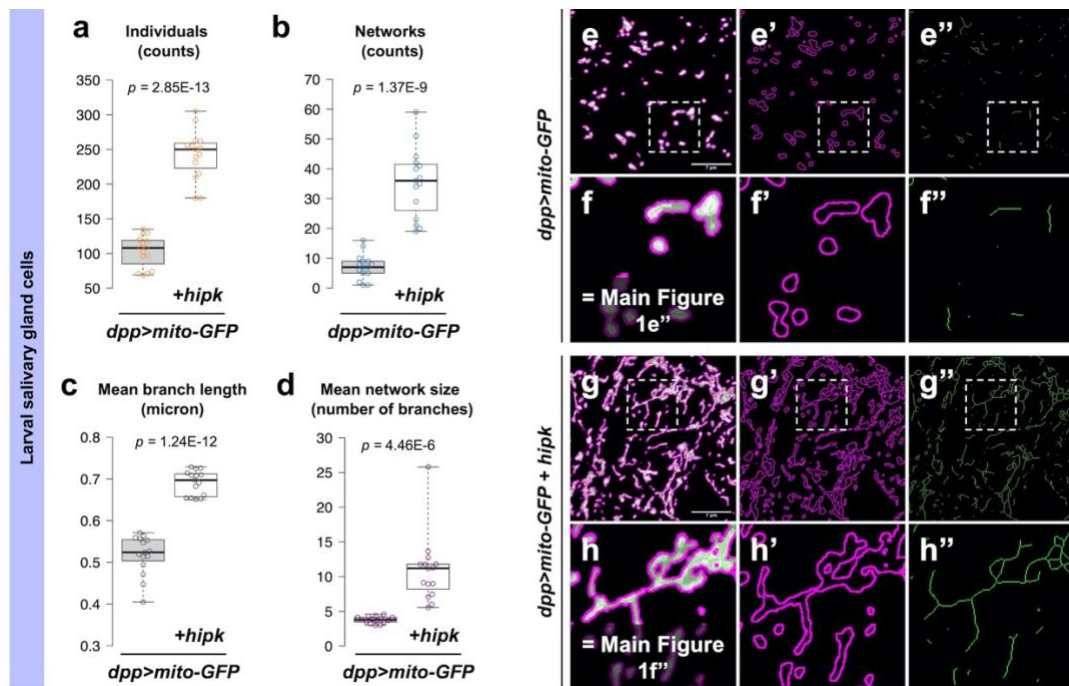


Figure 6.3. Quantification of mitochondrial morphology in control and *hipk*-overexpressing salivary gland cells.

(**a-d**) Box and whisker plots showing the quantification of mitochondrial morphology in control (*dpp > mito-GFP*) and *hipk*-overexpressing (*dpp > mito-GFP + hipk*) salivary gland cells. Four parameters, including number of individuals (without junctions) (**a**), number of networks (with at least one junction) (**b**), length of rods or branches (**c**) and network size (number of branches per network) (**d**) are calculated by the MiNA toolset. $n = 15$ cells per genotype. p values are shown and calculated using unpaired two-tailed *t*-test. (**e-h**) Mitochondria (grey in **e, f, g, h**) in control (*dpp > mito-GFP*) and *hipk*-overexpressing salivary gland cells (*dpp > mito-GFP + hipk*) were processed by the MiNA algorithm for mitochondrial network feature analysis. Insets in **e** and **g** are magnified in **f** and **h**, respectively. Mitochondrial outline is shown in magenta, and skeleton in green. Note that figures **1f** and **1h** are used in the main figure **1e''** (**Figure 6.2 e''**) and **1f''** (**Figure 6.2 f''**), respectively. Scale bars in **e** and **g**, 7 μ m.

Mitochondrial morphology is highly dynamic, which is determined by the balance of mitochondrial fusion and fission (van der Bliek et al., 2013). Mitochondrial fusion requires Mitofusins (MFN1-2 in mammals; Marf, Mitochondrial assembly regulatory factor, in *Drosophila*) and Opa1 (Optic atrophy protein 1). Both MFNs/Marf and Opa1 are dynamin related GTPases that mediate the fusion of outer membrane and inner membrane, respectively. The mitochondrial fusion phenotype observed in *hipk*-overexpressing salivary gland cells (Figure 6.4 b) was reversed when *marf* was knocked down, resulting in large, globular mitochondrial particles (Figure 6.4 c). In a similar fashion, upon *opa1* knockdown, the mitochondria appeared as tiny individual puncta (Figure 6.4 d), nearly indistinguishable from those in control cells (Figure 6.4 a). Thus, our data suggest that elevated Hipk promotes the formation of highly fused and interconnected mitochondria at least in part through the actions of Marf and Opa1.

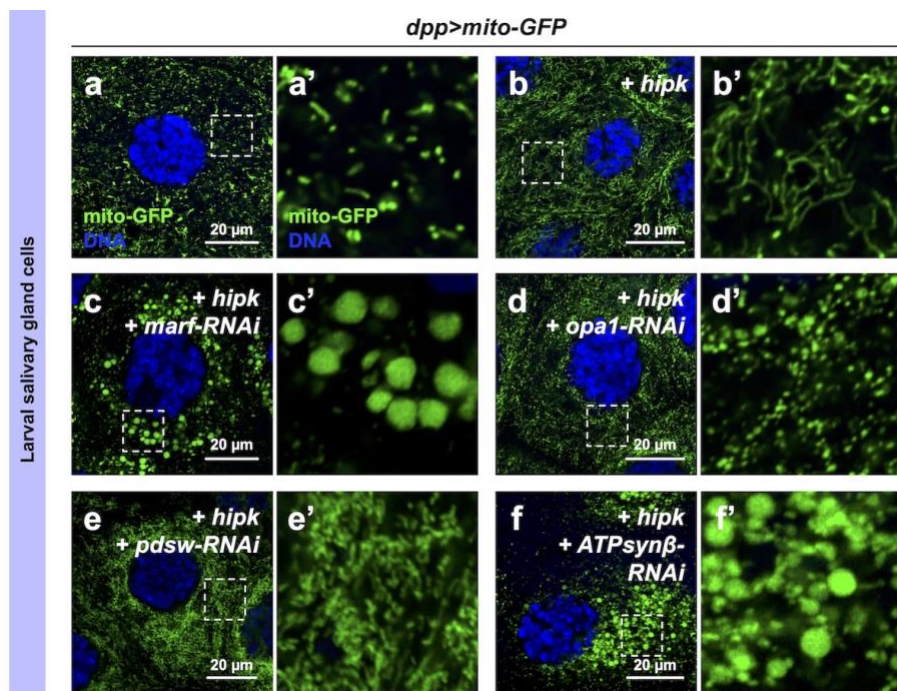


Figure 6.4. Elevated Hipk promotes mitochondrial fusion through Marf and Opa1.

(a-f) Airyscan images of mitochondria (marked by mito-GFP in green) in salivary gland cells of the indicated genotypes: (a) *dpp > mito-GFP*, (b) *dpp > mito-GFP + hipk*, (c) *dpp > mito-GFP + hipk + marf-RNAi*, (d) *dpp > mito-GFP + hipk + opa1-RNAi*, (e) *dpp > mito-GFP + hipk + pds-w-RNAi*, (f) *dpp > mito-GFP + hipk + ATPsynβ-RNAi*. Insets (dashed line) in a-f are magnified in the a'-f'. DNA was stained with DAPI (blue). Scale bars, 20 μ m.

6.4.2. Hipk tumor cells abound with active mitochondria.

Mitochondrial fusion is an adaptation of a cell to meet high metabolic needs as fusion optimizes respiratory functions by allowing efficient spreading and use of metabolites, mitochondrial DNA and proteins (Westermann, 2012). The morphological changes in Hipk tumor mitochondria prompted us to ask if mitochondrial activities are affected.

To assess the respiratory activity in mitochondria, we used MitoTracker Red, a red cationic and lipophilic fluorescent probe for monitoring the mitochondrial membrane potential ($\Delta\psi_m$), which correlates with the respiratory capacity to generate ATP (Figure 6.5). In active mitochondria where a negative $\Delta\psi_m$ is established (membrane hyperpolarization), MitoTracker Red will be retained in the mitochondrial matrix (Perry et al., 2011). In mitochondria where the membrane is depolarized, the dye will not accumulate in the matrix

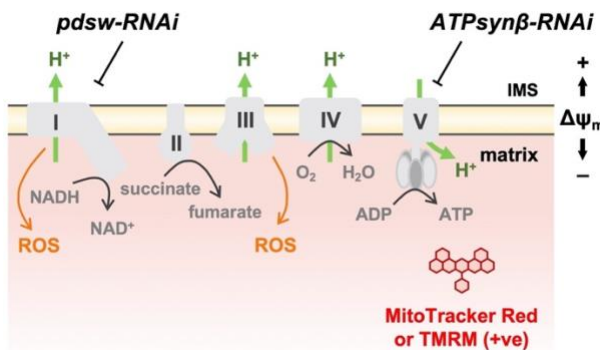


Figure 6.5. Use of $\Delta\psi_m$ -dependent dyes to monitor the respiratory activity

A diagram depicting the electron transfer chain (ETC) in the inner membrane of mitochondria. Complexes I-V are shown in grey. Green arrows indicate the proton transport. The flow of electrons is not shown for simplicity. Cationic MitoTracker Red or TMRM (red) accumulates in the matrix when a negative $\Delta\psi_m$ is established. ROS (orange) are produced primarily by complexes I and III. The activities of complexes I and V can be genetically inhibited by *pdsw-RNAi* and *ATPsynβ-RNAi*, respectively. IMS, intermembrane space.

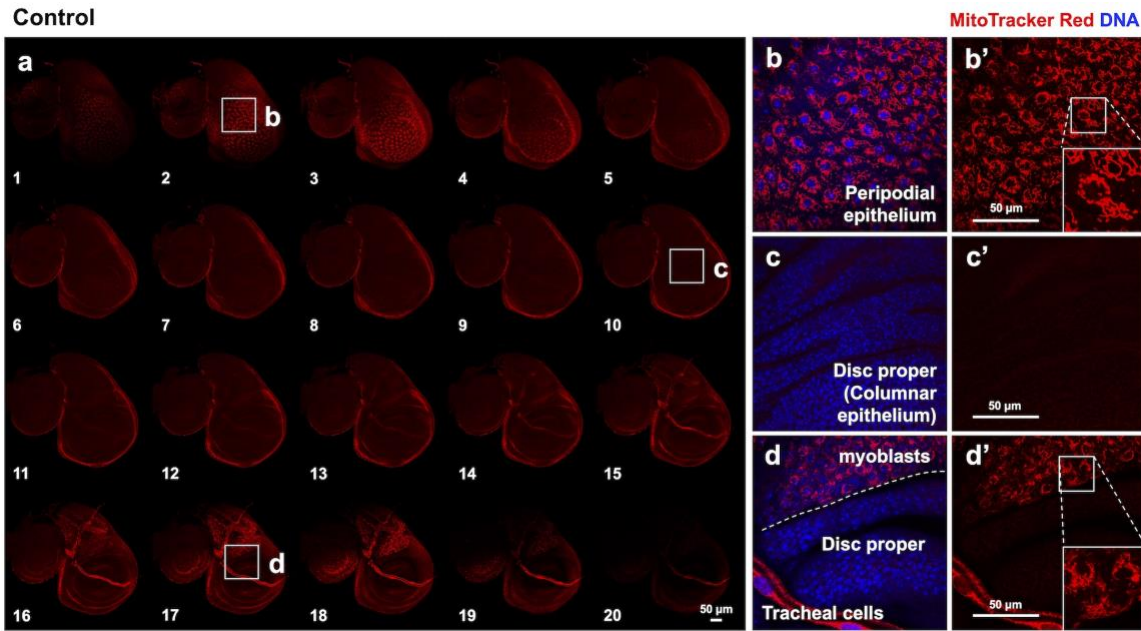


Figure 6.6. MitoTracker Red staining in a control wing disc.

(a) Gallery view of a series of z-stack images showing Mitotracker Red staining (red) of a control wing disc from the apical side (starting from 1) to the basal side. Insets (solid line) in stacks 2, 10 and 17 are magnified in b-d. In d, a dashed line separates the myoblast cells from the disc proper cells. DNA was stained with DAPI (blue). Scale bars, 50 µm.

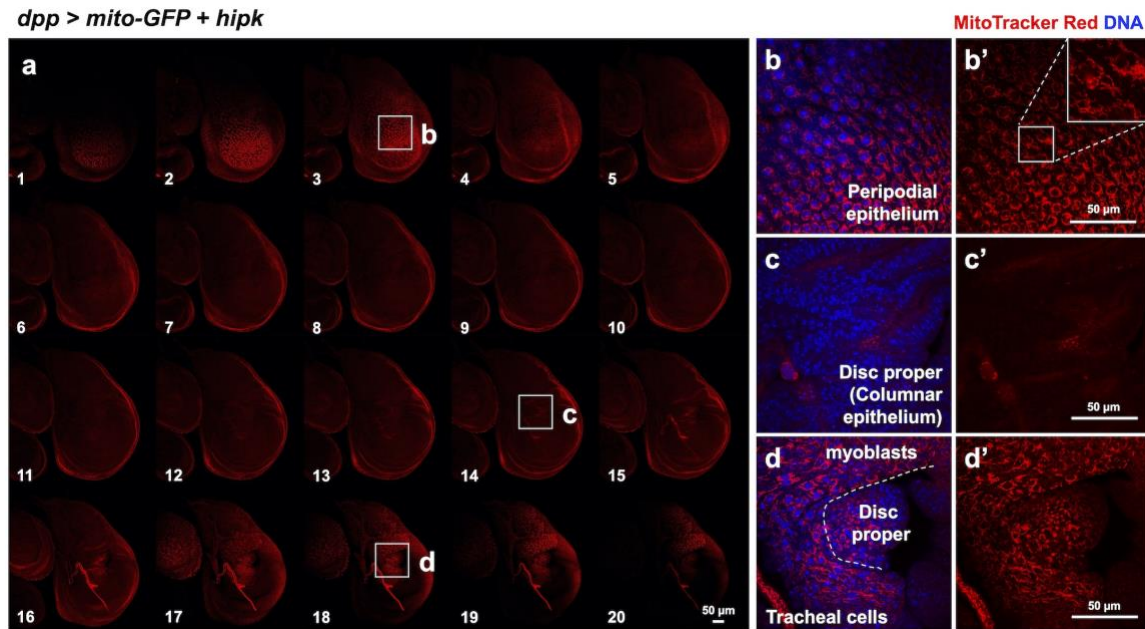


Figure 6.7. MitoTracker Red staining in a *hipk*-overexpressing wing disc.

(a) Gallery view of a series of z-stack images showing Mitotracker Red staining (red) of a *hipk*-overexpressing wing disc from the apical side (starting from 1) to the basal side. Insets

(solid line) in stacks 3, 14 and 18 are magnified in b-d. In d, a dashed line separates the myoblasts from the disc proper cells. We noticed that some myoblasts moved from the notum region into the hinge and pouch regions, possibly due to the tissue distortions caused by the tumor growth. Myoblasts are marked GFP-negative due to the absence of Gal4 expression driven by *dpp-Gal*. Also, myoblasts are larger in size and more flattened when compared with the squeezed, columnar disc proper cells. DNA was stained with DAPI (blue). Scale bars, 50 μ m.

We first examined the staining pattern of MitoTracker Red in the entire z-stacks of larval wing discs ([Figure 6.6](#), [Figure 6.7](#)). The larval wing disc is a sac-like structure composed of the peripodial epithelium (PE) on the apical side connected to the disc proper (DP, also known as the columnar epithelium) on the basal side ([Cohen, 1993](#)). Myoblasts (MB), which are the progenitors of adult flight muscles ([Gunage et al., 2014](#)), and tracheal branches are associated with wing discs on the basal surface of the columnar epithelium ([Guha et al., 2009](#)).

On the apical side of a control disc, the peripodial epithelium (PE) exhibited robust MitoTracker Red staining, and the labeled mitochondria were highly filamentous ([Figure 6.6 b](#)). In contrast, little staining was seen in the disc proper (DP) cells in the middle sections of the disc ([Figure 6.6 c](#)). It is possible that the dye fails to penetrate deeper within the tissue; the staining was only enriched at the periphery of the wing disc ([Figure 6.6 a see e.g. stack image 10](#)). On the basal side of the disc, MitoTracker Red accumulated in the associated myoblasts (MB) and tracheal cells, but not in the DP cells ([Figure 6.6 d](#)), reflecting differential mitochondrial activities among cell types.

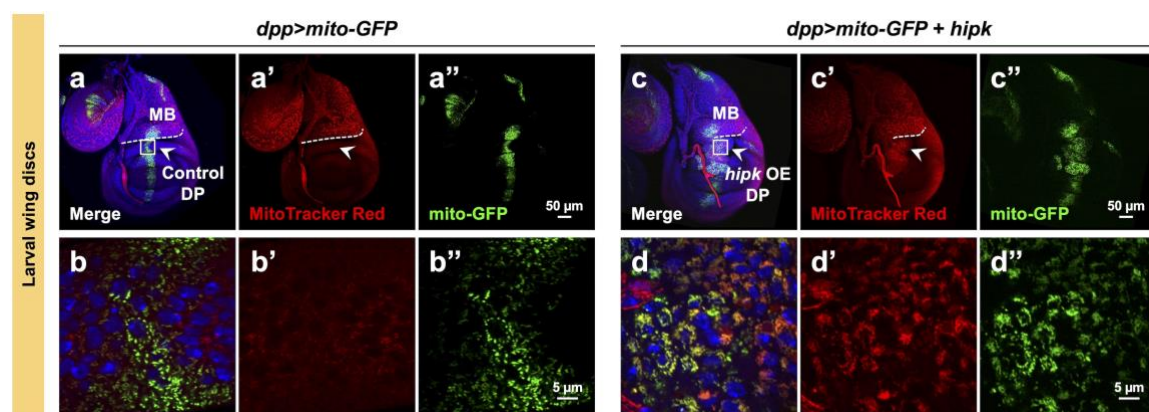


Figure 6.8. Hipk tumor cells abound with active mitochondria.

(a-d) The basal sides of control (*dpp > mito-GFP*) (**a-b**) and *hipk*-overexpressing (*dpp > mito-GFP + hipk*) (**c-d**) wing discs stained with MitoTracker Red (red). Mito-GFP (green) was expressed in the Dpp domain to label mitochondria. DNA was stained with DAPI (blue) to

reveal overall morphology. Insets (solid line) in **a** and **c** are magnified in **b** and **d**, respectively. The dashed lines in **a** and **c** separate the myoblasts (MB) (above the line) from the adjacent disc proper (DP) cells (below the line). The arrowheads in **a-a'** and **c-c'** point to the MitoTracker Red signals in control DP cells and *hipk* OE DP cells, respectively.

In light of the possible penetrance issue of MitoTracker Red, we focused on the basal side where we could use the robust staining in MB as a reference since *dpp-Gal4* is not expressed in these cells. In the control wing disc (*dpp > mito-GFP*), myoblasts (MB) and disc proper (DP) cells had robust and little MitoTracker Red incorporation, respectively (**Figure 6.8 a-b**, **Figure 6.6 d**). In contrast, in a *hipk*-overexpressing disc (*dpp > mito-GFP + hipk*) where tumorous growth was prominent (**Figure 6.8 c**), both MB and Hipk tumor cells (the *hipk*-overexpressing DP cells; *hipk* OE DP) had comparably high MitoTracker Red signals (**Figure 6.8 d**, **Figure 6.7**). Thus, our data demonstrate that Hipk tumor cells took up more MitoTracker Red than the control cells.

A similar result was obtained in larval muscle walls. In contrast to the basal levels of MitoTracker Red staining in control muscle cells (**Figure 6.9 a**), the highly convoluted mitochondria in *hipk*-overexpressing muscle cells display intense MitoTracker Red incorporation (**Figure 6.9 b**), showing elevated mitochondrial respiratory activity.

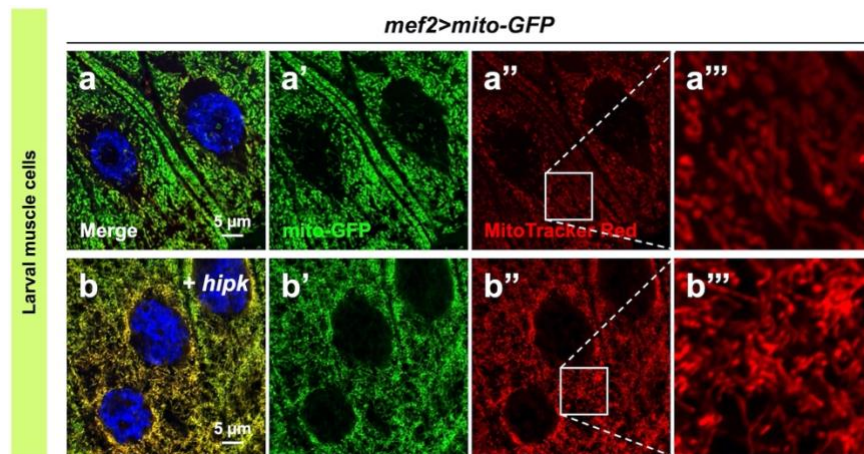


Figure 6.9. Elevated Hipk increases mitochondrial respiratory activity in larval muscle cells.

(**a-b**) Control (*mef2 > mito-GFP*) (**a**) and *hipk*-overexpressing (*mef2 > mito-GFP + hipk*) (**b**) larval muscle cells stained with MitoTracker Red (red). Mitochondria were marked by mito-GFP (green). DNA was stained with DAPI (blue). Insets in **a''-b''** are magnified in **a'''-b'''**. Scale bars, 5 μ m.

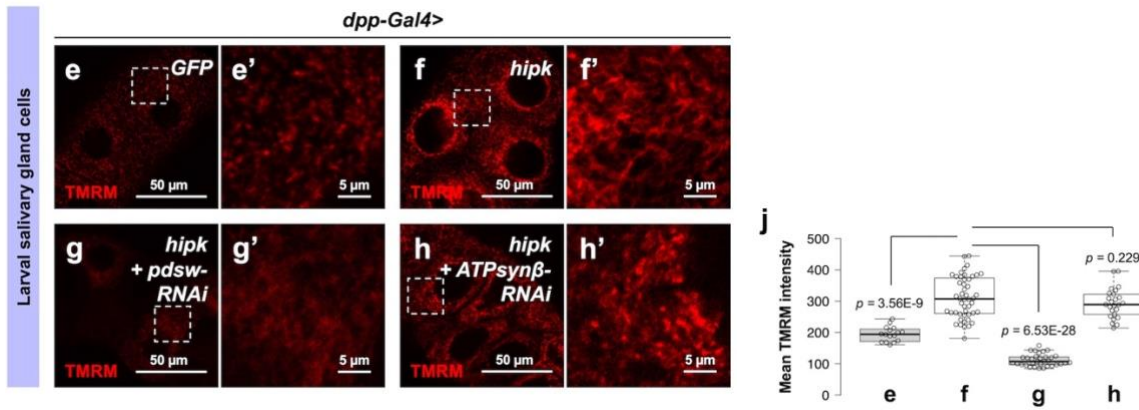


Figure 6.10. Cells with elevated Hipk bound with active mitochondria.

(e-h) Incorporation of TMRM (red) in live control (*dpp > GFP*) (e), *hipk*-overexpressing (*dpp > hipk*) (f), *hipk* and *pds*-*RNAi* co-expressing (*dpp > hipk + pds*-*RNAi*) (g) and *hipk* and *ATPsynβ*-*RNAi* co-expressing (*dpp > hipk + ATPsynβ*-*RNAi*) salivary gland cells (h). Insets in e-h are magnified in e'-h'. (j) A box and whisker plot showing the mean TMRM fluorescence in live salivary gland cells of the indicated genotypes. Letters e-h refer to the genotypes shown in Figure 6.10 e-h. n = 17 cells (e), 48 cells (f), 33 cells (g), 25 cells (h). Exact p values are shown and calculated using unpaired two-tailed t-test. Scale bars are shown as indicated.

Tetramethylrhodamine methyl ester (TMRM) is another $\Delta\psi_m$ -dependent, red fluorescent dye that accumulates in the matrix of active mitochondria (Scaduto and Grottohann, 1999). Similar to what we observed with mito-GFP (Figure 6.2 e-f), TMRM staining showed dot-like and highly fused mitochondria in control and *hipk*-overexpressing salivary gland cells, respectively (Figure 6.10 e-f), indicating that TMRM specifically labels mitochondria. More importantly, cells with elevated Hipk showed marked TMRM sequestration when compared with control cells (Figure 6.10 e-f, j).

A negative $\Delta\psi_m$ can be established by either the electron transfer chain (ETC, also known as the respiratory chain) in active mitochondria or through ATP hydrolysis by ATPase (the reversed work of ATP synthase) in damaged mitochondria (Campanella et al., 2009; Jonckheere et al., 2012). We found that genetic inhibition of complex V by knocking down one of its subunits, *ATPsynβ*, did not significantly affect TMRM accumulation in *hipk*-overexpressing cells (Figure 6.10 h, j), implying that elevated Hipk sustains negative $\Delta\psi_m$ by stimulating the rate of electron transfer but not by ATP hydrolysis. Indeed, inhibition of complex I (which pumps protons into the intermembrane space (IMS)) by knocking down *pds* (or *ND-pds* named after NADH dehydrogenase

[ubiquinone] with a N-terminal sequence Pro-Asp-Ser-Trp; a Complex I subunit) abrogated the TMRM accumulation seen with Hipk elevation (**Figure 6.10 g, j**). The mitochondria in *hipk* and *pds-w-RNAi* co-expressing cells remained abundant (**Figure 6.4 e**), suggesting that the suppression of the membrane hyperpolarization by *pds-w-RNAi* is due to reduced Complex I activity rather than a reduction in mitochondrial mass.

Given that we did not quantify the mitochondrial masses of control and Hipk tumor epithelial cells in wing discs because of the small cell size (**Figure 6.1**), the MitoTracker Red accumulation in the tumor cells (**Figure 6.8 c-d**) could be attributed to an increase in mitochondrial mass, membrane hyperpolarization or both. Therefore, instead of concluding that the Hipk tumor mitochondria are hyperactive, we favor the conclusion that Hipk tumor cells abound with functional, metabolically active mitochondria.

6.4.3. Hipk tumor cells do not display ROS accumulation

Mitochondrial damage is associated with massive generation of reactive oxygen species (ROS) (Ježek et al., 2018; Kushnareva et al., 2002). If the mitochondria in Hipk tumor cells were damaged, we would expect to detect elevated ROS production. To measure the ROS levels, we stained the wing discs with dihydroethidium (DHE), a fluorogenic probe for superoxide (O_2^-). DHE reacts with O_2^- to form ethidium (E_+) and 2-hydroxyethidium (2-OH- E_+), which are red fluorescent products (Zielonka and Kalyanaraman, 2010). For quantification, we calculated the ratio of the mean ROS levels in transgene-expressing cells (GFP positive) to those in the neighboring wild-type cells (GFP negative) of the same wing disc. Such normalization allows us to compare the relative ROS levels of disc cells of different genotypes. Based on these ratios, we classified the relative ROS levels into three categories – basal (a ratio of ~ 1), moderate (1 – 1.5) and high (> 1.5) (Figure 6.11 m).

DHE staining revealed basal ROS levels (an averaged ratio of 1.05) in control wing discs (Figure 6.11 a, m). As positive controls, we impaired mitochondrial functions using RNAi targeting complex subunits (Complex V subunit: ATPsyn β ; Complex I subunits: Pdsw, ND-75, ND-49 and ND-42). As expected, mitochondrial dysfunction led to moderate or high ROS production (ratios ranging from 1.21 to 1.74) (Figure 6.11 b-f, m). In *hipk*-overexpressing cells, the ROS levels (an averaged ratio of 1.04) were comparable to those in the neighboring wild-type cells (Figure 6.11 g, m) as well as the basal levels in control discs (Figure 6.11 a). The lack of ROS buildup in Hipk tumor cells suggests that the tumor mitochondria remain functional, rather than damaged, corroborating the MitoTracker Red results (Figure 6.8). When mitochondrial activities were impaired by using RNAi to target Complex I and V subunits in Hipk tumor cells, we detected high levels of ROS (ratios > 1.5) (Figure 6.11 h, j-m), except *pds*-RNAi co-expression which caused moderate ROS accumulation (an averaged ratio of 1.39) (Figure 6.11 i, m). Nonetheless, such a synergistic effect on ROS levels may be caused by an increase in mitochondrial mass in Hipk tumor cells or may suggest that the tumor mitochondria are particularly sensitive to perturbations in the respiratory activity.

Altogether, from direct (MitoTracker Red staining for $\Delta\psi_m$) and indirect (mito-GFP for morphology and DHE staining for ROS) assays, we showed that Hipk tumor cells are enriched with highly fused and functional mitochondria. In other words, we established

elevated Hipk as an *in vivo* fly tumor model characterized by active mitochondrial metabolism.

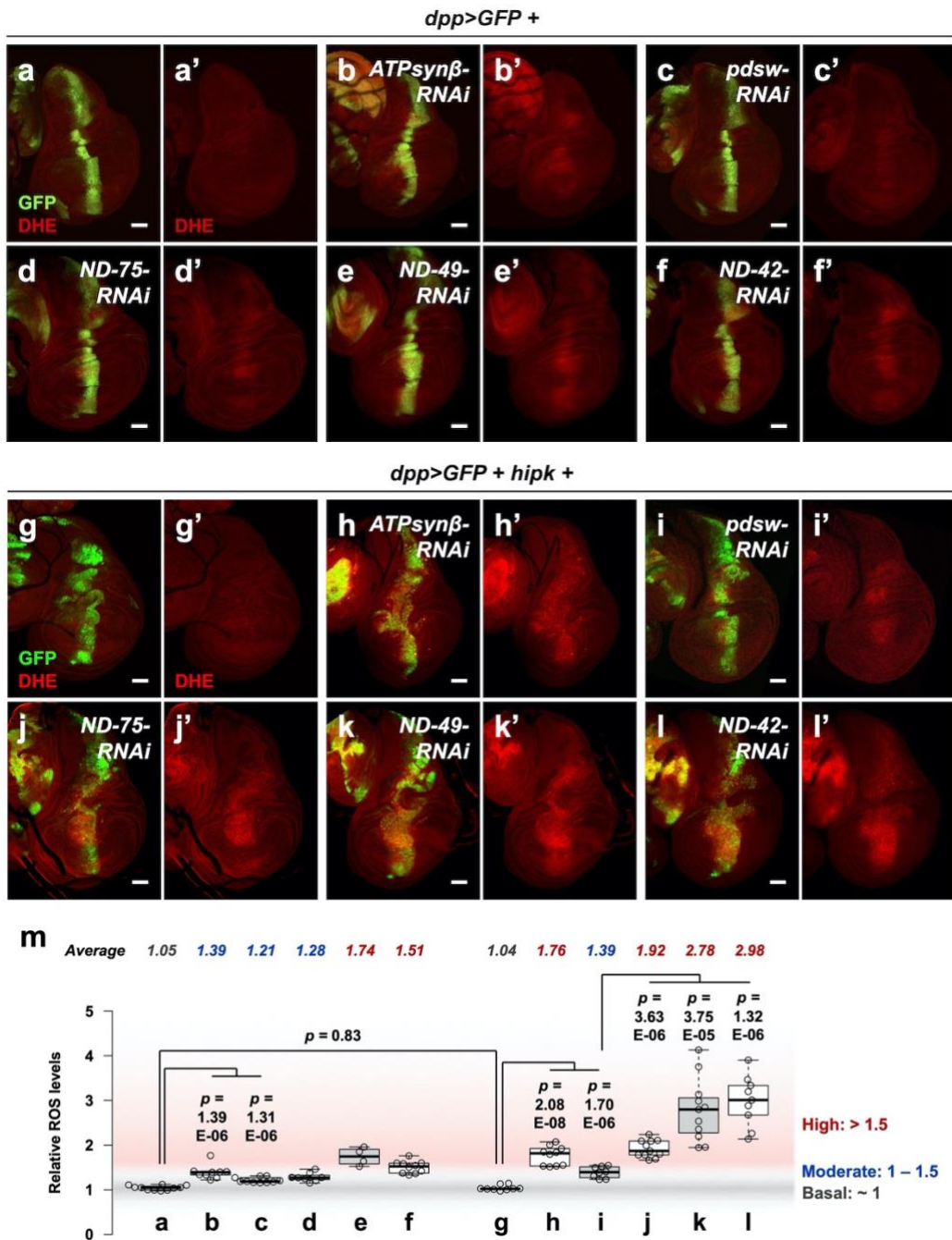


Figure 6.11. Hipk tumor cells do not display ROS accumulation.

(a-l) DHE staining (red) of wing discs of the indicated genotypes: dpp > GFP (a), dpp > GFP + ATPsynβ-RNAi (b), dpp > GFP + pdsrw-RNAi (c), dpp > GFP + ND-75-RNAi (d), dpp > GFP + ND-49-RNAi (e), dpp > GFP + ND-42-RNAi (f), dpp > GFP + hipk (g), dpp > GFP + hipk + ATPsynβ-RNAi (h), dpp > GFP + hipk + pdsrw-RNAi (i), dpp > GFP + hipk + ND-75-

RNAi (**j**) , dpp > GFP + hipk + ND-49-RNAi (**k**) , dpp > GFP + hipk + ND-42-RNAi (**l**). GFP (green) marks the transgene-expressing cells. Scale bars, 50 µm. (**m**) A box and whisker plot showing the relative ROS levels in the transgene-expressing cells of the indicated genotypes. Letters **a-l** correspond to the genotypes in the figure. N = 11 discs (**a**), 9 discs (**b**), 10 discs (**c**), 8 discs (**d**), 4 discs (**e**), 10 discs (**f**), 9 discs (**g**), 10 discs (**h**), 8 discs (**i**) 11 discs (**j**), 11 discs (**k**) and 9 discs (**l**). p values indicating the significant differences between **a** and **b-c**, **a** and **g**, **g** and **h-i**, and **i** and **j-l** were shown calculated using unpaired two-tailed Student's t-test. The averaged values of the relative ROS levels are shown on the top of the graph. ROS levels are categorized into basal (~ 1), moderate (1 – 1.5) and high (> 1.5) levels, which are labeled in grey, blue and red, respectively.

6.4.4. Mitochondrial fusion is dispensable for Hipk-mediated tumorigenesis

To gain comprehensive insights into the causes and functional consequences of active mitochondrial metabolism in Hipk tumor growth, we focused on three aspects, namely mitochondrial fusion, respiratory activity, and the positive feedback loop between Myc and aerobic glycolysis that we previously reported (Wong et al., 2019). We used the wing disc and salivary gland epithelial cells in the subsequent analyses, but not muscle cells because the mitochondrial morphology of the latter cell type bears little resemblance to the former two.

To examine the involvement of mitochondrial fusion in Hipk tumor growth, we used RNAi to knock down mitochondrial fusion regulators, Marf and Opa1. In Hipk tumor cells (the *hipk*-overexpressing disc proper cells; *hipk* OE DP), we observed both punctate and fused mitochondria (marked by mito-GFP) (**Figure 6.12 a''**). Most of them had high, albeit heterogenous, MitoTracker signals when compared with the neighboring wild-type (WT) DP cells (**Figure 6.12 a'**). When *marf* or *opa1* was knocked down in Hipk tumor cells (*hipk* OE + RNAi DP), mitochondria appeared as individual particles (**Figure 6.12 c'', e''**). Intriguingly, these mitochondria still sequestered higher levels of MitoTracker Red than those in the neighboring WT DP cells (**Figure 6.12 c', e'**), suggesting that these mitochondria remained relatively active even though fusion was inhibited. Comparable results were obtained in salivary gland cells (**Figure 6.13 a-c**). These data hint at a model where elevated Hipk alters mitochondrial morphology and overall activity through separate mechanisms. Notably, blocking mitochondrial fusion failed to prevent Hipk tumor growth and the disc morphologies remained distorted (**Figure 6.12 d, f**), suggesting the fusion may not be a key driver for tumor initiation or growth.

We therefore hypothesized that mitochondrial activity, rather than the morphology, is a critical factor for Hipk tumor growth. When *marf* (fusion regulator) and *pds* (complex I subunit) were simultaneously knocked down in Hipk tumor cells, only a few cells showed marked MitoTracker accumulation (**Figure 6.12 g**). More importantly, the double knockdown significantly blocked Hipk tumor growth and the tissue morphology resembled wildtype-like (compare **Figure 6.12 h** with **Figure 6.1 a**).

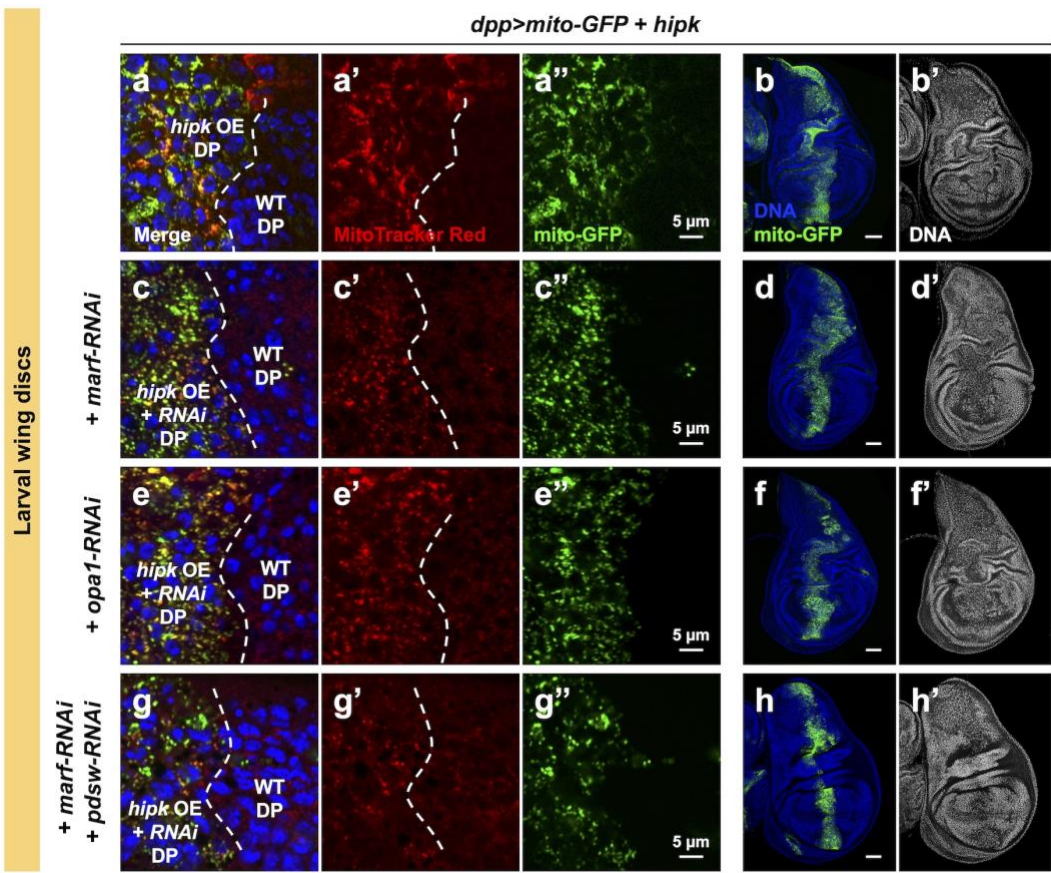


Figure 6.12. Mitochondrial fusion is dispensable for Hipk-mediated tumorigenesis.

Mitochondria (marked by mito-GFP in green) in disc proper (DP) cells (**a, c, e, g**) and the whole disc morphologies (**b, d, f, h**) of wing discs overexpressing (OE) *hipk* alone (*dpp > mito-GFP + hipk*) (**a-b**) or with *marf* knockdown (*dpp > mito-GFP + hipk + marf-RNAi*) (**c-d**), with *opa1* knockdown (*dpp > mito-GFP + hipk + opa1-RNAi*) (**e-f**) or with double knockdown of *marf* and *pds* (*dpp > mito-GFP + hipk + marf-RNAi + pds-RNAi*) (**g-h**). Wing discs were stained with MitoTracker Red (red). The dashed lines in **a, c, e, g** separate the transgene-expressing cells (either *hipk* OE DP or *hipk* OE + *RNAi* DP) from the neighboring GFP-negative wild-type (WT) DP cells (on the right). DAPI staining for DNA (blue, grey) reveals tissue morphology. Scale bars, 5 µm (**a, c, e, g**); 50 µm (**b, d, f, h**).

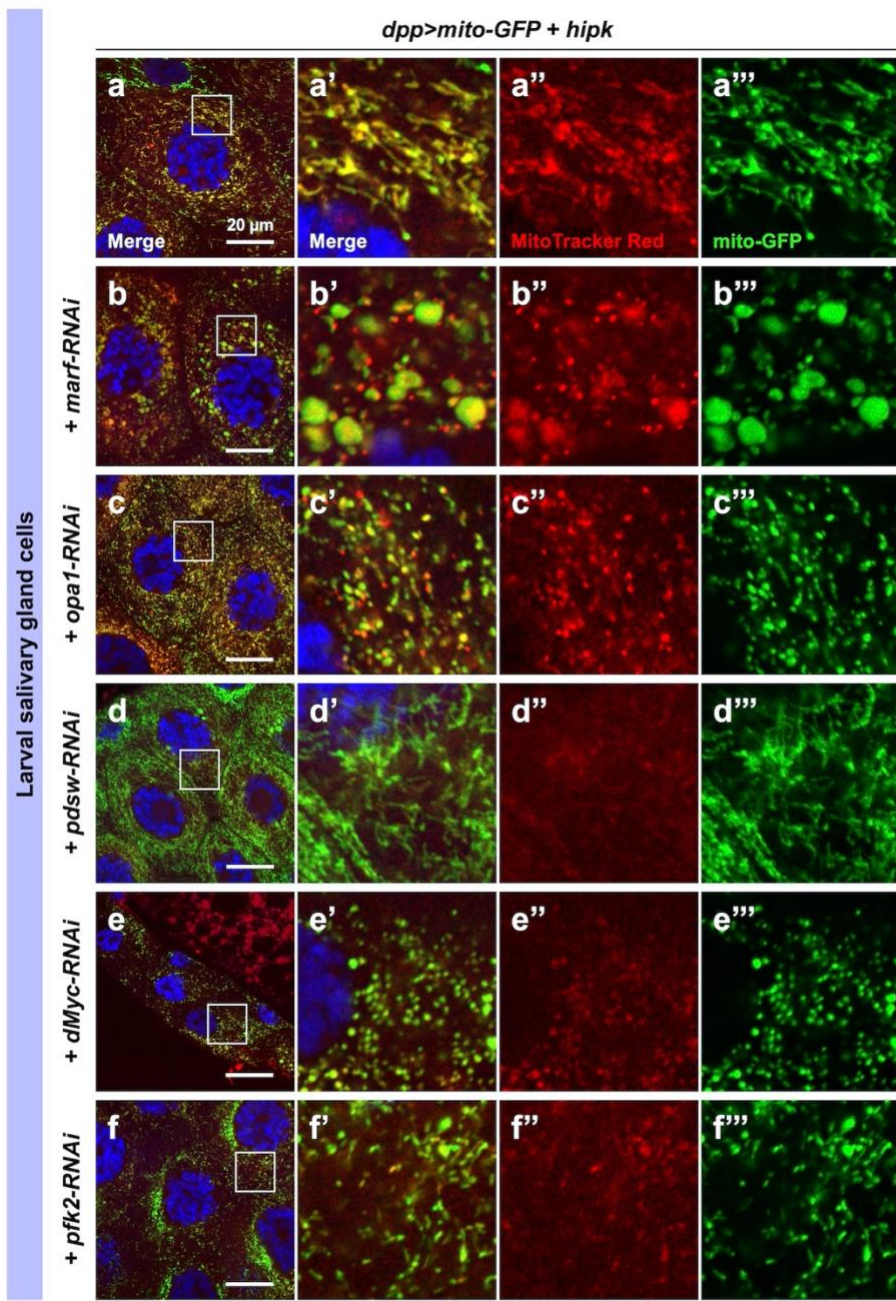


Figure 6.13. Effects by various knockdowns on mitochondrial activity and morphology in *hipk*-overexpressing salivary gland cells.

Mitochondria (marked by mito-GFP in green) and MitoTracker staining (red) in *hipk*-overexpressing salivary gland cells (*dpp > mito-GFP + hipk*) without (a) or with *marf* knockdown (*dpp > mito-GFP + hipk + marf-RNAi*) (b), with *opa1* knockdown (*dpp > mito-GFP + hipk + opa1-RNAi*) (c), with *pds*w knockdown (*dpp > mito-GFP + hipk + pds*w-RNAi) (d), with *dMyc* knockdown (*dpp > mito-GFP + hipk + dMyc-RNAi*) (e), or with *pfk2* knockdown (*dpp > mito-GFP + hipk + pfk2-RNAi*) (f). Insets in a-f are magnified in a'-f', a''-f'', and a'''-f'''. DNA (blue) was stained with DAPI. Scale bars, 20 μ m.

6.4.5. Targeted but not generic inhibition of mitochondrial activity suppresses Hipk tumor growth

To further evaluate the roles of mitochondrial activity in Hipk tumor growth, we inhibited the respiratory activity without interfering with the morphology.

In Hipk tumor cells (*hipk* OE DP), the Mitotracker Red signals were comparable to those in the neighboring myoblasts (MB) (**Figure 6.14 a'**). When *pds*-RNAi was co-expressed in Hipk tumor cells, the MitoTracker Red signals were much lower than those in the nearby MB (**Figure 6.14 c'**), indicating that *pds*-RNAi significantly reduced the overall mitochondrial activity. As revealed by mito-GFP, the mitochondrial fusion phenotype was not suppressed by *pds* knockdown (**Figure 6.14 c''** arrowheads). We observed similar effects of *pds* knockdown in salivary gland cells (**Figure 6.13 d**). Thus, our data once again imply that elevated Hipk impacts on mitochondrial morphology and overall activity independently. More importantly, depletion of Pds, regardless of the mitochondrial shape, was sufficient to abrogate Hipk tumor growth (**Figure 6.14 d**).

Next, we tested the possible inhibitory effects of RNAi targeting other respiratory complex subunits on Hipk tumor growth. As expected, knockdown of *ND75*, *ND49* and *ND42*, all of which encode complex I subunits, strongly reduced the MitoTracker Red incorporation in Hipk tumor cells (**Figure 6.14 e', g', i'**) with minor effects on the fusion phenotype (**Figure 6.14 e'', g'', i''**). However, unlike *pds* knockdown, knockdown of *ND75/49/42* failed to block Hipk tumor growth and the tissue morphologies remained severely distorted (**Figure 6.14 f, h, j**). Knockdown of *ATPsynβ*, a complex V subunit, did not suppress the MitoTracker Red accumulation in Hipk tumor cells (**Figure 6.14 k'**), which corroborates the TMRM results obtained in salivary gland cells (**Figure 6.10 h**). Nor did *ATPsynβ* knockdown rescue the tumor growth or tissue distortions (**Figure 6.14 l**). RNAi lines used in this study to target complex I or V have already been used and proved effective by others (Garcia et al., 2017; Song et al., 2017; Tomer et al., 2018; Zhang et al., 2013).

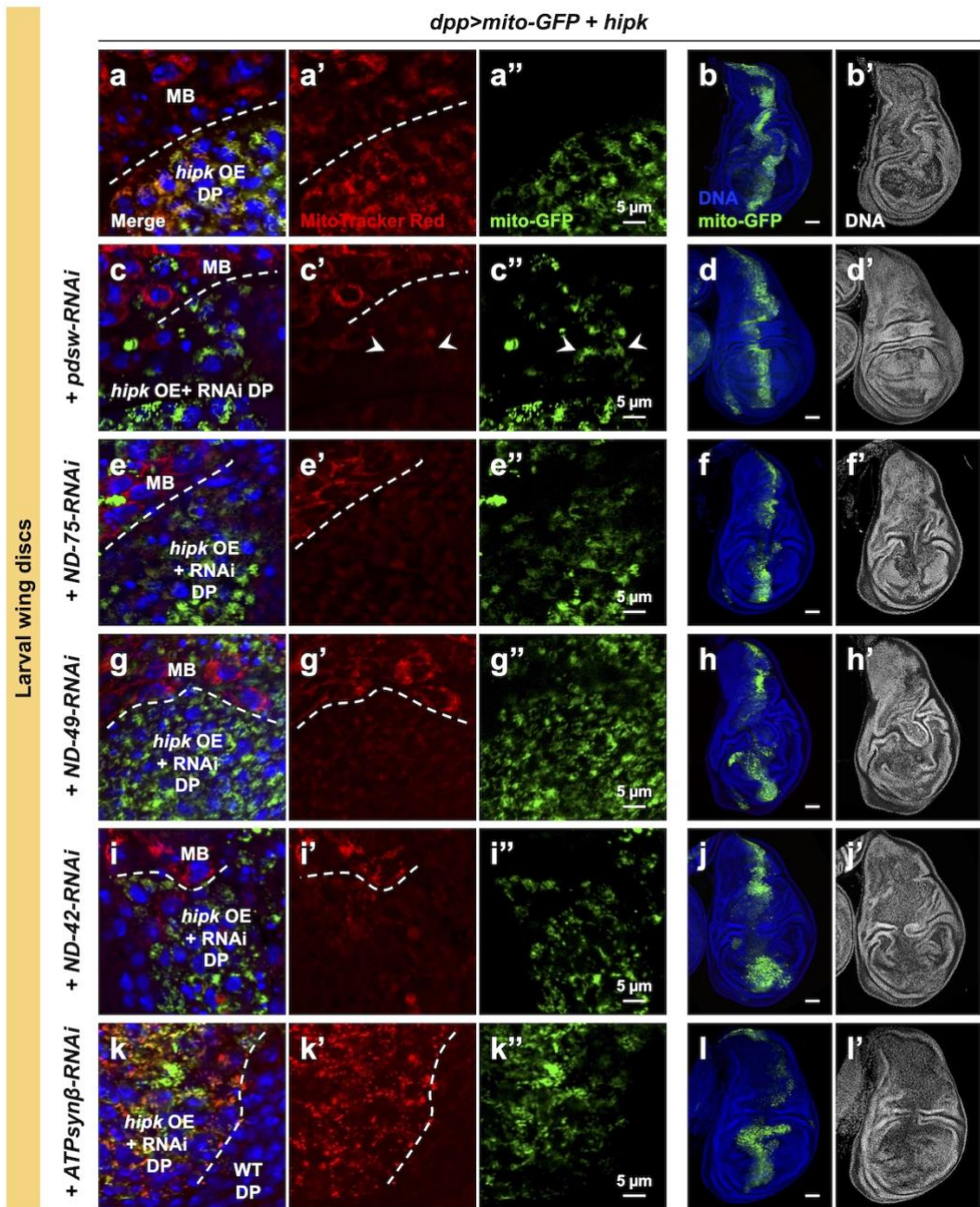


Figure 6.14. Targeted but not generic inhibition of mitochondrial activity suppresses Hip tumor growth.

Mitochondria (marked by mito-GFP in green) in disc proper (DP) cells (**a, c, e, g, i, k**) and the whole disc morphologies (**b, d, f, h, j, l**) of wing discs overexpressing (OE) *hipk* alone (*dpp > mito-GFP + hipk*) (**a-b**) or with *pdsrw* knockdown (*dpp > mito-GFP + hipk + pdsrw-RNAi*) (**c-d**), with *ND-75* knockdown (*dpp > mito-GFP + hipk + ND-75-RNAi*) (**e-f**), with *ND-49* knockdown (*dpp > mito-GFP + hipk + ND-49-RNAi*) (**g-h**), with *ND-42* knockdown (*dpp > mito-GFP + hipk + ND-42-RNAi*) (**i-j**) or with *ATPsynβ* knockdown (*dpp > mito-GFP + hipk + ATPsynβ-RNAi*) (**k-l**). Wing discs were stained with MitoTracker Red (red). The dashed lines in **a, c, e, g, i, k** separate the transgene-expressing cells (either *hipk* OE DP or *hipk* OE + *RNAi* DP).

from the neighboring myoblasts (MB). The dashed line in **k** separates the transgene-expressing cells (*hipk* DP + *RNAi* DP) from the neighboring wild-type (WT) DP cells (on the right). DAPI staining for DNA (blue, grey) reveals tissue morphology. Scale bars, 5 μm (**a, c, e, g, i, k**); 50 μm (**b, d, f, h, j, l**).

6.4.6. Complex subunit-dependent effects on ROS production in Hipk tumor cells

Mammalian respiratory complex I is composed of 45 different protein subunits (Zhu et al., 2016). 42 subunits are found highly conserved in *Drosophila* (Table 6-1) (Garcia et al., 2017). Complex I is L-shaped, with one arm in the inner membrane, another extending into the mitochondrial matrix (Figure 6.15 left) (Zhu et al., 2016). The matrix arm comprises two modules, namely the N and Q modules, which transfer electrons from NADH to ubiquinone (Coenzyme Q) (Sharma et al., 2009). The membrane arm hosts the P module, which is subdivided into Pd (distal) and Pp (proximal) modules, for the purpose of proton pumping (Sharma et al., 2009).

Table 6-1. A list of *Drosophila* mitochondrial complex subunits studied in this work with their human homologs.

<i>Drosophila</i> genes	Fly annotation symbol	Human homolog(s)	Location in complex I
Complex I			
<i>pds</i> w (or ND-PDSW)	CG8844	<i>NDUFB10</i>	Pd module
<i>ND-75</i>	CG2286	<i>NDUFS1</i>	N module
<i>ND-49</i>	CG1970	<i>NDUFS2</i>	Q module
<i>ND-42</i>	CG6343	<i>NDUFA10</i>	Pp module
Complex V			
<i>ATPsyn</i> β	CG11154	<i>ATP5F1B</i>	N/A

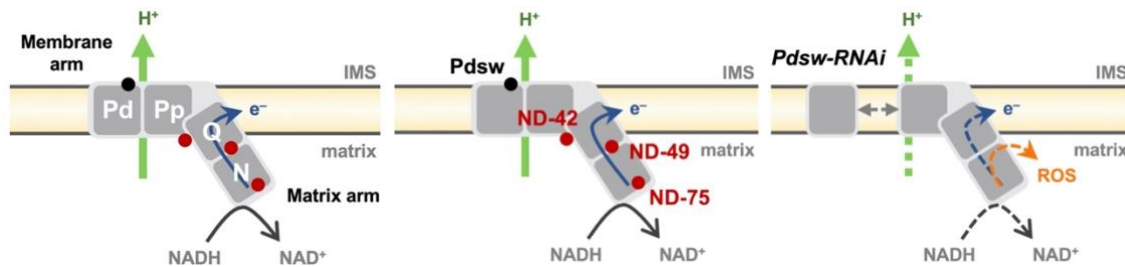


Figure 6.15. A schematic diagram of the respiratory complex I.

(Left) Complex I is composed of membrane and matrix arms, which host the Pd, Pp, Q and N modules. (middle) The locations of subunits Pds-w (black dot), ND-42, ND-49, ND-75 (red dots) are shown. IMS, intermembrane space. (right) A possible scenario of *pds-w-RNAi*. Pds-w may serve as a molecular clamp holding the Pd and Pp modules together. Depletion of Pds-w may lead to weakened interaction between the two modules, reduced complex I activity and ROS production to a certain extent.

To account for the distinct effects of knockdown of *pds*w and *ND-75/49/42*, we looked into the locations of these subunits in complex I. *Pds*w, a component of the Pd module, is located at the intermembrane space (IMS) face (**Figure 6.15 middle**) (Zhu et al., 2016). Interestingly, the other three subunits are close to or right at the electron path. We therefore hypothesized that depletion of *ND-75/49/42* in complex I would cause defects in the electron transfer, followed by electron leakage and massive ROS generation.

Using the DHE assay for ROS, we noticed that whereas knockdown of *ND-75/49/42* on its own caused moderate or high ROS levels (averaged ratios ranging from 1.28 to 1.74) (**Figure 6.11 d-f, m**), the knockdowns in Hipk tumor cells all led to high levels of ROS (ratios ranging from 1.92 to 2.98) (**Figure 6.11 j-m**). On the contrary, in both control cells and Hipk tumor cells, *pds*w knockdown only generated moderate levels of ROS (ratios of 1.21 and 1.39, respectively) (**Figure 6.11 c, i, m**). Thus, our data indicate that even though all knockdowns of *pds*w, *ND-75*, *ND-49* and *ND-42* potently reduced the overall respiratory activities in Hipk tumor cells (**Figure 6.14 c', e', g', i'**), the knockdowns had differential effects on ROS production. More notably, our data imply that the levels of ROS produced may account for the subunit-dependent, opposing effects on tumor growth.

We then considered the possibility that the use of RNAi targeting complex subunits may introduce unintended mitochondrial dysfunction in Hipk tumor cells. High levels of ROS have been shown to trigger activation of mitogen-activated protein kinases including ERKs, JNKs and p38 MAPKs (Owusu-Ansah and Banerjee, 2009; Son et al., 2013; Wang et al., 2016). Consistently, we found that knockdown of *ATPsynβ* in Hipk tumor cells not only caused high ROS levels (**Figure 6.11 h, m**), but also activated JNK as revealed by phospho-JNK (pJNK) staining (**Figure 6.16 b'**). In addition, we detected intensified staining of Matrix metalloproteinase 1 (MMP1) (**Figure 6.16 b''**), which is a downstream target of JNK (Uhlirova and Bohmann, 2006). Genetic inhibition of JNK by overexpressing of a dominant negative form of JNK (JNK-DN) largely suppressed MMP1 upregulation (**Figure 6.16 c''**), although JNK-DN remained highly phosphorylated (**Figure 6.16 c'**). MMP1 degrades basement membrane proteins, facilitating tumor invasion (Page-McCaw et al., 2007). Our data thus suggest that when mitochondrial dysfunction is associated with the high levels of ROS produced, the subsequent JNK

activation, possibly together with other perturbed signaling pathways, likely potentiates the invasive properties of Hipk tumor cells and exacerbates tumor growth.

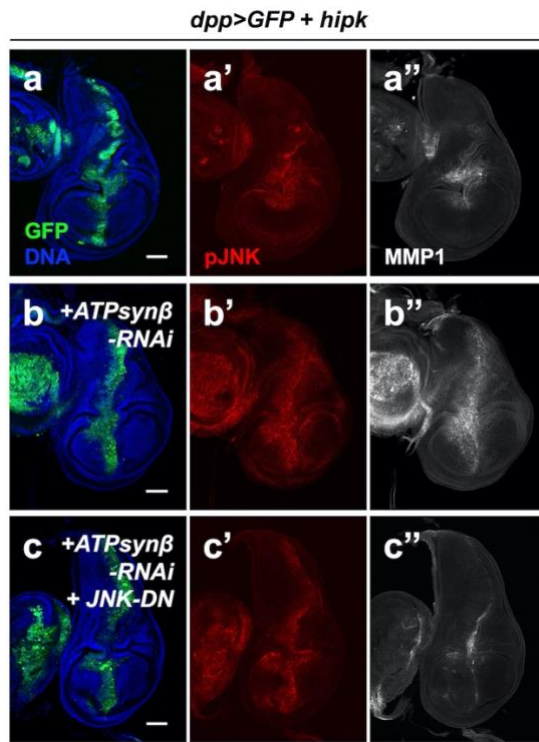


Figure 6.16. Mitochondrial impairment leads to JNK activation and the downstream MMP1 induction in Hipk tumor cells.

pJNK (red) and MMP1 (grey) staining in *hipk*-overexpressing discs (*dpp > GFP + hipk*) without (**a**) or with *ATPsynβ* knockdown (*dpp > GFP + hipk + ATPsynβ-RNAi*) (**b**), or with *ATPsynβ* knockdown and *JNK-DN* co-expression (*dpp > GFP + hipk + ATPsynβ-RNAi + JNK-DN*) (**c**). GFP (green) marks the transgene-expressing cells. DAPI staining for DNA (blue) reveals tissue morphology. Scale bars, 50 μ m.

6.4.7. The active mitochondrial metabolism depends on the positive feedback loop between Myc and aerobic glycolysis

Finally, we investigated how active mitochondrial metabolism is acquired in Hipk tumor cells. In our previous study, we demonstrated that *Drosophila* Myc (dMyc) and aerobic glycolysis, especially the committed step governed by 6-Phosphofructo-2-kinase/fructose-2,6-bisphosphatase (Pfk2; PFKFB in mammals) and Phosphofructokinase (Pfk), reciprocally stimulate each other, forming a positive feedback loop that drives Hipk tumor growth (Wong et al., 2019). Consistently, knockdown of *Myc* or *pfk2* in Hipk tumor cells prevented tumorous growth and the disc morphologies appeared wild type (Figure 6.17 b, d). In addition, both knockdowns reduced the overall mitochondrial activity (Figure 6.17 a, c). Comparable results were seen by examining salivary gland cells (Figure 6.13 e-f). Altogether, our data place the active mitochondrial metabolism downstream of the Myc-aerobic glycolysis feedback loop.

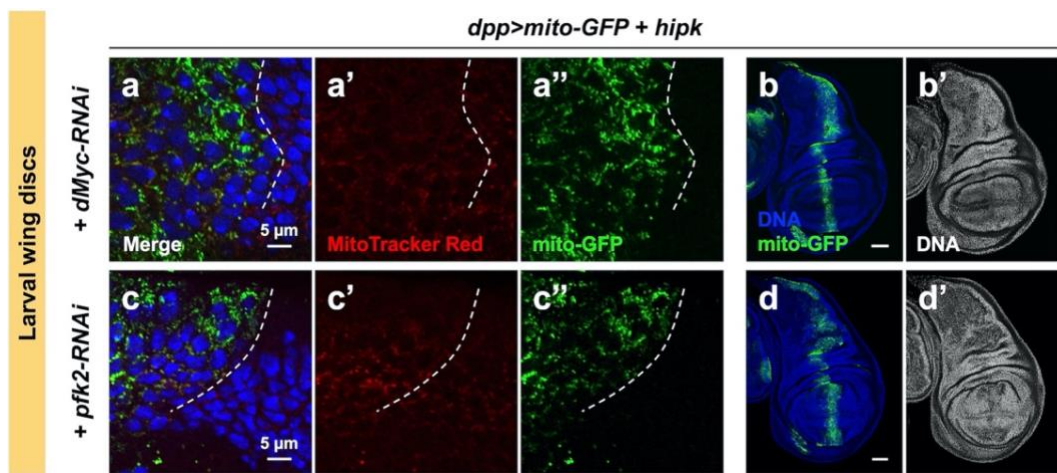


Figure 6.17. The active mitochondrial metabolism in Hipk tumor cells depends on both Myc and Pfk.

Mitochondria (marked by mito-GFP in green) in columnar epithelial cells on the basal side (a, c) and the whole disc morphologies (b, d) of *hipk*-overexpressing wing discs with either *dMyc* knockdown (*dpp > mito-GFP + hipk + dMyc-RNAi*) (a-b) or *pfk2* knockdown (*dpp > mito-GFP + hipk + pfk2-RNAi*) (c-d). Wing discs were stained with MitoTracker Red (red). The dashed line in a and c separate the transgene-expressing cells from the neighboring wild-type epithelial cells. DAPI staining for DNA (blue) reveals tissue morphology. Scale bars, 5 μ m (a, c); 50 μ m (b, d).

6.5. Discussion

6.5.1. Hipk elevation as an *in vivo* tumor model with active mitochondria

Distinct from the previously described tumor models with mitochondrial dysfunction (Ji et al., 2019; Katheder et al., 2017; Lee et al., 2013; Van Den Ameele and Brand, 2019; Wang et al., 2016), the elevated Hipk we present here is an *in vivo* tumor model with metabolically active mitochondria. Characterization of the Hipk tumor mitochondrial metabolism reveals a switch in morphology from fission to fusion (Figure 6.1), an increase in the overall respiratory activity (Figure 6.8) and a lack of ROS buildup (Figure 6.11). The Hipk-induced mitochondrial changes in the wing disc tumor cells seem not to be cell-type specific as comparable changes were observed in salivary gland cells and muscle cells (Figure 6.2, Figure 6.9, Figure 6.10).

Notably, knockdown of *Myc* or *Pfk2* in the tumor cells suppressed the MitoTracker Red incorporation and tumor growth phenotypes (Figure 6.17, Figure 6.13). *Myc*, a well-known oncprotein, plays conserved roles in cell growth, aerobic glycolysis and mitochondrial biogenesis (Li et al., 2005; Stine et al., 2015). In *Drosophila*, several genes encoding the mitochondrial ribosomal proteins have been found to be *Myc*-responsive (Orian et al., 2003). The fusion regulator genes, *marf* and *opa1*, together with *Myc*, are target genes of *Yki* (Nagaraj et al., 2012; Neto-Silva et al., 2010), and Hipk is a positive regulator of *Yki* (Chen and Verheyen, 2012). Thus, it is conceivable the elevated Hipk promotes active mitochondrial metabolism through the combined actions of *Myc* and *Yki*. In addition, because of the positive feedback loop between *Myc* and aerobic glycolysis (Wong et al., 2019), aerobic glycolysis (stimulated by *Pfk2*) likely maintains the mitochondrial functions through *Myc*. Thus, Hipk tumor growth and the associated metabolic profile seem to be acquired through highly orchestrated networks integrating multiple cell signaling molecules with metabolic pathways.

6.5.2. Regulation of mitochondrial fusion and activity by separate mechanisms

Mitochondrial morphology in general reflects the mitochondrial and cellular bioenergetic states as fused mitochondria are more prevalent in respiratory active cells (Westermann, 2012). Interestingly, we noted that suppressing mitochondrial fusion did not necessitate a loss of respiratory activity in Hipk tumor cells (Figure 6.12). Nor did inhibition of respiratory activity reverse the fusion phenotype (Figure 6.14). More importantly, inhibition of respiratory activity (by *pds-w-RNAi*) abrogated Hipk tumor growth whereas blocking mitochondrial fusion had negligible effects (Figure 6.12, Figure 6.14). This indicates that mitochondrial activity plays a predominant role in driving Hipk tumor growth. Our data also point to a model that the mitochondrial morphology and activity are governed separately and can be uncoupled from each other by genetic manipulations. This model is in line with recent findings showing that neuronal health depends on functional mitochondria, regardless of the shape (Trevisan et al., 2018). Therefore, we and others show a distinct scenario contrasting to the proposed mechanism of mitochondrial fusion in which a sufficiently large $\Delta\psi_m$ is required (Willems et al., 2015). Such a discrepancy could possibly be due to additional as yet unidentified mechanisms promoting fusion independent of $\Delta\psi_m$. Nevertheless, our observation that the highly fused mitochondria in Hipk tumor cells were metabolically active once again illustrates that tumor mitochondrial metabolism is achieved in a coordinated manner even though separate mechanisms may be involved.

6.5.3. A Pd subunit of complex I as a metabolic vulnerability in cancers

Upon perturbations of mitochondrial activity, we observed opposing tumorigenic outcomes. Depletion of Pdsw, but not ND-75/49/42 or ATPsyn β , abrogated Hipk tumor growth ([Figure 6.14](#)). In agreement with our findings, loss of mammalian NDUFB10 (Pdsw) reduces the growth of tumors with activated K-RAS ([Martin et al., 2017](#)), whereas low NDUFS1 (ND-75) is correlated with poor prognosis and metastasis in non-small cell lung cancer patients ([Su et al., 2016](#)). Here, we discuss the possible causes of these confounding results.

Subunits Pdsw, ND-75, ND-49, ND-42 are all required for complex I assembly ([Garcia et al., 2017](#)). NDUFB10 (Pdsw), which ‘interlocks’ with NDUFB5 (ND-SGDH in fly), may serve as a molecular clamp holding Pd and Pp modules together ([Fiedorczuk et al., 2016; Friederich et al., 2017; Guerrero-Castillo et al., 2017](#)). Based on the subunit locations within the complex, we hypothesized that depletion of Pdsw leaves the electron path of complex I relatively intact (where Pd module may only interact weakly with the Pp-Q-N subassembly) ([Figure 6.15 right](#)), whereas the inhibition of the other three subunits may disrupt the Q or N modules and causes defective electron transfer. Irrespective of the inhibitions, loss of the P module integrity or electron transfer renders proton pumping inefficient. Indeed, all tested RNAis targeting complex I subunits resulted in a reduction in the overall mitochondrial activity ([Figure 6.14](#)). Also, in support of our hypothesis, we observed moderate ROS in Hipk tumor cells with *pds*-RNAi and high ROS in tumor cells with *ND-75/49/42*-RNAi ([Figure 6.11](#)), suggestive of increased electron leakage in the latter tumors. Using *ATPsyn β* -RNAi as an example, we found that Hipk tumors with high ROS were associated with JNK-dependent MMP1 induction ([Figure 6.16](#)), which likely supports tumor invasion. In other words, excessive ROS caused by mitochondrial dysfunction may accelerate tumor progression. Therefore, we propose that, to evade massive ROS production and the consequent deleterious effects, targeted but not generic inhibition of mitochondrial activity is required to suppress tumor growth.

Intriguingly, although *ND-75*-RNAi or *ATPsyna*-RNAi failed to suppress Hipk tumor growth, they have been shown to reduce larval brain tumor growths ([Lee et al., 2013; Van Den Ameele and Brand, 2019](#)). The differential responses to mitochondrial

dysfunction may be accounted for by the intrinsic potentials of the tumors to remove excess ROS. Future work involving the introduction of ROS scavengers and antioxidant enzymes is warranted to address if generic inhibition of respiratory activity can suppress Hipk tumor growth in the absence of ROS.

In summary, we establish elevated Hipk as a tumor model characterized by functional mitochondria, which is distinct from the previously described models with mitochondrial dysfunction. Thus, we, together with others, develop essential *in vivo* fly tumor models to understand how mitochondria are linked to cancer. Of note, we observe complex I subunit-dependent, opposing tumorigenic outcomes, which may be determined by the architecture of complex I. Further studies employing the power of fly genetics may unravel specific roles of the subunits during tumorigenesis.

Chapter 7.

Conclusive remark

Here, we establish elevation of *Drosophila* Homeodomain-interacting protein kinase (Hipk) as an *in vivo* neoplastic tumor model featuring several hallmarks of cancer including proliferation, invasion and metabolic reprogramming. The formation of the tumor is likely attributable to perturbed Wingless (Wg), Hippo, Hedgehog, Notch and JNK signaling caused by elevated Hipk. Indeed, these aberrant signals converge at the transcriptional control of the oncogene Myc. Thus, rather than targeting the signaling pathways singly or simultaneously, we discover that inhibition of Myc blocks the tumorigenesis induced by Hipk.

In addition, we discover that Hipk activity is highly responsive to high sugar diet. The sugar effect is dependent on the nutrient-sensing hexosamine and insulin receptor (InR) signaling pathways. In particular, we identify that O-GlcNAc transferase (OGT) of the hexosamine pathway and salt-inducible kinase 2 (SIK2) of InR signaling are positive regulators of Hipk. OGT directly modifies Hipk by O-GlcNAcylation and controls its protein stability. SIK2 promotes Hipk phosphorylation and maintain Hipk protein expression levels, although whether the effects of SIK2 are direct or indirect remains unaddressed. More importantly, both OGT and SIK2 synergize with Hipk to induce tumorigenesis. *In silico* analyses show numerous putative O-GlcNAc or SIK target sites of HIPKs ([see Appendix](#)). Our work may serve as a seed for further investigations into whether nutrient signaling pathways participate in tumor progression by a complex interplay of post-translational modifications of cancer-related proteins.

Furthermore, we functionally characterize the metabolic profiles of the Hipk tumor model. The tumor cells display a positive feedback loop between Myc and aerobic glycolysis, and active mitochondrial metabolism downstream of the loop. Myc is considered ‘undruggable’ due to its nuclear localization. Intriguingly, inhibition of the glycolytic enzymes Phosphofructokinase 2 (Pfk2) and Pfk significantly abrogates Myc accumulation and therefore Hipk tumor growth. Also, we discover that precise inhibition of the mitochondrial complex I by targeting a Pd subunit called Pdsw blocks Hipk-mediated tumorigenesis.

Hence, our work exemplifies the use of a *Drosophila* tumor model to elucidate the nutrient-sensing and metabolic control of cancer-related proteins (Hipk and Myc), and to identify several metabolic vulnerabilities (OGT, SIK2, Pfk2/Pfk and Pdsw) that can be targeted to suppress tumor growth. Continued investigations are crucial for the development of novel, effective approaches in the prevention and treatment of cancer.

Chapter 8.

Materials and Methods

8.1. Materials and methods for Chapter 2

8.1.1. Drosophila culture

Flies were raised on standard media, and *w₁₁₁₈* was used as wild type. All crosses were raised at 29°C to increase the effectiveness of GAL4-driven *UAS* constructs unless otherwise noted. All genetic interaction studies included controls for GAL4 titration through the use of benign *UAS* lines such as *UAS-GFP*, *UAS-RFP* or *UAS-lacZ* to match the *UAS* construct dose in experimental crosses.

Fly strains used in this study were as follows: *dpp-GAL4* ([Staehling-Hampton et al., 1994](#)), *UAS-HA-hipk_{1M}* (II) ([Swarup and Verheyen, 2011](#)), *UAS-HA-hipk_{3M}* (III), *dpp-GAL4*, *UAS-HA-hipk_{3M}* [recombinant stock], *UAS-eGFP* (BL 5431), *UAS-eGFP* (BL 5430), *UAS-P35* (BL 5072), *ey-GAL4* (BL 5535), *UAS-Axin-GFP* (BL 7225), *UAS-Egfr-DN* (dominant negative) with inserts on both II and III, *UAS-bsk-DN* (BL 6409), *UAS-yki-RNAi* (BL 34067), *UAS-DI-DN* (BL 26697), *UAS-Ci-REP*, *UAS-Arm-S10* ([Mirkovic et al., 2011](#)), *UAS-Stat92E*, *UAS-Ras-act* (from H. Richardson), *UAS-Eiger*, *UAS-yki-S168A:GFP*, *UAS-N-act*, *UAS-Ci-5M*, *UAS-hipk-RNAi* (VDRC 108254), *UAS-hop-RNAi* (VDRC 102830), *UAS-upd-RNAi*, *UAS-pan-RNAi* (TCF; VDRC 3014), *yw hsflp[122]; sp/CyO; Act>CD2>GAL4 UAS-RFP/TM6B, Dll-lacZ, puc-LacZ, 10xStat92E-GFP* (BL 26197) and *MS1096-GAL4* (BL 8660). BL and VDRC refer to the stock numbers of the fly strains obtained from the Bloomington *Drosophila* Stock Center (Bloomington, IN, USA) and the Vienna *Drosophila* Resource Center (VDRC), respectively.

8.1.2. Immunofluorescence staining

Third instar imaginal discs were dissected and stained using standard protocols and, in most cases, we analyzed ≥ 20 discs per genotype. The following primary antibodies were used: mouse anti-Mmp1 (1:100; 3A6B4, 3B8D12, 5H7B11 DSHB; Rubin, G.M.), rat anti-Ci (1:20; 2A1 DSHB; Holmgren, R.), mouse anti-En (1:10; 4D9 DSHB; Goodman, C.), mouse anti-Dlg (1:100; 4F3 DSHB; Goodman, C.), mouse anti-

HA (1:200; ABM), rabbit anti-cleaved Caspase-3 (Asp175) (1:100; 9661S; Cell Signaling), rabbit anti-Ndg [1:500; gift of Anne Hölz ([Wolfstetter et al., 2009](#))], rabbit anti-Twi [1:3000; gift of Maria Leptin], mouse anti- β -Galactosidase (1:50; 40-1a DSHB; Sanes, J.R.), rabbit anti-CycE (1:100; d-300; Santa Cruz), mouse anti-Wg (1:40; 4D4 DSHB; Cohen, S.M.), mouse anti-Cut (1:50; 2B10 DSHB; Rubin, G.M.), mouse anti-Ptc (1:40; Apa1 DSHB; Guerrero, I.). Rabbit anti-Hipk antibodies were generated in our laboratory and used at 1:200 dilution. The following secondary antibodies were obtained from Jackson ImmunoResearch: DyLight 649 anti-rabbit, DyLight 649 anti-rat, Cy3 anti-mouse and Cy3 anti-rabbit. Nuclei were detected by staining with DAPI, and F-actin was detected by staining with Rhodamine phalloidin (R-415; Molecular Probes). Immunofluorescent images were acquired using a Nikon Air laser-scanning confocal microscope. Images were processed with Nikon Elements, Adobe Photoshop, Adobe Illustrator, ImageJ and Helicon Focus. For a subset of fluorescent images, channel colors were converted to accommodate color-blind viewers.

8.1.3. Measurements of proliferation and invasiveness

The proliferative effects of each transgene were assessed by measuring the area of the GFP positive cells (driven by *dpp-GAL4*) and dividing it by the total disc area (*dpp/total*). The difference in ratios was then quantified using one-way ANOVA, with the Holm-Sidak post hoc test applied for multiple comparisons. The scores for the Holm-Sidak tests are depicted as ‘ns’=not significant, * $p < 0.05$, ** $p < 0.01$, *** $p < 0.001$ and **** $p < 0.0001$. The invasive effects caused by each transgene were assessed by assigning a ‘relative degree of invasiveness’ score to each disc. We defined the ‘relative degree of invasiveness’ scores as follows: ‘None’ = no cells found outside the normal *dpp > GFP* region; ‘Weak’ = a few cells emerging from the *dpp > GFP* region, not only a widened GFP region attributable to proliferation; ‘Moderate’ = extensions of cells that have traveled to edges of the hinge region; or ‘Strong’ = all of the above and some solitary GFP masses found distinct from the main *dpp > GFP* region.

8.2. Materials and methods for Chapter 3

8.2.1. Drosophila culture

Crosses were kept at 25°C or 29°C as indicated on the food. The following fly strains were used: *dpp-Gal4*, *dpp-Gal4 UAS-HA-hipk_{3M}* (abbreviated as *dpp > hipk*) (Blaquiere et al., 2018), *en-Gal4 UAS-GFP*, *actin5c-Gal4* (BL 3954), *UAS-HA-hipk-3M* (Lee et al., 2009b), *UAS-ogt-RNAi* (VDRC 18610), *UAS-ogt-RNAi #2* (2824-1) (Sinclair et al., 2009), *UAS-ogt-flag* (D. Sinclair), *UAS-ogt* (Sinclair et al., 2009), *UAS-GFP* (BL 5431), *UAS-RFP* (BL 7118), *UAS-gfat1* (D. Sinclair), *UAS-gfat2* (gift from Linda Partridge), *UAS-gfat1-RNAi* (D. Sinclair), *UAS-gfat1-RNAi* (VDRC 24539), *UAS-gfat2-RNAi* (VDRC 105129), *UAS-gfat2-RNAi* (BL 34740), *UAS-hipk-RNAi* (VDRC 108254) and *UAS-white-RNAi* (BL 33762). The BL lines were obtained from Bloomington Drosophila Research Centre. The VDRC lines were obtained from Vienna Drosophila RNAi Centre. The *ogt* null alleles *sxc[4]*, *sxc[5]*, *sxc[6]* and *sxc[7]* have been described (Gambetta et al., 2009; Sinclair et al., 2009).

Regular cornmeal-molasses fly food containing 0.8 g agar, 2.3 g yeast, 5.7 g cornmeal and 5.2 mL molasses per 100 mL was used. Control diet (also known as low sucrose diet (LSD)) and high sucrose diet (HSD) have been previously described (Musselman et al., 2011). Briefly, control diet referred to semi-defined food containing 1 g agar, 8 g Brewer's yeast, 2 g yeast extract, 2 g peptone, 5.1 g sucrose per 100 mL. HSD contained 1 g agar, 8 g Brewer's yeast, 2 g yeast extract, 2 g peptone, 34.2 g sucrose per 100 mL. Glucosamine supplemented food was prepared by adding glucosamine to control semi-defined food at a final concentration of 0.1 M.

8.2.2. Immunofluorescence staining

Larval imaginal discs or salivary glands were dissected in phosphate-buffered saline (PBS) and fixed in 4% paraformaldehyde (PFA) for 15 min at room temperature. After fixation, samples were washed with PBS with 0.1% Triton X-100 (PBST). After blocking with 5% BSA in PBST for 1 hour at room temperature, samples were incubated with primary antibodies overnight at 4°C. The primary antibodies used include rabbit anti-phospho-Histone H3 (Ser10) (Cell Signaling Technology 9701), mouse anti-Mmp1 (1:100 DSHB 3A6B4, 1:100 3B8D12, 1:100 5H7B11), rabbit anti-Cyclin E (d-300) (1:100;

Santa Cruz sc-33748), rabbit anti-Hipk (1:200) ([Blaquiere et al., 2018](#)), rat anti-DE-Cadherin (1:50, DSHB DCAD2), rabbit anti-OGT (1:100, Santa Cruz sc-32921), rabbit anti-dMyc (d1-717) (1:500, Santa Cruz sc-28207) and mouse anti-O-GlcNAc (RL2) (1:100, BioLegend 677902). After washing with PBST, samples were incubated with Cy3- and/or Alexa Fluor 647-conjugated secondary antibodies (1:500, Jackson ImmunoResearch Laboratories, Inc.), DAPI (4',6-Diamidino-2-Phenylindole, Dihydrochloride) (final concentration: 0.2 µg per mL, Invitrogen D1306) for 2 hours at room temperature. Samples were mounted in 70% Glycerol/PBS after wash. Images were taken on a Nikon Air laser-scanning confocal microscope and processed by Image J. For O-GlcNAc (RL2) staining, in the washing steps between primary and secondary antibody incubations, tissue samples were incubated 37°C for 1.5 hours, which increases the penetrance of O-GlcNAc antibodies into the tissues.

8.2.3. Quantitative real time-PCR (qRT-PCR)

Total RNA isolation was performed using the RNeasy Mini Kit (Qiagen 74104), followed by first-strand cDNA synthesis using the PrimeScript Kit (Clontech 6110A). qRT-PCR was performed using the SensiFAST SYBR Kit (Bioline 92005) on the StepOne Real-Time PCR System (Applied Biosystems). See [Table 8-1](#) for the primers used.

Table 8-1. Primers used for qRT-PCR

Species	Gene	Forward sequence (5' → 3')	Reverse sequence (5' → 3')
<i>Drosophila</i>	<i>rp49</i>	ATCGGTTACGGATCGAACAA	GACAATCTCCTTGCCTTCT
<i>Drosophila</i>	<i>hipk</i>	GCACCACAACTGCAACTACG	ACGTGATGATGGTGCAGACTC
<i>Drosophila</i>	<i>ogt</i> (or <i>sxc</i>)	GCTATAACGCCCTGGAACAAA	CCTTGGCATACTGTGAGCA
Human	<i>HPRT1</i>	GCTATAAATTCTTGCTGACCT GCTG	AATTACTTTATGTCCCCGTGG ACTGG
Human	<i>HIPK2</i>	AATAGAGCCGAGTTCCAATGG	GTCTGCTCGTAAGGTAGGCTT
Human	<i>OGT</i>	CCTGGGTCGCTTGGAAAGA	TGGTTGCGTCTCAATTGCTTT
Human	<i>α-Tubulin</i>	CCAAGCTGGAGTTCTCA	CAATCAGAGTGCTCCAGG
Mouse	<i>β-Tubulin</i>	CTCCACCCAGAGAACGCACG	GC GGAGCTGATCGAAAATGTC
Mouse	<i>HIPK2</i>	TGCTTGACTCCCCATAGTG	CTTGCAAATCTCCATGTTTGG

8.2.4. Immunoblotting

Cells or tissues were lysed with 1× Cell Lysis Buffer (Cell Signaling Technology), supplemented with 1× Protease Inhibitors (Roche) and 1 mM phenylmethylsulfonyl

fluoride (PMSF). Protein lysates with 1× SDS sample buffer were resolved on SDS/PAGE and then transferred to nitrocellulose membranes. Membranes were blocked with 5% skimmed milk or 5% bovine serum albumin before primary and secondary antibody incubation. Images were acquired by a FujiFilm LAS-4000 Chemiluminescent Scanner or the Li-Cor Odyssey Imaging System. The primary antibodies used include mouse anti-β-Actin (1:5000, Santa Cruz sc-47778), mouse anti-β-Tubulin (1:1000, Abm G098), mouse anti-Flag (1:1000, Sigma F1804), rabbit anti-Hipk (1:2000) ([Blaquiere et al., 2018](#)), mouse anti-Myc (1:1000, Millipore 05-724) and rabbit anti-OGT (1:1000, Santa Cruz sc-32921). HRP (Jackson ImmunoResearch) or fluorescent dye-conjugated secondary antibodies were used.

8.2.5. Cycloheximide (CHX) chase assay

Wandering third-instar larvae were rinsed in PBS and dissected. The anterior half was cultured in insect medium (HyClone) supplemented with CHX (Sigma, 200 µg/mL) for 0 to 120 (or 150) min at room temperature. Tissues were then homogenized in lysis buffer by brief sonication and used for western blotting.

8.2.6. Co-immunoprecipitation

Protein extracts were incubated with indicated antibodies at 4°C overnight, followed by incubation with a mixture of protein A (Invitrogen 10002D) and protein G (NEB S1430S) magnetic beads for 3 h at 4°C. The beads were washed with lysis buffer and boiled in 3× SDS sample buffer. The supernatants were then analyzed by western blotting.

8.2.7. WGA pull down

WGA enrichment of O-GlcNAc modified proteins has been previously described ([Liu et al., 2017](#)). Protein extracts were incubated in a final volume of 1 ml IP buffer (15 mM Hepes pH 7.9, 200 mM KCl, 1.5 mM MgCl₂, 0.2 mM EDTA pH 8, 0.25% NP-40, 20% glycerol, 0.3 mM DTT, 1× Complete protease inhibitor cocktail, 1 mM PMSF) with 100 µl of a 50% slurry of washed succinylated WGA-agarose resin (Vector Labs) for 12 h at 4°C. Beads were washed with IP buffer containing 0.5 mM DTT and 0.4% NP-40,

followed by a 1 h incubation with 1 M GlcNAc (GALAB) on ice to elute resin-bound proteins.

8.2.8. GalNAz feeding and biotin-conjugation reaction

The metabolic labeling of O-GlcNAc modified proteins and subsequent chemoselective ligation has been described previously ([Liu et al., 2017](#)). Ac4GalNAz media was made by adding Ac4GalNAz (dissolved in DMSO) to standard cornmeal-molasses fly food at 55°C to a final concentration of 100 µM. Control food was made by adding an equal volume of DMSO. Parents mated on the indicated food and the progeny grew up on it since birth. To biotinylate O-GlcNAz-modified proteins, a Staudinger capture reaction using biotinylated phosphine capture reagent (biotin-azophosphine) was performed. Biotin-azo-phosphine was added to the protein extracts (in 1% SDS-PBS) at a final concentration of 200 µM. The mixture was incubated for overnight at room temperature. Unreacted probe was removed by chloroform-methanol purification. Biotinylated proteins were analyzed by Streptavidin (Strvn) blot using Odyssey (LI-COR Biosciences).

8.2.9. In vitro GalT labeling

In vitro Galactosyltransferase labeling using the Click-iT O-GlcNAc Enzymatic Labeling System (Invitrogen) has been described ([Liu et al., 2017](#)). Briefly, Gal-T1_{Y289L} was incubated with proteins in labeling buffer (containing 20 mM HEPES, pH 7.9; 50 mM NaCl; 2% NP-40; 5.5 mM MnCl₂; 25 µM UDP-GalNAz) according to manufacturer's recommendations. Reaction was performed at 4°C under gentle agitation for 24 h. After labeling, proteins were chloroform-methanol precipitated. The proteins were resuspended with 1% SDS, 20 mM HEPES pH 7.9 and iodoacetamide (IAA) was added to a final concentration of 15 mM to block the free cysteine thiols. The mixture was then under gentle agitation for 30 min at room temperature, followed by addition of DBCO-S-S-PEG₃-Biotin (Jena Bioscience) at a final concentration of 40 µM. The incubation of the mixture was protected from light and under gentle agitation for 30 min at room temperature. Excess nonreactive reagents were then removed by chloroform-methanol protein purification. Proteins were resuspended in 1% SDS, 20 mM HEPES pH 7.9 and incubated with streptavidin beads for 1-2 hour at 4°C on a rocking platform. The binding

proteins were released by final concentration of 50 mM DTT at 37°C for 30 min, followed by subsequent western blot analyses using 4-20% gradient SDS-PAGE.

8.2.10. Mammalian cell culture

HEK293 and MCF7 were cultured in Dulbecco's modified eagle medium (DMEM) high glucose (25 mM glucose) (Gibco 11965-092) supplemented with 10% fetal bovine serum (FBS). All cells were cultured in a humidified, 5% CO₂ incubator at 37°C. Cells were transiently transfected with mock (empty vector) or indicated plasmids using Lipofectamine 3000 (Invitrogen) or TransIT-2020 (Mirus Bio) according to the manufacturers' instructions. Cells were harvested 48 h after transfection unless otherwise indicated. pcDNA3.1-myc-HIPK2 and pcDNA3.1-myc-HIPK2-S1008A were synthesized and purchased from GenScript. pCMV-myc-OGT-WT has been described ([Martinez-Fleites et al., 2008](#)). MEF cells containing lentivirus encoding mutated estrogen receptor (mER)-Cre-2A-GFP construct were described previously ([Kazemi et al., 2010](#)). Cells were cultured in DMEM (high glucose, Gibco) with 10% (vol/vol) FBS and 1% (vol/vol) penicillin/ streptomycin at 37°C in a water-jacketed, humidified CO₂ (5%) incubator. Cells were plated at 30 to 50% confluence. Cre-recombinase was activated to excise OGT through incubation with 2 µM 4-hydroxytamoxifen (4HT in methanol, Bioshop) for 72 h after plating. Fresh medium and 4HT were changed every 24 h.

8.2.11. Site-directed mutagenesis

For single site-directed mutagenesis, PCRs were run for 18 cycles of 15 s at 95°C, 30 s at 60°C, and 18 min at 72°C using Q5 High-Fidelity DNA Polymerase (NEB M0491). In addition to GC enhancer, 3.5% DMSO was included in the PCR mix because of the GC-rich regions in the HIPK2 insert. The PCR products were treated with FastDigest DpnI (Thermo Scientific FD1704) to remove the template DNA, followed by transformation into One-Shot MAX Efficiency DH5α-T1 Competent Cells (Invitrogen 12297016). Multiple site-directed mutagenesis was performed using the GeneArt Site-Directed Mutagenesis PLUS System (Invitrogen A14604) with slight modifications. DNA methylation was not included prior to PCR. Instead, template DNA was removed using DpnI digestion, followed by in vitro recombination reaction. See [Table 8-2](#) for the mutagenic primers used. Mutations were then verified by DNA sequencing.

Table 8-2. Primers used for site-directed mutagenesis to replace the identified O-GlcNAc sites with alanine

Mutation site(s)	Forward sequence (5' → 3')	Reverse sequence (5' → 3')
S852A	CAGTAGCCCGGCCTGCGCCACCTCGGT CACCTG	CAGGTGACCGAGGTGGCGCAGGCCGGG CTACTG
T853A	CCCGGCCTGCAGCGCCTCGGTACCTG	CAGGTGACCGAGGCCTGCAGGCCGGG
S852A, T853A	CAGTAGCCCGGCCTGCGCCCGCTCGGT CACCTGTGG	CCACAGGTGACCGAGGCAGGCCAGGCC GGGCTACTG
T1009A	CAGCAACGTGACCTCCGCCAGCGGTCA CTCTTC	GAAGAGTGACCGCTGGCGGAGGTACCG TTGCTG
S1008A, T1009A	CAGCAACGTGACCGCCGCCAGCGGTCA CTCTTC	GAAGAGTGACCGCTGGCGGCGGTACCG TTGCTG
S1147A	CCACCAGGTCCCCGTGCCATGGGCC CCGGGTC	GACCCGGGGGCCATGCCACGGGAC CTGGTGG

8.2.12. Mapping of O-GlcNAc sites of human HIPK2

HEK293 cells were transfected with pcDNA3.1-myc-HIPK2, followed by treatment with Thiamet-G to block the removal of physiological relevant O-GlcNAc attachments. HIPK2 harvested from the cells was purified through immunoprecipitation using anti-Myc tag antibodies and succinylated wheat germ agglutinin (sWGA) enrichment. The resulting purified HIPK2 was run on gels, followed by in-gel tryptic digestion and then LC-MS/MS. Data were obtained from two biological samples.

For in-gel trypsin digestion, the 80~200 kDa protein bands from an SDS-PAGE gel were cut into ~1 mm cubes and subjected to in-gel digestion followed by extraction of the tryptic peptides. The excised gel pieces were destained repeatedly in 25 mM ammonium bicarbonate (ABC)/40% acetonitrile (ACN), reduced with 10 mM dithioerythritol for 1 h at 37°C, and alkylated with 55 mM iodoacetamide at room temperature in the dark for 1 h. The gel slices were then dried and digested first by Lyc-C protease at 37°C for 3 h, followed by trypsin at 37°C overnight. The digested peptides were extracted twice with 50% ACN/ 5% trifluoroacetic acid (TFA) and once with ACN. Extracts from each sample were combined and dried down by use of a SpeedVac. Following the digestion, peptide mixtures were desalted on C₁₈ StageTips ([Rappaport et al., 2007](#)) and resuspended in 0.1% formic acid for LC-MS/MS analysis.

LC-MS/MS analysis was performed on a Thermo UltiMate 3000 RSLC nano system connected to a Thermo Orbitrap Fusion™ Lumos™ Tribrid™ Mass Spectrometer (Thermo Fisher Scientific, Bremen, Germany) via a nanospray interface (New Objective,

Woburn, MA). Peptide mixtures were loaded onto a PepMap C18 column (75 µm ID, 25 cm length, 2 µm particles, pore size 100 Å, Thermo Fisher Scientific) and separated using a 90 min segmented gradient from 5% to 45% solvent B (80 % acetonitrile with 0.1 % formic acid) at a flow rate of 300 nL/min. Solvent A was 0.1% formic acid in water. The mass spectrometer was operated in the data-dependent mode. Briefly, survey scans of peptide precursors from 350 to 1800 *m/z* were performed at 120K resolution with a 2 × 10⁵ ion count target. The Top Speed method was enabled to ensure full MS spectra were acquired every 3 s. Most abundant precursor ions with 2-8 charges above a threshold ion count of 50,000 were selected for data-dependent higher energy collision dissociation (HCD) at a resolution of 30K and a normalized collision energy of 30%. If peaks at *m/z* 138.0545 (HexNAc oxonium fragment ions), or *m/z* 204.0867 (HexNAc oxonium ions) were detected within the top 50 most abundant peaks, a subsequent electron-transfer/higher energy collision dissociation (EThcD) MS/MS scan of the precursor ion was triggered and acquired in the Orbitrap at a resolution of 30K.

All MS and MS/MS raw spectra from each sample were searched against a uniprot human protein database using Byonic v. 2.16.11 (Protein Metrics, San Carlos, CA). The peptide search parameters were as follow: two missed cleavage for full trypsin digestion with fixed carbamidomethyl modification of cysteine, variable modifications of methionine oxidation, deamidation on asparagine or glutamine residues, and *N*-acetylhexosamine modification of serine and threonine. The peptide mass tolerance was 10 ppm and fragment mass tolerance values for HCD and EThcD spectra were 20 ppm. The maximum number of common and rare modifications were set at two and one, respectively.

8.2.13. Statistical analysis

The data were represented by mean ± SEM. The *p* values were determined by two-tailed Student's t tests. *p* < 0.05 was considered statistically significant. Bar graphs were generated by Microsoft Excel. Violin plots and box and whisker plots to represent the distribution of data were generated by BoxPlotR ([Spitzer et al., 2014](#)).

8.3. Materials and methods for Chapter 4

8.3.1. Drosophila culture

Crosses were kept at 25°C unless otherwise indicated. The following fly strains were used: *w₁₁₁₈*, *dpp-Gal4*, *dpp-Gal4 UAS-HA-hipk-WT* (abbreviated as *dpp>hipk*) (Blaquiere et al., 2018), *tGPH* (BL 8163), *en-Gal4*; *tGPH* (BL 8165), *UAS-HA-hipk-WT* (III) (abbreviated as *UAS-hipk*) (Lee et al., 2009b), *UAS-HA-hipk-WT* (II) (abbreviated as *UAS-hipk*), *UAS-GFP* (BL 5431), *UAS-RFP* (BL 7118), *UAS-SIK2-RNAi* (VDRC 26497), *UAS-SIK2-RNAi* (BL 55880), *UAS-SIK3-RNAi* (II) (VDRC 107458), *UAS-SIK3-RNAi* (III) (VDRC 39866), *UAS-SIK2/3-RNAi* (VDRC 103739), *UAS-InR-RNAi* (VDRC 992), *UAS-InR-CA* (also known as *UAS-InR-A1325D*) (BL 8263), *UAS-SIK2-CA* (also known as *UAS-SIK2-S1032A*) (Wehr et al., 2013). *UAS-myc-SIK2-WT*, *UAS-myc-SIK2-KD*, *SIK2Δ41* have been described previously (Choi et al., 2011). To generate heat-shock inducible actin flip-out clones, *yw hsFlp[122]*; *tGPH*; *act>CD2>Gal4 UAS-RFP/TM6B* was used. A 10-15 min heat shock (37°C) was applied to larvae grown for two to three days after egg laying (25°C). After heat shock, the larvae were grown at 29°C and dissected when they reached third instar larval stage.

Regular cornmeal-molasses fly food containing 0.8 g agar, 2.3 g yeast, 5.7 g cornmeal and 5.2 mL molasses per 100 mL was used. High sucrose diet (HSD) has been previously described (Musselman et al., 2011). Briefly, HSD contained 1 g agar, 8 g Brewer's yeast, 2 g yeast extract, 2 g peptone, 34.2 g sucrose per 100 mL.

8.3.2. Immunofluorescence staining

Larval imaginal discs, salivary glands and fat tissues were dissected in phosphate-buffered saline (PBS) and fixed in 4% paraformaldehyde (PFA) for 15 min at room temperature. After fixation, samples were washed with PBS with 0.1% Triton X-100 (PBST). After blocking with 5% BSA in PBST for 1 hour at room temperature, samples were incubated with primary antibodies overnight at 4°C. The primary antibodies used were rabbit anti-Hipk (1:200) (Blaquiere et al., 2018). After washing with PBST, samples were incubated with Cy3-conjugated secondary antibodies (1:500, Jackson ImmunoResearch Laboratories, Inc.), DAPI (4',6-Diamidino-2-Phenylindole, Dihydrochloride) (final concentration: 0.2 µg per mL, Invitrogen D1306) and/or Alexa

Fluor™ 647 Phalloidin (1:500, Invitrogen A22287) for 2 hours at room temperature. Samples were mounted in 70% Glycerol/PBS after wash. Images were taken on a Nikon Air laser-scanning confocal microscope and processed by Image J.

8.3.3. Quantitative real time-PCR (qRT-PCR)

Total RNA isolation was performed using the RNeasy Mini Kit (Qiagen 74104), followed by first-strand cDNA synthesis using the PrimeScript Kit (Clontech 6110A). qRT-PCR was performed using the SensiFAST SYBR Kit (Bioline 92005) on the StepOne Real-Time PCR System (Applied Biosystems). See **Table** 8-3 for primers used.

Table 8-3. Primers used for qRT-PCR

Drosophila gene	Forward sequence (5' → 3')	Reverse sequence (5' → 3')
rp49	ATCGGTTACGGATCGAACAA	GACAATCTCCTTGCCTCT
hipk	GCACCACAACTGCAACTACG	ACGTGATGATGGTGCAGACTC
InR	ACAAAATGTAAAACCTTGCAAATCC	GCAGGAAGCCCTCGATGA

8.3.4. Immunoblotting

Cells or tissues were lysed with 1× Cell Lysis Buffer (Cell Signaling Technology), supplemented with 1× Protease Inhibitors (Roche), 1 mM phenylmethylsulfonyl fluoride (PMSF) and/or 1 mM sodium fluoride (NaF). Protein lysates with 1× SDS sample buffer were resolved on SDS/PAGE and then transferred to nitrocellulose membranes. Membranes were blocked with 5% skimmed milk or 5% bovine serum albumin before primary and secondary antibody incubation. Images were acquired by a FujiFilm LAS-4000 Chemiluminescent Scanner or the ChemiDoc™ MP Imaging System (Bio-Rad). The primary antibodies used include mouse anti-β-Tubulin (1:1000, Abm G098), rabbit anti-Hipk (1:2000) ([Blaquiere et al., 2018](#)), mouse anti-Myc (1:1000, Millipore 05-724), rabbit anti-AKT (1:1000, Cell Signaling Technology 9272) and rabbit anti-p-AKT (S473 in human AKT) (1:2000, Cell Signaling Technology 4060S). S473 in human AKT corresponds to S505 in the shorter isoform of *Drosophila* Akt (isoform A; Uniprot entry: [A0A0B4LIA3](#)) and S586 in the longer isoform (isoform C; Uniprot entry: [Q8INB9](#)). HRP-conjugated secondary antibodies (Jackson ImmunoResearch) were used. HA-tagged Hipk was also detected using HRP-conjugated anti-HA-tag (6E2) antibodies (1:2000, Cell Signaling Technology 2999).

8.3.5. Co-immunoprecipitation

Protein extracts were incubated with indicated antibodies at 4°C overnight, followed by incubation with a mixture of protein A (Invitrogen 10002D) and protein G (NEB S1430S) magnetic beads for 3 hours at 4°C. The beads were washed with lysis buffer and boiled in 3x SDS sample buffer. The supernatants were then analyzed by western blotting.

8.3.6. Insulin stimulation

Wandering third-instar larvae were rinsed in PBS and dissected. The anterior half was cultured in insect medium (HyClone) supplemented with recombinant human insulin (Sigma I9278, 10 mg/mL or 1.7 mM) at 1 µM for 15 minutes at room temperature unless otherwise indicated. Tissues were then homogenized in lysis buffer by brief sonication, followed by centrifugation. The supernatants were used as protein samples.

8.3.7. Lambda phosphatase treatment

Protein samples were divided into three aliquots. SDS sample buffer was directly added to one of the aliquots, which was used as the untreated sample. The other two aliquots were treated with either mock (H_2O)- or lambda protein phosphatase (200 units, NEB P0753S) in the presence of the 1X NEBuffer and 1 mM MnCl₂ for 30 min at 30°C. SDS sample buffer was then added to the treated aliquots.

8.3.8. Site-directed mutagenesis

To generate the Hipk-6A (S133A, S753A, S858A, T1084A, S1195A and S1290A) mutant, two rounds of multiple site-directed mutagenesis were performed. In the first round, S133A, S858A and S1195A were introduced to pCMV-HA-Hipk-WT to generate the Hipk-3A mutant. In the second round, S753A, T1084A and S1290A were introduced to the Hipk-3A to generate the Hipk-6A. Multiple site-directed mutagenesis was performed using the GeneArt Site-Directed Mutagenesis PLUS System (Invitrogen A14604) with modifications. DNA methylation was not included prior to PCR. Instead, template DNA was removed using DpnI digestion, followed by *in vitro* recombination

reaction. See **Table 8-4** for the mutagenic primers used. Mutations were then verified by DNA sequencing.

Table 8-4. Primers used for site-directed mutagenesis to replace the putative SIK target sites with alanine in *Drosophila* Hipk

Mutation site(s)	Forward sequence (5' → 3')	Reverse sequence (5' → 3')
S133A	GGATCGAAAGCGGGAGCAGGACCAGGA CCAG	CTGGTCCTGGCCTGCTCCCGCTTCG ATCC
S753A	GCCAAGGGAACGCTTATCGCGTGC	GCACCGCGATAAGCGTTCCCTTGGC
S858A	CACCACATTGTAGCCAACTGCAACGC	GCGTTGCAGTTGGCTACAATGTGGTG
T1084A	GCCGCACATTCCCAGCCAAGCAGGAGCC	GGCTCCTGCTTGGCGGGAAATGTGCGGC
S1195A	CTATCGTCAGGCCAGCACAGCCGCTCC	GGAGGCGGCTGTGCTGGCTGACGATAG
S1290A	CGGCCCACAAACAGCGCCAGTCGTCAAG TG	CACCTGACGACTGGCGCTGTTGTGGC CG

8.3.9. Generation of transgenic fly

pCMV-HA-Hipk-6A was generated by site-directed mutagenesis from pCMV-HA-Hipk-WT. Using XbaI_HA forward primer and XbaI_Hipk reverse primer (**Table 8-5**), we amplified the HA-Hipk-6A construct with the introduction of XbaI restriction sites at both ends. The PCR-cloned HA-Hipk-6A was then subcloned into the XbaI site of the pUAST-attB empty vector. The transgenic fly was generated by BestGene using *attP40* as the injection stock. Five transformants (M1-M5) were generated and their overexpression all gave rise to tumor growth phenotype. Transformant M4 was used in this study.

Table 8-5. Primers used for subcloning

XbaI restriction sites are labeled in blue, DNA bases flanking the restriction sites in grey.

Mutation site(s)	Primer sequence (5' → 3')
XbaI_HA forward	TAAGCA TCTAGA ATGTACCCATACGATGTTCCAG
XbaI_Hipk reverse	TGCTTA TCTAGA CTACTCAGCCCCATACCATATG

8.4. Materials and methods for Chapter 5

8.4.1. Drosophila culture

Flies were raised on standard cornmeal-molasses food. Stocks were kept at 25°C and crosses at 29°C unless otherwise indicated. Three Gal4 fly lines, **(1)** *dpp-Gal4/TM6B*, **(2)** *hh-Gal4/TM6B* and **(3)** *act5c-Gal4/TM6B* (BL #3954) were used to induce transgene expression. To generate heat-shock inducible actin flip-out clones, **(4)** *yw hsFlp[122];; act>CD2>Gal4 UAS-RFP/TM6B* was used. A 10-15 min heat shock (37°C) was applied to larvae grown for two to three days after egg laying (25°C). After heat shock, the larvae were grown at 29°C and dissected when they reached third instar larval stage. To mark the transgene-expressing cells, **(5)** *UAS-GFP* (BL 5431) and **(6)** *UAS-RFP* (BL 7118) were used.

To generate the Hipk tumor model, **(7)** *UAS-HA-hipk-3M* (abbreviated as *UAS-hipk*) ([Swarup and Verheyen, 2011](#)) and **(8)** *dpp-Gal4, UAS-hipk/TM6B* were used. RNAi fly strains used include **(9)** *UAS-dMyc-RNAi* (BL 25783), **(10)** *UAS-dMyc-RNAi #2* (BL 25784), **(11)** *UAS-glut1-RNAi* (BL 40904), **(12)** *UAS-hex-A-RNAi* (BL 35155), **(13)** *UAS-hex-C-RNAi* (BL 57404), **(14)** *UAS-pfk2-RNAi* (BL 35380), **(15)** *UAS-pfk-RNAi* (BL 34336), **(16)** *UAS-Ldh-RNAi* (BL 33640), **(17)** *UAS-pgi-RNAi* (BL 51804), **(18)** *UAS-pgk-RNAi* (BL 33632) and **(19)** *UAS-pyk-RNAi* (BL 35218).

To perturb signaling pathway activities, the following strains were used: **(20)** *UAS-yki-S168A-GFP* (BL 28836), **(21)** *UAS-Arm-S10* ([Mirkovic et al., 2011](#)), **(22)** *UAS-Ci-5M*, **(23)** *UAS-N-act*. Other strains used include **(24)** *myc-lacZ/FM7c* (BL 12247) and **(25)** *UAS-dMyc* (BL 9674). **(26)** *UAS-FLII12Pglu-700μδ6* (Glucose sensor) is a generous gift from Dr. Stefanie Schirmeier ([Volkenhoff et al., 2018](#)). **(27)** *Ldh-GFP* is a generous gift from Dr. Ingrid Lohmann. Strains with BL stock number were obtained from Bloomington *Drosophila* Stock Center (Bloomington, IN, USA).

8.4.2. Immunofluorescence staining

Larval imaginal discs were dissected in PBS and fixed in 4% paraformaldehyde (PFA) for 15 min at room temperature. Samples were washed with PBS with 0.1% Triton X-100 (PBST). After blocking with 5% BSA in PBST for 1 hr at room temperature,

samples were incubated with primary antibodies overnight at 4°C. The following primary antibodies were used: **(1)** mouse anti-β-Galactosidase (1:50, DSHB 40-1a), **(2)** rabbit anti-dMyc (d1-717) (1:500, Santa Cruz Biotechnology, Inc sc-28207), **(3)** rabbit anti-Hipk (1:200; ([Blaquiere et al., 2018](#))), **(4)** mouse anti-Armadillo (1:50, diluted form, DSHB N2 7A1), **(5)** rabbit anti-Cyclin E (d-300) (1:100, Santa Cruz Biotechnology, Inc sc-33748). After washing with PBST, samples were incubated with Cy3- and/or Alexa Fluor 647-conjugated secondary antibodies (1:500, Jackson ImmunoResearch Laboratories, Inc), DAPI (4',6-Diamidino-2-Phenylindole, Dihydrochloride) (final concentration: 0.2 µg per mL, Invitrogen D1306) and/or Rhodamine phalloidin (1:500, Molecular Probes R415) for 2 hr at room temperature. Samples were mounted in 70% Glycerol/PBS after wash. Images were taken on a Nikon Air laser-scanning confocal microscope and processed by Image J.

8.4.3. Quantitative real time-PCR (qRT-PCR)

Imaginal discs from third instar larva were dissected in PBS and temporarily stored in RNAlater Stabilization solution (Invitrogen AM7020). Total RNA was extracted using RNeasy Mini Kits (Qiagen 74101). First strand cDNA was synthesized using OneScript Plus cDNA Synthesis Kit (Abm G236). qRT-PCR were performed using SensiFast SYBR Hi-ROS Kit (Bioline 92005) on StepOne Real-time PCR System (Applied Biosystems). Primers used are listed in [Table 8-6](#).

Table 8-6. Primer sequences for profiling the mRNA expression of glycolytic genes

Drosophila genes	Forward sequence (5' → 3')	Reverse sequence (5' → 3')
<i>rp49</i>	ATCGGTTACGGATCGAACAA	GACAATCTCCTTGCCTTCT
<i>βTub56D</i>	AGTGCTCGATGTTGT	GGAAATCAGCAGGGT
<i>hipk</i>	GCACCACAACTGCAACTACG	ACGTGATGATGGTGCAGACTC
<i>glut1</i>	TTACCGCGGAGCTCTTCTCC	GCCATCCAGTTGACCAGCAC
<i>hex-A</i>	CTGCTTCTAACGGACGAACAG	GCCTTGGGATGTGTATCCTTGG
<i>hex-C</i>	CAGGCCAACGTCAAGTGTGTTT	GTGGTGACCTTCAGCGAGA
<i>pgi</i>	CATCAAGGACCTGTTCGTGA	AGTCCAGCAGTATCTGCCAT
<i>pfk</i>	CGAGCCTGTGTCGTATGG	AGTTGGCTCCTGGATGCAG
<i>pfk2</i>	AGAGCGAGTACAACCTGAGC	TAGCGCATTGGCATACTGGT
<i>ald</i>	TTCAGCACTGACCCCAAGC	CCTTGATGCCAGAATGATTCC
<i>tpi</i>	AAGGACTGGAAGAACGTGGT	CCTCTTGAGCCTGATCGGG
<i>gapdh1</i>	TAAATTGACTCGACTCACGGT	CTCCACACATACTCGGCTC
<i>gapdh2</i>	GATGCTCCCATGTTCGTTGC	GTCCCATCACGCCACAACTTG
<i>pgk</i>	ATCACCAAGCAACCAGAGAATTG	TGCCAGGGTGTACTTGATGTT
<i>pglym78</i>	AGTCCGAGTGGAACCGAGAAGA	CCTCCTCCTGACCCTTTCG

<i>eno</i>	AGGCCATGAAGATGGGCTC	GCCTCCTTGTGGACTGGATG
<i>pyk</i>	GCAGGAGCTGATAACCCAATG	CGTGCATCCGTGAGAGAA
<i>Ldh</i>	CGAGGTGATCAAGCTAAAGG	CGAGAGGAACACATCCTTGT
<i>dMyc</i>	AAGCTATGCATCCAGCTGACC	CACTATCCACTAACCGAGCGC
<i>sima</i>	CCAATCTGCCGCCAAC	AGGCCAGGTGGTGGGAC

8.4.4. 2-NBDG uptake

Imaginal discs from third instar larva were dissected in PBS, followed by incubation with 2-NBDG (Invitrogen N13195) at 0.3 mM for 15 min in the dark at room temperature. After rinsing with PBS, samples were fixed and processed according to standard immunofluorescence staining protocol.

8.4.5. Intracellular glucose FRET analysis

The glucose sensor *UAS-FLII₁₂Pglu-700μδ6* was generated by Dr. Schirmeier's group ([Volkenhoff et al., 2018](#)). Imaginal discs expressing the sensor with or without overexpression of *hipk* were mounted and imaged on the same day. The same confocal settings as previously described ([Volkenhoff et al., 2018](#)) were used to record the CFP and FRET images. FRET efficiency (FRET/CFP) was calculated as quotient of FRET and CFP using Image J. Since we were not determining the actual values of intracellular glucose concentrations, we did not take into account a correction for spectral bleed through and thus uncorrected FRET/CFP ratios were used to compare glucose levels in discs of different genotypes. The values of FRET efficiency were displayed using the Fire Lookup Table (LUT) in figures and shown in boxplots.

8.4.6. Pyruvate measurement

Whole-body larvae were homogenized in PBS, followed by centrifugation at 14,000 g for 10 min. The supernatants were used for the pyruvate assay. The pyruvate assay was performed using EnzyChrom Pyruvate Assay Kit (BioAssay Systems EPYR-100) according to the manufacturer's instructions. Absorbance at 570 nm was measured in a SpectraMax M5 fluorescent microplate reader (Molecular Devices). Relative pyruvate levels were determined after normalizing with the protein levels. Protein quantification was performed using the Bio-Rad protein assay (Bio-Rad 500–0006) and absorbance at 595 nm was measured. Experiments were conducted with two biological replicates. Each assay was performed with two technical replicates.

8.4.7. Statistics

For data analyses, unpaired two-tailed Student *t*-tests were used to determine *p*-values using Microsoft Excel. Bar graphs were generated by Microsoft Excel. Boxplots were generated using BoxPlotR with data points included ([Spitzer et al., 2014](#)). We used the Spear definition to show the maximum and minimum values by the upper and lower whiskers, respectively. The third quartile, median and the first quartile are shown in the box accordingly to a standard boxplot.

8.5. Materials and methods for Chapter 6

8.5.1. Drosophila culture

Flies were raised on standard cornmeal-molasses food. Crosses were kept at 29°C unless otherwise indicated. Two Gal4 fly lines, (1) *dpp-Gal4*, (2) *mef2-Gal4* III were used to induce transgene expression. (3) *UAS-HA-hipk-3M* (abbreviated as *UAS-hipk*) ([Swarup and Verheyen, 2011](#)) and (4) *dpp-Gal4*, *UAS-hipk* ([Blaquiere et al., 2018](#)) were used to generate the Hipk tumor model. (5) *UAS-GFP* (BL 5431) was used to mark the transgene-expressing cells. To visualize the mitochondrial morphology, (6) *UAS-mito-HA-GFP* (abbreviated as *UAS-mitoGFP*; BL 8442) was used. RNAi fly strains used include (7) *UAS-marf-RNAi* (BL 55189), (8) *UAS-opa1-RNAi* (BL 32358), (9) *USA-ND-pdsw-RNAi* (BL 29592), (10) *UAS-ND-75-RNAi* (BL 27739), (11) *UAS-ND-49-RNAi* (BL 28573), (12) *UAS-ND-42-RNAi* (BL 28894), (13) *USA-ATPsynβ-RNAi* (BL 28056), (14) *UAS-JNK-DN* (also known as *UAS-bsk-DN*, BL 6409), (15) *UAS-dMyc-RNAi* (BL 25783), (16) *UAS-pfk2-RNAi* (BL 35380). Strains with BL stock number were obtained from Bloomington *Drosophila* Stock Center (Bloomington, IN, USA).

8.5.2. Immunofluorescence staining

Larval imaginal discs were dissected in PBS and fixed in 4% paraformaldehyde (PFA) for 15 min at room temperature. Samples were washed with PBS with 0.1% Triton X-100 (PBST). After blocking with 5% BSA in PBST for 1 hr at room temperature, samples were incubated with primary antibodies overnight at 4°C. The following primary antibodies were used: (1) rabbit anti-pJNK (pTPpY) (1:100, Promega V7931), (2) mouse anti-Mmp1 (1:100: 3A6B4, 3B8D12, 5H7B11 DSHB; Rubin, G.M.). After washing with PBST, samples were incubated with Cy3- and/or Alexa Fluor 647- conjugated secondary antibodies (1:500, Jackson ImmunoResearch Laboratories, Inc), DAPI (4',6-Diamidino-2-Phenylindole, Dihydrochloride) (final concentration: 0.2 µg per mL, Invitrogen D1306) for 2 hr at room temperature. Samples were mounted in 70% Glycerol/PBS after wash. Images were taken on a Nikon Air laser-scanning confocal microscope or a Zeiss LSM880 with Airyscan confocal microscope and processed by Image J.

8.5.3. Quantification of mitochondrial morphology

The quantification was done by an ImageJ macro tool known as Mitochondrial Network Analysis (MiNA). In a confocal image of salivary gland cells (~168 x 168 μm^2 , 3200 x 3200 pixels $_2$), 5 random areas (cells) (~29 x 29 μm^2 , 550 x 550 pixels $_2$ for each area) were selected and subject to the MiNA analyses using the following settings: **(1)** CLAHE: block size = 127, Histogram Bins = 5, Maximum Slope = 5; **(2)** Median Filter: Radius = 2; **(3)** Unsharp Mask: Radius = 2, Mask Strength = 0.60; **(4)** Tophat was not applied for processing. Mitochondrial morphology was quantified using the following four parameters: number of individuals (structure with no junctions), numbers of networks (structure with at least one junction), mean length of network branches (mean branch length), and mean number of branches per network (mean network size). Data collected from a total of 15 cells per genotype were pooled together for analyses and generating boxplots.

8.5.4. MitoTracker Red staining

Tissues of interest from third instar larvae were dissected in PBS, followed by incubation with MitoTracker Red CMXRos (Life Technologies, M7512) at 200 nM for 45 minutes in the dark at room temperature. After rinse with PBS, tissue samples were fixed and processed according to standard immunofluorescence staining protocol.

8.5.5. TMRM staining

Larval salivary glands were dissected in PBS, followed by incubation with tetramethylrhodamine methyl ester (TMRM) perchlorate (Cayman 21437) at 100 nM for 30 minutes in the dark at room temperature. After rinse with PBS briefly, samples were subjected to live cell imaging right away on a Nikon Air laser-scanning confocal microscope.

8.5.6. ROS assay

We followed the previously described protocol for *in vivo* detection of ROS ([Owusu-Ansah et al., 2008](#)). Briefly, larval wing discs were dissected in PBS and incubated with 30 μM DHE (Cayman 12013) for 7 mins in the dark at room temperature.

After rinse with PBS briefly, samples were fixed in 8% PFA and washed with PBS, each for 5 minutes before mounting. Images were taken within two days.

8.5.7. Statistics

For data analyses, unpaired two-tailed Student t-tests were used to determine p-values using Microsoft Excel. Boxplots were generated using BoxPlotR with data points included ([Spitzer et al., 2014](#)). We used the Spear definition to show the maximum and minimum values by the upper and lower whiskers, respectively. The third quartile, median and the first quartile are shown in the box accordingly to a standard boxplot.

References

- Agnew, C., Liu, L., Liu, S., Xu, W., You, L., Yeung, W., Kannan, N., Jablons, D., Jura, N., 2019. The crystal structure of the protein kinase HIPK2 reveals a unique architecture of its CMGC-insert region. *J. Biol. Chem.*
- Aikawa, Y., Nguyen, L.A., Isono, K., Takakura, N., Tagata, Y., Schmitz, M.L., Koseki, H., Kitabayashi, I., 2006. Roles of HIPK1 and HIPK2 in AML1- and p300-dependent transcription, hematopoiesis and blood vessel formation. *EMBO J.*
- AJCC Cancer Staging Manual, 2017. , AJCC Cancer Staging Manual.
- Al-Beiti, M.A.M., Lu, X., 2008. Expression of HIPK2 in cervical cancer: correlation with clinicopathology and prognosis. *Aust. N. Z. J. Obstet. Gynaecol.* 48, 329–336.
- Anand, P., Kunnumakara, A.B., Sundaram, C., Harikumar, K.B., Tharakan, S.T., Lai, O.S., Sung, B., Aggarwal, B.B., 2008. Cancer is a preventable disease that requires major lifestyle changes. *Pharm. Res.*
- Aoki, K., Taketo, M.M., 2007. Adenomatous polyposis coli (APC): A multi-functional tumor suppressor gene. *J. Cell Sci.*
- Aranda, S., Laguna, A., Luna, S. de la, 2011. DYRK family of protein kinases: evolutionary relationships, biochemical properties, and functional roles. *FASEB J.*
- Aretz, S., Uhlhaas, S., Sun, Y., Pagenstecher, C., Mangold, E., Caspary, R., Mösllein, G., Schulmann, K., Propping, P., Friedl, W., 2004. Familial adenomatous polyposis: Aberrant splicing due to missense or silent mutations in the APC gene. *Hum. Mutat.*
- Atkins, M., Potier, D., Romanelli, L., Jacobs, J., Mach, J., Hamaratoglu, F., Aerts, S., Halder, G., 2016. An Ectopic Network of Transcription Factors Regulated by Hippo Signaling Drives Growth and Invasion of a Malignant Tumor Model. *Curr. Biol.*
- Averous, J., Fonseca, B.D., Proud, C.G., 2008. Regulation of cyclin D1 expression by mTORC1 signaling requires eukaryotic initiation factor 4E-binding protein 1. *Oncogene.*
- Ban, L., Pettit, N., Li, L., Stuparu, A.D., Cai, L., Chen, W., Guan, W., Han, W., Wang, P.G., Mrksich, M., 2012. Discovery of glycosyltransferases using carbohydrate arrays and mass spectrometry. *Nat. Chem. Biol.*
- Bardella, C., Pollard, P.J., Tomlinson, I., 2011. SDH mutations in cancer. *Biochim. Biophys. Acta - Bioenerg.*
- Basler, K., Struhl, G., 1994. Compartment boundaries and the control of Drosophila limb pattern by hedgehog protein. *Nature.*
- Beaucher, M., Hersperger, E., Page-McCaw, A., Shearn, A., 2007. Metastatic ability of Drosophila tumors depends on MMP activity. *Dev. Biol.*

- Ben-Haim, S., Ell, P., 2008. 18F-FDG PET and PET/CT in the Evaluation of Cancer Treatment Response. *J. Nucl. Med.* 50, 88–99.
- Bensaad, K., Tsuruta, A., Selak, M.A., Vidal, M.N.C., Nakano, K., Bartrons, R., Gottlieb, E., Vousden, K.H., 2006. TIGAR, a p53-Inducible Regulator of Glycolysis and Apoptosis. *Cell*.
- Bilder, D., Li, M., Perrimon, N., 2000. Cooperative regulation of cell polarity and growth by Drosophila tumor suppressors. *Science* (80-.).
- Birben, E., Sahiner, U.M., Sackesen, C., Erzurum, S., Kalayci, O., 2012. Oxidative stress and antioxidant defense. *World Allergy Organ. J.*
- Bitomsky, N., Conrad, E., Moritz, C., Polonio-Vallon, T., Sombroek, D., Schultheiss, K., Glas, C., Greiner, V., Herbel, C., Mantovani, F., Del Sal, G., Peri, F., Hofmann, T.G., 2013. Autophosphorylation and Pin1 binding coordinate DNA damage-induced HIPK2 activation and cell death. *Proc. Natl. Acad. Sci. U. S. A.*
- Bittner, C.X., Loaiza, A., Ruminot, I., Larenas, V., Sotelo-Hitschfeld, T., Gutiérrez, R., Córdova, A., Valdebenito, R., Frommer, W.B., Barros, L.F., 2010. High resolution measurement of the glycolytic rate. *Front. Neuroenergetics* 2.
- Blaquiere, J.A., Verheyen, E.M., 2017. Homeodomain-Interacting Protein Kinases: Diverse and Complex Roles in Development and Disease. *Curr. Top. Dev. Biol.* 123, 73–103.
- Blaquiere, J.A., Wong, K.K.L., Kinsey, S.D., Wu, J., Verheyen, E.M., 2018. Homeodomain-interacting protein kinase promotes tumorigenesis and metastatic cell behavior. *Dis. Model. Mech.* 11, dmm031146.
- Bond, M.R., Hanover, J.A., 2015. A little sugar goes a long way: the cell biology of O-GlcNAc. *J. Cell Biol.* 208, 869–80.
- Boxer, L.M., Dang, C. V., 2001. Translocations involving c-myc and c-myc function. *Oncogene*.
- Boyce, M., Carrico, I.S., Ganguli, A.S., Yu, S.-H., Hangauer, M.J., Hubbard, S.C., Kohler, J.J., Bertozzi, C.R., 2011. Metabolic cross-talk allows labeling of O-linked beta-N-acetylglucosamine-modified proteins via the N-acetylgalactosamine salvage pathway. *Proc. Natl. Acad. Sci. U. S. A.* 108, 3141–6.
- Brand, A.H., Perrimon, N., 1993. Targeted gene expression as a means of altering cell fates and generating dominant phenotypes. *Development* 118, 401–15.
- Brenner, D.R., Weir, H.K., Demers, A.A., Ellison, L.F., Louzado, C., Shaw, A., Turner, D., Woods, R.R., Smith, L.M., 2020. Projected estimates of cancer in Canada in 2020. *CMAJ*.
- Britton, J.S., Lockwood, W.K., Li, L., Cohen, S.M., Edgar, B.A., 2002. Drosophila's insulin/PI3-kinase pathway coordinates cellular metabolism with nutritional conditions. *Dev. Cell*.

- Brown, M.S., Goldstein, J.L., 1997. The SREBP pathway: Regulation of cholesterol metabolism by proteolysis of a membrane-bound transcription factor. *Cell*.
- Brumby, A.M., Richardson, H.E., 2005. Using *Drosophila melanogaster* to map human cancer pathways. *Nat. Rev. Cancer*.
- Bunker, B.D., Nellimoottil, T.T., Boileau, R.M., Classen, A.K., Bilder, D., 2015. The transcriptional response to tumorigenic polarity loss in *Drosophila*. *Elife* 4.
- Cai, Q., Lin, T., Kamarajugadda, S., Lu, J., 2013. Regulation of glycolysis and the Warburg effect by estrogen-related receptors. *Oncogene*.
- Cai, W., Ye, Q., She, Q.B., 2014. Loss of 4E-BP1 function induces EMT and promotes cancer cell migration and invasion via cap-dependent translational activation of snail. *Oncotarget*.
- Calzado, M.A., de la Vega, L., Möller, A., Bowtell, D.D.L., Schmitz, M.L., 2009. An inducible autoregulatory loop between HIPK2 and Siah2 at the apex of the hypoxic response. *Nat. Cell Biol.* 11, 85–91.
- Campanella, M., Parker, N., Tan, C.H., Hall, A.M., Duchen, M.R., 2009. IF1: setting the pace of the F1Fo-ATP synthase. *Trends Biochem. Sci.*
- Campbell, K., Rossi, F., Adams, J., Pitsidianaki, I., Barriga, F.M., Garcia-Gerique, L., Batlle, E., Casanova, J., Casali, A., 2019. Collective cell migration and metastases induced by an epithelial-to-mesenchymal transition in *Drosophila* intestinal tumors. *Nat. Commun.*
- Canadian Cancer Statistics Advisory Committee, 2019. Canadian Cancer Statistics 2019, Canadian Cancer Statistics 2019.
- Cao, L., Yang, G., Gao, S., Jing, C., Montgomery, R.R., Yin, Y., Wang, P., Fikrig, E., You, F., 2019. HIPK2 is necessary for type I interferon-mediated antiviral immunity. *Sci. Signal.* 12, eaau4604.
- Chaffer, C.L., Weinberg, R.A., 2011. A perspective on cancer cell metastasis. *Science* (80-).).
- Chauvin, C., Koka, V., Nouschi, A., Mieulet, V., Hoareau-Aveilla, C., Dreazen, A., Cagnard, N., Carpenter, W., Kiss, T., Meyuhas, O., Pende, M., 2014. Ribosomal protein S6 kinase activity controls the ribosome biogenesis transcriptional program. *Oncogene*.
- Chen, J., Verheyen, E.M., 2012. Homeodomain-Interacting Protein Kinase Regulates Yorkie Activity to Promote Tissue Growth. *Curr. Biol.* 22, 1582–1586.
- Cheng, Y., Al-Beiti, M.A.M., Wang, J., Wei, G., Li, J., Liang, S., Lu, X., 2012. Correlation between homeodomain-interacting protein kinase 2 and apoptosis in cervical cancer. *Mol. Med. Rep.* 5, 1251–5.
- Choi, C.Y., Kim, Y.H., Kim, Y.O., Park, S.J., Kim, E.A., Riemenschneider, W., Gajewski,

- K., Schulz, R.A., Kim, Y., 2005. Phosphorylation by the DHIPK2 protein kinase modulates the corepressor activity of Groucho. *J. Biol. Chem.*
- Choi, D.W., Na, W., Kabir, M.H., Yi, E., Kwon, S., Yeom, J., Ahn, J.W., Choi, H.H., Lee, Y., Seo, K.W., Shin, M.K., Park, S.H., Yoo, H.Y., Isono, K. ichi, Koseki, H., Kim, S.T., Lee, C., Kwon, Y.K., Choi, C.Y., 2013. WIP1, a Homeostatic Regulator of the DNA Damage Response, Is Targeted by HIPK2 for Phosphorylation and Degradation. *Mol. Cell.*
- Choi, S., Kim, W., Chung, J., 2011. Drosophila salt-inducible kinase (SIK) regulates starvation resistance through cAMP-response element-binding protein (CREB)-regulated transcription coactivator (CRTS). *J. Biol. Chem.*
- Chou, T.Y., Dang, C. V., Hart, G.W., 1995a. Glycosylation of the c-Myc transactivation domain. *Proc. Natl. Acad. Sci.* 92, 4417–4421.
- Chou, T.Y., Hart, G.W., Dang, C. V., 1995b. c-Myc is glycosylated at threonine 58, a known phosphorylation site and a mutational hot spot in lymphomas. *J. Biol. Chem.*
- Classen, A.K., Bunker, B.D., Harvey, K.F., Vaccari, T., Bilder, D., 2009. A tumor suppressor activity of Drosophila Polycomb genes mediated by JAK-STAT signaling. *Nat. Genet.*
- Clemens, R.A., Jones, J.M., Kern, M., Lee, S.Y., Mayhew, E.J., Slavin, J.L., Zivanovic, S., 2016. Functionality of Sugars in Foods and Health. *Compr. Rev. Food Sci. Food Saf.*
- Cohen, S., 1993. Imaginal disc deveopment. In: *The Development of Drosophila Melanogaster*.
- Cordero, J.B., Macagno, J.P., Stefanatos, R.K., Strathdee, K.E., Cagan, R.L., Vidal, M., 2010. Oncogenic ras diverts a host TNF tumor suppressor activity into tumor promoter. *Dev. Cell.*
- Csibi, A., Lee, G., Yoon, S.O., Tong, H., Ilter, D., Elia, I., Fendt, S.M., Roberts, T.M., Blenis, J., 2014. The mTORC1/S6K1 pathway regulates glutamine metabolism through the eif4b-dependent control of c-Myc translation. *Curr. Biol.*
- D’Orazi, G., Cecchinelli, B., Bruno, T., Manni, I., Higashimoto, Y., Saito, S., Gostissa, M., Coen, S., Marchetti, A., Del Sal, G., Piaggio, G., Fanciulli, M., Appella, E., Soddu, S., 2002. Homeodomain-interacting protein kinase-2 phosphorylates p53 at Ser 46 and mediates apoptosis. *Nat. Cell Biol.* 4, 11–19.
- D’Orazi, G., Sciulli, M.G., Di Stefano, V., Riccioni, S., Frattini, M., Falcioni, R., Bertario, L., Sacchi, A., Patrignani, P., 2006. Homeodomain-interacting protein kinase-2 restrains cytosolic phospholipase A2-dependent prostaglandin E2 generation in human colorectal cancer cells. *Clin Cancer Res* 12, 735–741.
- Dang, C. V., 2012. MYC on the path to cancer. *Cell.*
- Dasgupta, S., Rajapakshe, K., Zhu, B., Nikolai, B.C., Yi, P., Putluri, N., Choi, J.M., Jung,

S.Y., Coarfa, C., Westbrook, T.F., Zhang, X.H.-F., Foulds, C.E., Tsai, S.Y., Tsai, M.-J., O’Malley, B.W., 2018. Metabolic enzyme PFKFB4 activates transcriptional coactivator SRC-3 to drive breast cancer. *Nature* 556, 249–254.

Davies, H., Bignell, G.R., Cox, C., Stephens, P., Edkins, S., Clegg, S., Teague, J., Woffendin, H., Garnett, M.J., Bottomley, W., Davis, N., Dicks, E., Ewing, R., Floyd, Y., Gray, K., Hall, S., Hawes, R., Hughes, J., Kosmidou, V., Menzies, A., Mould, C., Parker, A., Stevens, C., Watt, S., Hooper, S., Jayatilake, H., Gusterson, B.A., Cooper, C., Shipley, J., Hargrave, D., Pritchard-Jones, K., Maitland, N., Chenevix-Trench, G., Riggins, G.J., Bigner, D.D., Palmieri, G., Cossu, A., Flanagan, A., Nicholson, A., Ho, J.W.C., Leung, S.Y., Yuen, S.T., Weber, B.L., Seigler, H.F., Darrow, T.L., Paterson, H., Wooster, R., Stratton, M.R., Futreal, P.A., 2002. Mutations of the BRAF gene in human cancer. *Nature*.

de la Cova, C., Senoo-Matsuda, N., Ziosi, M., Wu, D.C., Bellosta, P., Quinzii, C.M., Johnston, L.A., 2014. Supercompetitor Status of Drosophila Myc Cells Requires p53 as a Fitness Sensor to Reprogram Metabolism and Promote Viability. *Cell Metab.* 19, 470–483.

de la Vega, L., Grishina, I., Moreno, R., Krüger, M., Braun, T., Schmitz, M.L., 2012. A Redox-Regulated SUMO/Acetylation Switch of HIPK2 Controls the Survival Threshold to Oxidative Stress. *Mol. Cell* 46, 472–483.

De Berardinis, R.J., Chandel, N.S., 2016. Fundamentals of cancer metabolism. *Sci. Adv.*

Deshmukh, H., Yeh, T.H., Yu, J., Sharma, M.K., Perry, A., Leonard, J.R., Watson, M.A., Gutmann, D.H., Nagarajan, R., 2008. High-resolution, dual-platform aCGH analysis reveals frequent HIPK2 amplification and increased expression in pilocytic astrocytomas. *Oncogene* 27, 4745–51.

Deshmukh, H., Yeh, T.H., Yu, J., Sharma, M.K., Perry, A., Leonard, J.R., Watson, M.A., Gutmann, D.H., Nagarajan, R., 2008. High-resolution, dual-platform aCGH analysis reveals frequent HIPK2 amplification and increased expression in pilocytic astrocytomas. *Oncogene*.

Dillekås, H., Rogers, M.S., Straume, O., 2019. Are 90% of deaths from cancer caused by metastases? *Cancer Med.*

Djiane, A., Krejci, A., Bernard, F., Fexova, S., Millen, K., Bray, S.J., 2013. Dissecting the mechanisms of Notch induced hyperplasia. *EMBO J.* 32, 60–71.

Dodd, K.M., Yang, J., Shen, M.H., Sampson, J.R., Tee, A.R., 2015. mTORC1 drives HIF-1 α and VEGF-A signalling via multiple mechanisms involving 4E-BP1, S6K1 and STAT3. *Oncogene*.

Doggett, K., Turkel, N., Willoughby, L.F., Ellul, J., Murray, M.J., Richardson, H.E., Brumby, A.M., 2015. BTB-zinc finger oncogenes are required for ras and notch-driven tumorigenesis in drosophila. *PLoS One*.

Dong, W.C., Seo, Y.M., Kim, E.A., Ki, S.S., Jang, W.A., Park, S.J., Lee, S.R., Cheol, Y.C., 2008. Ubiquitination and degradation of homeodomain-interacting protein

- kinase 2 by WD40 repeat/SOCS box protein WSB-1. *J. Biol. Chem.*
- Dongre, A., Weinberg, R.A., 2019. New insights into the mechanisms of epithelial–mesenchymal transition and implications for cancer. *Nat. Rev. Mol. Cell Biol.*
- Ducommun, S., Deak, M., Sumpton, D., Ford, R.J., Núñez Galindo, A., Kussmann, M., Viollet, B., Steinberg, G.R., Foretz, M., Dayon, L., Morrice, N.A., Sakamoto, K., 2015. Motif affinity and mass spectrometry proteomic approach for the discovery of cellular AMPK targets: Identification of mitochondrial fission factor as a new AMPK substrate. *Cell. Signal.*
- Duman-Scheel, M., Johnston, L.A., Du, W., 2004. Repression of dMyc expression by Wingless promotes Rbf-induced G1 arrest in the presumptive *Drosophila* wing margin. *Proc. Natl. Acad. Sci.* 101, 3857–3862.
- Eichenlaub, T., Villadsen, R., Freitas, F.C.P., Andrejeva, D., Aldana, B.I., Nguyen, H.T., Petersen, O.W., Gorodkin, J., Herranz, H., Cohen, S.M., 2018. Warburg Effect Metabolism Drives Neoplasia in a *Drosophila* Genetic Model of Epithelial Cancer. *Curr. Biol.* 28, 3220-3228.e6.
- Enzo, E., Santinon, G., Pocaterra, A., Aragona, M., Bresolin, S., Forcato, M., Grifoni, D., Pession, A., Zanconato, F., Guzzo, G., Bicciato, S., Dupont, S., 2015. Aerobic glycolysis tunes YAP/TAZ transcriptional activity. *EMBO J.* 34, 1349–1370.
- Estrella, V., Chen, T., Lloyd, M., Wojtkowiak, J., Cornnell, H.H., Ibrahim-Hashim, A., Bailey, K., Balagurunathan, Y., Rothberg, J.M., Sloane, B.F., Johnson, J., Gatenby, R.A., Gillies, R.J., 2013. Acidity generated by the tumor microenvironment drives local invasion. *Cancer Res.*
- Faubert, B., Boily, G., Izreig, S., Griss, T., Samborska, B., Dong, Z., Dupuy, F., Chambers, C., Fuerth, B.J., Viollet, B., Mamer, O.A., Avizonis, D., Deberardinis, R.J., Siegel, P.M., Jones, R.G., 2013. AMPK is a negative regulator of the warburg effect and suppresses tumor growth in vivo. *Cell Metab.*
- Faubert, B., Solmonson, A., DeBerardinis, R.J., 2020. Metabolic reprogramming and cancer progression. *Science* (80-.).
- Fehr, M., Lalonde, S., Lager, I., Wolff, M.W., Frommer, W.B., 2003. ***In Vivo Imaging of the Dynamics of Glucose Uptake in the Cytosol of COS-7 Cells by Fluorescent Nanosensors***. *J. Biol. Chem.* 278, 19127–19133.
- Ferlay, J., Colombet, M., Soerjomataram, I., Mathers, C., Parkin, D.M., Piñeros, M., Znaor, A., Bray, F., 2019. Estimating the global cancer incidence and mortality in 2018: GLOBOCAN sources and methods. *Int. J. Cancer.*
- Fernie, A.R., Carrari, F., Sweetlove, L.J., 2004. Respiratory metabolism: Glycolysis, the TCA cycle and mitochondrial electron transport. *Curr. Opin. Plant Biol.*
- Ferrer, C.M., Sodi, V.L., Reginato, M.J., 2016. O-GlcNAcylation in Cancer Biology: Linking Metabolism and Signaling. *J. Mol. Biol.* 428, 3282–3294.

- Ferres-Marco, D., Gutierrez-Garcia, I., Vallejo, D.M., Bolivar, J., Gutierrez-Aviño, F.J., Dominguez, M., 2006. Epigenetic silencers and Notch collaborate to promote malignant tumours by Rb silencing. *Nature*.
- Fiedorczuk, K., Letts, J.A., Degliesposti, G., Kaszuba, K., Skehel, M., Sazanov, L.A., 2016. Atomic structure of the entire mammalian mitochondrial complex i. *Nature*.
- Figueroa-Clarevega, A., Bilder, D., 2015. Malignant drosophila tumors interrupt insulin signaling to induce cachexia-like wasting. *Dev. Cell*.
- Fischer, M., 2017. Census and evaluation of p53 target genes. *Oncogene*.
- Flavahan, W.A., Gaskell, E., Bernstein, B.E., 2017. Epigenetic plasticity and the hallmarks of cancer. *Science* (80-).
- Friederich, M.W., Erdogan, A.J., Coughlin, C.R., Elos, M.T., Jiang, H., O'Rourke, C.P., Lovell, M.A., Wartchow, E., Gowan, K., Chatfield, K.C., Chick, W.S., Spector, E.B., Van Hove, J.L.K., Riemer, J., 2017. Mutations in the accessory subunit NDUFB10 result in isolated complex I deficiency and illustrate the critical role of intermembrane space import for complex I holoenzyme assembly. *Hum. Mol. Genet.*
- Gallant, P., 2013. Myc function in Drosophila. *Cold Spring Harb. Perspect. Med.* 3, a014324.
- Gambetta, M.C., Oktaba, K., Müller, J., 2009. Essential Role of the Glycosyltransferase Sxc/Ogt in Polycomb Repression. *Science* (80-). 325, 93–96.
- Ganapathy-Kanniappan, S., Geschwind, J.-F.H., 2013. Tumor glycolysis as a target for cancer therapy: progress and prospects. *Mol. Cancer* 12, 152.
- Gao, X., Pan, D., 2001. TSC1 and TSC2 tumor suppressors antagonize insulin signaling in cell growth. *Genes Dev.*
- Garber, J.E., Offit, K., 2005. Hereditary cancer predisposition syndromes. *J. Clin. Oncol.*
- Garcia, C.J., Khajeh, J., Coulanges, E., Chen, E.I. j., Owusu-Ansah, E., 2017. Regulation of Mitochondrial Complex I Biogenesis in Drosophila Flight Muscles. *Cell Rep.*
- Garcia, D., Shaw, R.J., 2017. AMPK: Mechanisms of Cellular Energy Sensing and Restoration of Metabolic Balance. *Mol. Cell*.
- Gatenby, R.A., Gawlinski, E.T., Gmitro, A.F., Kaylor, B., Gillies, R.J., 2006. Acid-mediated tumor invasion: A multidisciplinary study. *Cancer Res.*
- Gerber, S., Krasky, A., Rohwer, A., Lindauer, S., Closs, E., Rognan, D., Gunkel, N., Selzer, P.M., Wolf, C., 2006. Identification and characterisation of the dopamine receptor II from the cat flea *Ctenocephalides felis* (CfDopRII). *Insect Biochem. Mol. Biol.* 36, 749–758.

- Giacinti, C., Giordano, A., 2006. RB and cell cycle progression. *Oncogene*.
- Giovannucci, E., Harlan, D.M., Archer, M.C., Bergenstal, R.M., Gapstur, S.M., Habel, L.A., Pollak, M., Regensteiner, J.G., Yee, D., 2010. Diabetes and cancer: A consensus report. In: *Diabetes Care*.
- Goberdhan, D.C.I., Wilson, C., Harris, A.L., 2016. Amino Acid Sensing by mTORC1: Intracellular Transporters Mark the Spot. *Cell Metab.*
- Golic, K.G., Lindquist, S., 1989. The FLP recombinase of yeast catalyzes site-specific recombination in the drosophila genome. *Cell*.
- González, A., Hall, M.N., 2017. Nutrient sensing and TOR signaling in yeast and mammals . *EMBO J.*
- Gonzalez, C., 2013. Drosophila melanogaster: a model and a tool to investigate malignancy and identify new therapeutics. *Nat. Rev. Cancer* 13, 172–183.
- Gossage, L., Eisen, T., Maher, E.R., 2015. VHL, the story of a tumour suppressor gene. *Nat. Rev. Cancer*.
- Gottlieb, E., Tomlinson, I.P.M., 2005. Mitochondrial tumour suppressors: A genetic and biochemical update. *Nat. Rev. Cancer*.
- Granchi, C., Minutolo, F., 2012. Anticancer agents that counteract tumor glycolysis. *ChemMedChem* 7, 1318–50.
- Gresko, E., Möller, A., Roscic, A., Schmitz, M.L., 2005. Covalent modification of human homeodomain interacting protein kinase 2 by SUMO-1 at lysine 25 affects its stability. *Biochem. Biophys. Res. Commun.*
- Gresko, E., Roscic, A., Ritterhoff, S., Vichalkovski, A., Del Sal, G., Schmitz, M.L., 2006. Autoregulatory control of the p53 response by caspase-mediated processing of HIPK2. *EMBO J.*
- Gress, D.M., Edge, S.B., Greene, F.L., Washington, M.K., Asare, E.A., Brierley, J.D., Byrd, D.R., Compton, C.C., Jessup, J.M., Winchester, D.P., Amin, M.B., Gershenwald, J.E., 2017. Principles of Cancer Staging. In: *AJCC Cancer Staging Manual*.
- Guerrero-Castillo, S., Baertling, F., Kownatzki, D., Wessels, H.J., Arnold, S., Brandt, U., Nijtmans, L., 2017. The Assembly Pathway of Mitochondrial Respiratory Chain Complex I. *Cell Metab.*
- Guha, A., Lin, L., Kornberg, T.B., 2009. Regulation of Drosophila matrix metalloprotease Mmp2 is essential for wing imaginal disc:trachea association and air sac tubulogenesis. *Dev. Biol.*
- Gunage, R.D., Reichert, H., VijayRaghavan, K., 2014. Identification of a new stem cell population that generates Drosophila flight muscles. *Elife*.

- Haeusler, R.A., McGraw, T.E., Accili, D., 2018. Metabolic Signalling: Biochemical and cellular properties of insulin receptor signalling. *Nat. Rev. Mol. Cell Biol.*
- Hailemariam, K., Iwasaki, K., Huang, B.W., Sakamoto, K., Tsuji, Y., 2010. Transcriptional regulation of ferritin and antioxidant genes by HIPK2 under genotoxic stress. *J. Cell Sci.*
- Hanahan, D., Weinberg, R.A., 2000. The hallmarks of cancer. *Cell.*
- Hanahan, D., Weinberg, R.A.A., 2011. Hallmarks of cancer: The next generation. *Cell.*
- Hanover, J.A., Krause, M.W., Love, D.C., 2010. The hexosamine signaling pathway: O-GlcNAc cycling in feast or famine. *Biochim. Biophys. Acta - Gen. Subj.*
- Hardie, D.G., Ross, F.A., Hawley, S.A., 2012. AMPK: A nutrient and energy sensor that maintains energy homeostasis. *Nat. Rev. Mol. Cell Biol.*
- Hardivillé, S., Hart, G.W., 2014. Nutrient regulation of signaling, transcription, and cell physiology by O-GlcNAcylation. *Cell Metab.*
- Hart, G.W., 2014. Three decades of research on O-GlcNAcylation - A major nutrient sensor that regulates signaling, transcription and cellular metabolism. *Front. Endocrinol. (Lausanne).*
- Hart, G.W., 2019. Nutrient regulation of signaling and transcription. *J. Biol. Chem.*
- Hart, G.W., Slawson, C., Ramirez-Correa, G., Lagerlof, O., 2011. Cross Talk Between O-GlcNAcylation and Phosphorylation: Roles in Signaling, Transcription, and Chronic Disease. *Annu. Rev. Biochem.*
- Hattangadi, S.M., Burke, K.A., Lodish, H.F., 2010. Homeodomain-interacting protein kinase 2 plays an important role in normal terminal erythroid differentiation. *Blood* 115, 4853–4861.
- Havula, E., Teesalu, M., Hyötyläinen, T., Seppälä, H., Hasygar, K., Auvinen, P., Orešič, M., Sandmann, T., Hietakangas, V., 2013. Mondo/ChREBP-Mlx-Regulated Transcriptional Network Is Essential for Dietary Sugar Tolerance in Drosophila. *PLoS Genet.* 9, e1003438.
- Hawley, S.A., Ross, F.A., Gowans, G.J., Tibarewal, P., Leslie, N.R., Hardie, D.G., 2014. Phosphorylation by Akt within the ST loop of AMPK- α 1 down-regulates its activation in tumour cells. *Biochem. J.*
- He, P., Yu, Z., Sun, C., Jiao, S., Jiang, H., 2017. Knockdown of HIPK2 attenuates the pro-fibrogenic response of hepatic stellate cells induced by TGF- β 1. *Biomed. Pharmacother.* 85, 575–581.
- Heldin, C.H., 2013. Targeting the PDGF signaling pathway in tumor treatment. *Cell Commun. Signal.*
- Herranz, H., Cohen, S.M., 2017. Drosophila as a Model to Study the Link between

Metabolism and Cancer. J. Dev. Biol. 5.

- Herranz, H., Eichenlaub, T., Cohen, S.M., 2016. Cancer in Drosophila. In: Current Topics in Developmental Biology. pp. 181–199.
- Herranz, H., Pérez, L., Martín, F.A., Milán, M., 2008. A Wingless and Notch double-repression mechanism regulates G1-S transition in the Drosophila wing. EMBO J. 27, 1633–45.
- Herranz, H., Weng, R., Cohen, S.M., 2014. Crosstalk between epithelial and mesenchymal tissues in tumorigenesis and imaginal disc development. Curr. Biol.
- Hikasa, H., Ezan, J., Itoh, K., Li, X., Klymkowsky, M.W., Sokol, S.Y., 2010. Regulation of TCF3 by Wnt-dependent phosphorylation during vertebrate axis specification. Dev. Cell.
- Hikasa, H., Sokol, S.Y., 2011. Phosphorylation of TCF proteins by homeodomain-interacting protein kinase 2. J. Biol. Chem.
- Hirabayashi, S., Baranski, T.J., Cagan, R.L., 2013. Transformed Drosophila Cells Evade Diet-Mediated Insulin Resistance through Wingless Signaling. Cell 154, 664–675.
- Hirabayashi, S., Cagan, R.L., 2015. Salt-inducible kinases mediate nutrient-sensing to link dietary sugar and tumorigenesis in Drosophila. Elife 4, e08501.
- Hobbs, G.A., Der, C.J., Rossman, K.L., 2016. RAS isoforms and mutations in cancer at a glance. J. Cell Sci.
- Hofmann, T.G., Glas, C., Bitomsky, N., 2013. HIPK2: A tumour suppressor that controls DNA damage-induced cell fate and cytokinesis. BioEssays.
- Hofmann, T.G., Möller, A., Sirma, H., Zentgraf, H., Taya, Y., Dröge, W., Will, H., Schmitz, M.L., 2002. Regulation of p53 activity by its interaction with homeodomain-interacting protein kinase-2. Nat. Cell Biol. 4, 1–10.
- Hofmann, T.G., Stollberg, N., Schmitz, M.L., Will, H., 2003. HIPK2 Regulates Transforming Growth Factor-β-Induced c-Jun NH 2-Terminal Kinase Activation and Apoptosis in Human Hepatoma Cells. Cancer Res.
- Horike, N., Takemori, H., Katoh, Y., Doi, J., Min, L., Asano, T., Sun, X.J., Yamamoto, H., Kasayama, S., Muraoka, M., Nonaka, Y., Okamoto, M., 2003. Adipose-specific expression, phosphorylation of Ser794 in insulin receptor substrate-1, and activation in diabetic animals of salt-inducible kinase-2. J. Biol. Chem.
- Hsu, P.P., Sabatini, D.M., 2008. Cancer Cell Metabolism: Warburg and Beyond. Cell 134, 703–707.
- Hu, C.-M., Tien, S.-C., Hsieh, P.-K., Jeng, Y.-M., Chang, M.-C., Chang, Y.-T., Chen, Yi-Ju, Chen, Yu-Ju, Lee, E.Y.-H.P., Lee, W.-H., 2019. High Glucose Triggers Nucleotide Imbalance through O-GlcNAcylation of Key Enzymes and Induces KRAS Mutation in Pancreatic Cells. Cell Metab. 29, 1334–1349.e10.

- Huang, H., Du, G., Chen, H., Liang, X., Li, C., Zhu, N., Xue, L., Ma, J., Jiao, R., 2011. Drosophila Smt3 negatively regulates JNK signaling through sequestering Hipk in the nucleus. *Development* 138, 2477–2485.
- Huang, M., Weiss, W.A., 2013. Neuroblastoma and MYCN. *Cold Spring Harb. Perspect. Med.*
- Huang, Y., Tong, J., He, F., Yu, X., Fan, L., Hu, J., Tan, J., Chen, Z., 2015. MiR-141 regulates TGF- β 1-induced epithelial-mesenchymal transition through repression of HIPK2 expression in renal tubular epithelial cells. *Int. J. Mol. Med.*
- Ingber, D.E., 2008. Can cancer be reversed by engineering the tumor microenvironment? *Semin. Cancer Biol.*
- Inoki, K., Li, Y., Xu, T., Guan, K.L., 2003. Rheb GTPase is a direct target of TSC2 GAP activity and regulates mTOR signaling. *Genes Dev.*
- Inoki, K., Li, Y., Zhu, T., Wu, J., Guan, K.L., 2002. TSC2 is phosphorylated and inhibited by Akt and suppresses mTOR signalling. *Nat. Cell Biol.*
- Irby, R.B., Yeatman, T.J., 2000. Role of Src expression and activation in human cancer. *Oncogene.*
- Isaacs, J.S., Yun, J.J., Mole, D.R., Lee, S., Torres-Cabala, C., Chung, Y.L., Merino, M., Trepel, J., Zbar, B., Toro, J., Ratcliffe, P.J., Linehan, W.M., Neckers, L., 2005. HIF overexpression correlates with biallelic loss of fumarate hydratase in renal cancer: Novel role of fumarate in regulation of HIF stability. *Cancer Cell.*
- Isono, K., Nemoto, K., Li, Y., Takada, Y., Suzuki, R., Katsuki, M., Nakagawara, A., Koseki, H., 2006. Overlapping Roles for Homeodomain-Interacting Protein Kinases Hipk1 and Hipk2 in the Mediation of Cell Growth in Response to Morphogenetic and Genotoxic Signals. *Mol. Cell. Biol.* 26, 2758–2771.
- Isono, Kyoichi, Nemoto, K., Li, Y., Takada, Y., Suzuki, R., Katsuki, M., Nakagawara, A., Koseki, H., 2006. Overlapping roles for homeodomain-interacting protein kinases hipk1 and hipk2 in the mediation of cell growth in response to morphogenetic and genotoxic signals. *Mol. Cell. Biol.* 26, 2758–71.
- Jacob, K., Albrecht, S., Sollier, C., Faury, D., Sader, E., Montpetit, A., Serre, D., Hauser, P., Garami, M., Bognar, L., Hanzely, Z., Montes, J.L., Atkinson, J., Farmer, J.-P., Bouffet, E., Hawkins, C., Tabori, U., Jabado, N., 2009. Duplication of 7q34 is specific to juvenile pilocytic astrocytomas and a hallmark of cerebellar and optic pathway tumours. *Br. J. Cancer* 101, 722–733.
- Ježek, J., Cooper, K., Strich, R., 2018. Reactive Oxygen Species and Mitochondrial Dynamics: The Yin and Yang of Mitochondrial Dysfunction and Cancer Progression. *Antioxidants* 7, 13.
- Ji, T., Zhang, L., Deng, M., Huang, S., Wang, Y., Pham, T.T., Smith, A.A., Sridhar, V., Cabernard, C., Wang, J., Yan, Y., 2019. Dynamic MAPK signaling activity underlies a transition from growth arrest to proliferation in Drosophila scribble mutant tumors.

DMM Dis. Model. Mech.

- Jin, Y., Ratnam, K., Chuang, P.Y., Fan, Y., Zhong, Y., Dai, Y., Mazloom, A.R., Chen, E.Y., D'Agati, V., Xiong, H., Ross, M.J., Chen, N., Ma'ayan, A., He, J.C., 2012. A systems approach identifies HIPK2 as a key regulator of kidney fibrosis. *Nat. Med.* 18, 580–8.
- Jonckheere, A.I., Smeitink, J.A.M., Rodenburg, R.J.T., 2012. Mitochondrial ATP synthase: architecture, function and pathology. *J. Inherit. Metab. Dis.* 35, 211–25.
- Kamigaito, T., Okaneya, T., Kawakubo, M., Shimojo, H., Nishizawa, O., Nakayama, J., 2014. Overexpression of O-GlcNAc by prostate cancer cells is significantly associated with poor prognosis of patients. *Prostate Cancer Prostatic Dis.* 17, 18–22.
- Kang, X., Kong, F., Wu, X., Ren, Y., Wu, S., Wu, K., Jiang, Z., Zhang, W., 2015. High glucose promotes tumor invasion and increases metastasis-associated protein expression in human lung epithelial cells by upregulating heme oxygenase-1 via reactive oxygen species or the TGF- β 1 /PI3K/akt signaling pathway. *Cell. Physiol. Biochem.*
- Karim, F.D., Rubin, G.M., 1998. Ectopic expression of activated Ras1 induces hyperplastic growth and increased cell death in *Drosophila* imaginal tissues. *Development.*
- Katheder, N.S., Khezri, R., O'Farrell, F., Schultz, S.W., Jain, A., Schink, M.K.O., Theodossiou, T.A., Johansen, T., Juhász, G., Bilder, D., Brech, A., Stenmark, H., Rusten, T.E., O'Farrell, F., Schultz, S.W., Jain, A., Rahman, M.M., Schink, K.O., Theodossiou, T.A., Johansen, T., Juhász, G., Bilder, D., Brech, A., Stenmark, H., Rusten, T.E., 2017. Microenvironmental autophagy promotes tumour growth. *Nature* 541, 417–420.
- Kazemi, Z., Chang, H., Haserodt, S., McKen, C., Zachara, N.E., 2010. O-linked beta-N-acetylglucosamine (O-GlcNAc) regulates stress-induced heat shock protein expression in a GSK-3 β -dependent manner. *J. Biol. Chem.* 285, 39096–39107.
- Keibler, M.A., Wasylewko, T.M., Kelleher, J.K., Iliopoulos, O., Vander Heiden, M.G., Stephanopoulos, G., 2016. Metabolic requirements for cancer cell proliferation. *Cancer Metab.*
- Kerr, K.M., 2001. Pulmonary preinvasive neoplasia. *J. Clin. Pathol.*
- Khidekel, N., Arndt, S., Lamarre-Vincent, N., Lippert, A., Poulin-Kerstien, K.G., Ramakrishnan, B., Qasba, P.K., Hsieh-Wilson, L.C., 2003. A Chemoenzymatic Approach toward the Rapid and Sensitive Detection of O-GlcNAc Posttranslational Modifications. *J. Am. Chem. Soc.* 125, 16162–16163.
- Kim, E.A., Kim, J.E., Sung, K.S., Choi, D.W., Lee, B.J., Choi, C.Y., 2010. Homeodomain-interacting protein kinase 2 (HIPK2) targets β -catenin for phosphorylation and proteasomal degradation. *Biochem. Biophys. Res. Commun.*

- Kim, E.A., Yoon, T.N., Ryu, M.J., Kim, H.T., Lee, S.E., Kim, C.H., Lee, C., Young, H.K., Cheol, Y.C., 2006. Phosphorylation and transactivation of Pax6 by homeodomain-interacting protein kinase 2. *J. Biol. Chem.*
- Kim, J.-w., Zeller, K.I., Wang, Y., Jegga, A.G., Aronow, B.J., O'Donnell, K.A., Dang, C.V., 2004. Evaluation of Myc E-Box Phylogenetic Footprints in Glycolytic Genes by Chromatin Immunoprecipitation Assays. *Mol. Cell. Biol.* 24, 5923–5936.
- Kim, J.W., Dang, C.V., 2006. Cancer's molecular sweet tooth and the warburg effect. *Cancer Res.*
- Kim, Y.H.Y.H., Choi, C.Y., Lee, S.J., Conti, M.A., Kim, Y.H.Y.H., 1998. Homeodomain-interacting protein kinases, a novel family of co-repressors for homeodomain transcription factors. *J. Biol. Chem.* 273, 25875–9.
- King, A., Selak, M.A., Gottlieb, E., 2006. Succinate dehydrogenase and fumarate hydratase: Linking mitochondrial dysfunction and cancer. *Oncogene*.
- Kondo, S., Lu, Y., Debbas, M., Lin, A.W., Sarosi, I., Itie, A., Wakeham, A., Tuan, J., Saris, C., Elliott, G., Ma, W., Benchimol, S., Lowe, S.W., Mak, T.W., Thukral, S.K., 2003. Characterization of cells and gene-targeted mice deficient for the p53-binding kinase homeodomain-interacting protein kinase 1 (HIPK1). *Proc. Natl. Acad. Sci. U. S. A.* 100, 5431–6.
- Koppenol, W.H., Bounds, P.L., Dang, C.V., 2011. Otto Warburg's contributions to current concepts of cancer metabolism. *Nat. Rev. Cancer* 11, 325–337.
- Kovács, K.A., Steinmann, M., Halfon, O., Magistretti, P.J., Cardinaux, J.R., 2015. Complex regulation of CREB-binding protein by homeodomain-interacting protein kinase 2. *Cell. Signal.*
- Kreppel, L.K., Hart, G.W., 1999. Regulation of a cytosolic and nuclear O-GlcNAc transferase. Role of the tetratricopeptide repeats. *J. Biol. Chem.* 274, 32015–22.
- Kushnareva, Y., Murphy, A.N., Andreyev, A., 2002. Complex I-mediated reactive oxygen species generation: Modulation by cytochrome c and NAD(P)+ oxidation-reduction state. *Biochem. J.*
- Kwon, M.J., Kang, S.Y., Nam, E.S., Cho, S.J., Rho, Y.S., 2017. HIPK2 Overexpression and Its Prognostic Role in Human Papillomavirus-Positive Tonsillar Squamous Cell Carcinoma. *Biomed Res. Int.*
- Lamouille, S., Xu, J., Derynck, R., 2014. Molecular mechanisms of epithelial-mesenchymal transition. *Nat. Rev. Mol. Cell Biol.*
- Lan, H.-C., Li, H.-J., Lin, G., Lai, P.-Y., Chung, B., 2007. Cyclic AMP Stimulates SF-1-Dependent CYP11A1 Expression through Homeodomain-Interacting Protein Kinase 3-Mediated Jun N-Terminal Kinase and c-Jun Phosphorylation. *Mol. Cell. Biol.*
- Lan, H.C., Wu, C.F., Shih, H.M., Chung, B.C., 2012. Death-associated protein 6 (Daxx) mediates cAMP-dependent stimulation of Cyp11a1 (P450scc) transcription. *J. Biol.*

Chem.

- Lavra, L., Rinaldo, C., Olivieri, A., Luciani, E., Fidanza, P., Giacomelli, L., Bellotti, C., Ricci, A., Trovato, M., Soddu, S., Bartolazzi, A., Sciacchitano, S., 2011. The loss of the p53 activator HIPK2 is responsible for galectin-3 overexpression in well differentiated thyroid carcinomas. *PLoS One* 6, e20665.
- Lee, Andrews, B.C., Faust, M., Walldorf, U., Verheyen, E.M., 2009a. Hipk is an essential protein that promotes Notch signal transduction in the Drosophila eye by inhibition of the global co-repressor Groucho. *Dev. Biol.* 325, 263–272.
- Lee, K.S., Wu, Z., Song, Y., Mitra, S.S., Feroze, A.H., Cheshier, S.H., Lu, B., 2013. Roles of PINK1, mTORC2, and mitochondria in preserving brain tumor-forming stem cells in a noncanonical Notch signaling pathway. *Genes Dev.*
- Lee, Swarup, S., Chen, J., Ishitani, T., Verheyen, E.M., 2009b. Homeodomain-interacting protein kinases (Hipks) promote Wnt/Wg signaling through stabilization of β -catenin/Arm and stimulation of target gene expression. *Development* 136, 241–51.
- Lee, T., Luo, L., 1999. Mosaic analysis with a repressible neurotechnique cell marker for studies of gene function in neuronal morphogenesis. *Neuron*.
- Levine, Z.G., Walker, S., 2016. The Biochemistry of O -GlcNAc Transferase: Which Functions Make It Essential in Mammalian Cells? . *Annu. Rev. Biochem.*
- Li, F., Wang, Y., Zeller, K.I., Potter, J.J., Wonsey, D.R., O'Donnell, K.A., Kim, J. -w., Yuste, J.T., Lee, L.A., Dang, C. V., 2005. Myc Stimulates Nuclearly Encoded Mitochondrial Genes and Mitochondrial Biogenesis. *Mol. Cell. Biol.*
- Li, H., Hurlburt, A.J., Tennessen, J.M., 2018. A Drosophila model of combined D-2- and L-2-hydroxyglutaric aciduria reveals a mechanism linking mitochondrial citrate export with oncometabolite accumulation. *Dis. Model. Mech.* 11.
- Li, Z., Hu, S., Wang, J., Cai, J., Xiao, L., Yu, L., Wang, Z., 2010. MiR-27a modulates MDR1/P-glycoprotein expression by targeting HIPK2 in human ovarian cancer cells. *Gynecol. Oncol.*
- Liberti, M. V, Locasale, J.W., 2016. The Warburg Effect: How Does it Benefit Cancer Cells? *Trends Biochem. Sci.* 41, 211–218.
- Liu, K., Paterson, A.J., Chin, E., Kudlow, J.E., 2000. Glucose stimulates protein modification by O-linked GlcNAc in pancreatic beta cells: linkage of O-linked GlcNAc to beta cell death. *Proc. Natl. Acad. Sci. U. S. A.* 97, 2820–5.
- Liu, T.-W., Myschyshyn, M., Sinclair, D.A., Cecioni, S., Beja, K., Honda, B.M., Morin, R.D., Vocadlo, D.J., 2017. Genome-wide chemical mapping of O-GlcNAcylated proteins in *Drosophila melanogaster*. *Nat. Chem. Biol.* 13, 161–167.
- Loeb, K.R., Loeb, L.A., 2000. Significance of multiple mutations in cancer. *Carcinogenesis*.

- Logue, J.S., Morrison, D.K., 2012. Complexity in the signaling network: Insights from the use of targeted inhibitors in cancer therapy. *Genes Dev.*
- Louie, S.H., Yang, X.Y., Conrad, W.H., Muster, J., Angers, S., Moon, R.T., Cheyette, B.N.R., 2009. Modulation of the β -catenin signaling pathway by the dishevelled-associated protein hipk1. *PLoS One.*
- Love, D.C., Hanover, J.A., 2005. The Hexosamine Signaling Pathway: Deciphering the "O-GlcNAc Code" *Sci. Signal.* 2005, re13–re13.
- Lu, C., Thompson, C.B., 2012. Metabolic regulation of epigenetics. *Cell Metab.* 16, 9–17.
- Lu, J., Tan, M., Cai, Q., 2015. The Warburg effect in tumor progression: mitochondrial oxidative metabolism as an anti-metastasis mechanism. *Cancer Lett.* 356, 156–64.
- Lu, W., Pelicano, H., Huang, P., 2010. Cancer metabolism: Is glutamine sweeter than glucose? *Cancer Cell.*
- Lunt, S.Y., Vander Heiden, M.G., 2011. Aerobic Glycolysis: Meeting the Metabolic Requirements of Cell Proliferation. *Annu. Rev. Cell Dev. Biol.*
- Luo, J., Solimini, N.L., Elledge, S.J., 2009. Principles of Cancer Therapy: Oncogene and Non-oncogene Addiction. *Cell.*
- Ma, H., Zhang, J., Zhou, L., Wen, S., Tang, H.Y., Jiang, B., Zhang, F., Suleman, M., Sun, D., Chen, A., Zhao, W., Lin, F., Tsau, M.T., Shih, L.M., Xie, C., Li, X., Lin, D., Hung, L.M., Cheng, M.L., Li, Q., 2020. c-Src Promotes Tumorigenesis and Tumor Progression by Activating PFKFB3. *Cell Rep.*
- Ma, J., Hart, G.W., 2014. O-GlcNAc profiling: from proteins to proteomes. *Clin. Proteomics* 11, 8.
- Ma, Z., Vosseller, K., 2014. Cancer metabolism and elevated O-GlcNAc in oncogenic signaling. *J. Biol. Chem.* 289, 34457–65.
- MacKenzie, E.D., Selak, M.A., Tennant, D.A., Payne, L.J., Crosby, S., Frederiksen, C.M., Watson, D.G., Gottlieb, E., 2007. Cell-Permeating α -Ketoglutarate Derivatives Alleviate Pseudohypoxia in Succinate Dehydrogenase-Deficient Cells. *Mol. Cell. Biol.*
- Mamane, Y., Petroulakis, E., Rong, L., Yoshida, K., Ler, L.W., Sonenberg, N., 2004. eIF4E - From translation to transformation. *Oncogene*.
- Manning, B.D., Toker, A., 2017. AKT/PKB Signaling: Navigating the Network. *Cell.*
- Mao, J.-H., Wu, D., Kim, I.-J., Kang, H.C., Wei, G., Climent, J., Kumar, A., Pelorosso, F.G., DelRosario, R., Huang, E.J., Balmain, A., 2012. Hipk2 cooperates with p53 to suppress γ -ray radiation-induced mouse thymic lymphoma. *Oncogene* 31, 1176–1180.
- Marín-Hernández, A., Gallardo-Pérez, J.C., Ralph, S.J., Rodríguez-Enríquez, S.,

- Moreno-Sánchez, R., 2009. HIF-1alpha modulates energy metabolism in cancer cells by inducing over-expression of specific glycolytic isoforms. *Mini Rev. Med. Chem.* 9, 1084–101.
- Marshall, S., 2006. Role of Insulin, Adipocyte Hormones, and Nutrient-Sensing Pathways in Regulating Fuel Metabolism and Energy Homeostasis: A Nutritional Perspective of Diabetes, Obesity, and Cancer. *Sci. STKE* 2006, re7–re7.
- Marshall, S., Bacote, V., Traxinger, R.R., 1991. Discovery of a metabolic pathway mediating glucose-induced desensitization of the glucose transport system: role of hexosamine in the induction of insulin resistance. *J. Biol. Chem.*
- Martin, T.D., Cook, D.R., Choi, M.Y., Li, M.Z., Haigis, K.M., Elledge, S.J., 2017. A Role for Mitochondrial Translation in Promotion of Viability in K-Ras Mutant Cells. *Cell Rep.*
- Martinez-Fleites, C., Macauley, M.S., He, Y., Shen, D.L., Vocadlo, D.J., Davies, G.J., 2008. Structure of an O-GlcNAc transferase homolog provides insight into intracellular glycosylation. *Nat. Struct. Mol. Biol.* 15, 764–765.
- Martinez, A.M., Schuettengruber, B., Sakr, S., Janic, A., Gonzalez, C., Cavalli, G., 2009. Polyhomeotic has a tumor suppressor activity mediated by repression of Notch signaling. *Nat. Genet.*
- Mayne, S.T., Playdon, M.C., Rock, C.L., 2016. Diet, nutrition, and cancer: Past, present and future. *Nat. Rev. Clin. Oncol.*
- McClure, K.D., Schubiger, G., 2005. Development analysis and squamous morphogenesis of the peripodial epithelium in *Drosophila* imaginal discs. *Development.*
- McGuire, S., 2016. World Cancer Report 2014. Geneva, Switzerland: World Health Organization, International Agency for Research on Cancer, WHO Press, 2015. *Adv. Nutr.*
- Menut, L., Vaccari, T., Dionne, H., Hill, J., Wu, G., Bilder, D., 2007. A mosaic genetic screen for *Drosophila* neoplastic tumor suppressor genes based on defective pupation. *Genetics* 177, 1667–77.
- Miller, D., Hannon, C., Ganetzky, B., 2012. A mutation in *Drosophila* Aldolase causes temperature-sensitive paralysis, shortened lifespan, and neurodegeneration. *J. Neurogenet.* 26, 317–27.
- Miller, D.M., Thomas, S.D., Islam, A., Muench, D., Sedoris, K., 2012. c-Myc and cancer metabolism. *Clin. Cancer Res.* 18, 5546–53.
- Mirkovic, I., Gault, W.J., Rahnama, M., Jenny, A., Gaengel, K., Bessette, D., Gottardi, C.J., Verheyen, E.M., Mlodzik, M., 2011. Nemo kinase phosphorylates β-catenin to promote ommatidial rotation and connects core PCP factors to E-cadherin-β-catenin. *Nat. Struct. Mol. Biol.* 18, 665–72.

- Mirzoyan, Z., Sollazzo, M., Allocca, M., Valenza, A.M., Grifoni, D., Bellosta, P., 2019. *Drosophila melanogaster*: A model organism to study cancer. *Front. Genet.*
- Momcilovic, M., Jones, A., Bailey, S.T., Waldmann, C.M., Li, R., Lee, J.T., Abdelhady, G., Gomez, A., Holloway, T., Schmid, E., Stout, D., Fishbein, M.C., Stiles, L., Dabir, D. V., Dubinett, S.M., Christofk, H., Shirihi, O., Koehler, C.M., Sadeghi, S., Shackelford, D.B., 2019. In vivo imaging of mitochondrial membrane potential in non-small-cell lung cancer. *Nature*.
- Musselman, L.P., Fink, J.L., Narzinski, K., Ramachandran, P.V., Hathiramani, S.S., Cagan, R.L., Baranski, T.J., 2011. A high-sugar diet produces obesity and insulin resistance in wild-type *Drosophila*. *DMM Dis. Model. Mech.* 4, 842–9.
- Nagaraj, R., Gururaja-Rao, S., Jones, K.T., Slattery, M., Negre, N., Braas, D., Christofk, H., White, K.P., Mann, R., Banerjee, U., 2012. Control of mitochondrial structure and function by the Yorkie/YAP oncogenic pathway. *Genes Dev.*
- Neto-Silva, R.M., de Beco, S., Johnston, L.A., 2010. Evidence for a growth-stabilizing regulatory feedback mechanism between Myc and Yorkie, the drosophila homolog of Yap. *Dev. Cell.*
- Niccoli, T., Cabecinha, M., Tillmann, A., Kerr, F., Wong, C.T., Cardenes, D., Vincent, A.J., Bettledi, L., Li, L., Grönke, S., Dols, J., Partridge, L., 2016. Increased Glucose Transport into Neurons Rescues A β Toxicity in *Drosophila*. *Curr. Biol.* 26, 2291–2300.
- Nunes, R.D., Romeiro, N.C., De Carvalho, H.T., Moreira, J.R., Sola-Penna, M., Silva-Neto, M.A.C., Braz, G.R.C., 2016. Unique PFK regulatory property from some mosquito vectors of disease, and from *Drosophila melanogaster*. *Parasit. Vectors* 9, 107.
- O'Neil, R.G., Wu, L., Mullani, N., 2005. Uptake of a Fluorescent Deoxyglucose Analog (2-NBDG) in Tumor Cells. *Mol. Imaging Biol.* 7, 388–392.
- Obici, S., Rossetti, L., 2003. Minireview: Nutrient Sensing and the Regulation of Insulin Action and Energy Balance. *Endocrinology*.
- Oh, H.J., Kato, M., Deshpande, S., Zhang, E., Das, S., Lanting, L., Wang, M., Natarajan, R., 2016. Inhibition of the processing of miR-25 by HIPK2-Phosphorylated-MeCP2 induces NOX4 in early diabetic nephropathy. *Sci. Rep.* 6, 38789.
- Ohsawa, S., Sato, Y., Enomoto, M., Nakamura, M., Betsumiya, A., Igaki, T., 2012. Mitochondrial defect drives non-autonomous tumour progression through Hippo signalling in *Drosophila*. *Nature*.
- Okamoto, M., Takemori, H., Katoh, Y., 2004. Salt-inducible kinase in steroidogenesis and adipogenesis. *Trends Endocrinol. Metab.*
- Olivier-Van Stichelen, S., Dehennaut, V., Buzy, A., Zachayus, J.L., Guinez, C., Mir, A.M., El Yazidi-Belkoura, I., Copin, M.C., Boureme, D., Loyaux, D., Ferrara, P., Lefebvre, T., 2014. O-GlcNAcylation stabilizes β -catenin through direct competition with

phosphorylation at threonine 41. *FASEB J.*

- Olson, A.K., Bouchard, B., Zhu, W.Z., Chatham, J.C., Rosiers, C. Des, 2020. First characterization of glucose flux through the hexosamine biosynthesis pathway (HBP) in ex vivo mouse heart. *J. Biol. Chem.*
- Onodera, Y., Nam, J.-M., Bissell, M.J., 2014. Increased sugar uptake promotes oncogenesis via EPAC/RAP1 and O-GlcNAc pathways. *J. Clin. Invest.* 124, 367–84.
- Orian, A., Van Steensel, B., Delrow, J., Bussemaker, H.J., Li, L., Sawado, T., Williams, E., Loo, L.W.M., Cowley, S.M., Yost, C., Pierce, S., Edgar, B.A., Parkhurst, S.M., Eisenman, R.N., 2003. Genomic binding by the Drosophila Myc, Max, Mad/Mnt transcription factor network. *Genes Dev.*
- Owusu-Ansah, E., Banerjee, U., 2009. Reactive oxygen species prime Drosophila haematopoietic progenitors for differentiation. *Nature*.
- Owusu-Ansah, E., Yavari, A., Banerjee, U., 2008. A protocol for in vivo detection of reactive oxygen species. *Protoc. Exch.*
- Pacheco-Pinedo, E.C., Durham, A.C., Stewart, K.M., Goss, A.M., Lu, M.M., DeMayo, F.J., Morrisey, E.E., 2011. Wnt/β-catenin signaling accelerates mouse lung tumorigenesis by imposing an embryonic distal progenitor phenotype on lung epithelium. *J. Clin. Invest.*
- Page-McCaw, A., Ewald, A.J., Werb, Z., 2007. Matrix metalloproteinases and the regulation of tissue remodelling. *Nat. Rev. Mol. Cell Biol.*
- Page-McCaw, A., Serano, J., Santé, J.M., Rubin, G.M., 2003. Drosophila matrix metalloproteinases are required for tissue remodeling, but not embryonic development. *Dev. Cell.*
- Pagliarini, R.A., Xu, T., 2003. A Genetic Screen in Drosophila for Metastatic Behavior. *Science* (80-).
- Pallavi, S.K., Ho, D.M., Hicks, C., Miele, L., Artavanis-Tsakonas, S., 2012. Notch and Mef2 synergize to promote proliferation and metastasis through JNK signal activation in Drosophila. *EMBO J.*
- Palm, W., Thompson, C.B., 2017. Nutrient acquisition strategies of mammalian cells. *Nature*.
- Park, S.Y., Kim, H.S., Kim, N.H., Ji, S., Cha, S.Y., Kang, J.G., Ota, I., Shimada, K., Konishi, N., Nam, H.W., Hong, S.W., Yang, W.H., Roth, J., Yook, J.I., Cho, J.W., 2010. Snail1 is stabilized by O-GlcNAc modification in hyperglycaemic condition. *EMBO J.*
- Pastor-Pareja, J.C., Ming, W., Tian, X., 2008. An innate immune response of blood cells to tumors and tissue damage in Drosophila. *DMM Dis. Model. Mech.*

- Pastushenko, I., Blanpain, C., 2019. EMT Transition States during Tumor Progression and Metastasis. *Trends Cell Biol.*
- Patra, K.C., Hay, N., 2014. The pentose phosphate pathway and cancer. *Trends Biochem. Sci.*
- Pavlova, N.N., Thompson, C.B., 2016. The Emerging Hallmarks of Cancer Metabolism. *Cell Metab.*
- Payne, S.R., Kemp, C.J., 2005. Tumor suppressor genetics. *Carcinogenesis.*
- Pelicano, H., Martin, D.S., Xu, R.-H., Huang, P., 2006. Glycolysis inhibition for anticancer treatment. *Oncogene* 25, 4633–4646.
- Peng, C., Zhu, Y., Zhang, W., Liao, Q., Chen, Y., Zhao, X., Guo, Q., Shen, P., Zhen, B., Qian, X., Yang, D., Zhang, J.-S., Xiao, D., Qin, W., Pei, H., 2017. Regulation of the Hippo-YAP Pathway by Glucose Sensor O-GlcNAcylation. *Mol. Cell* 68, 591-604.e5.
- Perry, S.W., Norman, J.P., Barbieri, J., Brown, E.B., Gelbard, H.A., 2011. Mitochondrial membrane potential probes and the proton gradient: a practical usage guide. *Biotechniques* 50, 98–115.
- Pfeiffer, T., Schuster, S., Bonhoeffer, S., 2001. Cooperation and competition in the evolution of ATP-producing pathways. *Science* (80-.).
- Phoomak, C., Vaeteewoottacharn, K., Silsirivanit, A., Saengboonmee, C., Seubwai, W., Sawanyawisuth, K., Wongkham, C., Wongkham, S., 2017. High glucose levels boost the aggressiveness of highly metastatic cholangiocarcinoma cells via O-GlcNAcylation. *Sci. Rep.*
- Pierantoni, G.M., Bulfone, A., Pentimalli, F., Fedele, M., Iuliano, R., Santoro, M., Chiariotti, L., Ballabio, A., Fusco, A., 2002. The Homeodomain-Interacting Protein Kinase 2 Gene Is Expressed Late in Embryogenesis and Preferentially in Retina, Muscle, and Neural Tissues. *Biochem. Biophys. Res. Commun.* 290, 942–947.
- Pilling, A.D., Horiuchi, D., Lively, C.M., Saxton, W.M., 2006. Kinesin-1 and Dynein Are the Primary Motors for Fast Transport of Mitochondria in *Drosophila* Motor Axons. *Mol. Biol. Cell* 17, 2057–2068.
- Poon, C.L.C., Zhang, X., Lin, J.I., Manning, S.A., Harvey, K.F., 2012. Homeodomain-Interacting Protein Kinase Regulates Hippo Pathway-Dependent Tissue Growth. *Curr. Biol.* 22, 1587–1594.
- Potter, C.J., Turencchalk, G.S., Xu, T., 2000. Drosophila in cancer researchan expanding role. *Trends Genet.*
- Prior, I.A., Lewis, P.D., Mattos, C., 2012. A comprehensive survey of ras mutations in cancer. *Cancer Res.*
- Puram, S. V., Tirosh, I., Parikh, A.S., Patel, A.P., Yizhak, K., Gillespie, S., Rodman, C.,

- Luo, C.L., Mroz, E.A., Emerick, K.S., Deschler, D.G., Varvares, M.A., Mylvaganam, R., Rozenblatt-Rosen, O., Rocco, J.W., Faquin, W.C., Lin, D.T., Regev, A., Bernstein, B.E., 2017. Single-Cell Transcriptomic Analysis of Primary and Metastatic Tumor Ecosystems in Head and Neck Cancer. *Cell*.
- Quinones-Coello, A.T., Petrella, L.N., Ayers, K., Melillo, A., Mazzalupo, S., Hudson, A.M., Wang, S., Castiblanco, C., Buszczak, M., Hoskins, R.A., Cooley, L., 2006. Exploring Strategies for Protein Trapping in *Drosophila*. *Genetics* 175, 1089–1104.
- Quintás-Cardama, A., Cortes, J., 2009. Molecular biology of bcr-abl1-positive chronic myeloid leukemia. *Blood*.
- Rad, E., Murray, J.T., Tee, A.R., 2018. Oncogenic signalling through mechanistic target of rapamycin (mTOR): A driver of metabolic transformation and cancer progression. *Cancers (Basel)*.
- Raich, W.B., Moorman, C., Lacefield, C.O., Lehrer, J., Bartsch, D., Plasterk, R.H.A., Kandel, E.R., Hobert, O., 2003. Characterization of *Caenorhabditis elegans* homologs of the Down syndrome candidate gene DYRK1A. *Genetics*.
- Ranuncolo, S.M., Ghosh, S., Hanover, J.A., Hart, G.W., Lewis, B.A., 2012. Evidence of the involvement of O-GlcNAc-modified human RNA polymerase II CTD in transcription in vitro and in vivo. *J. Biol. Chem.*
- Rappaport, J., Mann, M., Ishihama, Y., 2007. Protocol for micro-purification, enrichment, pre-fractionation and storage of peptides for proteomics using StageTips. *Nat. Protoc.* 2, 1896–1906.
- Rechsteiner, M.C., 1970. *Drosophila* lactate dehydrogenase: partial purification and characterization. *J. Insect Physiol.* 16, 957–77.
- Redza-Dutordoir, M., Averill-Bates, D.A., 2016. Activation of apoptosis signalling pathways by reactive oxygen species. *Biochim. Biophys. Acta - Mol. Cell Res.*
- Rey, C., Soubeyran, I., Mahouche, I., Pedeboscq, S., Bessede, A., Ichas, F., De Giorgi, F., Lartigue, L., 2013. HIPK1 drives p53 activation to limit colorectal cancer cell growth. *Cell Cycle* 12, 1879–91.
- Ricci, A., Cherubini, E., Olivieri, A., Lavra, L., Sciacchitano, S., Scozzi, D., Mancini, R., Ciliberto, G., Bartolazzi, A., Bruno, P., Graziano, P., Mariotta, S., 2013. Homeodomain-interacting protein kinase2 in human idiopathic pulmonary fibrosis. *J. Cell. Physiol.* 228, 235–241.
- Rinaldo, C., Moncada, A., Gradi, A., Ciuffini, L., D'Eliseo, D., Siepi, F., Prodromo, A., Giorgi, A., Pierantoni, G.M., Trapasso, F., Guarugnini, G., Bartolazzi, A., Cundari, E., Schininà, M.E., Fusco, A., Soddu, S., 2012. HIPK2 Controls Cytokinesis and Prevents Tetraploidization by Phosphorylating Histone H2B at the Midbody. *Mol. Cell* 47, 87–98.
- Rinaldo, C., Prodromo, A., Mancini, F., Iacovelli, S., Sacchi, A., Moretti, F., Soddu, S., 2007. MDM2-Regulated Degradation of HIPK2 Prevents p53Ser46 Phosphorylation

and DNA Damage-Induced Apoptosis. *Mol. Cell.*

Rivlin, N., Brosh, R., Oren, M., Rotter, V., 2011. Mutations in the p53 tumor suppressor gene: Important milestones at the various steps of tumorigenesis. *Genes and Cancer.*

Robey, R.B., Hay, N., 2009. Is Akt the “Warburg kinase”? -Akt-energy metabolism interactions and oncogenesis. *Semin. Cancer Biol.*

Röder, P. V., Wu, B., Liu, Y., Han, W., 2016. Pancreatic regulation of glucose homeostasis. *Exp. Mol. Med.*

Rogers, S., Wells, R., Rechsteiner, M., 1986. Amino acid sequences common to rapidly degraded proteins: The PEST hypothesis. *Science* (80-).

Rosenzweig, R., Bronner, V., Zhang, D., Fushman, D., Glickman, M.H., 2012. Rpn1 and Rpn2 Coordinate Ubiquitin Processing Factors at Proteasome. *J. Biol. Chem.* 287, 14659–14671.

Rosin, D., Schejter, E., Volk, T., Shilo, B.Z., 2004. Apical accumulation of the Drosophila PDGF/VEGF receptor ligands provides a mechanism for triggering localized actin polymerization. *Development.*

Rossetti, L., 2000. Perspective: Hexosamines and Nutrient Sensing. *Endocrinology.*

Roy, R., Chun, J., Powell, S.N., 2012. BRCA1 and BRCA2: Different roles in a common pathway of genome protection. *Nat. Rev. Cancer.*

Rozanski, W., Krzeslak, A., Forma, E., Brys, M., Blewniewski, M., Wozniak, P., Lipinski, M., 2012. Prediction of bladder cancer based on urinary content of MGEA5 and OGT mRNA level. *Clin. Lab.* 58, 579–83.

Rudrapatna, V.A., Bangi, E., Cagan, R.L., 2013. Caspase signalling in the absence of apoptosis drives Jnk-dependent invasion. *EMBO Rep.*

Rudrapatna, V.A., Cagan, R.L., Das, T.K., 2012. Drosophila cancer models. *Dev. Dyn.*

Rui, L., 2014. Energy metabolism in the liver. *Compr. Physiol.*

Rui, Y., Xu, Z., Lin, S., Li, Q., Rui, H., Luo, W., Zhou, H.M., Cheung, P.Y., Wu, Z., Ye, Z., Li, P., Han, J., Lin, S.C., 2004. Axin stimulates p53 functions by activation of HIPK2 kinase through multimeric complex formation. *EMBO J.*

Sakamoto, K., Huang, B.W., Iwasaki, K., Hailemariam, K., Ninomiya-Tsuji, J., Tsuji, Y., 2010. Regulation of genotoxic stress response by homeodomain-interacting protein kinase 2 through phosphorylation of cyclic AMP response element-binding protein at serine 271. *Mol. Biol. Cell.*

Samuels, Y., Waldman, T., 2010. Oncogenic mutations of PIK3CA in human cancers. *Curr. Top. Microbiol. Immunol.*

Sancak, Y., Bar-Peled, L., Zoncu, R., Markhard, A.L., Nada, S., Sabatini, D.M., 2010.

Ragulator-rag complex targets mTORC1 to the lysosomal surface and is necessary for its activation by amino acids. *Cell*.

Sanchez-Vega, F., Mina, M., Armenia, J., Chatila, W.K., Luna, A., La, K.C., Dimitriadoy, S., Liu, D.L., Kantheti, H.S., Saghafinia, S., Chakravarty, D., Daian, F., Gao, Q., Bailey, M.H., Liang, W.W., Foltz, S.M., Shmulevich, I., Ding, L., Heins, Z., Ochoa, A., Gross, B., Gao, J., Zhang, Hongxin, Kundra, R., Kandoth, C., Bahceci, I., Dervishi, L., Dogrusoz, U., Zhou, W., Shen, H., Laird, P.W., Way, G.P., Greene, C.S., Liang, H., Xiao, Y., Wang, C., Iavarone, A., Berger, A.H., Bivona, T.G., Lazar, A.J., Hammer, G.D., Giordano, T., Kwong, L.N., McArthur, G., Huang, C., Tward, A.D., Frederick, M.J., McCormick, F., Meyerson, M., Caesar-Johnson, S.J., Demchok, J.A., Felau, I., Kasapi, M., Ferguson, M.L., Hutter, C.M., Sofia, H.J., Tarnuzzer, R., Wang, Z., Yang, L., Zenklusen, J.C., Zhang, J. (Julia), Chudamani, S., Liu, J., Lolla, L., Naresh, R., Pihl, T., Sun, Q., Wan, Y., Wu, Y., Cho, J., DeFreitas, T., Frazer, S., Gehlenborg, N., Getz, G., Heiman, D.I., Kim, J., Lawrence, M.S., Lin, P., Meier, S., Noble, M.S., Saksena, G., Voet, D., Zhang, Hailei, Bernard, B., Chambwe, N., Dhankani, V., Knijnenburg, T., Kramer, R., Leinonen, K., Liu, Y., Miller, M., Reynolds, S., Shmulevich, I., Thorsson, V., Zhang, W., Akbani, R., Broom, B.M., Hegde, A.M., Ju, Z., Kanchi, R.S., Korkut, A., Li, J., Liang, H., Ling, S., Liu, W., Lu, Y., Mills, G.B., Ng, K.S., Rao, A., Ryan, M., Wang, Jing, Weinstein, J.N., Zhang, J., Abeshouse, A., Armenia, J., Chakravarty, D., Chatila, W.K., de Brujin, I., Gao, J., Gross, B.E., Heins, Z.J., Kundra, R., La, K., Ladanyi, M., Luna, A., Nissan, M.G., Ochoa, A., Phillips, S.M., Reznik, E., Sanchez-Vega, F., Sander, C., Schultz, N., Sheridan, R., Sumer, S.O., Sun, Y., Taylor, B.S., Wang, Jiaojiao, Zhang, Hongxin, Anur, P., Peto, M., Spellman, P., Benz, C., Stuart, J.M., Wong, C.K., Yau, C., Hayes, D.N., Parker, J.S., Wilkerson, M.D., Ally, A., Balasundaram, M., Bowlby, R., Brooks, D., Carlsen, R., Chuah, E., Dhalla, N., Holt, R., Jones, S.J.M., Kasaian, K., Lee, D., Ma, Y., Marra, M.A., Mayo, M., Moore, R.A., Mungall, A.J., Mungall, K., Robertson, A.G., Sadeghi, S., Schein, J.E., Sipahimalani, P., Tam, A., Thiessen, N., Tse, K., Wong, T., Berger, A.C., Beroukhim, R., Cherniack, A.D., Cibulskis, C., Gabriel, S.B., Gao, G.F., Ha, G., Meyerson, M., Schumacher, S.E., Shih, J., Kucherlapati, M.H., Kucherlapati, R.S., Baylin, S., Cope, L., Danilova, L., Bootwalla, M.S., Lai, P.H., Maglinte, D.T., Van Den Berg, D.J., Weisenberger, D.J., Auman, J.T., Balu, S., Bodenheimer, T., Fan, C., Hoadley, K.A., Hoyle, A.P., Jeffrys, S.R., Jones, C.D., Meng, S., Mieczkowski, P.A., Mose, L.E., Perou, A.H., Perou, C.M., Roach, J., Shi, Y., Simons, J. V., Skelly, T., Soloway, M.G., Tan, D., Veluvolu, U., Fan, H., Hinoue, T., Laird, P.W., Shen, H., Zhou, W., Bellair, M., Chang, K., Covington, K., Creighton, C.J., Dinh, H., Doddapaneni, H.V., Donehower, L.A., Drummond, J., Gibbs, R.A., Glenn, R., Hale, W., Han, Y., Hu, J., Korchina, V., Lee, S., Lewis, L., Li, W., Liu, X., Morgan, M., Morton, D., Muzny, D., Santibanez, J., Sheth, M., Shinbrot, E., Wang, L., Wang, M., Wheeler, D.A., Xi, L., Zhao, F., Hess, J., Appelbaum, E.L., Bailey, M., Cordes, M.G., Ding, L., Fronick, C.C., Fulton, L.A., Fulton, R.S., Kandoth, C., Mardis, E.R., McLellan, M.D., Miller, C.A., Schmidt, H.K., Wilson, R.K., Crain, D., Curley, E., Gardner, J., Lau, K., Mallory, D., Morris, S., Paulauskis, J., Penny, R., Shelton, C., Shelton, T., Sherman, M., Thompson, E., Yena, P., Bowen, J., Gastier-Foster, J.M., Gerken, M., Leraas, K.M., Lichtenberg, T.M., Ramirez, N.C., Wise, L., Zmuda, E., Corcoran, N., Costello, T., Hovens, C., Carvalho, A.L., de Carvalho, A.C., Fregnani, J.H., Longatto-Filho, A., Reis, R.M., Scapulatempo-Neto, C., Silveira, H.C.S., Vidal, D.O., Burnette, A., Eschbacher, J., Hermes, B., Noss, A., Singh, R., Anderson, M.L., Castro, P.D., Ittmann, M., Huntsman, D., Kohl, B., Le, X., Thorp, R., Andry,

C., Duffy, E.R., Lyadov, V., Paklina, O., Setdikova, G., Shabunin, A., Tavobilov, M., McPherson, C., Warnick, R., Berkowitz, R., Cramer, D., Feltmate, C., Horowitz, N., Kibel, A., Muto, M., Raut, C.P., Malykh, A., Barnholtz-Sloan, J.S., Barrett, W., Devine, K., Fulop, J., Ostrom, Q.T., Shimmel, K., Wolinsky, Y., Sloan, A.E., De Rose, A., Giulante, F., Goodman, M., Karlan, B.Y., Hagedorn, C.H., Eckman, J., Harr, J., Myers, J., Tucker, K., Zach, L.A., Deyarmin, B., Hu, H., Kvecher, L., Larson, C., Mural, R.J., Somiari, S., Vicha, A., Zelinka, T., Bennett, J., Iacocca, M., Rabeno, B., Swanson, P., Latour, M., Lacombe, L., Têtu, B., Bergeron, A., McGraw, M., Staugaitis, S.M., Chabot, J., Hibshoosh, H., Sepulveda, A., Su, T., Wang, T., Potapova, O., Voronina, O., Desjardins, L., Mariani, O., Roman-Roman, S., Sastre, X., Stern, M.H., Cheng, F., Signoretti, S., Berchuck, A., Bigner, D., Lipp, E., Marks, J., McCall, S., McLendon, R., Secord, A., Sharp, A., Behera, M., Brat, D.J., Chen, A., Delman, K., Force, S., Khuri, F., Magliocca, K., Maithel, S., Olson, J.J., Owonikoko, T., Pickens, A., Ramalingam, S., Shin, D.M., Sica, G., Van Meir, E.G., Zhang, Hongzheng, Eijkenboom, W., Gillis, A., Korpershoek, E., Looijenga, L., Oosterhuis, W., Stoop, H., van Kessel, K.E., Zwarthoff, E.C., Calatozzolo, C., Cuppini, L., Cuzzubbo, S., DiMeco, F., Finocchiaro, G., Mattei, L., Perin, A., Pollo, B., Chen, C., Houck, J., Lohavanichbutr, P., Hartmann, A., Stoehr, C., Stoehr, R., Taubert, H., Wach, S., Wullich, B., Kyeler, W., Murawa, D., Wiznerowicz, M., Chung, K., Edenfield, W.J., Martin, J., Baudin, E., Bubley, G., Bueno, R., De Rienzo, A., Richards, W.G., Kalkanis, S., Mikkelsen, T., Noushmehr, H., Scarpace, L., Girard, N., Aymerich, M., Campo, E., Giné, E., Guillermo, A.L., Van Bang, N., Hanh, P.T., Phu, B.D., Tang, Y., Colman, H., Eason, K., Dottino, P.R., Martignetti, J.A., Gabra, H., Juhl, H., Akeredolu, T., Stepa, S., Hoon, D., Ahn, K., Kang, K.J., Beuschlein, F., Breggia, A., Birrer, M., Bell, D., Borad, M., Bryce, A.H., Castle, E., Chandan, V., Cheville, J., Copland, J.A., Farnell, M., Flotte, T., Giama, N., Ho, T., Kendrick, M., Kocher, J.P., Kopp, K., Moser, C., Nagorney, D., O'Brien, D., O'Neill, B.P., Patel, T., Petersen, G., Que, F., Rivera, M., Roberts, L., Smallridge, R., Smyrk, T., Stanton, M., Thompson, R.H., Torbenson, M., Yang, J.D., Zhang, L., Brimo, F., Ajani, J.A., Gonzalez, A.M.A., Behrens, C., Bondaruk, J., Broaddus, R., Czerniak, B., Esmaeli, B., Fujimoto, J., Gershenwald, J., Guo, C., Logothetis, C., Meric-Bernstam, F., Moran, C., Ramondetta, L., Rice, D., Sood, A., Tamboli, P., Thompson, T., Troncoso, P., Tsao, A., Wistuba, I., Carter, C., Haydu, L., Hersey, P., Jakrot, V., Kakavand, H., Kefford, R., Lee, K., Long, G., Mann, G., Quinn, M., Saw, R., Scolyer, R., Shannon, K., Spillane, A., Stretch, J., Synott, M., Thompson, J., Wilmott, J., Al-Ahmadie, H., Chan, T.A., Ghossein, R., Gopalan, A., Levine, D.A., Reuter, V., Singer, S., Singh, B., Tien, N.V., Broudy, T., Mirsaidi, C., Nair, P., Drwiga, P., Miller, J., Smith, J., Zaren, H., Park, J.W., Hung, N.P., Kebebew, E., Linehan, W.M., Metwalli, A.R., Pacak, K., Pinto, P.A., Schiffman, M., Schmidt, L.S., Vocke, C.D., Wentzensen, N., Worrell, R., Yang, H., Moncrieff, M., Goparaju, C., Melamed, J., Pass, H., Botnariuc, N., Caraman, I., Cernat, M., Chemencedji, I., Clipca, A., Doruc, S., Gorincioi, G., Mura, S., Pirtac, M., Stancul, I., Tcaciuc, D., Albert, M., Alexopoulou, I., Arnaout, A., Bartlett, J., Engel, J., Gilbert, S., Parfitt, J., Sekhon, H., Thomas, G., Rassl, D.M., Rintoul, R.C., Bifulco, C., Tamakawa, R., Urba, W., Hayward, N., Timmers, H., Antenucci, A., Facciolo, F., Grazi, G., Marino, M., Merola, R., de Krijger, R., Gimenez-Roqueplo, A.P., Piché, A., Chevalier, S., McKercher, G., Birsoy, K., Barnett, G., Brewer, C., Farver, C., Naska, T., Pennell, N.A., Raymond, D., Schilero, C., Smolenski, K., Williams, F., Morrison, C., Borgia, J.A., Liptay, M.J., Pool, M., Seder, C.W., Junker, K., Omberg, L., Dinkin, M., Manikhas, G., Alvaro, D., Bragazzi, M.C., Cardinale, V., Carpino, G., Gaudio, E., Chesla, D., Cottingham, S., Dubina, M., Moiseenko, F., Dhanasekaran, R., Becker,

K.F., Janssen, K.P., Slotta-Huspenina, J., Abdel-Rahman, M.H., Aziz, D., Bell, S., Cebulla, C.M., Davis, A., Duell, R., Elder, J.B., Hilty, J., Kumar, B., Lang, J., Lehman, N.L., Mandt, R., Nguyen, P., Pilarski, R., Rai, K., Schoenfield, L., Senecal, K., Wakely, P., Hansen, P., Lechan, R., Powers, J., Tischler, A., Grizzle, W.E., Sexton, K.C., Kastl, A., Henderson, J., Porten, S., Waldmann, J., Fassnacht, M., Asa, S.L., Schadendorf, D., Couce, M., Graefen, M., Huland, H., Sauter, G., Schlomm, T., Simon, R., Tennstedt, P., Olabode, O., Nelson, M., Bathe, O., Carroll, P.R., Chan, J.M., Disaia, P., Glenn, P., Kelley, R.K., Landen, C.N., Phillips, J., Prados, M., Simko, J., Smith-McCune, K., VandenBerg, S., Roggin, K., Fehrenbach, A., Kendler, A., Sifri, S., Steele, R., Jimeno, A., Carey, F., Forgie, I., Mannelli, M., Carney, M., Hernandez, B., Campos, B., Herold-Mende, C., Jungk, C., Unterberg, A., von Deimling, A., Bossler, A., Galbraith, J., Jacobus, L., Knudson, M., Knutson, T., Ma, D., Milhem, M., Sigmund, R., Godwin, A.K., Madan, R., Rosenthal, H.G., Adebamowo, C., Adebamowo, S.N., Boussioutas, A., Beer, D., Giordano, T., Mes-Masson, A.M., Saad, F., Bocklage, T., Landrum, L., Mannel, R., Moore, K., Moxley, K., Postier, R., Walker, J., Zuna, R., Feldman, M., Valdivieso, F., Dhir, R., Luketich, J., Pinero, E.M.M., Quintero-Aguilo, M., Carlotti, C.G., Dos Santos, J.S., Kemp, R., Sankarankuty, A., Tirapelli, D., Catto, J., Agnew, K., Swisher, E., Creaney, J., Robinson, B., Shelley, C.S., Godwin, E.M., Kendall, S., Shipman, C., Bradford, C., Carey, T., Haddad, A., Moyer, J., Peterson, L., Prince, M., Rozek, L., Wolf, G., Bowman, R., Fong, K.M., Yang, I., Korst, R., Rathmell, W.K., Fantacone-Campbell, J.L., Hooke, J.A., Kovatich, A.J., Shriver, C.D., DiPersio, J., Drake, B., Govindan, R., Heath, S., Ley, T., Van Tine, B., Westervelt, P., Rubin, M.A., Lee, J. II, Arede, N.D., Mariamidze, A., Van Allen, E.M., Cherniack, A.D., Ciriello, G., Sander, C., Schultz, N., 2018. Oncogenic Signaling Pathways in The Cancer Genome Atlas. *Cell*.

Saraei, P., Asadi, I., Kakar, M.A., Moradi-Kor, N., 2019. The beneficial effects of metformin on cancer prevention and therapy: A comprehensive review of recent advances. *Cancer Manag. Res.*

Saul, V. V., De La Vega, L., Milanovic, M., Krüger, M., Braun, T., Fritz-Wolf, K., Becker, K., Schmitz, M.L., 2013. HIPK2 kinase activity depends on cis-autophosphorylation of its activation loop. *J. Mol. Cell Biol.*

Saul, V. V., Schmitz, M.L., 2013. Posttranslational modifications regulate HIPK2, a driver of proliferative diseases. *J. Mol. Med. (Berl)*. 91, 1051–8.

Scaduto, R.C., Grotyohann, L.W., 1999. Measurement of mitochondrial membrane potential using fluorescent rhodamine derivatives. *Biophys. J.*

Schmitz, M.L., Rodriguez-Gil, A., Hornung, J., 2014. Integration of stress signals by homeodomain interacting protein kinases. *Biol. Chem.*

Scott, D.A., Richardson, A.D., Filipp, F. V., Knutzen, C.A., Chiang, G.G., Ronai, Z.A., Osterman, A.L., Smith, J.W., 2011. Comparative metabolic flux profiling of melanoma cell lines: Beyond the Warburg effect. *J. Biol. Chem.*

Sears, R., Nuckolls, F., Haura, E., Taya, Y., Tamai, K., Nevins, J.R., 2000. Multiple Ras-dependent phosphorylation pathways regulate Myc protein stability. *Genes Dev.*

- Selak, M.A., Armour, S.M., MacKenzie, E.D., Boulahbel, H., Watson, D.G., Mansfield, K.D., Pan, Y., Simon, M.C., Thompson, C.B., Gottlieb, E., 2005. Succinate links TCA cycle dysfunction to oncogenesis by inhibiting HIF- α prolyl hydroxylase. *Cancer Cell.*
- Senyilmaz, D., Teleman, A.A., 2015. Chicken or the egg: Warburg effect and mitochondrial dysfunction. *F1000Prime Rep.* 7, 41.
- Sever, R., Brugge, J.S., 2015. Signal transduction in cancer. *Cold Spring Harb. Perspect. Med.*
- Seyfried, T.N., Flores, R.E., Poff, A.M., D'Agostino, D.P., 2014. Cancer as a metabolic disease: implications for novel therapeutics. *Carcinogenesis* 35, 515–27.
- Shang, Y., Doan, C.N., Arnold, T.D., Lee, S., Tang, A.A., Reichardt, L.F., Huang, E.J., 2013. Transcriptional Corepressors HIPK1 and HIPK2 Control Angiogenesis Via TGF- β -TAK1-Dependent Mechanism. *PLoS Biol.* 11, e1001527.
- Sharma, L., Lu, J., Bai, Y., 2009. Mitochondrial Respiratory Complex I: Structure, Function and Implication in Human Diseases. *Curr. Med. Chem.*
- Shenolikar, S., Nairn, A.C., 1991. Protein phosphatases: recent progress. *Adv. Second Messenger Phosphoprotein Res.*
- Shima, Y., Shima, T., Chiba, T., Irimura, T., Pandolfi, P.P., Kitabayashi, I., 2008. PML Activates Transcription by Protecting HIPK2 and p300 from SCFFbx3-Mediated Degradation. *Mol. Cell. Biol.*
- Shimizu, N., Ishitani, S., Sato, A., Shibuya, H., Ishitani, T., 2014. Hipk2 and PP1c Cooperate to Maintain Dvl Protein Levels Required for Wnt Signal Transduction. *Cell Rep.*
- Shortt, J., Johnstone, R.W., 2012. Oncogenes in cell survival and cell death. *Cold Spring Harb. Perspect. Biol.*
- Sinclair, D.A.R., Syrzycka, M., Macauley, M.S., Rastgardani, T., Komljenovic, I., Vocadlo, D.J., Brock, H.W., Honda, B.M., 2009. Drosophila O-GlcNAc transferase (OGT) is encoded by the Polycomb group (PcG) gene, super sex combs (sxc). *Proc. Natl. Acad. Sci. U. S. A.* 106, 13427–32.
- Sjolund, J., Pelorosso, F.G., Quigley, D.A., DelRosario, R., Balmain, A., 2014. Identification of Hipk2 as an essential regulator of white fat development. *Proc. Natl. Acad. Sci.* 111, 7373–7378.
- Slaninova, V., Krafcikova, M., Perez-Gomez, R., Steffal, P., Trantirek, L., Bray, S.J., Krejci, M., 2016. Notch stimulates growth by direct regulation of genes involved in the control of glycolysis and the tricarboxylic acid cycle. *Open Biol.*
- Son, Y., Kim, S., Chung, H.T., Pae, H.O., 2013. Reactive oxygen species in the activation of MAP kinases. In: *Methods in Enzymology*.

- Song, M.S., Salmena, L., Pandolfi, P.P., 2012. The functions and regulation of the PTEN tumour suppressor. *Nat. Rev. Mol. Cell Biol.*
- Song, Q., Merajver, S.D., Li, J.Z., 2015. Cancer classification in the genomic era: five contemporary problems. *Hum. Genomics.*
- Song, W., Owusu-Ansah, E., Hu, Y., Cheng, D., Ni, X., Zirin, J., Perrimon, N., 2017. Activin signaling mediates muscle-to-adipose communication in a mitochondria dysfunction-associated obesity model. *Proc. Natl. Acad. Sci. U. S. A.*
- Sonoshita, M., Cagan, R.L., 2017. Modeling Human Cancers in *Drosophila*. In: *Current Topics in Developmental Biology*.
- Soucek, L., Evan, G.I., 2010. The ups and downs of Myc biology. *Curr. Opin. Genet. Dev.* 20, 91–5.
- Spitzer, M., Wildenhain, J., Rappaport, J., Tyers, M., 2014. BoxPlotR: a web tool for generation of box plots. *Nat. Methods* 11, 121–122.
- Srivastava, A., Pastor-Pareja, J.C., Igaki, T., Pagliarini, R., Xu, T., 2007. Basement membrane remodeling is essential for *Drosophila* disc eversion and tumor invasion. *Proc. Natl. Acad. Sci. U. S. A.*
- Staehling-Hampton, K., Jackson, P.D., Clark, M.J., Brand, A.H., Hoffmann, F.M., 1994. Specificity of bone morphogenetic protein-related factors: Cell fate and gene expression changes in *Drosophila* embryos induced by decapentaplegic but not 60A. *Cell Growth Differ.*
- Stanley, P., 2011. Golgi glycosylation. *Cold Spring Harb. Perspect. Biol.*
- Steinmetz, E.L., Dewald, D.N., Luxem, N., Walldorf, U., 2019. *Drosophila* homeodomain-interacting protein kinase (Hipk) phosphorylates the homeodomain proteins homeobrain, empty spiracles, and muscle segment homeobox. *Int. J. Mol. Sci.*
- Steinmetz, E.L., Dewald, D.N., Walldorf, U., 2018. Homeodomain-interacting protein kinase phosphorylates the *Drosophila* Paired box protein 6 (Pax6) homologues Twin of eyeless and Eyeless. *Insect Mol. Biol.*
- Stine, Z.E., Walton, Z.E., Altman, B.J., Hsieh, A.L., Dang, C. V., 2015. MYC, metabolism, and cancer. *Cancer Discov.*
- Stoyanova, T., Riedinger, M., Lin, S., Faltermeier, C.M., Smith, B.A., Zhang, K.X., Going, C.C., Goldstein, A.S., Lee, J.K., Drake, J.M., Rice, M.A., Hsu, E.C., Nowroozizadeh, B., Castor, B., Orellana, S.Y., Blum, S.M., Cheng, D., Pienta, K.J., Reiter, R.E., Pitteri, S.J., Huang, J., Witte, O.N., 2016. Activation of Notch1 synergizes with multiple pathways in promoting castration-resistant prostate cancer. *Proc. Natl. Acad. Sci. U. S. A.*
- Struhl, G., Basler, K., 1993. Organizing activity of wingless protein in *Drosophila*. *Cell.*
- Su, C.Y., Chang, Y.C., Yang, C.J., Huang, M.S., Hsiao, M., 2016. The opposite

prognostic effect of NDUFS1 and NDUFS8 in lung cancer reflects the oncojanus role of mitochondrial complex i. *Sci. Rep.*

Sullivan, L.B., Chandel, N.S., 2014. Mitochondrial reactive oxygen species and cancer. *Cancer Metab.*

Sun, W., Yang, J., 2010. Functional mechanisms for human tumor suppressors. *J. Cancer.*

Swarup, S., Verheyen, E.M., 2011. Drosophila homeodomain-interacting protein kinase inhibits the Skp1-Cul1-F-box E3 ligase complex to dually promote Wingless and Hedgehog signaling. *Proc. Natl. Acad. Sci.* 108, 9887–9892.

Tamori, Y., Suzuki, E., Deng, W.-M., 2016. Epithelial Tumors Originate in Tumor Hotspots, a Tissue-Intrinsic Microenvironment. *PLOS Biol.* 14, e1002537.

Tan, M., Gong, H., Zeng, Y., Tao, L., Wang, J., Jiang, J., Xu, D., Bao, E., Qiu, J., Liu, Z., 2014. Downregulation of homeodomain-interacting protein kinase-2 contributes to bladder cancer metastasis by regulating Wnt signaling. *J. Cell. Biochem.*

Tennessen, J.M., Baker, K.D., Lam, G., Evans, J., Thummel, C.S., 2011. The Drosophila estrogen-related receptor directs a metabolic switch that supports developmental growth. *Cell Metab.* 13, 139–48.

Tennessen, J.M., Barry, W.E., Cox, J., Thummel, C.S., 2014. Methods for studying metabolism in Drosophila. *Methods* 68, 105–115.

TeSlaa, T., Teitell, M.A., 2014. Techniques to monitor glycolysis. *Methods Enzymol.* 542, 91–114.

Tettweiler, G., Blaquiere, J.A., Wray, N.B., Verheyen, E.M., 2019. Hipk is required for JAK/STAT activity during development and tumorigenesis. *PLoS One.*

Thiery, J.P., Acloque, H., Huang, R.Y.J., Nieto, M.A., 2009. Epithelial-Mesenchymal Transitions in Development and Disease. *Cell.*

Tomer, D., Chippalkatti, R., Mitra, K., Rikhy, R., 2018. ERK regulates mitochondrial membrane potential in fission deficient Drosophila follicle cells during differentiation. *Dev. Biol.*

Torrence, M.E., Manning, B.D., 2018. Nutrient Sensing in Cancer. *Annu. Rev. Cancer Biol.*

Torrente, L., Sanchez, C., Moreno, R., Chowdhry, S., Cabello, P., Isono, K., Koseki, H., Honda, T., Hayes, J.D., Dinkova-Kostova, A.T., de la Vega, L., 2017. Crosstalk between NRF2 and HIPK2 shapes cytoprotective responses. *Oncogene* 36, 6204–6212.

Trapasso, F., Aqeilan, R.I., Iuliano, R., Visone, R., Gaudio, E., Ciuffini, L., Alder, H., Paduano, F., Pierantoni, G.M., Soddu, S., Croce, C.M., Fusco, A., 2009. Targeted disruption of the murine homeodomain-interacting protein kinase-2 causes growth

- deficiency in vivo and cell cycle arrest in vitro. *DNA Cell Biol.*
- Trevisan, T., Pendin, D., Montagna, A., Bova, S., Ghelli, A.M., Daga, A., 2018. Manipulation of Mitochondria Dynamics Reveals Separate Roles for Form and Function in Mitochondria Distribution. *Cell Rep.*
- Tsai, J.H., Yang, J., 2013. Epithelial-mesenchymal plasticity in carcinoma metastasis. *Genes Dev.*
- Udan, R.S., Kango-Singh, M., Nolo, R., Tao, C., Halder, G., 2003. Hippo promotes proliferation arrest and apoptosis in the Salvador/Warts pathway. *Nat. Cell Biol.*
- Uhlirova, M., Bohmann, D., 2006. JNK- and Fos-regulated Mmp1 expression cooperates with Ras to induce invasive tumors in Drosophila. *EMBO J.*
- Valastyan, S., Weinberg, R.A., 2011. Tumor metastasis: Molecular insights and evolving paradigms. *Cell.*
- Valente, A.J., Maddalena, L.A., Robb, E.L., Moradi, F., Stuart, J.A., 2017. A simple ImageJ macro tool for analyzing mitochondrial network morphology in mammalian cell culture. *Acta Histochem.* 119, 315–326.
- Valvona, C.J., Fillmore, H.L., Nunn, P.B., Pilkington, G.J., 2016. The Regulation and Function of Lactate Dehydrogenase A: Therapeutic Potential in Brain Tumor. *Brain Pathol.* 26, 3–17.
- Van Den Ameele, J., Brand, A.H., 2019. Neural stem cell temporal patterning and brain tumour growth rely on oxidative phosphorylation. *Elife.*
- van der Bliek, A.M., Shen, Q., Kawajiri, S., 2013. Mechanisms of mitochondrial fission and fusion. *Cold Spring Harb. Perspect. Biol.*
- Vander Heiden, M.G., Cantley, L.C., Thompson, C.B., 2009. Understanding the Warburg effect: the metabolic requirements of cell proliferation. *Science* 324, 1029–33.
- Vasconcelos-Dos-Santos, A., Loponte, H.F.B.R., Mantuano, N.R., Oliveira, I.A., De Paula, I.F., Teixeira, L.K., De-Freitas-Junior, J.C.M., Gondim, K.C., Heise, N., Mohana-Borges, R., Morgado-Díaz, J.A., Dias, W.B., Todeschini, A.R., 2017. Hyperglycemia exacerbates colon cancer malignancy through hexosamine biosynthetic pathway. *Oncogenesis.*
- Vidal, M., Warner, S., Read, R., Cagan, R.L., 2007. Differing Src signaling levels have distinct outcomes in Drosophila. *Cancer Res.*
- Vocadlo, D.J., Hang, H.C., Kim, E.-J., Hanover, J.A., Bertozzi, C.R., 2003. A chemical approach for identifying O-GlcNAc-modified proteins in cells. *Proc. Natl. Acad. Sci.* 100, 9116–9121.
- Volkenhoff, A., Hirrlinger, J., Kappel, J.M., Klämbt, C., Schirmeier, S., 2018. Live imaging using a FRET glucose sensor reveals glucose delivery to all cell types in the Drosophila brain. *J. Insect Physiol.* 106, 55–64.

- Volkenhoff, A., Weiler, A., Letzel, M., Stehling, M., Klämbt, C., Schirmeier, S., 2015. Glial Glycolysis Is Essential for Neuronal Survival in Drosophila. *Cell Metab.* 22, 437–447.
- Vyas, S., Zaganjor, E., Haigis, M.C., 2016. Mitochondria and Cancer. *Cell.*
- Walgren, J.L.E., Vincent, T.S., Schey, K.L., Buse, M.G., 2003. High glucose and insulin promote O-GlcNAc modification of proteins, including α -tubulin. *Am. J. Physiol. Metab.* 284, E424–E434.
- Wang, B., Goode, J., Best, J., Meltzer, J., Schilman, P.E., Chen, J., Garza, D., Thomas, J.B., Montminy, M., 2008. The Insulin-Regulated CREB Coactivator TORC Promotes Stress Resistance in Drosophila. *Cell Metab.*
- Wang, B., Moya, N., Niessen, S., Hoover, H., Mihaylova, M.M., Shaw, R.J., Yates, J.R., Fischer, W.H., Thomas, J.B., Montminy, M., 2011. A hormone-dependent module regulating energy balance. *Cell.*
- Wang, C., Zhao, R., Huang, P., Yang, F., Quan, Z., Xu, N., Xi, R., 2013. APC loss-induced intestinal tumorigenesis in Drosophila: Roles of Ras in Wnt signaling activation and tumor progression. *Dev. Biol.*
- Wang, L.H., Wu, C.F., Rajasekaran, N., Shin, Y.K., 2019. Loss of tumor suppressor gene function in human cancer: An overview. *Cell. Physiol. Biochem.*
- Wang, Purkayastha, A., Jones, K.T., Thaker, S.K., Banerjee, U., 2016. In vivo genetic dissection of tumor growth and the Warburg effect. *Elife* 5.
- Wang, Z.N., Takemori, H., Halder, S.K., Nonaka, Y., Okamoto, M., 1999. Cloning of a novel kinase (SIK) of the SNF1/AMPK family from high salt diet-treated rat adrenal. *FEBS Lett.*
- WARBURG, O., 1956. On the origin of cancer cells. *Science* 123, 309–14.
- Warburg, O., Wind, F., Negelein, E., 1927. THE METABOLISM OF TUMORS IN THE BODY. *J. Gen. Physiol.* 8, 519–30.
- Ward, P.S., Thompson, C.B., 2012. Metabolic reprogramming: a cancer hallmark even warburg did not anticipate. *Cancer Cell* 21, 297–308.
- Wehr, M.C., Holder, M. V., Gailite, I., Saunders, R.E., Maile, T.M., Ciardaeva, E., Instrell, R., Jiang, M., Howell, M., Rossner, M.J., Tapon, N., 2013. Salt-inducible kinases regulate growth through the Hippo signalling pathway in Drosophila. *Nat. Cell Biol.*
- Wei, G., Ku, S., Ma, G.K., Saito, S., Tang, A.A., Zhang, J., Mao, J.-H., Appella, E., Balmain, A., Huang, E.J., 2007. HIPK2 represses beta-catenin-mediated transcription, epidermal stem cell expansion, and skin tumorigenesis. *Proc. Natl. Acad. Sci.* 104, 13040–13045.
- Westermann, B., 2012. Bioenergetic role of mitochondrial fusion and fission. *Biochim. Biophys. Acta - Bioenerg.* 1817, 1833–1838.

- Whelan, S.A., Dias, W.B., Thiruneelakantapillai, L., Daniel Lane, M., Hart, G.W., 2010. Regulation of insulin receptor substrate 1 (IRS-1)/AKT kinase-mediated insulin signaling by O-linked β -N-acetylglucosamine in 3T3-L1 adipocytes. *J. Biol. Chem.*
- Willems, P.H.G.M., Rossignol, R., Dieteren, C.E.J., Murphy, M.P., Koopman, W.J.H., 2015. Redox Homeostasis and Mitochondrial Dynamics. *Cell Metab.* 22, 207–218.
- Winter, M., Sombroek, D., Dauth, I., Moehlenbrink, J., Scheuermann, K., Crone, J., Hofmann, T.G., 2008. Control of HIPK2 stability by ubiquitin ligase Siah-1 and checkpoint kinases ATM and ATR. *Nat. Cell Biol.* 10, 812–824.
- Wishart, D.S., 2015. Is Cancer a Genetic Disease or a Metabolic Disease? *EBioMedicine* 2, 478–9.
- Wolfstetter, G., Shirinian, M., Stute, C., Grabbe, C., Hummel, T., Baumgartner, S., Palmer, R.H., Holz, A., 2009. Fusion of circular and longitudinal muscles in *Drosophila* is independent of the endoderm but further visceral muscle differentiation requires a close contact between mesoderm and endoderm. *Mech. Dev.*
- Wolin, K.Y., Carson, K., Colditz, G.A., 2010. Obesity and Cancer. *Oncologist* 15, 556–565.
- Won, H.Y., Sang, Y.P., Hyung, W.N., Do, H.K., Jeong, G.K., Eun, S.K., Yu, S.K., Hyun, C.L., Kwan, S.K., Jin, W.C., 2008. NF κ B activation is associated with its O-GlcNAcylation state under hyperglycemic conditions. *Proc. Natl. Acad. Sci. U. S. A.*
- Wong, K.K.L., Liao, J.Z., Verheyen, E.M., 2019. A positive feedback loop between Myc and aerobic glycolysis sustains tumor growth in a *Drosophila* tumor model. *Elife* 8.
- Wong, K.K.L., Liu, T.-W., Parker, J.M., Sinclair, D.A.R., Chen, Y.-Y., Khoo, K.-H., Vocadlo, D.J., Verheyen, E.M., 2020. The nutrient sensor OGT regulates Hipk stability and tumorigenic-like activities in *Drosophila*. *Proc. Natl. Acad. Sci.* 117, 2004–2013.
- Woods, A., Johnstone, S.R., Dickerson, K., Leiper, F.C., Fryer, L.G.D., Neumann, D., Schlattner, U., Wallimann, T., Carlson, M., Carling, D., 2003. LKB1 Is the Upstream Kinase in the AMP-Activated Protein Kinase Cascade. *Curr. Biol.*
- World Health, O., 2020. WHO report on cancer: Setting priorities investing wisely and providing care for all., *Investing Wisely and Providing Care for All*.
- Wu, H., Ying, M., Hu, X., 2016. Lactic acidosis switches cancer cells from aerobic glycolysis back to dominant oxidative phosphorylation. *Oncotarget*.
- Wu, M., Pastor-Pareja, J.C., Xu, T., 2010. Interaction between RasV12 and scribbled clones induces tumour growth and invasion. *Nature*.
- Xie, J., Wu, H., Dai, C., Pan, Q., Ding, Z., Hu, D., Ji, B., Luo, Y., Hu, X., 2014. Beyond Warburg effect - Dual metabolic nature of cancer cells. *Sci. Rep.*

- Yadav, A.K., Srikrishna, S., 2019. scribble (scrib) knockdown induces tumorigenesis by modulating Drp1-Parkin mediated mitochondrial dynamics in the wing imaginal tissues of *Drosophila*. *Mitochondrion*.
- Yang, J., Nishihara, R., Zhang, X., Ogino, S., Qian, Z.R., 2017. Energy sensing pathways: Bridging type 2 diabetes and colorectal cancer? *J. Diabetes Complications*.
- Yang, S.A., Portilla, J.M., Mihailovic, S., Huang, Y.C., Deng, W.M., 2019. Oncogenic Notch Triggers Neoplastic Tumorigenesis in a Transition-Zone-like Tissue Microenvironment. *Dev. Cell*.
- Yang, W.H., Kim, J.E., Nam, H.W., Ju, J.W., Kim, H.S., Kim, Y.S., Cho, J.W., 2006. Modification of p53 with O-linked N-acetylglucosamine regulates p53 activity and stability. *Nat. Cell Biol.* 8, 1074–1083.
- Yang, X., Ongusaha, P.P., Miles, P.D., Havstad, J.C., Zhang, F., So, W.V., Kudlow, J.E., Michell, R.H., Olefsky, J.M., Field, S.J., Evans, R.M., 2008. Phosphoinositide signalling links O-GlcNAc transferase to insulin resistance. *Nature*.
- Yang, X., Qian, K., 2017. Protein O-GlcNAcylation: emerging mechanisms and functions. *Nat. Rev. Mol. Cell Biol.* 18, 452–465.
- Yi, W., Clark, P.M., Mason, D.E., Keenan, M.C., Hill, C., Goddard, W.A., Peters, E.C., Driggers, E.M., Hsieh-Wilson, L.C., 2012. Phosphofructokinase 1 glycosylation regulates cell growth and metabolism. *Science* 337, 975–80.
- Ying, H., Kimmelman, A.C., Lyssiotis, C.A., Hua, S., Chu, G.C., Fletcher-Sananikone, E., Locasale, J.W., Son, J., Zhang, H., Coloff, J.L., Yan, H., Wang, W., Chen, S., Viale, A., Zheng, H., Paik, J.H., Lim, C., Guimaraes, A.R., Martin, E.S., Chang, J., Hezel, A.F., Perry, S.R., Hu, J., Gan, B., Xiao, Y., Asara, J.M., Weissleder, R., Wang, Y.A., Chin, L., Cantley, L.C., Depinho, R.A., 2012. Oncogenic kras maintains pancreatic tumors through regulation of anabolic glucose metabolism. *Cell*.
- Yip, K.W., Reed, J.C., 2008. Bcl-2 family proteins and cancer. *Oncogene*.
- Yokota, J., 2000. Tumor progression and metastasis. *Carcinogenesis*.
- Yoshioka, K., Saito, M., Oh, K.-B., Nemoto, Y., Matsuoka, H., Natsume, M., Abe, H., 1996. Intracellular Fate of 2-NBDG, a Fluorescent Probe for Glucose Uptake Activity, in *Escherichia coli* Cells. *Biosci. Biotechnol. Biochem.* 60, 1899–1901.
- Yu, D., Hung, M.C., 2000. Overexpression of ErbB2 in cancer and ErbB2-targeting strategies. *Oncogene*.
- Yu, J., Deshmukh, H., Gutmann, R.J., Emmett, R.J., Rodriguez, F.J., Watson, M.A., Nagarajan, R., Gutmann, D.H., 2009. Alterations of BRAF and HIPK2 loci predominate in sporadic pilocytic astrocytoma. *Neurology* 73, 1526–31.
- Yuan, H.-X., Xiong, Y., Guan, K.-L., 2013. Nutrient Sensing, Metabolism, and Cell Growth Control. *Mol. Cell* 49, 379–387.

- Yuzwa, S.A., Macauley, M.S., Heinonen, J.E., Shan, X., Dennis, R.J., He, Y., Whitworth, G.E., Stubbs, K.A., McEachern, E.J., Davies, G.J., Vocadlo, D.J., 2008. A potent mechanism-inspired O-GlcNAcase inhibitor that blocks phosphorylation of tau in vivo. *Nat. Chem. Biol.* 4, 483–490.
- Zhang, D., Tang, Z., Huang, H., Zhou, G., Cui, C., Weng, Y., Liu, W., Kim, S., Lee, S., Perez-Neut, M., Ding, J., Czyz, D., Hu, R., Ye, Z., He, M., Zheng, Y.G., Shuman, H.A., Dai, L., Ren, B., Roeder, R.G., Becker, L., Zhao, Y., 2019. Metabolic regulation of gene expression by histone lactylation. *Nature*.
- Zhang, J., Wang, S., Jiang, B., Huang, L., Ji, Z., Li, X., Zhou, H., Han, A., Chen, A., Wu, Y., Ma, H., Zhao, W., Zhao, Q., Xie, C., Sun, X., Zhou, Y., Huang, H., Suleman, M., Lin, F., Zhou, L., Tian, F., Jin, M., Cai, Y., Zhang, N., Li, Q., 2017. C-Src phosphorylation and activation of hexokinase promotes tumorigenesis and metastasis. *Nat. Commun.*
- Zhang, K., Li, Z., Jaiswal, M., Bayat, V., Xiong, B., Sandoval, H., Charng, W.L., David, G., Haueter, C., Yamamoto, S., Graham, B.H., Bellen, H.J., 2013. The C8ORF38 homologue Sicily is a cytosolic chaperone for a mitochondrial complex i subunit. *J. Cell Biol.*
- Zhang, Q., Nottke, A., Goodman, R.H., 2005. Homeodomain-interacting protein kinase-2 mediates CtBP phosphorylation and degradation in UV-triggered apoptosis. *Proc. Natl. Acad. Sci. U. S. A.*
- Zhang, X., Qiao, Y., Wu, Q., Chen, Yan, Zou, S., Liu, X., Zhu, G., Zhao, Y., Chen, Yuxin, Yu, Y., Pan, Q., Wang, J., Sun, F., 2017. The essential role of YAP O-GlcNAcylation in high-glucose-stimulated liver tumorigenesis. *Nat. Commun.* 8, 15280.
- Zhao, R.-X., Xu, Z.-X., 2014. Targeting the LKB1 Tumor Suppressor. *Curr. Drug Targets*.
- Zhu, J., Vinothkumar, K.R., Hirst, J., 2016. Structure of mammalian respiratory complex i. *Nature*.
- Zhu, Q., Zhou, L., Yang, Z., Lai, M., Xie, H., Wu, L., Xing, C., Zhang, F., Zheng, S., 2012. O-GlcNAcylation plays a role in tumor recurrence of hepatocellular carcinoma following liver transplantation. *Med. Oncol.* 29, 985–993.
- Zhuang, H., Codreanu, I., 2015. Growing applications of FDG PET-CT imaging in non-oncologic conditions. *J. Biomed. Res.*
- Zielonka, J., Kalyanaraman, B., 2010. Hydroethidine- and MitoSOX-derived red fluorescence is not a reliable indicator of intracellular superoxide formation: Another inconvenient truth. *Free Radic. Biol. Med.*
- Ziosi, M., Baena-López, L.A., Grifoni, D., Froldi, F., Pession, Andrea, Garoia, F., Trotta, V., Bellosta, P., Cavicchi, S., Pession, Annalisa, 2010. dMyc Functions Downstream of Yorkie to Promote the Supercompetitive Behavior of Hippo Pathway Mutant Cells. *PLoS Genet.* 6, e1001140.

Zoranovic, T., Manent, J., Willoughby, L., Matos de Simoes, R., La Marca, J.E., Golenkina, S., Cuiping, X., Gruber, S., Angjeli, B., Kanitz, E.E., Cronin, S.J.F., Neely, G.G., Wernitznig, A., Humbert, P.O., Simpson, K.J., Mitsiades, C.S., Richardson, H.E., Penninger, J.M., 2018. A genome-wide *Drosophila* epithelial tumorigenesis screen identifies Tetraspanin 29Fb as an evolutionarily conserved suppressor of Ras-driven cancer. *PLoS Genet.*

Zu, X.L., Guppy, M., 2004. Cancer metabolism: facts, fantasy, and fiction. *Biochem. Biophys. Res. Commun.* 313, 459–65.

Appendix A.

Amino acid sequence of the myc-tagged human HIPK2 protein

Labels: myc-tag + flanking amino acids, human HIPK2 amino acids (UniProtKB – Q9H2X6), O-GlcNAc modified peptides, O-GlcNAc sites (S852/T853, S1008/ T1009 and S1147) (Wong et al., 2020)

MEQKLISEEDLGTAPVYEGMASHVQVFSPTHQLQSSAFCSVKKLIEPSSNWDMTGYGSHSKVYSQ
SKNIPLSQPATTVSTSLPVNPNSLPYEQTIVFPGSTGHIVVTSASSTSVTGQLGGPHNLMRRS
TVSLLDTYQKCGLKRKSEEIENTSSVQIIIEHPPMIQNNASGATVATATTSTATSKNSGSNSEGD
YQLVQHEVLCSMTNTYEVLEFLGRGTFGQVVKCWKRGTEIVAIKILKNHPSYARQQIEVSILA
RLSTESADDYNFVRAYECFQHKNHTCLVFEMLEONLYDFLKQNKFSPPLKYIRPVIQQVATALM
KLKSLGLIHADLKPEINMLVDPSRQPYRVKVIDFGSASHVSKAVCSTYLQSRYYRAPEIILGLPF
CEAIDMWSLGCVIAELFLGWPLYPGASEYDQIRYISQTQGLPAEYLLSAGTKTRFFNRD TDSPY
PLWRLKTPDDHEAETGIKSKEARKYIFNCLDDMAQVNMTTDLEGSDMLVEKADRREFIDLLKKML
TIDADKRITPIETLNHPFVTMTHLLDFPHSTHVKSFCQNMEICKRRVNMYDTVNQSKTPFITHVA
PSTSTNLTMFTNNQLTTVHNQAPSSTSATISLANPEVSILNYPSTLYQPSAASMAAVAQRSMPLQ
TGTAQICARPDPFQQALIVCPPGFQGLQASPSKHAGYSVRMENAVPIVTQAPGAQPLQIOPGLLA
QQAWPSGTQQILLPPAWQQLTGVATHTSVQHATVI PETMAGTQQLADWRNTHAHGSHYNPIMQQP
ALLTGHVTLPAAQPLNVGVAHVMRQQPTSTSSRKSKHQSSVRNVSTCEVSSQAISSPQRSKR
VKENTPPRCAMVHSSPACSTSVTCGWDVASSTTRERQRQTIVIPDTPSPTVSVITISSDTDEEE
EQKHAPTSTVSKQRKNVISCVTVHDSPYSDSSSNTSPY SVQQRAGHNNANAFDTKGSL ENHCTGN
PRTIIVPPLKTQASEVLVECDSLVPVNTSHHSSSYKSKSSSNVTSTSGHSSGSSSGAITYRQQRP
GPHFQQQQPLNLSQAQQHITTDRTGSHRRQQAYITPTMAQAPYSFPHNSPSHGTVHPHLAAAAAA
AHLPTQPHLYTYTAPAALGSTGTVAHLVASQGSARHTVQHTAYPASIVHQVPVSMGPRVLPSPTI
HPSQYPAQFAHQTYISASPASTVYTGYPLSPAKVNQYPYI*

Amino acid sequence of the HA-tagged *Drosophila* Hipk protein

Labels: HA-tag + flanking amino acids, *Drosophila* Hipk amino acids (UniProtKB – Q9W0Q1), SIK target motifs (Φ x[HKR]xx[ST]xxx Φ) (Horike et al., 2003), putative SIK target sites (S133, S753, S858, T1084, S1195, S1290)

MYPYDVPDYALMAMEARIQMKTSYPPKASDFVDYAVAGGGSGFCGLGAGLSVRATSFYGDQTV
TATTGDTRHQEQQQQQLQQQQQQHILRQPATSASTSSVAAAATSKRKQTDCCGVDSYNSSHG
PPVQQDSSAAAGAGSV**GSKAGSGPGP**DGIGPISSLKTAHTKVATSGGHANTQPPSKRSSSGADGD
YQLVQHEVLYSLSAEYEVLEFLGRGTFGQVVKCWKRGTEIVAIKILKNHPSYARQGQIEVSILS
RLSQENADEFNFVRAFECFQHKNHTCLVFEMLEONLYDFLKQNKFSPPLKYIRPILEQVLTALL
KLKQLGLIHADLKPEINIMLVDPVRQPYRVKVIDFGSASHVSKTVCNTYLQSRYYRAPEIILGLPF
CEAIDMWSLGCVVAELFLGWPLYPGSSEFDQIRYISQTQGLPTEHMLNSASKTSKFFYRDVDSTY
PFWRLKTTEEHEAETNTKSKEARKYIFNCLDDIGQVNPTDLEGGQLLAEKTDREFIDLLKRM
TIDQERRLTPAEALNHSFTRLTHLVYVCNNVKASVQMMEVCRRGDFHTVQPASTLVTNFVPSS
TENMTFTINNQLTSQVQRLVRDGRPLAYEGLYQIYNGRSVARQYPQRTDSFQHQLVSNILCPPS
YQTMPSPTKHVVVGSATMQPPLQVPPQQYVNVPVPVSMVEPTSGQRMLLTNRVQASGVAWPQTGR
QMALVPSWPQQAPAHSLIVDSTPLFNVEEIYPKHHNLPRNDLKKESPAHH**IAKGN SYRVP**RHEK
KEHQQLSPVKRKVKESSPPHQQRYQRAAHVSPQYHAHNHCNYNGNSGYSASAGSVVASSAASSN
IVNGSSSSHHHPVVAHQPYSSSS**GHHIVSNCNA**ANGGAGGAVVYQQPPAHAHQHQHQQPHPQS
SQHPQHVQOPTITIHDTSPPTAVITISDSEDEGGAEAGGAQVPVLQRAHAQSOTSGSLLQHAPSS
SCSRSSAHQQPHPHPQQQQQQQINYGDHDPEARRHAAAAAAVGSPKHHHQQQQQPAPPPQQ
QQQQYQPQPPPQQVLPQPQPSIKYE PGQSQKKRILAMAQSECGYQPQVPSQPSAS**LPHIP TKQ**
EPAEFYPEYAAAPPQQLDTKRSSWAPTSSGSGVSALPLAHPKREAPSVAPISYVAPSVAAPPLAHS
KSSSASSSSSISAATAAAAAAAAAAVGPPSWGPPQ**VYRQPSQPPP**GSVGLPGSTQPPPSSVA
PHPHHHSHGHHHHQAGTPLGGSPSSTAAALLQPDHYAQGDIYRRPTVFVSQAAPSAYANRAVV
APP**PAHNSSSRQV**IPSHPLPAHIQIPTQYSQFGPLSPAQVAASKHAAHFAPTNIWYGAE *

In silico identification of putative O-GlcNAc sites in human HIPK2 and *Drosophila* Hipk

Human HIPK2 (a.a. 1-1198)

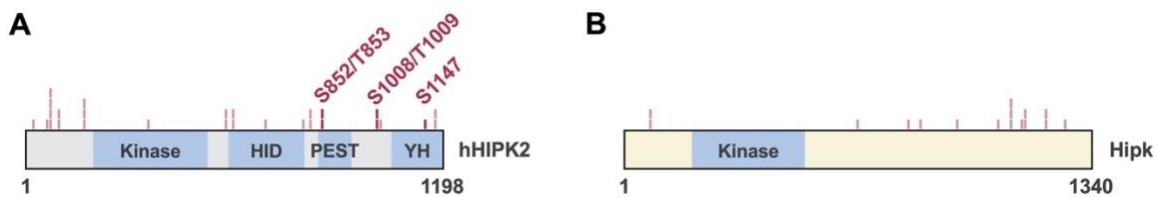
a.a. site	O-GlcNAc sites		
19	VFSPH	T	LQSSA
60	KNIPL	S	QPATT
64	LSQPA	T	TTVST
65	SQPAT	T	TVSTS
66	QPATT	T	VSTSL
68	ATTTV	S	TSLPV
96	GHIVV	T	SASST
97	HIVVT	S	ASSTS
168	VATAT	T	STATS
169	ATATT	S	TATSK
173	TSTAT	S	KNSGS
354	SASHV	S	KAVCS
575	THVAP	S	TSTNL
577	VAPST	S	TNLTM
598	NQAPS	S	TSATI
599	QAPSS	T	SATIS
687	AVPIV	T	QAPGA
797	RQQPT	S	TTSSR
820	STCEV	S	SSQAI
822	CEVSS	S	QAIISS
852*	SSPAC	S	TSVTC
886	PSPTV	S	VITIS
906	KHAPT	S	TVSKQ
927	HDSPY	S	DSSSN
974	VPPLK	T	QASEV
992	VPVNT	S	HHSSS
1008*	SSNVT	S	TSGHS
1009*	SNVTS	T	SGHSS
1018	SSGSS	S	GAITY
1147*	HQVPV	S	MGPRV
1176	TYISA	S	PASTV
1179	SASPA	S	TVYTG

Drosophila Hipk (a.a. 1-1340)

a.a. site	O-GlcNAc sites		
77	LRQPA	T	SASTS
78	RQPAT	S	ASTSS
668	VPVPV	S	MVEPT
819	GSVVA	S	SAASS
849	HAQPY	S	SSSGH
956	QHAPS	S	SCSRS
1075	PSQPS	S	SASLP
1113	SSWAP	T	SSGSG
1114	SWAPT	S	SGSGV
1115	WAPTS	S	GSGVS
1143	SYVAP	S	VAPPL
1151	PPLAH	S	KSSSA
1154	AHSKS	S	SASSS
1213	TQPPP	S	SVAPH
1214	QPPPS	S	VAPHF
1267	PTVFV	S	QAAPS

In silico predictions of O-GlcNAc sites by OGTSite (<http://csb.cse.yzu.edu.tw/OGTSite/>). The parameters of the prediction are as follows: motif specificity level: medium (80%); score: > 0.9. Predicted O-GlcNAc sites are shown in red, neutral amino acids in the putative OGT target motifs in green. *By MS/MS analyses, we identified S852/T853

S1008/T1009 and S1147 as O-GlcNAc sites in our study ([Wong et al., 2020](#)). a.a.
Amino acid.



Schematic diagrams showing the distribution of the predicted O-GlcNAc sites (light red) of human HIPK2 (**A**) and *Drosophila* Hipk (**B**). O-GlcNAc sites of human HIPK2 identified in our study ([Wong et al., 2020](#)) are labeled in dark red.